

Stellar radio beacons
for Galactic astrometry

Stellar radio beacons for Galactic astrometry

Proefschrift

ter verkrijging van
de graad van Doctor aan de Universiteit Leiden,
op gezag van Rector Magnificus prof.mr. C.J.J.M. Stolker,
volgens besluit van het College voor Promoties
te verdedigen op donderdag 12 maart 2020
klokke 15:00 uur

door

Luis Henry Quiroga Nuñez

geboren te Bogotá, Colombia
in 1989

Promotiecommissie

Promotors: Prof. dr. H. J. van Langevelde
Dr. A. G. A. Brown

Overige leden: Prof. dr. K. H. Kuijken
Prof. dr. A. G. G. M. Tielens
Prof. dr. Y. M. Pihlström University of New Mexico
Dr. A. Brunthaler Max-Planck-Institut
 für Radioastronomie
Prof. dr. H. J. A. Rottgering

ISBN: 978-94-6402-117-2

Cover design by Juan Sebastián Leal at Blackbird Studios (Colombia)

Dedicada a aquellos seres amados que se fueron
y que llegaron a mi vida durante este PhD:
Miguel & Chiara

*“Start by doing what is necessary, then do what is possible
and suddenly you will be doing the impossible”*

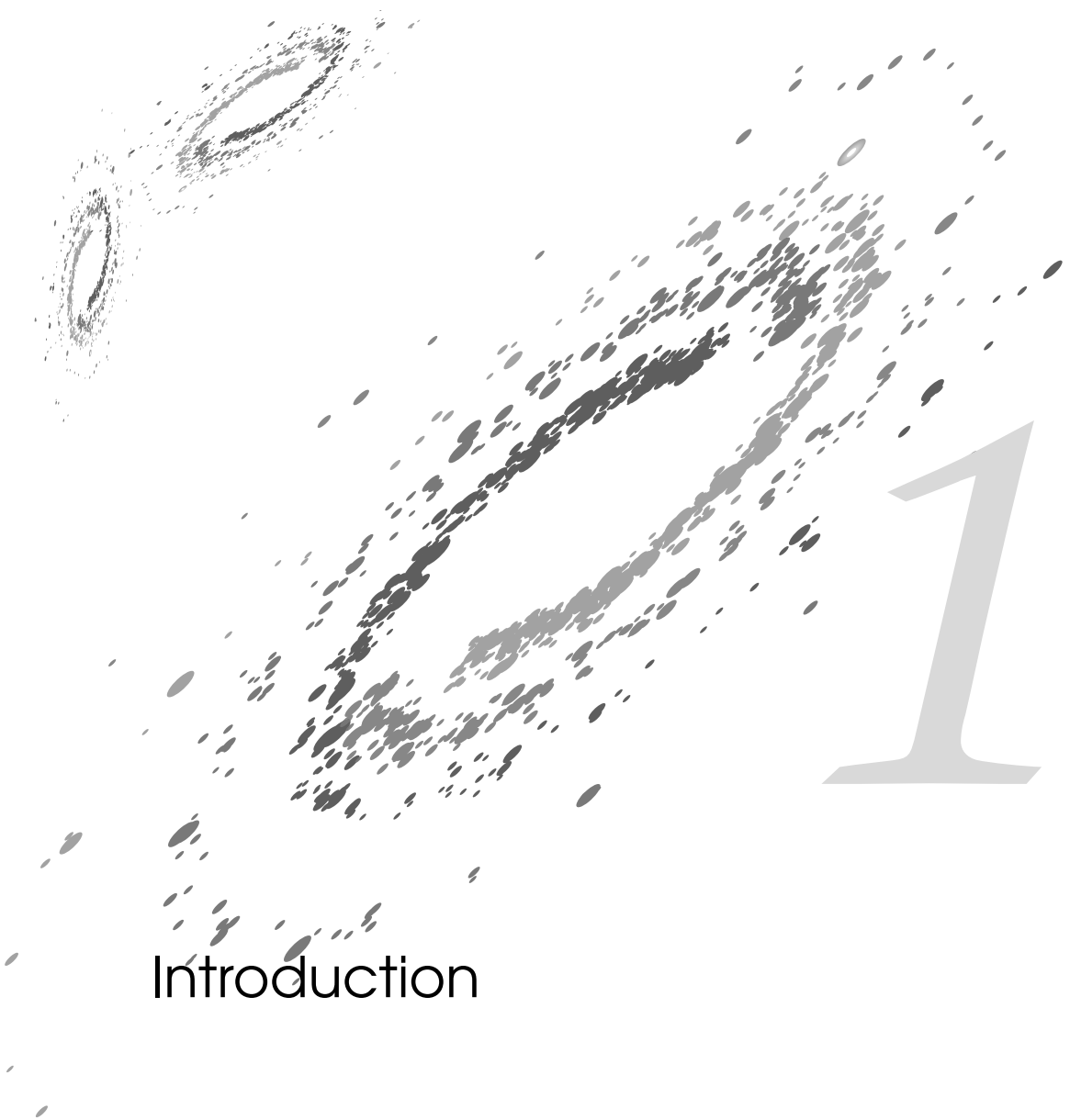
–Francesco d’ Assisi

Contents

1	Introduction	1
1.1	Historical review of the Milky Way	3
1.2	The importance of Galactic plane studies	5
1.2.1	Spiral Structure	5
1.2.2	The inner Galaxy: Galactic bulge	6
1.3	Precise astrometric measurements	8
1.3.1	Hipparcos mission	8
1.3.2	<i>Gaia</i> revolution	9
1.3.3	Advantages of radio astrometry	10
1.4	Masers as tracers of stellar populations	10
1.4.1	Maser theory in Astronomy	11
1.4.2	VLBI maser projects	14
1.5	This thesis	17
1.6	Outlook	19
2	Resolving the distance controversy for Sharpless 269: A kink in the Outer arm	23
2.1	Introduction	25
2.2	Observations	26
2.3	Results	27
2.3.1	Elongated water maser emission	27
2.3.2	Astrometric measurements for S269	30
2.3.3	Cross-matching with Gaia DR2	32
2.4	Discussion	32
2.4.1	Long-lived and extended water maser emission	32
2.4.2	S269 astrometric parameters	35
2.4.3	Membership in the Perseus or outer arm	37
2.4.4	Outer arm structure	38
2.4.5	Optical members of the same stellar association	40
2.5	Conclusions	41
2.6	Appendix	42
2.6.1	Additional Tables	42
3	Simulated Galactic maser distribution to constrain the Milky Way	45
3.1	Introduction	47
3.2	Model for the 6.7 GHz methanol maser distribution in the spiral structure	48
3.2.1	Initial parameters	49
3.2.2	Spatial distribution	49
3.2.3	Velocity distribution	52
3.2.4	Methanol masers represented in the model	53
3.2.5	Luminosity distribution	53
3.2.6	Error allocation	53
3.2.7	Fitting procedure	54
3.3	Results	55
3.3.1	Luminosity function for 6.7 GHz methanol masers	56

3.3.2	Galactic parameters and selection of sample	58
3.3.3	Parameter correlations	61
3.4	Discussion	62
3.4.1	Luminosity function of 6.7 GHz methanol masers	62
3.4.2	Galactic parameters analysis	62
3.5	Conclusions	65
4	Characterizing the evolved stellar population in the Galactic foreground	67
4.1	Introduction	69
4.2	Cross-match between radio, IR and optical observations	70
4.2.1	BAaDE target sample selection	73
4.2.2	Cross-match description	73
4.2.3	Refining the <i>BAaDE-Gaia</i> sample	75
4.2.4	Resulting cross-match: <i>local</i> sample	77
4.3	Results	77
4.3.1	Features of the <i>BAaDE-Gaia</i> sample	77
4.3.2	The <i>local</i> sample	83
4.4	Discussion	84
4.4.1	Absolute magnitudes for the foreground Mira population	84
4.4.2	Bolometric magnitudes for the foreground Mira population	84
4.4.3	Mira distribution around the Sun	88
4.4.4	Period-Luminosity relations	90
4.4.5	<i>SiO</i> maser emission from Mira variables	91
4.5	Conclusions	91
5	Different radio emission from Ross 867-8: Astrometric application at several λ	95
5.1	Introduction	97
5.2	Observations	98
5.3	Results	98
5.3.1	Radio Light Curves	101
5.4	Discussion	103
5.4.1	Identical stellar origin	103
5.4.2	Nature of the flare emission	103
5.4.3	Historical radio observations	103
5.4.4	Probability of observing during a non-flaring event	105
5.4.5	Comparison of stellar properties with respect to a similar binary system	105
5.5	Summary and conclusions	107
5.6	Appendix	108
5.6.1	SPAM pipeline for GMRT data on Ross 867-868	108
5.6.2	LOFAR observations	109
5.6.3	Radio observations for NVSS J171949+263007 and for Ross 867-8	109
	Bibliography	113
	Nederlandse Samenvatting	123
	English Summary	127
	Resumen en Español	131

List of Publications	135
Curriculum Vitae	137
Acknowledgments	139



Introduction

1.1 Historical review of the Milky Way

One hundred years before the publication of this thesis, the “Great Debate” took place at the Smithsonian Museum of Natural History in Washington D.C. At that time, there was a discussion about the actual dimensions and nature of our Galaxy led by Harlow Shapley and Herber Curtis. During the debate, divergent conclusions were drawn from the interpretation of the limited astronomical information available. Shapley explained that the Sun was located in what he defined as an island universe with an approximate size of 90 kpc surrounded by nearby smaller gaseous nebulae. He also suggested that other galaxies (or island universes) might exist but they were too far away, and thus undetectable. In contrast, Curtis explained that the Sun was centrally located in a smaller galaxy ($\lesssim 10$ kpc size) surrounded by other similar galaxies (<3 Mpc). Curtis argued that these distant galaxies were only visible near the Galactic poles because of the obscuring matter within the Galactic disk. Notably, Shapley and Curtis were equally right and wrong regarding their descriptions of the Milky Way. All in all, the main issue hampering this debate was the lack of reliable distance estimates that could be used to determine which objects were faint nearby or bright faraway sources. During the following years, several methods were used and refined to estimate precise distances in astronomy as we will briefly show. However, as I will highlight throughout this thesis, three specific methods stood out and have been widely used in astronomy to establish the fundamentals of our current understanding of the Galaxy: the trigonometric parallax, Hertzsprung Russel diagram main sequence fitting (spectroscopic parallax) and the period-luminosity relation.

Some insights about the “Great Debate” came at the end of 1902’s. Edwin Hubble (1929), on the one side, identified individual Cepheids in M31 and M33. He then used the period-luminosity relations to estimate distances to these satellite galaxies, i.e., 275 and 263 kpc respectively (Hubble 1926, 1929). During the same decade, Bertil Lindblad and Jan Oort also made some advances. On the one hand, Lindblad proposed a kinematic model of the Milky Way based on measurements of radial velocities and proper motions of individual stars (Lindblad 1927a,b). On the other hand, Oort estimated the location of the center of the Milky Way (at ~ 6.3 kpc in the direction of the Sagittarius constellation) as well as the solar rotational velocity (Oort 1927). Although by the beginning of the 1930’s some aspects of the Milky Way were already established (size, structure, rotational speed, rotational center and relative sizes and distances of close-by galaxies), the Galactic disk remained hidden due to the obscuring clouds of gas and dust. In fact, Robert Trumpler confirmed the presence of obscuring clouds of gas and dust by showing that the diameter of open stellar clusters diminished with distance less rapidly than the apparent brightness of the individual stars contained in the cluster (Trumpler 1930). Moreover, he showed that this matter of gas and dust estimated that the reduction of the apparent brightness of the stars was around 0.7 mag kpc^{-1} , which at some point will entirely block the light at optical wavelengths. Since this obscuration was mainly at shorter wavelengths, it produces a corresponding apparent reddening in the of stars.

In 1951, Walter Baade demonstrated that dark clouds and star-forming regions in the Andromeda galaxy were confined to the visible spiral arms (Baade 1951). Following this idea, Morgan et al. (1953) obtained spectroscopic parallaxes to 27 OB associations, HII regions and K giant stars. The distribution of these objects started suggesting a Galactic spiral structure, particularly three arm segments of three spiral arms close to the Sun. Thereafter, future investigations follow this path by enlarging the samples of young stellar objects and refining the spiral arm fitting (see e.g., Becker & Fenkart 1970).

Close to the beginning of the second half of the XX century, Van De Hulst (1949) proposed that the 21 cm emission (hyperfine emission line of neutral atomic hydrogen) would easily pass through the gas and dust. This conjecture triggered radio observations of Galactic hydro-

gen clouds (Oort, Kerr and Westerhout). By combining these observations with the kinematic theory proposed by Oort to interpret the radial velocity data coming from a spiral structure, the first accurate image of the structure within the Galactic plane was revealed. Subsequent studies included spectroscopic parallaxes in order to improve the distance accuracy to young stellar clusters that were already presumed to be tracers of spiral structure Humphreys (1976). Finally 1976, Geogelin & Geogelin (1976) combined precise astrometric measurements of HII regions and radial velocities of the spiral structure obtained at radio wavelengths to generate the first draft of our current understanding of the Galactic spiral model (see Fig. 1.1). Nowadays, although the fundamental Galactic parameter values have been exceedingly refined, our current consensus model of the Galactic structure basically follows the proposal made by Geogelin & Geogelin (1976).

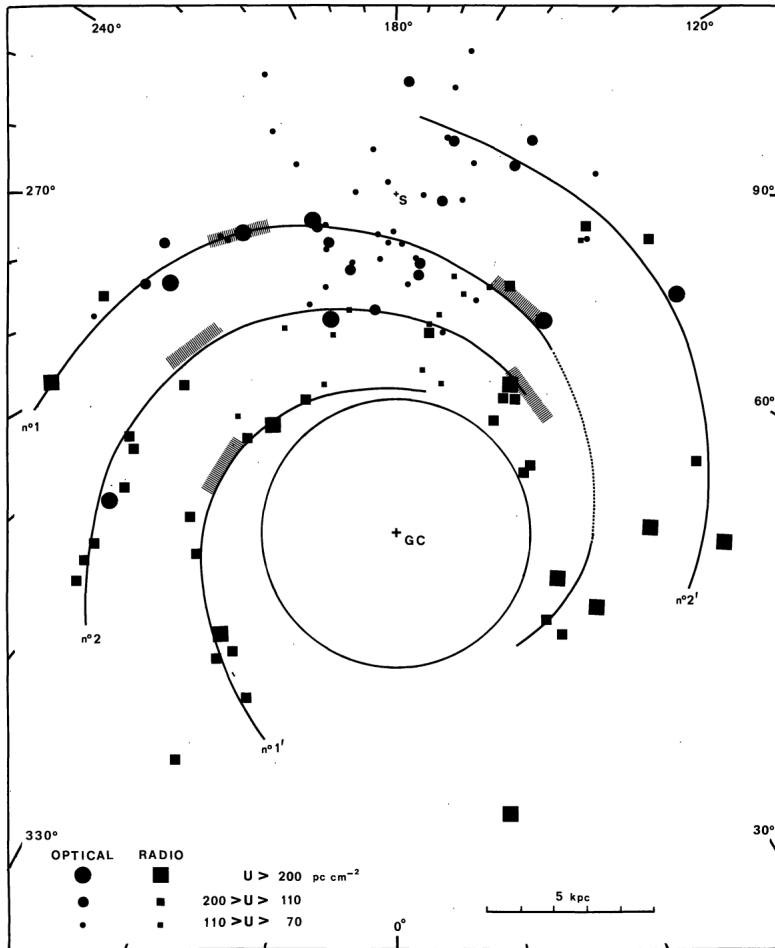


Figure 1.1: Spiral model of the Milky Way proposed by Geogelin & Geogelin (1976) using excited HII regions in the Galaxy. The positions of the Sun and the Galactic center are marked with an “S” and “GC”, respectively.

1.2 The importance of Galactic plane studies

The Milky Way represents the cornerstone of our understanding of the diversity of galaxies in the universe. The structure and kinematics of the gas and stars in the Milky Way can be studied with unique detail given our privileged position. In fact, we have already identified that our Galaxy has a pronounced spiral structure that includes a prominent central bar, and therefore, it is classified as a as a Hubble type Sb (Vaucouleurs type SB(rs)bc II) galaxy. Furthermore, there are two fundamental Galactic processes directly associated with the spiral structure and the bar: rotation and star formation. These processes are happening mainly in the Galactic plane, where the flat disk slowly rotates as a near liquid, producing spiral arms, which in turn, are constantly being populated with young stars. Gas and dust, enriched by heavy elements released in supernova explosions, are continuously condensing to form stars. All of these Galactic constituents (i.e., stars, dust, gas, etc.) radiate across the entire electromagnetic spectrum, from radio to X-rays. However, being well located within the Galactic disk, and thereby observing the Milky Way from within, making it very difficult to accurately map its large-scale morphology, notably in the inner Galaxy. The importance of a kinematic analysis made in the Galactic plane is that it clarifies the behavior of the Galaxy as a gravitational system, which leads to important conclusions about its mass, evolution and history (including previous mergers). In the following subsections, we describe the major structures of the Galactic plane: the spiral structure and the Galactic bulge.

1.2.1 Spiral Structure

Spiral galaxies have been documented by astrophotographers back to the end of the XIX century, since then, the hypothesis that the Milky Way harbors spiral structure gained attraction. This view was only confirmed until the Galactic spiral structure was resolved using radio observations. To begin, we can consider the Galactic model illustrated by R. Hurt (see background in Fig. 1.3), which is an informed artistic impression constrained by the available data (Churchwell et al. 2009) of the face-on Milky Way. Nowadays, the discussion of the Galaxy's structure is framed in terms of four major spiral arms (or two, see e.g., Drimmel 2000; Xu et al. 2018) and a central bar.

- The elongated central bar is considered to be a prominent feature of spiral galaxies. However, the physical mechanisms that generate this type of structure are still poorly understood. IR surveys revealed that in the Milky Way, we can distinguish two bar substructures. On the one hand, a “narrow” Galactic bar oriented about 45° with respect to the Sun's direction and about 8.7 kpc long. On the other hand, a “boxy” bar oriented about 22° with respect to the direction to the Sun about 6.5 kpc long.
- The Sagittarius-Carina arm seems to begin at the far end of the boxy bar, with a continuous and dense concentration of bright stellar clusters and High Mass Star Forming Regions (HMSFRs) along the arm. This arm extends from quadrant I up to quadrant IV, and it has a width of ~ 250 pc. It is the closest arm with respect to the Sun in the direction of the Galactic center (~ 1 kpc).
- The Scutum-Crux arm originates at ~ 6 kpc in the direction of the Galactic center at the near end of the narrow central bar and it arcs in front of the Galactic center. Additional information from Southern observatories is needed to confirm how this arm extends in the far side of the Milky Way.

- The Norma-Outer arm seems to originate at the near end of the boxy central bar. It circles behind the Galactic center, it curves outward beyond the Perseus arm and it reaches the anti-Galactic center region. Its nearest distance to the Sun is approximately 5.4 kpc, but plausible kinks in this arm have been suggested based on gas and stellar components evidence.
- The Perseus arm is the closest arm to the Sun (or in general with respect to the local arm). It is believed to be one of two dominant spiral arms (along with the Scutum-Crux arm). It originates at the far end of the narrow central bar, and, as the Outer arm, it curves around the Galaxy reaching the anti-Galactic center region.

Finally, I want to highlight that the first tracers used to map the structure of the Galactic plane were massive and very bright optical stars. The location of these stars can be determined by spectroscopic parallax, and since they have very short lifetimes, they are expected to remain close to their place of birth (similar to what it is assumed for masers in HMS-FRs, see section 1.3.3). Follow up surveys of young stellar clusters, OB associations and H II regions have been carried out to augment the original observations. Moreover, the observational limitations at optical wavelengths throughout the Galactic plane were overcome by radio observations of neutral hydrogen, and carbon monoxide, which in turn are associated with molecular hydrogen (H_2), a significant characteristic of star-forming regions (see e.g., Xu et al. 2018). The fact that radio wavelengths are not obstructed by interstellar matter is an important element of this thesis as we explain in the following section. It is worth knowing that other methods such as X-ray binary stars distributions, motions of variable stars, synchrotron emission, interstellar extinction, density stars based on infrared and optical surveys are further improving the tracing the spiral structure.

1.2.2 The inner Galaxy: Galactic bulge

The inner Galaxy is now understood to be strongly dominated by a massive bar, based on infrared morphology studies (e.g., Blitz & Spergel 1991; Dwek et al. 1995), the spatial distribution of red clump stars (e.g., Babusiaux & Gilmore 2005), maser stars (Habing et al. 2006) and the dynamics of red giants (Rich et al. 2007; Kunder et al. 2012). Indeed, an N -body model in which the bar forms via dynamical buckling from a preexisting massive disk fits the red giants dataset so well that $< 10\%$ of the bar might be in the form of a classical bulge, a result that is sustained by the clear demonstration of cylindrical rotation, a signature of strongly triaxial or boxy bulges (Howard et al. 2008). Recently, compelling evidence emerged for an additional X-shaped structure (see Fig. 1.2), similar to that seen in a number of extragalactic edge-on boxy bulges (McWilliam & Zoccali 2010; Wegg & Gerhard 2013). It has proven hard to isolate the population responsible for this structure and to study the kinematics (De Propris et al. 2011; Vázquez et al. 2013). However, there is a growing consensus that the X-shaped structure is dominated by the metal rich bar (Ness et al. 2012).

The stellar population in the inner Galaxy has a scale height of about 0.3 kpc, and a radial velocity dispersion of about 100 km s^{-1} . This population contains an old, relaxed stellar component ($< 10 \text{ Gyr}$), where its abundance distribution is broad, with a mean of $[Fe/H] \sim -0.25 \text{ dex}$ (McWilliam & Rich 1994). Given these conditions, most of the stars in the bulge are loss-mass stars that are expected to produce maser emission as the matter that is going in the outflows is the proper environment for the production of OH, H_2O , SiO masers (Habing et al. 2006). Very Long Baseline Interferometry (VLBI) observations of OH, H_2O , SiO masers in the Galactic plane have been used to study the kinematic conditions of the Milky Way. Habing et al. (2006) reported a strong effect in the corotational resonance at 3.3 kpc, a small effect

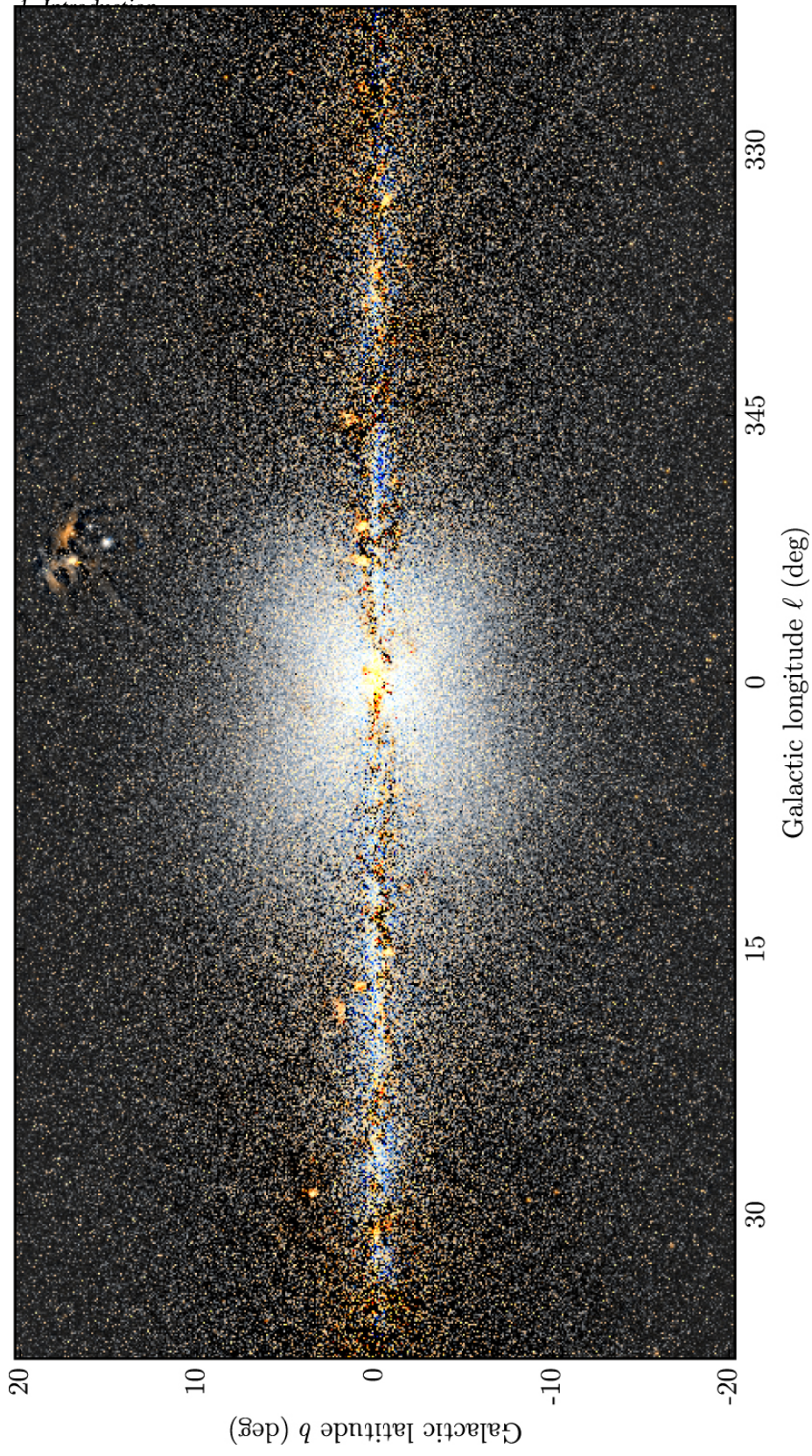


Figure 1.2: Milky Way view in Galactic coordinates obtained by WISE which reveals an X-shape morphology in the Galactic bulge similar to what it has been seen in other (edge-on) galaxies. Ness & Lang (2016).

of the Outer Lindblad Resonance at 5kpc and no effect of the Inner Lindblad Resonance at 0.8 kpc; those are important parameters in order to understand the evolution of our galaxy. Finally, the centre of our Galaxy contains a massive black hole. A dense cluster of stars surrounds Sgr A*, and proper motions indicate high velocities of up to $5,000 \text{ km s}^{-1}$ (hyper velocities stars) that have been also detected by *Gaia* at high Galactic latitudes. Thereby, the mass of the central black hole has been estimated to be $(3.3 \pm 0.7) \times 10^6 M_{\odot}$ (e.g., Ghez et al. 2000; Schödel et al. 2003). Future VLBI investigations are expected to resolved by the massive black hole in the Galactic center (Event Horizon Telescope).

The understanding of the structures in the Galactic plane previously related (i.e., spiral structure and Galactic bulge) strongly depends on precise astrometric measurements, where recently the *Gaia* mission and radio astrometric measurements have revolutionized our view of the Milky Way.

1.3 Precise astrometric measurements

In general, precise astrometric measurements are fundamental to research in any branch of astronomy. In particular, distance estimates (which are derived from accurate positional measurements) are crucial to establish the physics of astronomical objects. They are not only needed for tracking trajectories but also for estimating quantities such as mass, size, mass-loss and total emission energy of a body. A good fraction of our understanding of stellar, Galactic and extragalactic structures and their evolution over time heavily relies on this factor, yet distance determination still poses a challenging task.

Trigonometric parallax is a powerful and widely used technique to estimate unbiased distances in astronomy (Brunthaler et al. 2005; Reid & Honma 2014; Gaia-Collaboration et al. 2018). Precise parallaxes are obtained by measuring the apparent relative motions of an astrophysical object caused by the change of the position of the observer. The challenge then becomes detecting relative motion in astronomical scales with the required precision to produce physically relevant quantities. The measurement of the apparent relative motions to several stars is used to be made with ground-based observatories at optical wavelengths, but the technique was limited to nearby stars in the solar neighborhood Uppgren (1978). Since then, several studies have been developed, as in Monet et al. (1992), showing that modern ground optical based instruments can reach a high accuracy to determine the relative parallax. This technique started to show its greatest potential with the Hipparcos mission and later on with *Gaia*.

1.3.1 Hipparcos mission

It was not until 1989 that high precision in the absolute parallax was reached with the Hipparcos satellite. The Hipparcos mission, a scientific project of the European Space Agency (ESA), was designed to drastically improve the precision in the measurement of positions in the optical band and to provide absolute measurements of proper motion and parallax for a large amount of stars. In 1997, the Hipparcos Catalogue was published containing more than 118.000 stars for which positions, parallaxes, and proper motions were presented with accuracies of $0.8\text{--}3 \text{ mas}(\text{yr}^{-1})$. With this accuracy, precise distances could be obtained out to $\sim 200 \text{ pc}$. Nevertheless, this is only a fraction of the scales covered by the Milky Way, as seen in Figure 1.3 (Perryman et al. 1995).

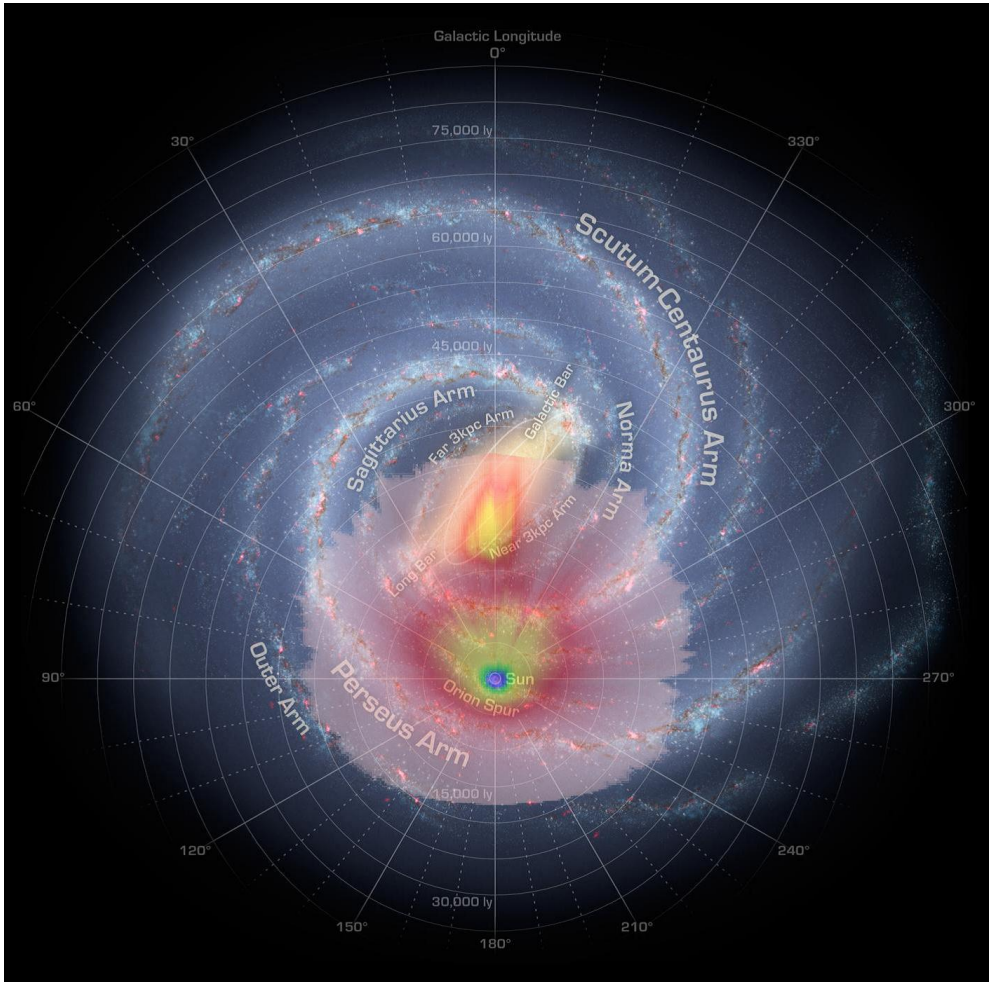


Figure 1.3: Comparison between the Galactic areas observed by Hipparcos in blue and green, and Gaia as red maps density distributions (X. Luri and CU2/DPAC). In the background, an informed artistic impression of the Milky Way as reference (NASA/JPL-Caltech/R. Hurt).

1.3.2 Gaia revolution

The new era for the astrometry in the optical regime has come with the *Gaia* satellite. *Gaia* is an ongoing mission of the European Space Agency which launched in 2013 (Perryman et al. 1995; Gaia Collaboration et al. 2016b). *Gaia* was designed to precisely measure 3D positions and 3D velocities of a billion of stars. Using this astrometric information, one can determine astrophysical properties of the stellar objects, such as effective temperature and total luminosity, in order to unravel the formation, structure, and dynamics of the Milky Way.

In 2016, the first *Gaia* data release (DR1) provided positions (0.3 mas uncertainty) and photometric data (0.03 mag uncertainty) in the *G*-band for ~ 1 billion stars. Light curves in the *G*-band for Cepheids and RR Lyrae were provided. Finally, parallaxes (0.3 mas uncertainty) and proper motions (1 mas yr^{-1} uncertainty) were estimated for ~ 2 million objects for which Hipparcos data was available from Tycho-2 catalogue (Tycho-*Gaia* Astrometric

Solution, TGAS).

The second *Gaia* data release (DR2) was accessible from 2018. In this data release, precise parallaxes, proper motions, and multiband photometry (G , G_{BP} , G_{RP}) were estimated for 1.3 billion stars. For different subsets of several (7 to 60) million stars, radial velocities, stellar effective temperature, extinction, reddening, radius and luminosity were published. Finally, and fundamental for this thesis, variability information was provided in the form of variable type classifications and light curves for 0.5 million stars.

1.3.3 Advantages of radio astrometry

Even with the high accuracy data that *Gaia* is providing, at low Galactic latitudes the absorption and scattered behavior of the electromagnetic radiation caused by dense regions of dust and gas complicate precise astrometric measurements. Stellar radio emission from powerful sources is not dramatically affected by the Interstellar Medium (ISM). Together with the low absorption index of the atmosphere at radio frequencies, we have a scenario in which radio astrometry provides complementary data to all the astrometric missions at different wavelengths, particularly in the Galactic plane. However, radio astronomy studies the sky properties between 10 meters (30 MHz) and 1 millimeter (300 GHz)¹, hence in order to reach high angular resolution measurements, single dish observations are insufficient. For instance, one of the largest single dish antennas, the Robert C. Byrd Green Bank Telescope (120 m diameter), can reach angular resolutions up to $\sim 30''$, which is comparable to the human eye at optical frequencies.

In order to reach higher angular resolutions using radio telescopes, radio astronomers use interferometry. By using at least two receivers, we are able to detect the signal from a source that is unresolved with one receiver. The signal will arrive first to one of the receivers and later to the other due to the difference in path that one signal has to cross with respect to the other (see Figure 1.4). The interference of these signals will cause fringes similar to those seen in interferometry experiments at optical wavelengths. If we take several pairs of receivers, each interferometer pair will measure a Fourier component of the entire brightness distribution of the source. In addition to the technology used to create an electronic delay, they also have to use high computational power to make the Fourier transform to recreate radio images from the interferometer data. The astrometric result is an image with the same angular resolution as an instrument of the whole collection. The resolution in this case goes as λ/B , where B is the baseline between the receivers.

The interferometry technique applied by connecting telescopes over long distances is known as VLBI. In general terms, each received signal from each radio telescope must be connected to a central station to correlate the data (see Fig. 1.4). This connection can be made by fiber-optic, coaxial cable or even by recording the measurements on tapes that are, then, transported to a central location where they are correlated.

1.4 Masers as tracers of stellar populations

During the past decade, several VLBI astrometry campaigns have shown their potential to detect radio stellar beacons with $\sim 1\mu\text{as}$ resolution. In order to obtain 6D phase space information from these radio emitters, they must be not only very bright (high brightness temperature that allows VLBI) but also possess narrow spectral lines (for radial velocity estimates from Doppler

¹In addition, it also studies wavelengths longer than about 20 centimeters (1.5 GHz), but at this point there are some irregularities in the ionosphere that distort the incoming radio signals via scintillation.

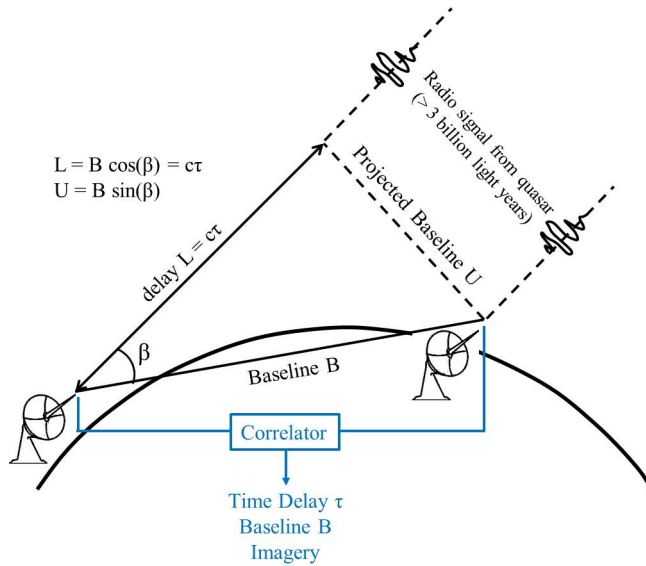


Figure 1.4: Principle of Radio Interferometry is illustrated here by two antennas which detect a radio sources a different time due to the delay (L). Image provided by Computational Physics INC.

effect). In the following subsections, we explain starting from the theory how astronomical masers satisfy those conditions, and therefore, are widely use for radio astronomic campaigns to trace the structure of the Galaxy (see Fig. 1.5) and even external galaxies (see Fig. 1.6).

1.4.1 Maser theory in Astronomy

Astronomical microwave amplification by stimulated emission of radiation (maser) has been detected for more than half century (see e.g. Litvak 1969). Maser emission can occurs and can be detected if a number of conditions are full filled: (1) there must be a sufficient abundance of molecules, (2) the gas must be out of thermal equilibrium and a population inversion must occur so that higher energy states of the atoms (or molecules) are over-populated, (3) a seed photon with the right frequency must be available and (4) a long amplification path must be present (see for example, Elitzur 1992). In order to explain the maser emission, consider a two level system (a ground state with energy E_0 and its first excited state E_1) with an energy difference between the levels of $E_{10} > 0$ and number densities of n_0 and n_1 respectively. In addition, a background radiation with a specific energy density u_ν at frequencies near $\nu = E_{10}/h$ (h is Planck's constant) is assumed to be present. It is possible to write the rate of change of n_1 as:

$$\frac{dn_1}{dt} = n_0 n_c k_{01} + n_0 \bar{n}_\gamma \frac{g_1}{g_0} A_{10} - n_1 n_c k_{10} - n_1 A_{10} - n_1 \bar{n}_\gamma A_{10}, \quad (1.1)$$

where n_c is the density of collisional species, k_{01} and k_{10} are the collisional rate coefficients, A_{01} and A_{10} are the Einstein coefficients, $\bar{n}_\gamma = c^3 u_\nu / 8\pi h \nu^3$ defined as the dimensionless photon occupation number, and g_1 and g_0 are the statistical weight of the two levels. In equation 1.1, the terms on the right correspond to the following processes: collisional excitation,

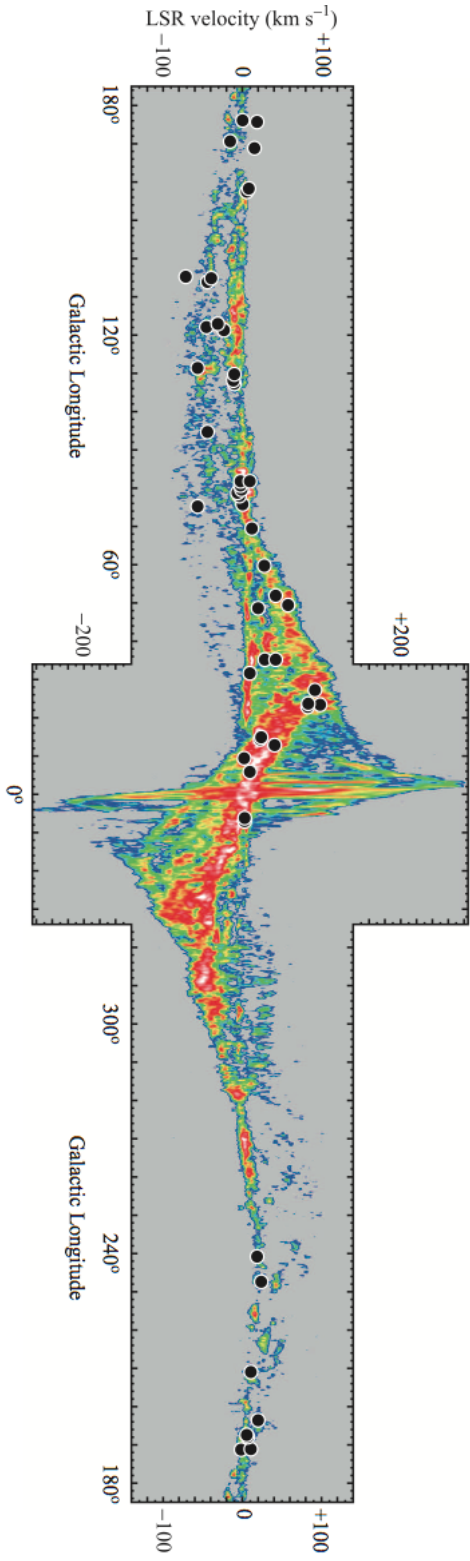


Figure 1.5: Location of 52 maser sources for which accurate astrometric data is available, superposed on the longitude-velocity diagram of CO (Honma et al. 2012).

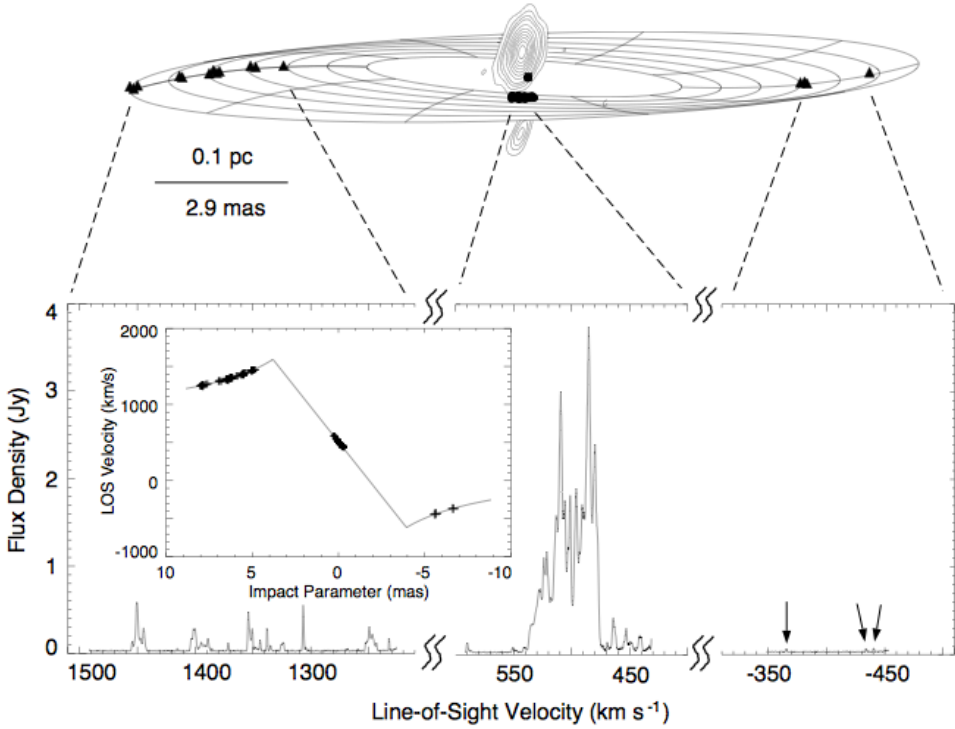


Figure 1.6: The upper panel shows the best-fitting warped disk model for the galaxy NGC4258 overplotted on actual maser positions as measured by the VLBA. The total power spectrum is displayed in the lower panel (Herrnstein et al. 1999).

radiative excitation, collisional deexcitation, spontaneous emission and stimulated emission, respectively. Positive terms correspond to populating processes and negative to depopulating processes. Under specific conditions, a process may act to “pump” the excited state by radiative excitation or collisional excitation to a higher level that then decays back to level (1). If this process is faster than the depopulating processes, the populations may satisfy the following relation $n_1 > g_1 n_0 / g_0$.

Therefore, the excitation temperature $T_{\text{exc},10} = E_{10} / k \ln\left(\frac{n_0 g_1}{n_1 g_0}\right)$ (k denotes the Boltzmann constant), is negative and, it can be shown, that stimulated emission is stronger than radiative de-excitation. As an additional consequence of population inversion, the absorption coefficient ($k_\nu \propto (1 - n_1 g_0 / n_0 g_1)$) and the optical depth ($\tau_\nu = \int k_\nu dS$; S =surface) are also negative. Finally, The antenna temperature T_A , which is a measured quantity in radio astronomy, is proportional to the emission I_ν and it can be written as:

$$T_A = T_A(0)e^{-\tau_\nu} + \frac{h\nu/k}{e^{kT_{\text{exc}}}}(1 - e^{-\tau_\nu}). \quad (1.2)$$

Given that $\tau_\nu < 0$, then $e^{-\tau_\nu} > 1$ indicating that there is an amplification of the emission rather than attenuation. This exponential amplification of the seed radiation, caused by the population inversion (created by collisional or radiative processes), can reach a critical value resulting in a “saturated” maser. In this maser, the amplification is linear with respect to the

path length rather than exponential and because of the total gain depends on the path length, the maser radiation is even more beamed (Elitzur 1992; Pandian 2007). All in all, the emission can reach beamed high brightness temperatures that allow using masers as optimal targets for high-resolution VLBI observations.

1.4.2 VLBI maser projects

Maser emission is associated with both the early and late stages in the life of a star. Galactic maser emission has been detected in the cores of dense molecular clouds that are regions of active star formation (so-called interstellar masers), and also around late-type stars, in which case the masers are referred to as circumstellar. Maser radiation probes small-scale structures in these sources and is now used to measure distances by (1) kinematic means (the equivalent of the classic moving cluster method), and (2) trigonometric parallax Reid et al. (2019). In the following subsections, two major maser projects that are the basis of this thesis are described. Each project is observing different maser species in the Galactic plane, unraveling different stellar populations in the spiral arms and the inner Galaxy. Additionally, although individual radio continuum studies have shown their potential to enlighten the physical processes behind radio stellar emission, VLBI stellar observations could provide additional resolution and sensitivity to detect planetary systems at radio frequencies (Katarzyński et al. 2016).

Finally, it is worth mentioning that although this thesis focuses on maser emission in the Milky Way, extragalactic maser emission has also been detected and studied. These extragalactic detections have been used to study nearby galaxies (Brunthaler et al. 2005) as well as cosmological parameters. In fact, the Megamaser Cosmology Project (MCP) is trying to improve the Hubble Constant value (to a prediction of 3%) by measuring the distance to 10 galaxies in the Hubble flow using VLBI data.

Bar and Spiral Structure Legacy Survey

The Bar and Spiral Structure Legacy (BeSSeL²) is a VLBA Key Science project aiming to study the spiral structure and kinematics of the Milky Way (Reid et al. 2009a, 2014). This survey uses VLBI arrays to detect water (22 GHz) and methanol (6.7 & 12.2 GHz) maser emission directly associated with young massive stars and HII regions. The spatial and kinematic distributions of these objects seem to trace the Galactic spiral structure. For more than ten years, the BeSSeL survey has refined data processing techniques to reach comparable parallax uncertainties with respect to *Gaia* in regions where optical measurements are limited by extinction.

The stellar targets are observed at different epochs over a period of a year to estimate accurate positions, distances, proper motions and radial velocities (from the maser lines via the Doppler effect) of these HMSRFs. The motion of water (in the outflow) and methanol masers (in the disk) are averaged to estimate the motion and position of the massive central object (see Fig 1.7). Given this 6D phase-space information, the position for each spiral arm is estimated as well as the fundamental parameters of the Galaxy such as the distance to the Galactic center (R_0), the circular rotation speed of the Sun (Θ_0), the rotation curve and the 3D peculiar motion of the Sun ($U_\odot, V_\odot, W_\odot$).

Currently, the BeSSeL survey has published precise astrometric data for more than 150 sources. This has allowed us to locate several spiral arms (see Fig 1.8). In their most recent publication, Reid et al. (2019) determined a distance to the Galactic center of $R_0 = 8.15 \pm 0.15$ kpc, solar rotation speed $\Theta_0 = 236 \pm 7$ km s⁻¹, and a flat rotation curve (-0.2 km s⁻¹ kpc⁻¹).

²<http://bessel.vlbi-astrometry.org/>

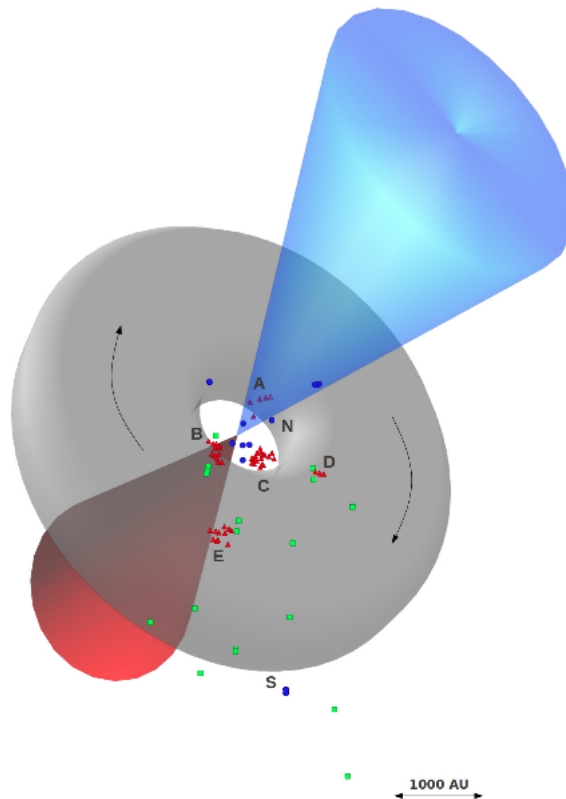


Figure 1.7: Three-dimensional sketch of a massive star-forming region (NGC 7538-IRS 1). The two cones are the red- and blue-shifted part of the large-scale molecular bipolar outflow. The triangles, circles, and boxes represent the CH_3OH , H_2O and OH masers detected, respectively (Surcis et al. 2011).

The BeSSeL survey continues with additional VLBI observations of masers associated with HMSFRs, improving constraints on the size and morphology of the Milky Way, as well as refining its fundamental parameters, and structure.

Bulge Asymmetries and Dynamical Evolution Project

To a great extent, surveys in the optical/IR bands have begun to reach impasses that cannot be easily resolved with increases in sample sizes. Red giant maser sources, as can be exploited with ALMA, VLA, and the VLBI arrays, offer a bold new approach to address the most pressing problems in the study of the bulge/bar. Evolved AGB stars that harbor several maser species (see Fig 1.9), particularly SiO maser emission are part of an older, dynamically relaxed population in the inner Galaxy. The dynamics of such evolved stars still carry the signature of past star-formation and merger events (Pasetto et al. 2016). In this context, the Bulge Asymmetries and Dynamical Evolution (BAaDE³) collaboration has made considerable progress by constructing a sample of $\sim 30,000$ stellar targets of SiO masers candidates in the Galactic plane and comparable to the 20,000 stellar counterparts in optical surveys (Sjouwerman et al.

³<http://www.phys.unm.edu/~baade/>

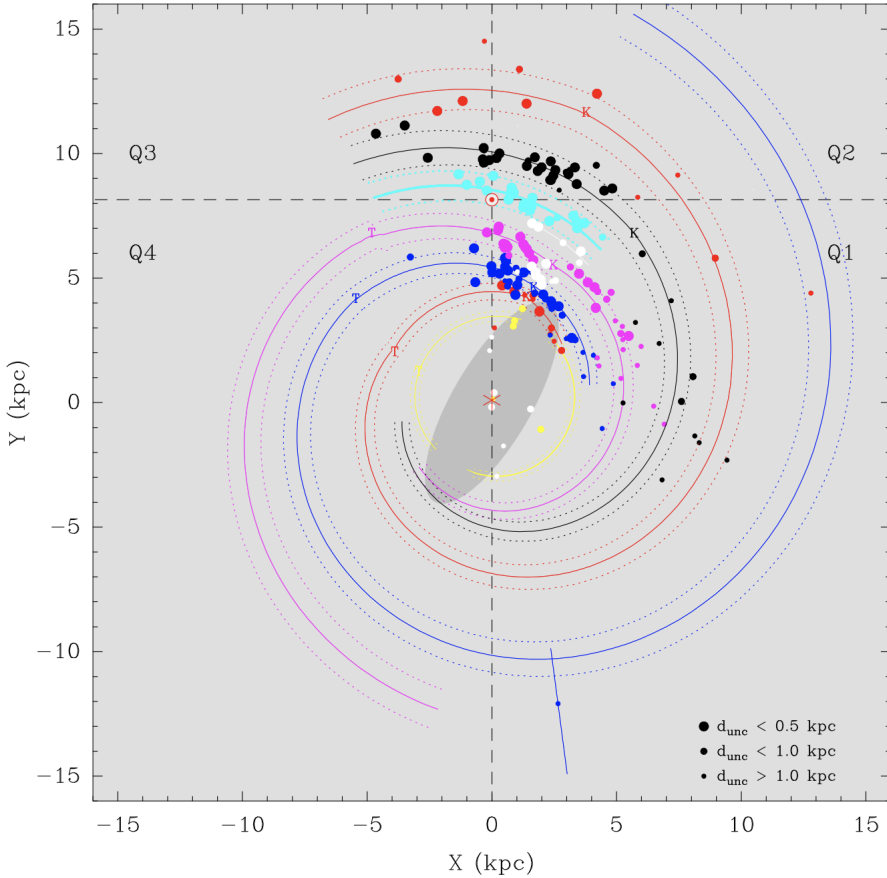


Figure 1.8: Plan view of the Milky Way from the north Galactic pole showing (1) the positions of the high-mass star-forming regions measured by the BeSSeL survey and (2) the inferred positions of the spiral arms (Reid et al. 2019). For these star-forming regions precise trigonometric parallaxes were measured using different maser species. In this view, the Sun is located at $(0, 8.15)$ kpc and the Galaxy rotates in clockwise direction.

2015). Indeed, optical surveys of the bulge are a powerful approach to learn about the populations and dynamics in the less reddened and obscured regions $|b| > 4^\circ$. By using SiO masers, which are detectable in red giants spanning a wide range in luminosity, the BAaDE project has the possibility of densely sampling the highest extinction, most crowded regions of the Milky Way: the plane and the Galactic center.

The sample of 30,000 evolved stars are being observed at the frequencies of the SiO maser (43 GHz and 86 GHz) using the VLA and ALMA for which extremely accurate line-of-sight stellar velocities ($\sim 1 \text{ km s}^{-1}$), flux densities and positions are determined. This number of sources is large enough to trace complex structures and minority populations that are partially obscured by extinction in optical campaigns. The velocity structure of these tracers is to be compared with the kinematic structures seen in molecular gas near the Galactic center, and thereby highlight kinematically coherent stellar systems, complex orbit structure in the bar, or stellar streams resulting from recently infallen systems. Preliminary statistics of the flux

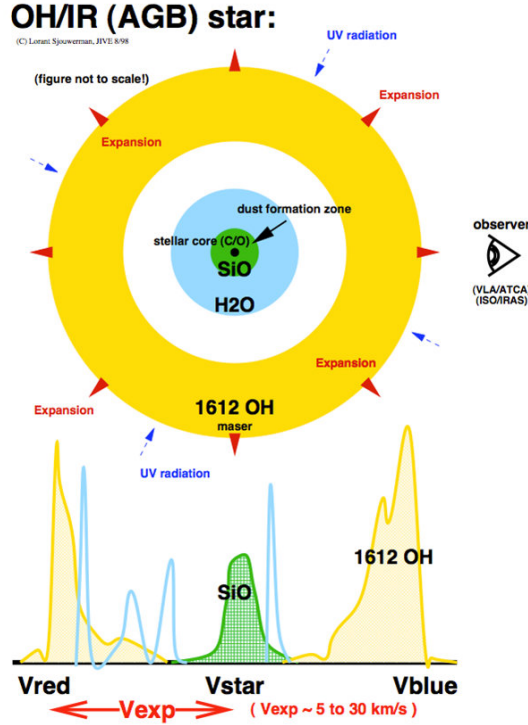


Figure 1.9: Schematic view of the an evolved star and the different regions where specific molecules are been formed. Excepted maser emission lines from those molecules (affected by Doppler effect in the line of sight) are expected to be detected as it shown in the lower panel. Image courtesy: Lorant Sjouwerman (NRAO).

density distribution and analysis of the population of SiO stars through IR association already shows exciting results in which very old and younger AGB stars in the inner Galaxy (see Fig. 1.10) show different kinematics (Stroh et al. 2018; Trapp et al. 2018). Finally, modeling of the bar and bulge dynamics will be done using the new kinematic information in the inner Galaxy region. The BAaDE project also identifies sufficiently luminous SiO masers suitable for follow-up orbit and parallax determination using VLBI. The specific aim of BAaDE is to eventually determine in detail orbits of stars supporting the stellar bar.

1.5 This thesis

In this thesis, I researched stellar radio emitters and their counterparts at different wavelengths throughout the Galactic plane. In each investigation, the astrometry was refined to provide insights about the stellar population in different environments. Moreover, these stellar populations were used (1) to trace different Galactic structures, and for some cases, (2) to further investigate particular astrophysical objects. Chapter 2 and 3 are investigations made in the context of the BeSSeL survey for which we used HMSFRs to trace the spiral structure, as well as the fundamental parameters of the Milky Way. In both investigations, high fidelity VLBI

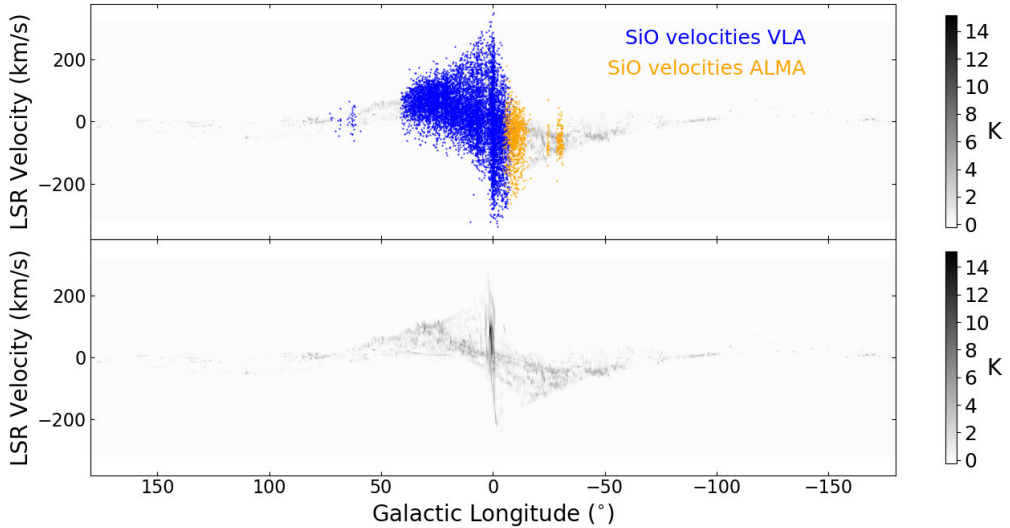


Figure 1.10: Velocity with respect to the Local Standard of Rest (LSR) as a function of the Galactic longitude for the SiO masers detected by the BAaDE project with the VLA and ALMA. The figure also shows the CO emission ($J = 1-0$) in grayscale (Dame et al. 2001).

observations were used to refine the astrometry of the stellar beacons analyzed. In chapter 4, we used another type of maser bearing stellar population, i.e., evolved stars. Although these stars are part of more relaxed population mainly found in the bulge, we focus on the solar neighborhood ($<2\text{kpc}$), where we can estimate precise distances by cross-matching and refining data from IR and optical surveys. This research was made in the context of BAaDE project, using a preliminary data release. Finally in chapter 5, we present an interesting result that showed up when we were inspecting the astrometry of low frequency archival radio data from the Giant Metrewave Radio Telescope (GMRT). The abrupt change in position and flux of one source triggered a whole investigation into the nature of flare emission from a binary system composed of two similar dwarfs with very different behavior at radio frequencies. In the following paragraphs, I expand each investigation in more detail.

In Chapter 2, we present a maser astrometry analysis of the star-forming region S269, an HII region with strong water maser emission that has been monitored for more than 20 years. Based on new, high fidelity multi-epoch observations using the VLBA at 22 GHz (part of the BeSSeL survey), we estimate the 6D phase-space information for this source, resolving the distance disagreement previously found in VERA data. We compare the new distance of S269 (4.15 kpc) with the *Gaia* astrometry of young, early-type stars that would be likely members of the same stellar association finding three candidates. The location of S269, at a distance of 4.15 kpc roughly in the direction of the Galactic anti-center, makes the astrometry of this source very significant for the model of the spiral structure of our Galaxy and its rotation curve. We have found that the new astrometry of S269 is still in agreement with a flat rotation curve. Its 3D position, together with the positions of a number of other BeSSeL targets indicate a more complex structure of the Outer arm than previously inferred. Three scenario's are presented, of which we favor the one that has a kink in the Outer arm, dividing the arm in two segments (at $l = 140^\circ$) with different pitch angles.

In Chapter 3, I present a model that can be used to test with what confidence one can esti-

mate the fundamental Galactic parameters from maser observations from the BeSSeL survey (water and methanol masers astrometry from star-forming regions). We simulate the BeSSeL database, which consists of astrometric information of masers associated with Galactic young massive stars. The model was compared with blind observational surveys (MMB and Arecibo surveys) in order to refine the simulations, but also to determine the luminosity function of methanol masers. We test different mock samples to investigate possible quantitative biases in the Galactic parameters. The results show that the Galactic parameters can be established robustly and with high accuracy using only sources in the Northern hemisphere (where most of the radio telescopes are located). However, we also quantitatively prove that data from future Southern observatories will reduce the uncertainties and inter-correlations between some Galactic parameters, besides tracing the spiral arms and —notably— the bar.

In Chapter 4, we cross-match the entire BAaDE sample ($\sim 30,000$ AGB stars) with 2MASS, and *Gaia* for a subsample of BAaDE targets. We show that IR counterparts can be easily identified, while *Gaia* matching is more restricted given extinction at optical wavelengths in the Galactic plane. These multi-wavelength cross-matches compile samples of approximately 2,000 evolved stars around the Sun with precise positional information as well as radio detections of SiO maser emission (radial velocities and flux densities) for a subsample. Variability information from *Gaia* was also used to test period-luminosity relation for a population of faint AGB stars around the Sun and compared with the results obtained in the Magellanic Clouds. All these observables are being used to characterize the stellar population of evolved stars within 2 kpc around the Sun, which was found to be predominately Long Period Variables, optically detectable Miras and carbon stars. The characterization of this stellar population was made in terms of luminosity, variability and dynamics.

Finally, in chapter 5 we present low frequency archival images from the GMRT that were observed to investigate a distant cluster of galaxies. However, the data also show a flare Galactic source that coincides with the position of Ross 867 in optical surveys. This star is part of a binary system with Ross 868, where both dwarfs have been categorized as flaring stars. More interestingly, the stars share several stellar features, however, after reviewing archival data from several radio observatories from 1984 up to 2017, only Ross 867 has been detected in radio frequencies. Given that the binary system has a large orbital separation, we conclude that the detection of radio emission from only one component of the binary points to either significantly different magnetic field topologies or dynamo mechanisms between the two stars. Finally, we emphasize that Ross 867-8 provides a coeval laboratory for future investigations in order to constrain the stellar properties linked to the radio flare emission detected in M dwarfs. We expect that in the future, VLBI observations of Ross 867 and similar stars can be used to link the optical and radio reference frames (Lindgren 2019).

1.6 Outlook

In this thesis, I have shown how astrometric measurements of stellar radio beacons, together with information at other wavelengths, can be used to study different components of the Milky Way, particularly spiral arms, stellar populations, dynamics of stellar groups and specific individual sources in the Galactic plane. In this area, the radio astrometry can provide more accurate results than in any other band. However, it is through the synergy between different spectral bands that a deeper understanding of stellar and Galactic processes can be reached.

This thesis has demonstrated show how masers coming from different stellar populations (young massive and evolved mass losing stars) offer a unique opportunity to sample the dynamical structure of the Galaxy (Habing et al. 2006; Reid & Honma 2014). On the one hand,

water and methanol masers are associated with very young stars, still tied to the dissipative gas component of the Galaxy; astrometry of these provides clues on the rotation curve of the Galaxy and the location of the spiral arms (Reid et al. 2014; Quiroga-Nuñez et al. 2017). On the other hand, evolved AGB stars, such as Mira variables producing SiO and OH masers are part of an older, dynamically relaxed population. By matching these findings with surveys at other bands, we are starting to characterize the evolutionary status of the evolved stellar population in the Galactic plane. This would constrain the dynamics of the Galaxy, notably the existence of a bar associated with the inner bulge (Blitz & Spergel 1991; Rich et al. 2007). Moreover, it can be anticipated that the dynamics of such evolved stars still carry the signature of past star-formation and merging events (Pasetto et al. 2016). Finally, VLBI with future southern radio arrays (as SKA) will allow us to do many more sources with substantial better accuracy, because of the improved sensitivity and better calibration options, particularly at 6.7 GHz (methanol maser emission). Below, I add some future work in the field that I am expecting to complete in the following years.

***Gaia*-VLBI**

Gaia detectors are known to become saturated for bright sources, and hence, inaccurate distance estimates are expected for bright stars. VLBI astrometry can offer an independent and supporting technique that validates *Gaia* observations for very bright stars in the Galactic plane, but also to the rotation of the reference frame and parallax zero point Lindegren (2019). Based on the BeSSeL survey, we can establish an accurate and scalable method for inverse phase-referencing using SiO masers in order to propose VLBA follow-up for several BAaDE targets and, therefore, obtain 6D phase-space information. A VLBA pilot project targeting four Mira variables with confirmed *Gaia* counterparts was recently observed aiming to determine extremely accurate line-of-sight stellar velocities and precise positions.

Besides this fundamental comparison of *Gaia* astrometry with VLBI, we are particularly interested in aligning the OH maser and optical photosphere with greater accuracy. Using the EVN baselines at 18cm, we can reach a resolution of around 10 mas and possibly sub-mas astrometric accuracy using the latest advances in radio astrometry (Dorson and Rioja, Orosz). It has been already argued that the alignment was consistent with a model in which the brightest, most blue-shifted spot originates from the front of the shell, exactly on the line of sight to the star (van Langevelde et al. 2019). This is predicted to happen if the radio emission from the stellar surface provides the seed photons for the maser amplification. New *Gaia* data and VLBI measurements would allow us to test this alignment with improved accuracy.

Next step BeSSeL

Future radio observatories (such as the ngVLA, SKA2-Mid, African VLBI Network) as well as ongoing projects as the “BeSSeL Survey South” (currently under development in Australia at the University of Tasmania) will complete the mapping and then generate a better 3D positional distribution of masers in our Galaxy. This will allow us (1) to understand better the kinematics of the galaxy and (2) to determine the fundamental Galactic parameter values with even higher accuracy, which is crucial to calibrate Galactic and extragalactic measurements. In support of this, Galactic simulations complement the observations by demonstrating their robustness and potential. Moreover, simulated distributions of the sources on the sky provide a framework for the observational conditions required for future radio astrometric campaigns.

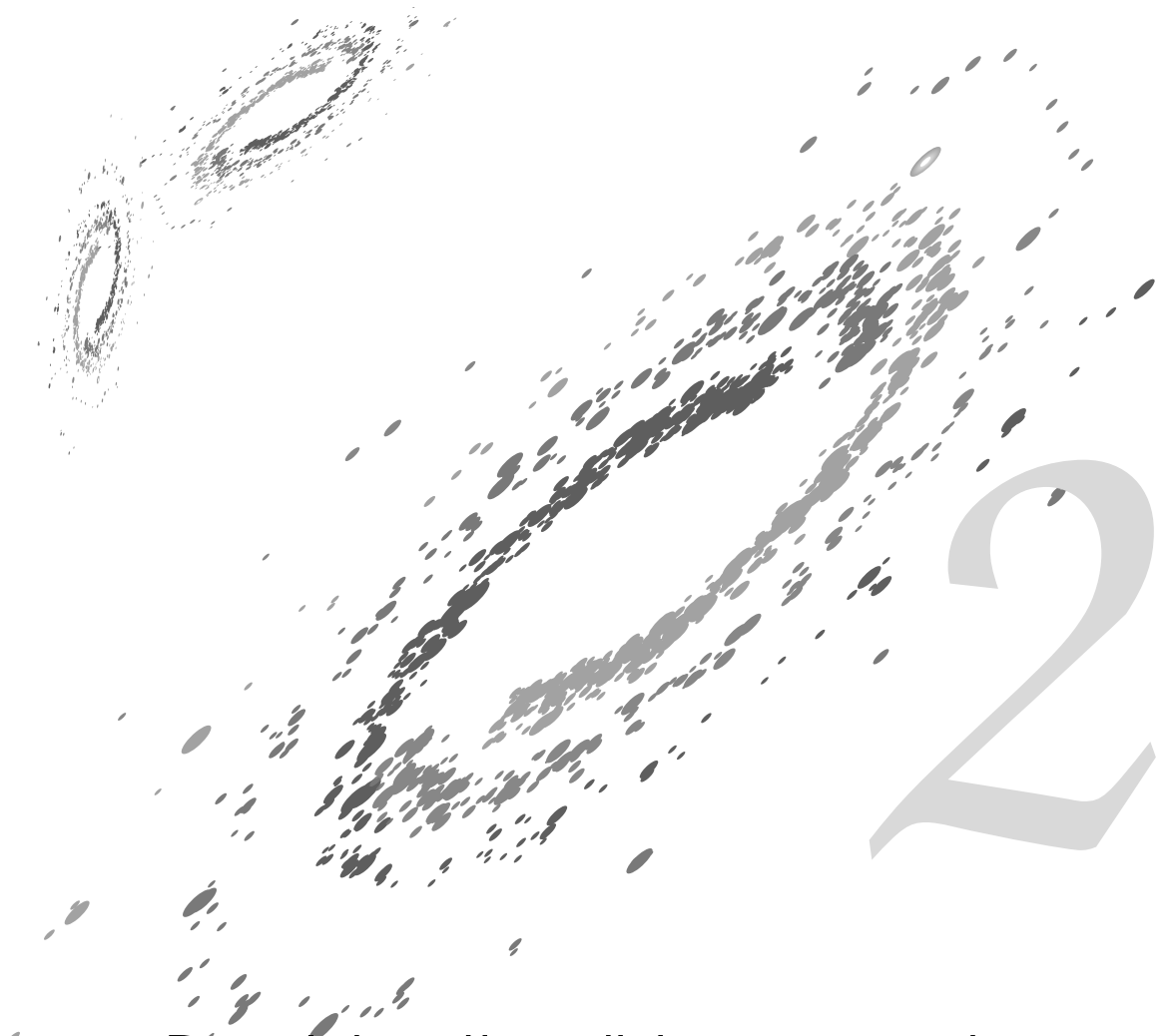
For the BeSSeL survey, I have recently started a campaign to cross-matching VLBI astrometric measurements of HMSFRs in the closest arms with IR catalogs and *Gaia*. We are

attempting to accurately describe the spiral arms position as well as quantify the physical parameters of the stellar populations present in these structures.

Next step in BAaDE

We are expecting that the distribution of BAaDE targets in 6D phase-space can be measured to constrain the dynamics of the inner Galaxy. Notably, we have a chance to resolve the populations associated with the Galactic bar Rich et al. (2007), and the X-shaped structure Vásquez et al. (2013). However, astrometric measurements of evolved stars using SiO masers present several complications such as unstable structure close to the stellar surface, and lack of calibrators at X and Q bands which are crucial for phase-referencing (Min et al. 2014). In most cases, the SiO masers are bright enough to allow for reverse phase-referencing, but even so, having nearby calibrators is critical at high frequency where coherence times are short. For this, recent EVN and VLBA proposals have made progress detecting potential calibrators which are key for making progress with VLBI astrometry of these inner Galaxy targets. Moreover, a new VLBA proposal for Mira variables with SiO maser emission located out of the Galactic plane was ranked with the highest priority, and it was observed in 2019. Progress will lead to a new VLBA astrometric proposal to obtain parallax and proper motions for a BAaDE subsample with confirmed *Gaia* counterparts.

I will expand my simulations of maser distributions in the Milky Way to include the inner Galaxy. For this, various key processes that have yet to be modeled must be implemented, such as maximum likelihood estimators for evolved stars in the presence of the Galactic bar in order to make full use of *Gaia* DR3 data. Additionally, I aim to model the source population in order to optimize future astrometric observations using VLBI arrays. Not only will I predict the accuracy that can be reached, but also, the uncertainties in stellar parameters that are expected for a wide range of instrumental conditions. Finally, it is exciting that new wide-band systems will be able to observe the (non-thermal emission) associated with active stars. The μ Jy sky could be full of targets for which high accuracy astrometry is possible, even to the level that we can detect planets.



Resolving the distance controversy for Sharpless 269: A kink in the Outer arm

Quiroga-Nuñez, L. H.; Immer, K.; van Langevelde, H. J.; Reid, M. J. & Burns, R. A. *Resolving the distance controversy for Sharpless 269: A possible kink in the outer arm*. 2019, A&A, 625, A70.

Abstract

Sharpless 269 (S 269) is one of a few HII regions in the outer spiral arm of the Milky Way with strong water maser emission. Based on data from the Very Long Baseline Interferometry (VLBI) Exploration of Radio Astrometry (VERA) array, two parallax measurements have been published, which differ by nearly 2σ . Each distance estimate supports a different structure for the outer arm. Moreover, given its large Galactocentric radii, S 269 has special relevance as its proper motion and parallax have been used to constrain the Galactic rotation curve at large radii. Using recent Very Long Baseline Array (VLBA) observations, we accurately measure the parallax and proper motion of the water masers in S 269. We interpret the position and motion of S 269 in the context of Galactic structure, and possible optical counterparts. S 269's 22 GHz water masers and two close by quasars were observed at 16 epochs between 2015 and 2016 using the VLBA. We calibrated the data by inverse phase referencing using the strongest maser spot. The parallax and proper motion were fitted using the standard protocols of the Bar and Spiral Structure Legacy survey. We measure an annual parallax for S 269 of 0.241 ± 0.012 mas corresponding to a distance from the Sun of $4.15^{+0.22}_{-0.20}$ kpc by fitting four maser spots. The mean proper motion for S 269 was estimated as 0.16 ± 0.26 mas yr⁻¹ and -0.51 ± 0.26 mas yr⁻¹ for $\mu_\alpha \cos\delta$ and μ_δ respectively, which corresponds to the motion expected for a flat Galactic rotation curve at large radius. This distance estimate, Galactic kinematic simulations and observations of other massive young stars in the outer region support the existence of a kink in the outer arm at $l \approx 140^\circ$. Additionally, we find more than 2,000 optical sources in the Gaia DR2 catalog within 125 pc radius around the 3D position of the water maser emission; from those only three sources are likely members of the same stellar association that contains the young massive star responsible for the maser emission (S 269 IRS 2w).

2.1 Introduction

The Very Long Baseline Interferometry (VLBI) Exploration of Radio Astrometry (VERA¹) project and the Bar and Spiral Structure Legacy (BeSSeL²) survey have elucidated important aspects of the Milky Way galaxy, including values of its fundamental parameters and the nature of its spiral structure (Brunthaler et al. 2011; Reid et al. 2014; Honma et al. 2015; Sakai et al. 2015; Xu et al. 2016). The BeSSeL survey continues with additional VLBI observations of masers associated with High Mass Star-Forming Regions (HMSFRs) to better constrain the size and morphology of the Milky Way (see, e.g., Quiroga-Nuñez et al. 2017; Sanna et al. 2017). This is relevant at large Galactocentric radii (> 12 kpc), where only a few HMSFRs have been observed and their astrometric parameters are harder to measure (Hachisuka et al. 2015, and references within). Also, the outer Galactic region is particularly interesting as it gauges the Galactic rotation curve, which is a crucial key to understand the role of dark matter in Galactic dynamics (see, e.g., Kent 1986; Sofue 2017).

In 2004, the VERA project started to monitor several maser bearing stars and star-forming regions to accurately determine their astrometric parameters (Honma 2013). Their first result was the parallax and proper motion of the star-forming region Sharpless 269 (S 269), also known as Sh2-269, LBN 196.49–0.160 or G196.45–01.67 (Honma et al. 2007). S 269 is a compact HII region in the outer Galaxy toward the Galactic anticenter at $l = 196.5$ and $b = -1.7$ (Sharpless 1959). It hosts several bright near-infrared (NIR) sources, in particular S 269 IRS 2w. This is a massive young O star with associated Herbig-Haro objects (Eiroa et al. 1994) and several species of masers (Minier et al. 2002; Sawada-Satoh et al. 2013). Water (22 GHz), methanol (6.7 and 12.2 GHz) and OH (1.6 GHz) maser emission around S 269 IRS 2w have been detected and studied for decades (Clegg 1993; Minier et al. 2002; Lekht et al. 2001a) as the region presents signposts of star-forming activity (Jiang et al. 2003; Sawada-Satoh et al. 2013) and intermediate scale interstellar turbulence (Lekht et al. 2001b). S 269, therefore, represents one of a few well observed HII regions at large Galactocentric radii (> 13 kpc, Honma et al. 2007).

Using the VERA array, Honma et al. (2007) monitored the water maser emission from S 269 IRS 2w from 2004 to 2006. They reported strong maser emission of 480 Jy at 22 GHz with $V_{\text{LSR}} = 19.7 \text{ km s}^{-1}$, and measured an annual parallax of 0.189 ± 0.008 mas, corresponding to a distance from the Sun of $5.28_{-0.22}^{+0.24}$ kpc and a Galactic rotational velocity similar to the Sun. This result suggested that the rotation curve of the Galaxy remains flat out to 13.5 kpc from the Galactic center (adopting $R_{\odot} = 8.34$ kpc, Reid et al. 2014).

Later Miyoshi et al. (2012) and Asaki et al. (2014) disputed the distance to S 269 reported by Honma et al. (2007), firstly pointing out that kinematic and optical photometric distance estimates reported shorter values (3.7–3.8 kpc, see Moffat et al. 1979; Wouterloot & Brand 1989; Xu et al. 2009). Moreover, they reanalyzed the VERA data specifically using more compact maser spots than those used by Honma et al. (2007), and reported a parallax value 0.247 ± 0.034 mas, which corresponds to a distance of $4.05_{-0.49}^{+0.65}$ kpc (Asaki et al. 2014). The tension between the two parallax distances is crucial for two reasons. First, the S 269 astrometric parameters have been used to constrain the Galactic rotation curve at large Galactocentric radii due to the limited number of sources with accurately measured distances in this area of the Galaxy. Second, the two distance estimates support a different structure of the outer spiral arm. The nearer distance estimate of $4.05_{-0.49}^{+0.65}$ kpc by Asaki et al. (2014) is inconsistent with previous distance estimates of the outer arm (Hachisuka et al. 2015), suggesting a kink or bifurcation, whereas the larger distance of $5.28_{-0.22}^{+0.24}$ kpc by Honma et al. (2007) supports a

¹VERA is part of the National Astronomical Observatory of Japan

²<http://bessel.vlbi-astrometry.org/>

smoother arm.

We now present the results and implications of a large number of recent Very Long Baseline Array (VLBA) observations of the S 269 region at 22 GHz. In Sect. 2.2, we describe the observations, the data reduction procedure and the methods used. The astrometric results and the search for optical members within the *Gaia* catalog are described in Sect. 2.3. Then, in Sect. 2.4, we analyze the maser emission structure, and the implications of the parallax and proper motion obtained regarding the structure of the outer arm and optical associations. Finally, we present the main conclusions of this work in Sect. 2.5.

2.2 Observations

From August 2015 to October 2016, we conducted 16 epochs of phase reference observations of water masers present in S 269, using two extragalactic continuum sources (J0613+1306 and J0619+1454) as close by position references at 0.73° and 1.67° , respectively, from S 269. The observations were made using the VLBA operated by the National Radio Astronomy Observatory (NRAO³) under program BR210E. Table 2.5 shows the dates and times of the 16 observations, which correspond to a sequence of four observations (i.e., one in late summer, two in late winter or early spring, and one more in the next late summer) repeated four times, close in time during each sequence.

Table 2.1: Information of the strongest S 269 maser spot detected, and both extragalactic sources used for parallax and proper motion estimate.

Source Name	α (J2000) (hh:mm:ss)	δ (J2000) ($^\circ$: ' : ")	S_ν (Jy beam ⁻¹)
S 269	06:14:37.6410	+13:49:36.6930	95.8
J0613+1306	06:13:57.6928	+13:06:45.4010	0.2
J0619+1454	06:19:52.8723	+14:54:02.7346	0.1

Notes. S 269 spot is shown in Fig. 2.1 and corresponds to spot I in Fig. 2.2. The peak flux density corresponds to the observations made at Epoch H.

Four adjacent 16 MHz bands, each in right and left circular polarization, were used with the third band centered on an V_{LSR} of 15 km s^{-1} , assuming a rest frequency of the water maser $J_{K_a K_c} = 6_{16} \rightarrow 5_{23}$ transition of 22,235.080 MHz. The observations were processed with the VLBI software correlator VLBA-DiFX⁴, producing 2,000 and 32 spectral channels per band for the line and continuum data, respectively. This yielded a velocity spacing of 0.108 km s^{-1} for the line data. In addition, to estimate and then remove residual tropospheric delays relative to the correlator model, we inserted four geodetic blocks during each observational epoch (details about geodetic observations can be found in Reid et al. 2009b). The observation cycles were designed such that S 269 was observed for 30 seconds (typically a 10 second slew and 20 seconds on source) followed by a compact extragalactic source for 30 seconds. Therefore, the center of the maser scans used for phase referencing were 60 seconds apart, which is shorter than the coherence time for VLBA observations at this frequency. Positions and flux densities for the dominant maser spot ($V_{\text{LSR}} = 19.6 \text{ km s}^{-1}$), used as the phase

³The National Radio Astronomy Observatory is a facility of the National Science Foundation operated under cooperative agreement by Associated Universities, Inc.

⁴DiFX is developed as part of the Australian Major National Research Facilities Programme by the Swinburne University of Technology and operated under license.

Table 2.2: Relative position, radial velocities and flux density peaks at certain observational epoch for the water maser spots shown in Fig. 2.2.

Spot ID (Fig. 2.2)	$\Delta\alpha$ (mas)	$\Delta\delta$ (mas)	V_{LSR} (km s ⁻¹)	F_{max} (Jy beam ⁻¹)	Peak epoch
I	-0.101 ± 0.005	-0.020 ± 0.002	19.6	95.8	H
II	24.984 ± 0.044	4.116 ± 0.024	19.0	0.5	H
III	305.924 ± 0.007	4.652 ± 0.012	18.2	1.4	B
IV	190.894 ± 0.025	-105.335 ± 0.044	20.4	0.3	D
V	109.886 ± 0.006	-143.253 ± 0.010	16.6	1.4	O
VI	-86.811 ± 0.080	-232.680 ± 0.062	19.8	12.9	H
VII	-586.729 ± 0.011	-666.299 ± 0.005	16.0	2.5	P
VIII	-758.007 ± 0.009	-741.869 ± 0.013	19.2	8.5	O
IX	-795.345 ± 0.015	-743.615 ± 0.022	17.4	0.6	A

Notes. The offsets were measured with respect to the strongest water maser spot, for which the absolute position is given in Table 5.1. The epoch of fit was taken as the middle time of the VLBA observations, which is 2016.2.

reference for the extragalactic sources, and the two continuum sources are shown in Table 5.1. The data reduction was performed using the NRAO Astronomical Image Processing System (AIPS), together with scripts written in ParseITongue (Kettenis et al. 2006), following standard BeSSeL survey data reduction methods (see Reid et al. 2009b).

2.3 Results

Sixteen data cubes were constructed (one per epoch), each measuring 32,768 pixels × 32,768 pixels × 300 channels. This corresponds to an image of 1.64'' × 1.64'' using a cellsize of 0.05 mas pixel⁻¹ within a radial velocity range between -6.4 and 25.7 km s⁻¹. The range values for the data cube were calculated to include all the maser spots reported in Miyoshi et al. (2012) and Asaki et al. (2014).

We detected nine maser spots that were persistent for at least three epochs. Gaussian brightness distributions were fitted to the maser images by a least-squares method using the task *JMFIT* within AIPS. Table 2.2 shows the results of the fitting for each maser spot, together with its radial velocity and the maximum flux density across all epochs. Figure 2.1 shows the strongest water maser detected at representative epochs, while Fig. 2.2 shows the distribution of the maser spots, proper motion and radial velocities found in our VLBA data together with those reported in Honma et al. (2007) and Asaki et al. (2014). The strongest maser spot is labeled as “I” and it was used as central reference. In the VLBA observations, the water masers are confined to a radial velocity range between 16.0 and 20.4 km s⁻¹. This is within the velocity range found in single dish spectra for S269 (Lekht et al. 2001a).

2.3.1 Elongated water maser emission

The strongest maser spot was detected in all sixteen epochs with a flux density maximum of 95.8 Jy beam⁻¹ at epoch H. This spot has a distinctive elongated shape at all epochs (see Fig. 2.1), as was firstly reported by Miyoshi et al. (2012) and highlighted by Asaki et al. (2014). The spot varies somewhat over time but retains its basic shape throughout all our observations.

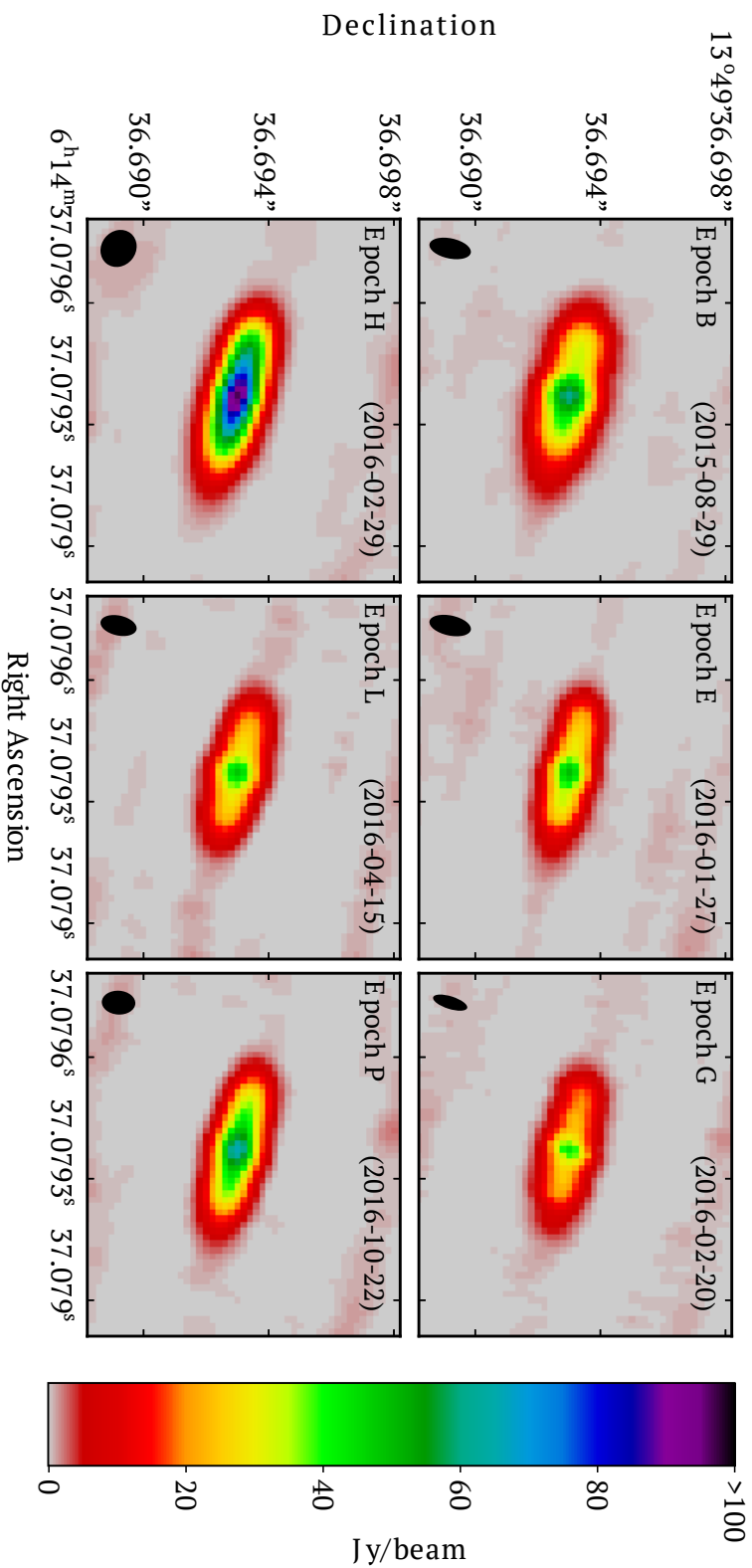


Figure 2.1: Strongest 22 GHz maser spot in S 269 region showing an elongated shape at six different epochs in the VLBA observations between 2015 and 2016. Based on its position and V_{LSR} (but not its motion, see Sect. 2.4.1), it seems to correspond to the strongest maser spot reported by Honma et al. (2007), using VERA observations in 2004 and 2005. This maser spot corresponds to the spot I in Fig. 2.2. The shape and size of the beam for each epoch is shown in the bottom left corner.

Table 2.3: Fitting results of parallax and proper motion for four 22 GHz water maser spots present in S 269 with respect to two extragalactic continuum sources, under the usual assumption that the quasars are stationary during our observations. Radial velocities of those masers are also shown. The description of how the combined parallax and proper motion were obtained is described in Sect. 2.3.2.

Maser Spot	Quasar	π (mas)	$\mu_\alpha \cos \delta$ (mas yr ⁻¹)	μ_δ (mas yr ⁻¹)	V_{LSR} (km s ⁻¹)	Combined $\mu_\alpha \cos \delta$ (mas yr ⁻¹)	Combined μ_δ (mas yr ⁻¹)
I	J0613+1306	0.244 ± 0.010	-0.091 ± 0.024	-0.003 ± 0.029	19.6	-0.099 ± 0.019	-0.008 ± 0.020
	J0619+1454	0.243 ± 0.013	-0.107 ± 0.032	-0.012 ± 0.028			
II	J0613+1306	-	0.518 ± 0.187	0.408 ± 0.099	19.0	0.507 ± 0.128	0.438 ± 0.076
	J0619+1454	-	0.497 ± 0.187	0.464 ± 0.124			
III	J0613+1306	0.226 ± 0.013	0.173 ± 0.033	0.049 ± 0.039	18.2	0.170 ± 0.025	0.063 ± 0.028
	J0619+1454	0.228 ± 0.017	0.166 ± 0.041	0.078 ± 0.042			
IV	J0613+1306	-	0.767 ± 0.115	-0.234 ± 0.194	20.4	0.763 ± 0.089	-0.185 ± 0.139
	J0619+1454	-	0.762 ± 0.144	-0.137 ± 0.206			
V	J0613+1306	0.234 ± 0.033	-0.189 ± 0.032	-0.177 ± 0.057	16.6	-0.187 ± 0.052	-0.177 ± 0.057
	J0619+1454	0.214 ± 0.042	-0.108 ± 0.133	-0.207 ± 0.085			
VI	J0613+1306	-	-0.639 ± 0.215	0.085 ± 0.068	19.8	-0.650 ± 0.147	0.080 ± 0.050
	J0619+1454	-	-0.661 ± 0.212	0.069 ± 0.082			
VII	J0613+1306	0.254 ± 0.026	-0.108 ± 0.064	-1.255 ± 0.034	16.0	-0.111 ± 0.043	-1.254 ± 0.024
	J0619+1454	0.248 ± 0.024	-0.115 ± 0.060	-1.254 ± 0.035			
VIII	J0613+1306	-	-0.209 ± 0.286	-1.602 ± 0.490	19.2	-0.031 ± 0.160	-1.580 ± 0.250
	J0619+1454	-	0.152 ± 0.120	-1.542 ± 0.347			
IX	J0613+1306	-	0.950 ± 0.819	-2.142 ± 0.213	17.4	1.052 ± 0.529	-1.959 ± 0.139
	J0619+1454	-	1.149 ± 0.839	-1.772 ± 0.140			
Combined Parallax		0.241 ± 0.012		Average Proper Motion		0.157 ± 0.066	-0.509 ± 0.037

Notes. The first column gives the maser spot number used in Fig. 2.2. The annual parallax values (π) provided in the third column were fitted for only four masers (see Sect. 2.3.2). For the absolute proper motion fittings (columns 4,5,7,8), we fixed the parallax value in 0.241 ± 0.012 mas. The procedures to obtain the combined and average values reported in this table are described in Sect 2.3.2.

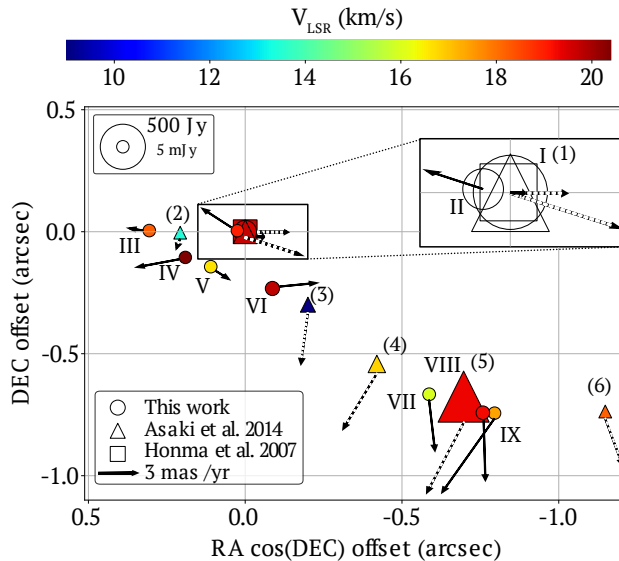


Figure 2.2: Distribution of water maser spots around the strongest maser emission (where several maser spots coincide, see zoom in) with their radial velocity values expressed using a color scheme indicated by the bar at the top. The maser spots detected by the VLBA in 2015–2016 (see Table 2.2) are shown as circles, with Roman numerals and their proper motion as continuum arrows. Whereas, the main maser spots detected by VERA in 2004–2005 and published by Honma et al. (2007) and Asaki et al. (2014) are shown as squares and triangles, with Arabic numerals and their proper motion as dashed arrows. The size of the markers is proportional to the flux density peak of each maser spot (see upper left corner convention).

The inner core for this elongated spot could be well fitted by a single, compact, Gaussian brightness distribution, and we used the AIPS task *JMFIT* with a 2 mas box to fit the core.

2.3.2 Astrometric measurements for S269

Only four of the nine 22 GHz water maser spots were detected in at least ten epochs, which allow a robust fitting for the annual parallax sinusoidal signature in right ascension and declination. We also added error floor values to the position uncertainties in both sky coordinates and adjusted them to obtain $\chi^2_{\nu} \approx 1$ (see details in Reid et al. 2009b).

The four maser spots used in the parallax fitting are labeled in Fig. 2.2 as spots I, III, V and VII and were detected in 16, 15, 10 and 16 epochs, respectively. As the four spots gave consistent parallax results (including the elongated spot, see Table 2.3 and Figure 2.3), we also have calculated a combined fit by simultaneously fitting all data (i.e., four spots measured for both quasars). This yields a combined annual parallax value of 0.241 ± 0.012 mas. The uncertainty in the parallax includes an additional scaling factor of \sqrt{N} , where N is the number of maser spots used for the fit. This accounts for the correlated systematic position variations among maser spots caused by atmospheric effects (Reid et al. 2009b).

To estimate an average proper motion of the region, we fixed the annual parallax (previously calculated with only four maser spots) and fit the proper motions for the nine masers with respect to both (labeled as combined in Table 2.3) continuum extragalactic sources. Then, we averaged the proper motions of all nine maser spots detected by a standard mean (labeled as average proper motion in Table 2.3). Moreover, we include a 5 km s^{-1} uncertainty

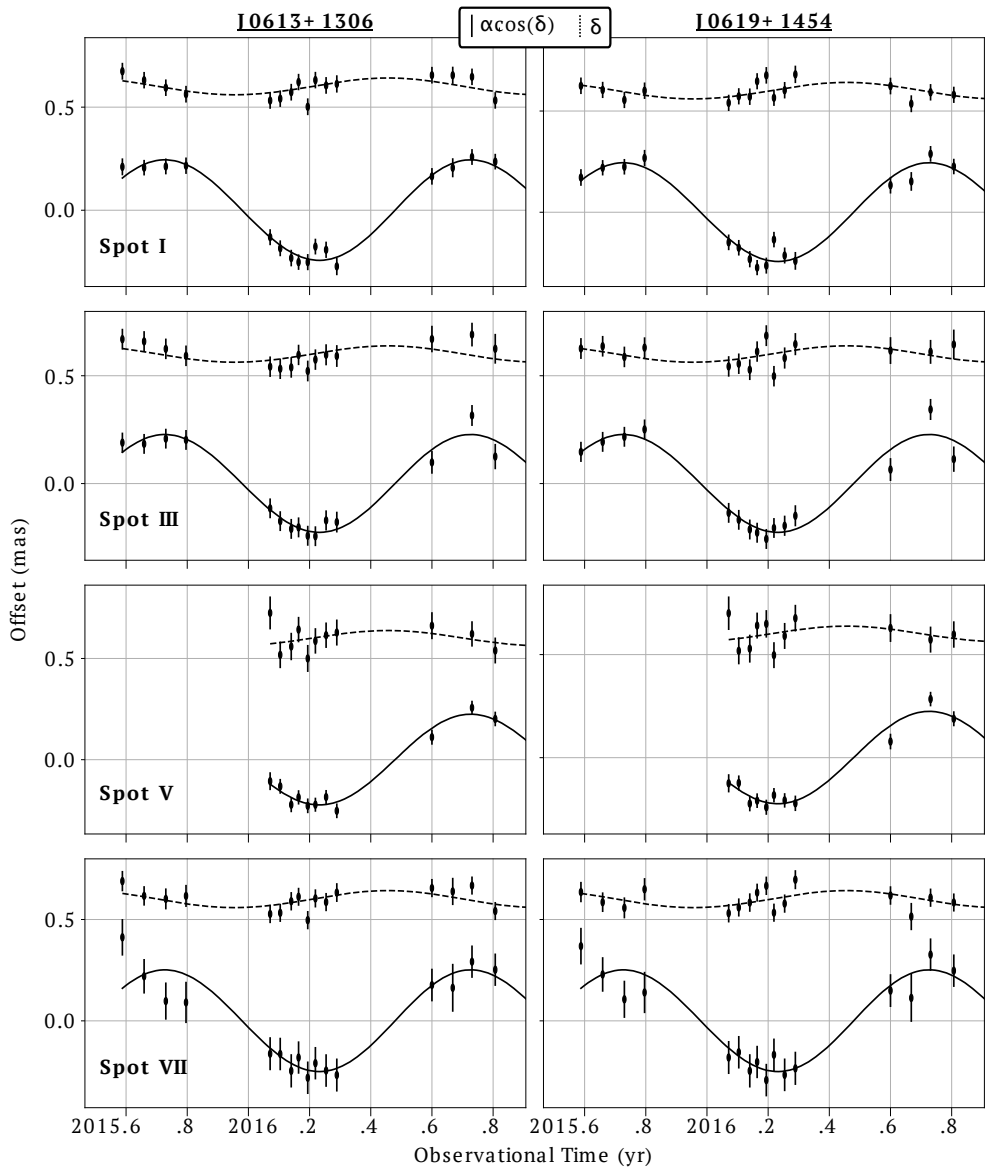


Figure 2.3: Astrometric offsets for four different water masers with respect to the quasars used as reference position: J0613+1306 in the left plots and J0619+1454 in the right plots. The proper motions were subtracted from the parallax signatures. The solid and dashed lines represent the eastward ($f \cos \text{fi}$) and northward (fi) individual fitting listed in Table 2.3, respectively. The Northward offset (fi) was shifted $+0.6$ mas for visualization purposes.

that accounts for the uncertainty of the motion of the masers with respect to the center of mass of the HMSFR. We note that the quiescent gas has V_{LSR} similar to the masers (i.e., 17.7, 16.5 and 18.2 km s⁻¹ for CO, [SII] and HCN, respectively, Carpenter et al. 1990; Godbout et al. 1997; Pirogov 1999). Finally, we estimate $\bar{\mu}_{\text{ff}} \cos \text{ffi} = 0.16 \pm 0.26$ mas yr⁻¹ and $\bar{\mu}_{\text{ff}} = -0.51 \pm 0.26$ mas yr⁻¹ for the average proper motion of S 269.

2.3.3 Cross-matching with Gaia DR2

S 269 IRS 2w is located in a CO molecular cloud with a projected size of 7' × 10' (Heydari-Malayeri et al. 1982; Carpenter et al. 1990). Other massive young stars, which could belong to the same stellar association, are expected to be detected in the vicinity of the CO molecular cloud. Since molecular gas is mostly confined to the Galactic plane (and mainly in the Galactic spiral arms) in a layer with FWHM of several hundred pc for Galactic radii greater than 10 kpc (Heyer & Dame 2015), we searched in the *Gaia* DR2 catalog within a spherical region around S 269's location in 3D. As GMCs usually extend from 5 pc up to 120 pc, with a very few exceptional cases over 150 pc (Murray 2011), we used a radius 125 pc (1.73 at S 269's distance) as a conservative value to guarantee that most of the plausible sources associated with the S269 region were included in the inspected range. This corresponds to a parallax range (including $\pm\sigma$) from 0.2225 to 0.2615 mas. Figure 2.4 shows the S 269 region using data from the Digital Sky Survey 2 (DSS2⁵ Lasker & McLean 1994) and the Two Micron All Sky Survey (2MASS⁶ Skrutskie et al. 2006) centered on the maser emission.

We only selected sources with confident parallax measurements in *Gaia* DR2 (i.e. $\sigma_{\pi}/\pi < 0.2$) that allow direct distance estimates (Bailer-Jones 2015). In total, there are 2,279 sources that fall into the spherical region defined. The closest ten *Gaia* counterparts in 3D are highlighted in red in Fig. 2.4, and their astrometric information is shown in Table 2.6. We did not find an optical counterpart in *Gaia* DR2 that corresponds to the massive young star which surrounding material is yielding the water maser emission detected at 22 GHz. This is expected for a newly forming star that is deeply embedded in its placental material. However, the three closest optical counterparts (first three rows in Table 2.6) were found within a core size of the S 269 HII region (3.9 pc × 2.8 pc) estimated by Godbout et al. (1997). These three *Gaia* DR2 sources have an average parallax that differs with respect to the VLBA observations by -32 ± 23 μas (assuming a *Gaia* zero-point correction of ~ -0.03 mas) and an average proper motion that differs by 0.02 ± 0.65 and -0.16 ± 0.77 mas yr⁻¹ for $\bar{\mu}_{\text{ff}} \cos \text{ffi}$ and $\bar{\mu}_{\text{ff}}$ respectively. Therefore, they are likely members of the stellar association that contains S 269 IRS 2w.

2.4 Discussion

2.4.1 Long-lived and extended water maser emission

Elongated maser spot

The unusual morphology of the spot I over many (from VERA in 2004 to VLBA in 2016) observations (Fig. 2.1) compared to typical maser spots vouches for its authenticity. An instrumental artifact, instead, would manifest a similar structural appearance in all similarly calibrated maser emission in the data cube, which is not the present case. We further analyzed the maser structure using DIFmap's modelfit and projplot tools. The structure of the maser is well fit by an elongated structure (P.A. $\sim 78^\circ$) plus a compact core as it is evident in Fig. 2.1.

⁵<http://archive.eso.org/dss/dss>

⁶<https://www.ipac.caltech.edu/2mass/>

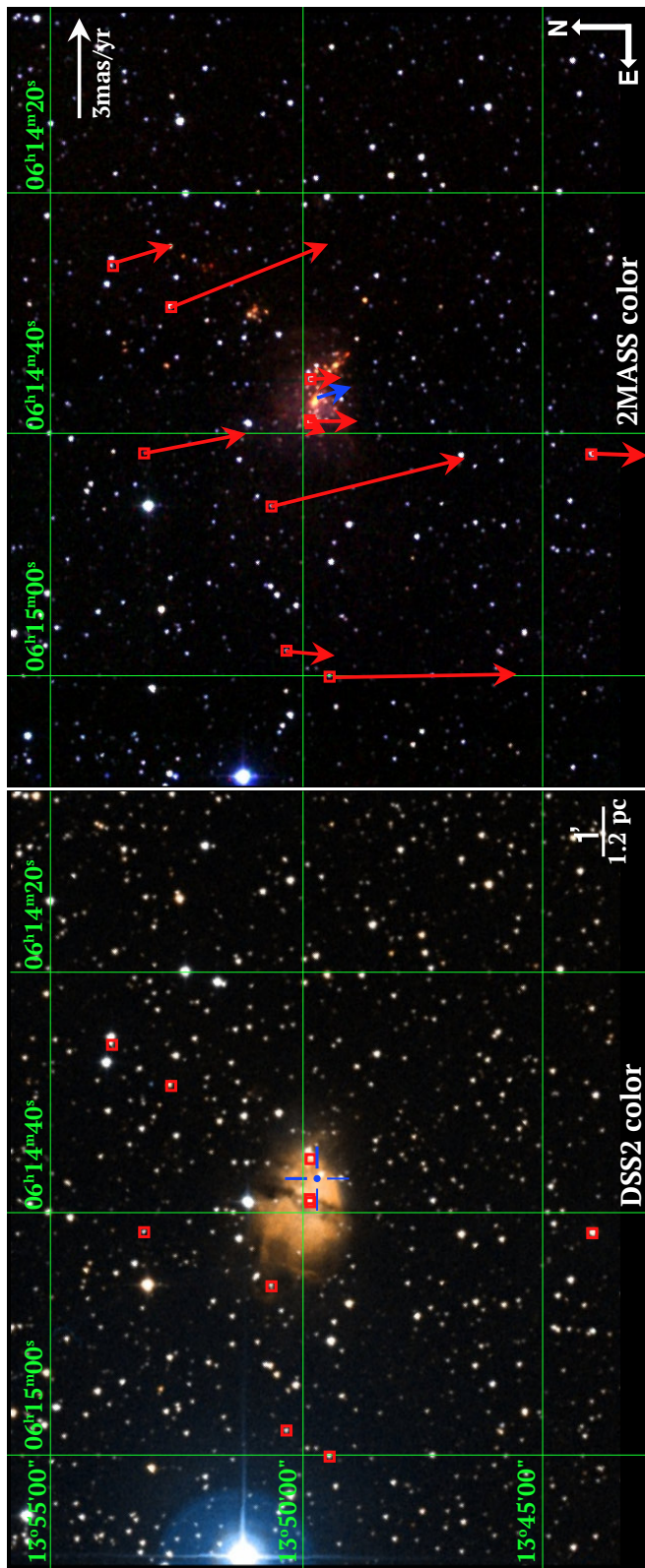


Figure 2.4: Image of the S 269 region using data from DSS2 (left panel) and 2MASS (right panel) with a sky projected size of $15.65' \times 12.33'$, centered on the water maser emission (blue central sign) detected with the VLBA (Table 5.1), that seems to be triggered by the massive young star S 269 IRS 2w (Asaki et al. 2014). In the left panel, the molecular cloud appears as a butterfly with two wings separated by a dark fringe where a B0.5 star has been detected in the center (Moffat et al. 1979). In contrast, near-infrared observations (right panel) show that the center of the clustered region of massive young objects coincides with the position of S 269 IRS 2w. The red squares are the closest optical sources around S 269 found within the *Gaia* DR2 catalog (see Sects. 2.3.3 and 2.4.5) and their astrometric information is shown in Table 2.6. The red arrows display the proper motions for such sources, whereas the blue arrow is the proper motion calculated by us using the water masers in the region. The images were generated with the Aladdin interface (Bonnarel et al. 2000), where the color map descriptions of DSS2 and 2MASS can be found through alasky.u-strasbg.fr/DSS/DSSColor/ and alasky.u-strasbg.fr/2MASS/Color/.

Correspondence with previous water maser observations

As a collisionally pumped maser transition, 22 GHz water masers are typically found in turbulent regions of post-shocked gas associated with star formation outflows (see, e.g., Liljestrom & Gwinn 2000; Hollenbach et al. 2013, and the references within). While a shocked region at some radial velocity may consistently produce maser emission around the shock velocity, the individual maser spots are typically short-lived ($\lesssim 1$ yr, see e.g., Tarter & Welch 1986). With this in mind, the persistent appearance of the maser spot I in Fig. 2.2 at about the same location in the source makes it remarkable. Its position and shape seem to correspond to the maser spot reported by Honma et al. (2007) for the VERA observations made between 2004 and 2005, and the reanalysis of VERA data made by Miyoshi et al. (2012) and Asaki et al. (2014). Its longevity may be related to its complex structure, maser spots typically being much more compact. In principle, this could allow us to fit the parallax and proper motion over a 10 year baseline for this spot.

Although this region seems to persistently yield elongated maser emission over decades, indicating it is the same masering cloud, there is a significant difference between the proper motion measured for the observing set in 2004 using VERA and 2015 using the VLBA, with respect to the same quasar (J0613+1306). On the one hand, Honma et al. (2007) reported for the elongated maser spot $\mu_\alpha \cos \delta = -0.388 \pm 0.014$ mas yr $^{-1}$ and $\mu_\delta = -0.118 \pm 0.071$ mas yr $^{-1}$, and Asaki et al. (2014) reported -0.738 ± 0.008 mas yr $^{-1}$ and -0.249 ± 0.007 mas yr $^{-1}$ (Spot ID 6 in Asaki et al. 2014). In contrast, we estimated a much slower proper motion of $\mu_\alpha \cos \delta = -0.099 \pm 0.019$ mas yr $^{-1}$ and $\mu_\delta = -0.008 \pm 0.020$ mas yr $^{-1}$. It seems likely that small changes in the coherent amplification path of the maser account for these differences. Thus, we cannot fit the parallax and proper motion for this spot on a 10 year baseline given its velocity discrepancy, but its peculiar morphology hints that those spots represent the same maser region.

Source of the elongated water maser emission

In principle, an amplified background source could mimic the particular properties (morphology and longevity) of the elongated maser spot, however, there is no sign of such continuum source when we inspected the continuum bands of our observations. Alternatively, the linear distribution of the water maser spots (Fig. 2.2) suggests that we are observing the front shock of the outflow moving in the southeastern direction. This direction is confirmed by infrared data from the Simultaneous-3color InfraRed Imager for Unbiased Survey (SIRIUS), where S 269 IRS 2 shows a bipolar jet in the southeastern-northwestern direction (Jiang et al. 2003, but it remains unclear if it is associated with S 269 IRS 2w or S 269 IRS 2e). This fact suggests that material may have been compressed yielding an elongated maser emission, which indeed is perpendicular to the shock motion. Moreover, CO, [SII] and HCN observations of the S 269 region reported a V_{LSR} of 17.7, 16.5 and 18.2 km s $^{-1}$, respectively (Carpenter et al. 1990; Godbout et al. 1997; Pirogov 1999), which differs with respect to our maser observations supporting the jet origin of the maser emission.

Cyclic maser emission in S 269

Lekht et al. (2001a) monitored the water maser emission toward S 269 for more than 20 years (1980-2001) using the 22 meter telescope of the Pushchino Radio Astronomy Observatory. They reported a V_{LSR} range of [19.6 – 20.4] km s $^{-1}$ in which our VLBA observations and also those made by Honma et al. (2007) fall. Although this single dish effort could not image the water maser, they found that the integrated flux of the strongest maser had cyclic

emission between 70 and 600 Jy with a period of between 4.8 and 6.6 years. Assuming the cyclic emission suggested by Lekht et al. (2001a), subsequent peak emissions (over 200 Jy) should have occurred between [2004.4-2006.2], [2009.2-2012.8] and [2014-2019.4]. Both VERA (Honma et al. 2007) and VLBA (this work) observations spanned more than one year within these time ranges, but only VERA observations showed enhanced emission of 480 Jy. Although there is evidence of previous flares at radio wavelengths in S 269 (see, e.g., Clegg 1993), the cyclic emission proposed by Lekht et al. (2001a) does not seem consistent with our VLBA observations.

2.4.2 S269 astrometric parameters

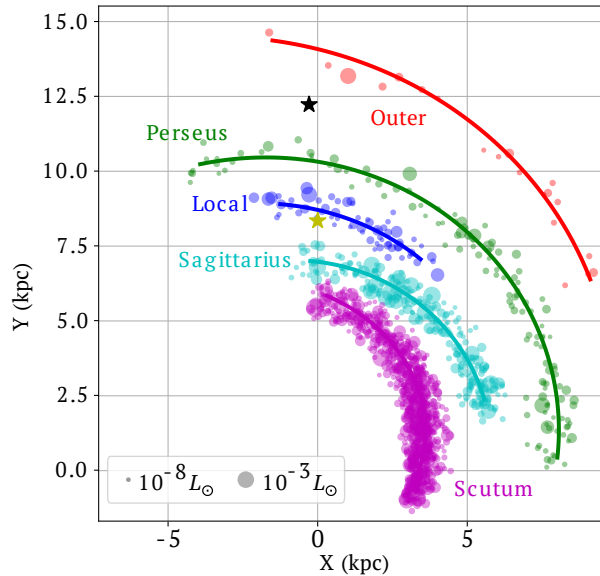


Figure 2.5: Plan view of a simulation of the Galactic maser distribution for maser bearing stars around the spiral structure using the model developed by Quiroga-Nuñez et al. (2017). The spiral structure estimated by Reid et al. (2014) was populated with artificial sources to compare the phase-space density distribution of the spiral arms with S 269 properties (see Sect. 2.4.3). The Galactic center is located at (0,0), and the yellow and black stars correspond to the position of the Sun (Reid et al. 2014) and S 269, respectively, where their positional error bars are smaller than the size of the marker.

Distance

The combined fit of the four 22 GHz water maser spots presented in Table 2.3 yielded a parallax value of 0.241 ± 0.012 mas, which corresponds to a distance of $4.15^{+0.22}_{-0.20}$ kpc from the Sun and 12.36 ± 0.27 kpc from the Galactic center (adopting $R_{\odot} = 8.34$ kpc, Reid et al. 2014). The annual parallax is in agreement with 0.247 ± 0.034 mas obtained by Asaki et al. (2014) for the VERA data taken between 2004 and 2005.

Although Honma et al. (2007) reported a smaller annual parallax of 0.189 ± 0.008 mas, and hence a larger distance of $5.28^{+0.24}_{-0.22}$ kpc for the elongated maser spot, Asaki et al. (2014) claimed that VERA data for that single spot yielded an inexact parallax estimate. They suggested that this problematic morphology caused an erratic positional estimate. Indeed, VERA

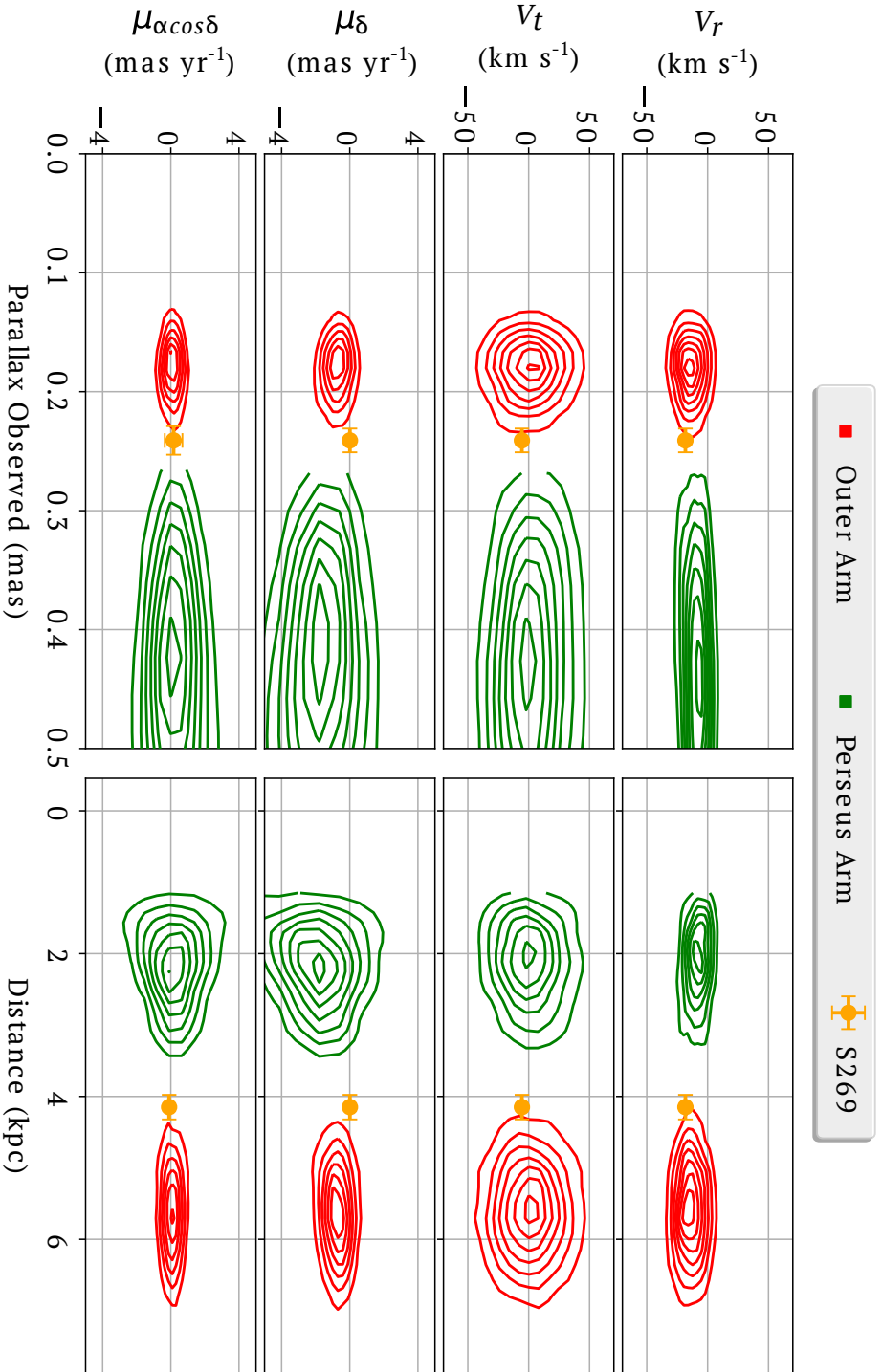


Figure 2.6: Radial velocity (V_r), transversal velocity (V_t) and proper motion for S269 seen from the Sun as a function of observed parallax (left plots) and distance (right plots). The contours show the distribution of sources per arm for a simulated Galactic maser distribution around the position of S269 where the pitch angles of each arm were constant (see Sect. 2.4.3). The simulations were made using the code developed by Quiroga-Núñez et al. (2017). Each single contour represents a percentage of the arm sources contained in a specific region of the plot from the inside as [0.14,0.28,0.42,0.56,0.70,0.84,0.98].

baselines are short and few compared to the VLBA, and therefore they could not resolve and fit the inner core of the elongated spot. However, with the new VLBA observations, we have been able to fit and constrain the annual parallax to the compact core (0.244 ± 0.012 mas) with respect to both extragalactic sources (see Table 2.3). This fact could explain the distance discrepancy between Honma et al. (2007) and this work's measurement. Also, as it was mentioned by Asaki et al. (2014), parallax uncertainties reported by Honma et al. (2007) might be larger than quoted as the possibility of correlated positional variations among the three spots used was not considered.

Peculiar Velocity

We transformed the estimated 3D average motion of the maser spots (see Sect. 2.3.2), that is $\bar{\mu}_{\text{ff}} \cos \text{ffl} = 0.16 \pm 0.26$ mas yr $^{-1}$, $\bar{\mu}_{\text{fl}} = -0.51 \pm 0.26$ mas yr $^{-1}$ and $V_{\text{LSR}} = 19.6 \pm 5$ km s $^{-1}$, to the (U, V, W) reference frame that rotates with the Galactic disk, yielding $U_{\text{S}269} = 3 \pm 5$, $V_{\text{S}269} = -1 \pm 5$ and $W_{\text{S}269} = 6 \pm 5$ in km s $^{-1}$, where U increases toward the Galactic center, V in the direction of Galactic rotation and W toward the north Galactic pole. We assumed a rotation model defined by Reid et al. (2014) with $R_0 = 8.31$ kpc and $\Theta_0 = 241$ km s $^{-1}$, $U_{\odot} = 10.5$ km s $^{-1}$, $V_{\odot} = 14.4$ km s $^{-1}$, $W_{\odot} = 8.9$ km s $^{-1}$ and $d\Theta/dR = -0.2$ km s $^{-1}$ kpc $^{-1}$. The obtained values are consistent with previous findings of near-zero peculiar motion for water masers associated with HMSFRs (Reid et al. 2014).

The tangential motion of S 269 allows us to constrain the Galactic rotation at 12.4 kpc radius from the center of the Milky Way. The errors in $V_{\text{S}269}$ reported in this work are comparable to those reported by Honma et al. (2007), where a different model for the Galactic rotation was used. As a consequence, we find that the S 269 tangential motion is within 2% of a flat Galactic rotation curve, as it was initially claimed by Honma et al. (2007), albeit at a larger distance compared with this work.

2.4.3 Membership in the Perseus or outer arm

In order to investigate whether S 269 lies within a spiral arm, we generated simulations of Galactic maser sources following the model proposed by Quiroga-Nuñez et al. (2017). Although that model was initially developed for methanol masers associated with HMSFRs, it can be used to estimate the kinematics of other masers at certain regions of the Galaxy. There are three differences with respect to the model that Quiroga-Nuñez et al. (2017) implemented. First, we did not consider any luminosity function for water masers, since it is not necessary for our kinematic study. Second, we populated the phase space of our model with many more (up to half million) sources to allow an accurate sampling. Third, the spiral structure model follows the arm description derived by Reid et al. (2014). Although this spiral structure model was obtained using the the S269's distance estimated by Honma et al. (2007), S269 was not the only source used for the spiral structure model, and also, this model was a smooth extension of the spiral arm from the first to the second quadrant. Figure 2.5 shows the simulated distribution that was obtained by this way but displaying only 2,000 sources for plotting purposes.

The phase-space density distributions of masers simulated for the outer Galaxy is shown in Fig. 2.6, with the observational values of S 269 plotted. For the distributions, all the variables are measured from the Sun and simulated errors in these observables were also generated (see Quiroga-Nuñez et al. 2017, for details). In all cases, the kinematic parameters of S 269 seem to suggest that this source is more likely member of the outer arm than the Perseus arm, as was pointed out by Sakai et al. (2012) based on the distance estimate made by Honma et al.

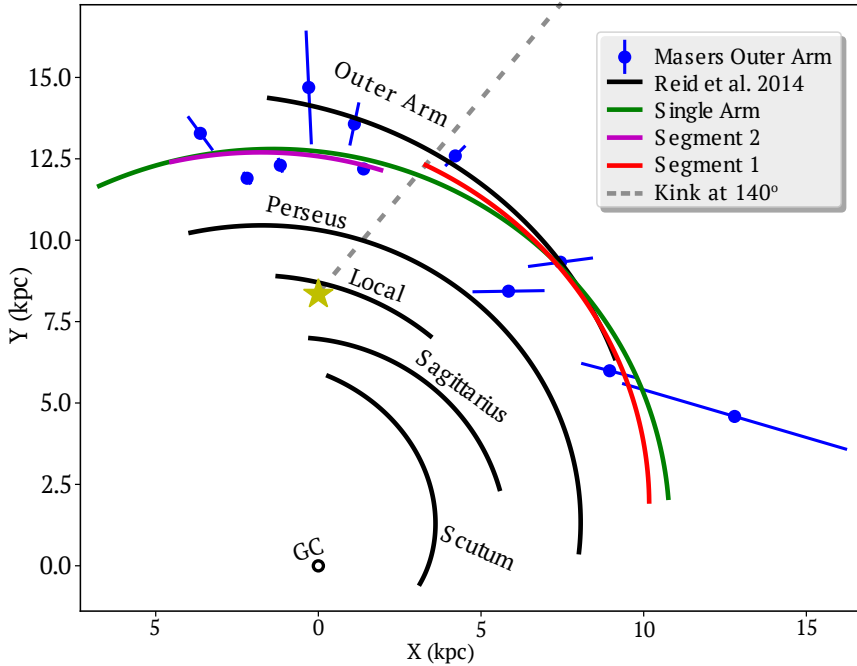


Figure 2.7: Plan view of Galactic spiral structure. The spiral structure estimated by Reid et al. (2014) is shown as black lines for reference. Maser emission from 11 HMSFRs has been used to estimate the position of the outer arm. The different outer arm descriptions discussed in Sect. 2.4.3 are highlighted in color curves. The Galactic center is located at (0,0), and the yellow star corresponds to the Solar position (Reid et al. 2014), while the dashed line demarcates the latitude of the outer arm kink suggested (i.e., 140°).

(2007).

2.4.4 Outer arm structure

Previous pitch angle estimates for the outer arm (e.g., Reid et al. 2014) were obtained based on the large distance to S 269 published by Honma et al. (2007). Moreover, several sources were excluded from the pitch angle fit since they were considered interarm sources (Reid et al. 2014; Hachisuka et al. 2015). To investigate this, we recalculated the outer arm position using recent astrometric information from ten other HMSFRs coming from the BeSSeL survey (Reid priv. comm.). These sources seem to belong to the outer arm based on their kinematics and parallaxes (see Table 2.4). We assess three possible scenarios for the outer arm: a single arm with a constant pitch angle, an arm with two segments that form a kink where they join, and an arm that bifurcates. In all cases, the new fit locates the outer arm in the third quadrant closer to the Sun, compared to what was previously reported (Sanna et al. 2012; Reid et al. 2014).

A single arm

Following the procedure in Reid et al. (2009b) and assuming a width of 0.63 ± 0.18 kpc for the outer arm (estimated by Reid et al. 2014), we fitted 11 sources (see Table 2.4), finding that

Table 2.4: Astrometric information for 11 HMSFRs obtained with the VLBA in the outer arm region. These sources were used for the outer arm fitting (Sect. 2.4.3).

Name	α (hh:mm:ss)	δ (° : ' : '')	π (mas)	Ref.
G073.65+00.19	20:16:21.932	+35:36:06.094	0.075 ± 0.020	*
G075.30+01.32	20:16:16.012	+37:35:45.810	0.108 ± 0.010	1
G090.92+01.48	21:09:12.969	+50:01:03.664	0.171 ± 0.031	*
G097.53+03.18	21:32:12.434	+55:53:49.689	0.133 ± 0.017	2
G135.27+02.79	02:43:28.568	+62:57:08.388	0.167 ± 0.011	7
G160.14+03.16	05:01:40.244	+47:07:19.026	0.244 ± 0.006	*
G168.06+00.82	05:17:13.744	+39:22:19.915	0.187 ± 0.022	2,3
G182.67−03.26	05:39:28.425	+24:56:31.946	0.157 ± 0.042	2,4
G196.45−01.68 (S 269)	06:14:37.641	+13:49:36.693	0.242 ± 0.011	5
G211.60+01.06	06:52:45.321	+01:40:23.072	0.239 ± 0.010	*
V838 Mon	07:04:04.822	−03:50:50.636	0.163 ± 0.016	6

Notes. The names include the galactic coordinates except for V838 Mon which is (217.80,+01.05). The parallax of each source might differ from the published values in the references as we combined independent measurements (one per reference) to increase their accuracy. The parallaxes marked with * will be published as part of the BeSSeL survey (Reid priv. comm.). **References:** (1) Sanna et al. (2012), (2) Hachisuka et al. (2015), (3) Honma et al. (2011), (4) Data reanalyzed of Hachisuka et al. (2015), (5) Variance averaged between Asaki et al. (2014) and results of Table 2.3 (6) Sparks et al. (2008), (7) Hachisuka et al. (2009).

the spiral arm can be described using the form:

$$\ln(R) = (2.50 \pm 0.02) - (\pi/180) (\beta - 17^\circ.9) \tan(\Psi), \quad (2.1)$$

where R is the Galactocentric radii in kpc at a Galactocentric azimuth β (which is zero toward the Sun and increases with Galactic longitude) and Ψ the pitch angle with a value of $6^\circ.2 \pm 3^\circ.1$. This description applies for $73^\circ \lesssim l \lesssim 218^\circ$, which corresponds to the Galactic longitude range of the sources used.

Figure 2.7 shows a plan view of the Milky Way, where the spiral arm positions estimated by Reid et al. (2014) are shown as black curves for reference. The pitch angle for the outer arm calculated by Reid et al. (2014) (i.e. $13^\circ.8 \pm 3^\circ.3$) is within the errors compared to other published values based on masers associated with massive young objects (e.g., Sanna et al. (2012) and Hachisuka et al. (2015) reported $12^\circ.1 \pm 4^\circ.2$ and $14^\circ.9 \pm 2^\circ.7$, respectively). In contrast, the outer arm position with our estimate of the pitch angle (i.e., $6^\circ.2 \pm 3^\circ.1$) is shown in the same figure as a green line. This pitch angle is unusually small compared with previous studies—even without considering S 269 as an outer arm source—and entirely attributed to the sources at large Galactic longitudes ($> 140^\circ$) suggesting that a kink in the outer arm is another plausible explanation. Finally, although the outer arm sampling used is sparse, the reconstruction of the arm is still the best procedure with the limited astrometric solutions available.

Two arm segments forming a kink

Honig & Reid (2015) analyzed the positions of a large number of HII regions in four face-on galaxies, and concluded that spiral arms seem to be composed of segments that join up and sometimes produce abrupt changes in pitch angle (kinks). We have tested if the outer arm presents a similar feature by splitting the sample into two balanced subsamples, that is five

sources with $l < 140^\circ$ and six sources with $l > 140^\circ$. We estimated a pitch angle for the first segment ($l < 140^\circ$) $10^\circ.5 \pm 5^\circ.9$, and $7^\circ.9 \pm 5^\circ.8$ for the second segment ($l > 140^\circ$). The fits to both segments are shown in Fig. 2.7. While, with the small number of sources, the pitch angle estimates are quite uncertain, Fig. 2.7 suggests either a kink or bifurcation in the outer arm somewhere near a longitude of $l \sim 140^\circ$. Note also that this representation calls for a kink with a change of pitch angle of $\gtrsim 25\%$ ($\Delta\Psi/|\Psi|$), comparable to values of $\sim 20\%$ which are common in spiral galaxies (Savchenko & Reshetnikov 2013). Moreover, the position of the outer arm observed in HI maps by Koo et al. (2017) for the third quadrant requires a significant displacement (or kink) within the range of $140^\circ < l < 210^\circ$. Clearly, more sources with accurate measurements are needed to refine the position of a possible kink in the outer arm.

Bifurcation of the arm

As mentioned above, looking at the parallax positions of sources in Fig. 2.7, one could hypothesize that some sources follow the outer arm model of Reid et al. (2014) into quadrant 3, while others rather follow the new single arm model with a smaller pitch angle or the segmented arm model, forming thus a bifurcation at $l \sim 140^\circ$. Although HI maps of the Milky Way suggest that bifurcations of the Galactic arms (e.g., Koo et al. 2017) might occur, we cannot establish if this is the case for the outer arm at the Galactic longitudes investigated here, especially in the Galactic anticenter direction, where HI maps are inaccurate due to the largest velocity component (caused by the Galactic rotation) not being radial but transversal with respect to the Sun. More sources are needed to evaluate the likelihood of this hypothesis.

2.4.5 Optical members of the same stellar association

Massive young stars are understood to be formed from Giant Molecular Clouds that collapse generating high- and low-mass stellar cores (e.g., Tan et al. 2014). We can search for associated stars using *Gaia* DR2, but given that the HMSFR that hosts the S 269 IRS 2w massive young star is located close to the Galactic plane ($b = -1^\circ.46$), and at 4.15 kpc from the Sun, only the brightest, early-type members of the same stellar association are expected to be detectable with *Gaia*.

We review the proper motion for the stars within 125 pc around S 269 (see Sect. 2.3.3) using the *Gaia* DR2, finding that the closest (~ 37 pc projected distance) stellar cluster is NGC 2194. The *Gaia* parallax for NGC 2194 (i.e., 0.232 ± 0.027 calculated for 217 stellar members with $\sigma_\pi/\pi < 20\%$ including zero-point correction of -0.03 mas) is consistent with the S 269 parallax. However, there are several reasons to suggest that S 269 may not be directly associated with NGC 2194. First, based on chemical composition, Amado et al. (2004) and Netopil et al. (2016) have estimated an age of 0.87 ± 0.19 Gyr and 0.60 ± 0.25 Gyr for NGC 2194, whereas HMSFRs are expected to be two orders of magnitude younger (see, e.g., Battersby et al. 2017). Indeed, Jiang et al. (2003) reported a dynamic age of 10^5 yr for S 269. Second, there seems to be a serious discrepancy between the published luminosity distance (1.9 ± 0.1 kpc, Jacobson et al. 2011) and the distance estimate that one can obtain with *Gaia* data.

Finally, the three closest *Gaia* sources to S 269 IRS 2w found within the core of the S 269 HII region defined by Godbout et al. (1997) (i.e., 3.9 pc \times 2.8 pc) correspond to the three first rows in Table 2.6. Given that these sources have an average parallax and proper motion that are consistent with respect to the VLBA observations (i.e., -32 ± 23 μ as, 0.02 ± 0.65 and -0.16 ± 0.77 mas yr $^{-1}$), we suggest that they are likely early-type members of the same stellar

association that contains S 269 IRS 2w. However, further studies of these companion stars and their reddening could be used to estimate the age of S 269 and possibly refine its astrometry.

2.5 Conclusions

We present the results of high-accuracy VLBA observations of the S 269 region using relative astrometry. We detected nine water maser spots in S 269 that were prominent during at least three observing epochs. Four maser spots were detected in at least ten epochs, which allows a precise annual parallax fitting of 0.241 ± 0.012 mas corresponding to a distance of $4.15^{+0.22}_{-0.20}$ kpc.

Although the calculated distance corroborates the results previously published by Asaki et al. (2014), we show that the strongest maser spot (which was left out from their analysis because of its elongated shape) yields a well-constrained annual parallax, when the inner core position is used for the fit. Also, the longevity of the elongated water maser spot in the region is remarkable as it spans more than ten years (i.e., 2004-2016, between Honma et al. 2007, and our observations), however given the significant changes in proper motion between both observational sets, we could not estimate a 10-year astrometric fit. In addition, the VLBA images and the distribution of maser spots indicate that this spot could be originated from the compression of material in a shock front that propagates perpendicular to the elongation. Moreover, water maser emission detected in the same region from 1980 to 2001 by Lekht et al. (2001b) is likely to be the same that the VLBA detected in 2015-2016. However, the cyclic emission period previously estimated does not seem consistent with our observations.

We calculated a Galactic peculiar velocity for S 269 to be $(2 \pm 6, 4 \pm 14, 4 \pm 13)$ km s⁻¹ in the (U, V, W) Galactic frame, which confirms that the rotation curve at large radii (~ 12.4 kpc) is fairly flat. On the other hand, since there is no model that ties the masers in a shock front to the motion of the underlying star, the accuracy with which we know the motion of the system is limited.

By comparing S 269's position and proper motion with respect to other sources in the outer region of the Milky Way, we fitted the outer arm position, locating it closer to the Sun than previously thought. We explored three different scenarios: a new single outer arm pitch angle of $6^{\circ}2 \pm 3^{\circ}1$, a kink in the outer arm between two different segments and a bifurcation of the arm. Although all three are plausible explanations, the low value of a single arm pitch angle with respect to other arms and the lack of astrometric information to test a secondary segment coming from a bifurcation, lead us to favor a kink model. This kink can be described by two segments with pitch angles of $7^{\circ}9 \pm 5^{\circ}8$ and $10^{\circ}5 \pm 5^{\circ}9$, locating the kink in the second quadrant ($\sim 140^{\circ}$). This explanation is consistent with HI maps at $l > 180^{\circ}$, and is also supported by observations of similar features in other galaxies. Future observations are needed to assess if this is the case for the outer arm.

Finally, the *Gaia* DR2 catalog was inspected around S 269 for optical companions, which could be members of the stellar association. We did not find an optical counterpart for S 269 IRS 2w which could be exciting the water maser emission. However, we did find three optical sources that are likely members of the same stellar association that contains S 269 IRS 2w. Moreover, only one cluster (NGC 2194) was detected in the vicinity, but it is unlikely to be associated with S 269 given the difference in age. Future explorations of optical associations with respect to VLBI astrometric data are planned (e.g., Pihlström et al. 2018a) to refine the criteria for optical stellar companions around HMSFRs and evolved stars.

Acknowledgements. The National Radio Astronomy Observatory is a facility of the National Science Foundation operated under cooperative agreement by Associated Universities, Inc. This work made use

of the Swinburne University of Technology software correlator, developed as part of the Australian Major National Research Facilities Programme and operated under license. This work has also made use of data from the European Space Agency (ESA) mission *Gaia*⁷, processed by the *Gaia* Data Processing and Analysis Consortium (DPAC⁸). Funding for the DPAC has been provided by national institutions, in particular the institutions participating in the *Gaia* Multilateral Agreement. Moreover, this research has made use of “Aladin sky atlas” developed at CDS⁹, Strasbourg Observatory, France. The Digitized Sky Survey was produced at the Space Telescope Science Institute under U.S. Government grant NAG W-2166. The images of these surveys are based on photographic data obtained using the Oschin Schmidt Telescope on Palomar Mountain and the UK Schmidt Telescope. The plates were processed into the present compressed digital form with the permission of these institutions. This publication makes use of data products from the Two Micron All Sky Survey, which is a joint project of the University of Massachusetts and the Infrared Processing and Analysis Center/California Institute of Technology, funded by the National Aeronautics and Space Administration and the National Science Foundation. The authors sincerely acknowledge the anonymous referee for the suggestions that have improved this manuscript. L.H.Q.-N. would also deeply thank Dr. A.G.A Brown at Leiden Observatory for his comments and suggestions regarding the *Gaia* cross-match.

2.6 Appendix

2.6.1 Additional Tables

Table 2.5: VLBA observational epochs for S269 as part of the BR210E program during 2015-2016.

Epoch	Date (dd/mm/yyyy)	Time range (UTC) (hh:mm:ss - hh:mm:ss)
A	03/Aug/2015	11:55:29 - 18:57:42
B	29/Aug/2015	10:13:15 - 17:15:28
C	24/Sep/2015	08:31:02 - 15:33:14
D	18/Oct/2015	06:56:40 - 13:58:53
E	27/Jan/2016	00:19:33 - 07:19:45
F	07/Feb/2016	23:32:22 - 06:32:34
G	20/Feb/2016	22:41:15 - 05:41:27
H	29/Feb/2016	22:05:52 - 05:06:04
I	11/Mar/2016	21:22:37 - 04:22:49
J	20/Mar/2016	20:47:14 - 03:47:26
K	02/Apr/2016	19:56:07 - 02:56:19
L	15/Apr/2016	19:05:00 - 02:05:12
M	07/Aug/2016	11:36:47 - 18:36:58
N	01/Sep/2016	09:58:29 - 16:58:40
O	24/Sep/2016	08:28:03 - 15:28:14
P	22/Oct/2016	06:37:58 - 13:38:09

⁷<https://www.cosmos.esa.int/gaia>

⁸<https://www.cosmos.esa.int/web/gaia/dpac/consortium>

⁹<http://cds.u-strasbg.fr/>

Table 2.6: Astrometric parameters, mean g apparent magnitude and color given by *Gaia* DR2 for ten optical sources found in the vicinity of S 269 ($10' \times 7'$, Carpenter et al. 1990) or 12.1 pc \times 8.4 pc assuming our distance estimate of 4.15 kpc. The sky distribution of the sources is shown in optical and NIR images in Fig. 2.4. The projected distance (d_{S269}) between the *Gaia* sources and maser position S269 (06:14:37.6410,+13:49:36.6930).

<i>Gaia</i> source ID	α (J2015.5) (hh:mm:ss)	δ (J2015.5) ($^{\circ}$: ' : '')	d_{S269} (arcmin)	π (mas)	$\mu_{\alpha} \cos \delta$ (mas yr $^{-1}$)	μ_{δ} (mas yr $^{-1}$)
3344575631369939200	06:14:38.73	+13:49:45.06	0.30	0.232 \pm 0.043	-0.012 \pm 0.078	-0.739 \pm 0.069
3344575627071194240	06:14:38.99	+13:49:43.90	0.35	0.247 \pm 0.028	-0.113 \pm 0.052	-0.247 \pm 0.046
3344578586307442560	06:14:35.35	+13:49:43.40	0.57	0.238 \pm 0.042	0.020 \pm 0.077	-0.491 \pm 0.068
3344575695792364672	06:14:45.94	+13:50:30.56	2.20	0.304 \pm 0.056	0.711 \pm 0.097	-2.908 \pm 0.088
3344578959966755200	06:14:29.28	+13:52:32.46	3.56	0.255 \pm 0.029	0.919 \pm 0.058	-2.379 \pm 0.052
3344580506155003776	06:14:41.50	+13:53:05.03	3.60	0.284 \pm 0.055	0.280 \pm 0.099	-1.547 \pm 0.089
3344576937039978624	06:14:57.98	+13:50:12.24	4.97	0.238 \pm 0.047	-0.070 \pm 0.080	-0.732 \pm 0.073
3344579784600525952	06:14:25.88	+13:53:43.46	5.01	0.260 \pm 0.037	0.257 \pm 0.069	-0.864 \pm 0.066
3344576181125735424	06:15:00.10	+13:49:20.22	5.46	0.262 \pm 0.034	0.029 \pm 0.064	-2.753 \pm 0.058
3344573909084277632	06:14:41.57	+13:44:02.90	5.64	0.279 \pm 0.025	-0.031 \pm 0.043	-0.854 \pm 0.038

Notes. The sources are organized by proximity to the water mater emission with the closest first. The three first rows are the optical stars that were found within the size of the HII region S 269 defined by Godbout et al. (1997) as 3.9 pc \times 2.8 pc and are likely to be associated with the S 269 HII region (Sect. 2.4.5).



Simulated Galactic methanol maser distribution to constrain Milky Way parameters

Quiroga-Nuñez, L. H.; van Langevelde, H. J.; Reid, M. J. & Green, J. A. *Simulated Galactic methanol maser distribution to constrain Milky Way parameters*. 2017, A&A, 604, A72.

Abstract

Using trigonometric parallaxes and proper motions of masers associated with massive young stars, the Bar and Spiral Structure Legacy (BeSSeL) survey has reported the most accurate values of the Galactic parameters so far. The determination of these parameters with high accuracy has a widespread impact on Galactic and extragalactic measurements. This research is aimed at establishing the confidence with which such parameters can be determined. This is relevant for the data published in the context of the BeSSeL survey collaboration, but also for future observations, in particular from the southern hemisphere. In addition, some astrophysical properties of the masers can be constrained, notably the luminosity function. We have simulated the population of maser-bearing young stars associated with Galactic spiral structure, generating several samples and comparing them with the observed samples used in the BeSSeL survey. Consequently, we checked the determination of Galactic parameters for observational biases introduced by the sample selection. Galactic parameters obtained by the BeSSeL survey do not seem to be biased by the sample selection used. In fact, the published error estimates appear to be conservative for most of the parameters. We show that future BeSSeL data and future observations with southern arrays will improve the Galactic parameters estimates and smoothly reduce their mutual correlation. Moreover, by modeling future parallax data with larger distance values and, thus, greater relative uncertainties for a larger numbers of sources, we found that parallax-distance biasing is an important issue. Hence, using fractional parallax uncertainty in the weighting of the motion data is imperative. Finally, the luminosity function for 6.7 GHz methanol masers was determined, allowing us to estimate the number of Galactic methanol masers.

3.1 Introduction

A lack of accurate distance measurements throughout the Galaxy combined with our location within the Milky Way have complicated the interpretation of astrometric measurements (Reid & Honma 2014). Consequently, the most fundamental Galactic parameters, such as the distance to the Galactic center (R_0), the rotation speed at the solar radius (Θ_0), and the rotation curve (e.g., $d\Theta/dR$) have not been established with high accuracy. At Galactic scales, distance estimates through radial velocities, mass and luminosity calculations of sources within the Galaxy, as well as the mass and luminosity estimates of the Milky Way, depend on the Galactic parameters. Additionally, extragalactic measurements are based on Galactic calibrations that are made using the Milky Way parameter values. Therefore, highly accurate estimates of the fundamental Galactic parameters are vitally important.

A step forward came with the Hipparcos satellite (Perryman et al. 1997). It provided astrometric accuracies of the order of 1 milliarcsecond (mas), which allows distance estimations in the solar neighborhood (~ 100 pc) with 10% accuracy. However, this is a tiny portion of the Milky Way. The ongoing European Space Agency mission, Gaia, aims to measure parallaxes and proper motions of 10^9 stars with accuracies up to $20 \mu\text{as}$ at 15 mag with a distance horizon of 5 kpc with 10% accuracy and 10 kpc with 20% accuracy (Perryman et al. 2001; Gaia Collaboration et al. 2016a). Although Gaia will transform our knowledge of the Milky Way, the mission is restricted to optical wavelengths and due to significant dust obscuration, it will not be able to probe the Galactic plane freely. In contrast, radio wavelengths are not affected by dust extinction and can be used throughout the Galaxy.

Direct accurate distances and proper motions have been measured for maser-bearing young stars (e.g. Sanna et al. 2014; Burns et al. 2017); this data was obtained employing Very Long Baseline Interferometry (VLBI). This astrometric information has provided us with a better understanding of the Milky Way's spiral structure, insights into the formation and evolution of our Galaxy, its 3D gravitational potential, and the Galactic baryonic and dark matter distribution (Efremov 2011).

The most suitable radio beacons for astrometry are methanol (6.7 and 12.2 GHz) and water (22 GHz) masers (Brunthaler et al. 2011). In addition to being bright, water masers can be associated with high mass star forming regions (HMSFRs), while class II 6.7 and 12 GHz methanol masers are uniquely associated with HMSFRs (e.g. Breen et al. 2013; Surcis et al. 2013). By detecting 6.7 GHz methanol masers, we trace the Galactic spiral structure because HMSFRs are expected to be born close to a spiral arm and evolve more quickly than low-mass stars (Yusof et al. 2013). Therefore, HMSFRs should follow the disk rotation with low dispersion (compared, for example, to masers in evolved stars).

Given parallax, proper motion measurements, source coordinates, and line-of-sight velocities (from Doppler shifts of spectral lines) to methanol and water masers, it is possible to sample complete phase-space information. This provides direct and powerful constraints on the fundamental parameters of the Galaxy. The Bar and Spiral Structure Legacy (BeSSeL¹) survey has addressed this task using different arrays: the Very Long Baseline Array (VLBA) in USA and the European VLBI Network (EVN) in Europe, Asia and South Africa. Additionally similar parallax and proper motion data has come from the VLBI Exploration of Radio Astrometry (VERA) in Japan. The most recent summary paper (Reid et al. 2014) lists astrometric data for 103 parallax measurements with typical accuracies of $20 \mu\text{as}$. By fitting these sources to an axially symmetric Galactic model, they provide accurate values for the fundamental Galactic parameters: $R_0 = 8.34 \pm 0.16$ kpc, $\Theta_0 = 240 \pm 8$ km s⁻¹, and $d\Theta/dR = -0.2 \pm 0.4$ km s⁻¹ kpc⁻¹ between Galactocentric radii of 5 and 16 kpc.

¹<http://bessel.vlbi-astrometry.org/>

Although the BeSSeL survey data is very accurate, the target selection used was necessarily biased. It has targeted the brightest known masers accessible to the (northern hemisphere) VLBI arrays used. Most of the published targets used by BeSSeL for astrometric measurements are 22 GHz water masers and 12 GHz methanol masers that were originally selected based on 6.7 GHz surveys. In the current study, a model used to simulate the 6.7 GHz methanol maser distribution in the Milky Way is presented. The model was compared with systematic surveys, allowing us to determine the luminosity function. Also, it is used to generate different artificial samples that can be used to test how accurately they can fit a Galactic model and how a given level of incompleteness can bias the Galactic parameter values. This is particularly important when more sources are being added to the BeSSeL sample.

In Sect. 3.2 the components and assumptions of the model are presented. Next, Sect. 3.3 describes the luminosity function fitted using observational surveys, the Galactic parameter results, and the correlation among parameters using several samples. Finally, the discussion and conclusions of the results compared to the BeSSeL findings are shown in Sects. 3.4 and 3.5, respectively.

3.2 Model for the 6.7 GHz methanol maser distribution in the spiral structure

The main components of the Milky Way can be identified as a halo, nuclear bulge (or bar), and two disk components: a thin and a thick disk (see e.g. Gilmore & Reid 1983; Rix & Bovy 2013). The current model is centered on the thin disk component, more specifically on a spiral structure between 3 kpc and 15 kpc as traced by HMSFRs that contains methanol maser bearing stars. Following the analysis made by Reid et al. (2014), the model is based on a galaxy with spiral structure. The analysis of the rotation and scale of the galaxy does not seem directly dependent on this assumption.

Model Variable	Distribution Type	Distribution Parameters
Galactic Plane (X,Y)	Radial decay and Monte Carlo rejection	$h_r = 2.44$ kpc (1) $\sigma_d = 0.35$ kpc (1)
Vertical Position (Z) (2)	Gaussian	$\mu_z = 0$ kpc $\sigma_z = 25$ pc
Radial Velocity (U)	Gaussian	$\mu_r = 0$ km s ⁻¹ $\sigma_r = 5$ km s ⁻¹
Tangential Velocity (V)	Gaussian	$\mu_t = \Theta_0 = 240$ km s ⁻¹ (1) $\sigma_t = 9$ km s ⁻¹
Vertical Velocity (W)	Gaussian	$\mu_v = 0$ km s ⁻¹ $\sigma_v = 5$ km s ⁻¹
Luminosity Function (L) (3)	Power Law	Cutoffs: $10^{-8} L_\odot$, $10^{-3} L_\odot$ and $\alpha = -1.43$

Table 3.1: *Spatial, velocity and luminosity distributions used in the current model. We assumed the sun’s vertical position to be $z=0$ pc and any change in this value, which Goodman et al. (2014) suggested to be 25 pc, was found negligible at these scales. References: (1) Reid et al. (2014), (2) Green & McClure-Griffiths (2011), and (3) Pestalozzi et al. (2007). Radial, tangential and vertical velocity dispersion values are discussed in Sect. 3.2.3.*

The aim of the model is to build a simulated database ready to be processed with the

Galactic parameter fitting method used by the BeSSeL survey. To do this, each simulated 6.7 GHz methanol maser has spatial coordinates, velocity components, and an associated intrinsic luminosity (and their respective uncertainties). In the following subsections, we explain each of the distributions and the initial parameters adopted, as well as the fitting procedure used to obtain the Galactic parameters from the astrometric data. Table 3.1 presents a summary of the distributions and values used.

3.2.1 Initial parameters

Reid et al. (2014) presented their best estimates of the Galactic parameter values (Model A5), which we adopt here (see Table 3.2):

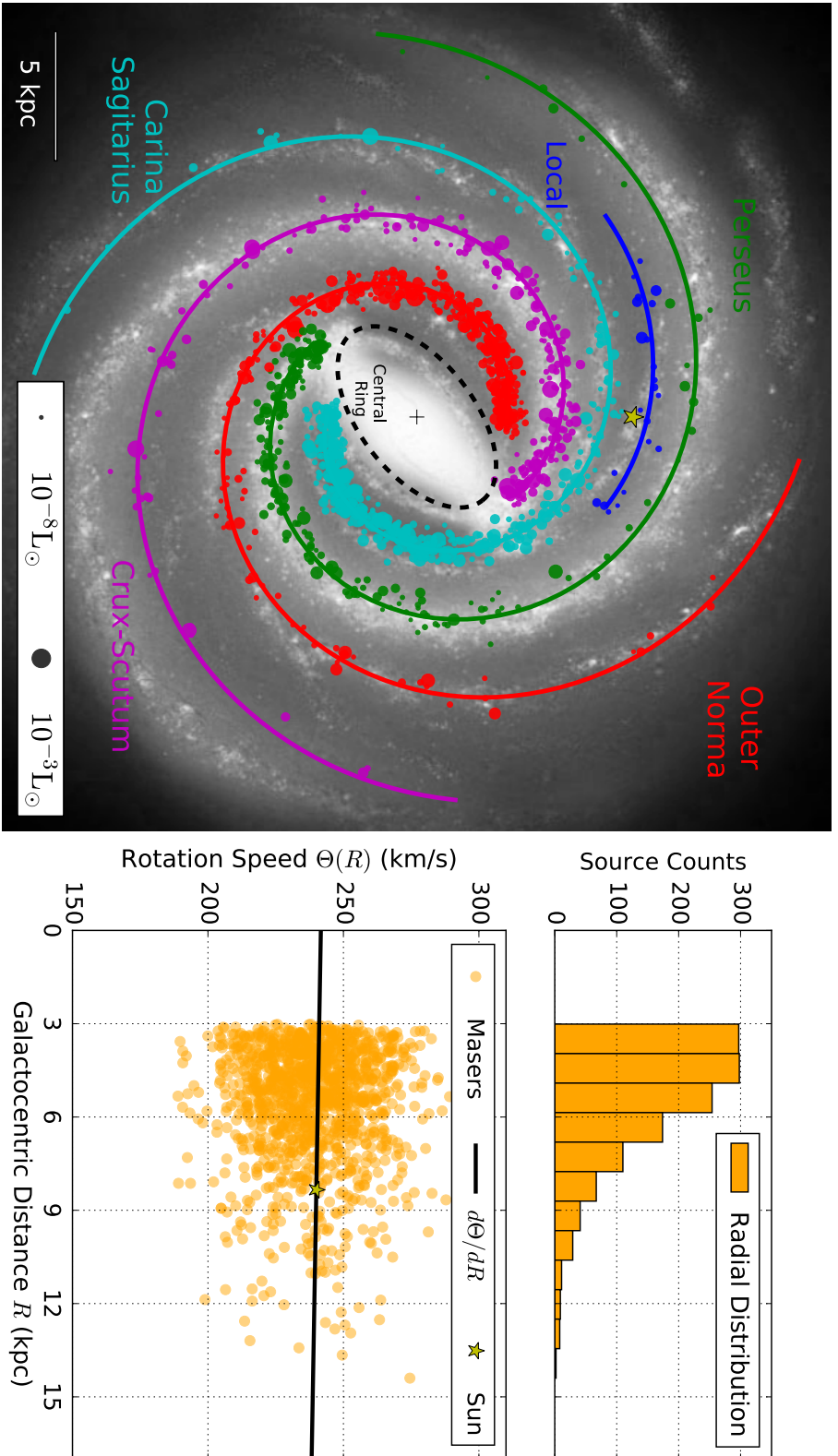
- $R_0, \Theta_0, d\Theta/dR$: **fundamental Galactic parameters.** We took the current results of the BeSSeL survey, which assumes a Galactic model as a disk rotating at a speed of $\Theta(R) = \Theta_0 + \frac{d\Theta}{dR}(R - R_0)$;
- \bar{U}_s, \bar{V}_s : **average source peculiar motion.** When velocities are measured, systematic extra velocity components can appear as a result of two effects: gas approaching a spiral arm with enhanced gravitational attraction and magneto-hydrodynamic shocks as the gas enters the arm; therefore, these extra velocity components, which are defined at the position of each source, account for any average peculiar motion of the masers;
- $U_\odot, V_\odot, W_\odot$: **solar motion.** Because the model predicts the velocities with respect to the local standard of rest (LSR) for all masers, the solar motion must be taken into account in order to make the proper heliocentric corrections;
- N : **number of sources.** The total number of 6.7 GHz methanol masers in the Galaxy is a required parameter to populate the spiral arms. In Sect. 3.3, this parameter is fitted by comparing the model with the results of Methanol Multibeam Survey (MMB, see: Green et al. 2009, 2010, 2012; Caswell et al. 2010, 2011) results given the adopted spatial distribution (Sect. 3.2.2) and luminosity function (Sect. 3.2.5).

Parameter	Definition	Value
R_0	Sun-Galactocentric distance	8.34 kpc
Θ_0	Solar rotation speed	240 km s ⁻¹
$d\Theta/dR$	Rotation curve	-0.2 km s ⁻¹ kpc ⁻¹
U_\odot	Inward radial solar velocity	10.7 km s ⁻¹
V_\odot	Tangential solar velocity	15.6 km s ⁻¹
W_\odot	Vertical solar velocity	8.9 km s ⁻¹
\bar{U}_s	Inward radial average peculiar motion	2.9 km s ⁻¹
\bar{V}_s	Tangential average peculiar motion	-1.5 km s ⁻¹

Table 3.2: Description of initial parameters values used in the model which are based on the Model A5 results published in Reid et al. (2014).

3.2.2 Spatial distribution

The spatial distribution along the spiral arms can be split into two components, a Galactic plane distribution and a vertical component distribution (Z). The latter can be drawn using a



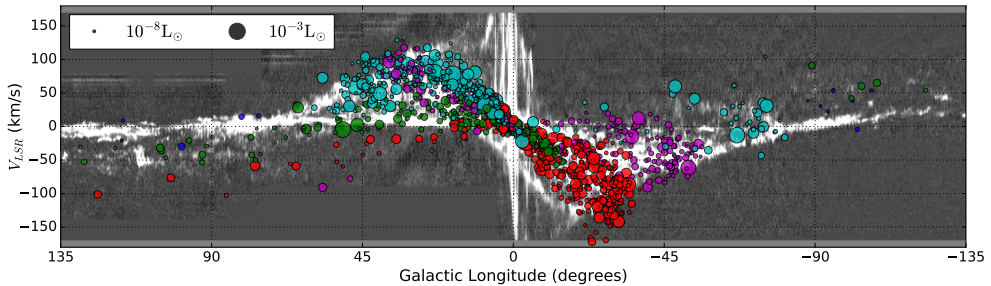


Figure 3.2: Velocity with respect to the LSR as a function of the Galactic longitude for the simulated 6.7 GHz methanol masers distribution. The point size is a measure of the peak luminosity function (Sect. 3.2.5). Masers associated with different spiral arms are color-coded as in Fig. 3.1. The figure is overlaid on the CO emission ($J = 1 - 0$) plotted in grayscale and taken from Dame et al. (2001).

random generator from a Gaussian distribution with a mean of 0 pc and $\sigma = 25$ pc since massive young stars are found to be born close to the Galactic plane (see e.g. Green & McClure-Griffiths 2011; Bobylev & Bajkova 2016).

The Galactic plane distribution is drawn following two constraints. First, the density of HMSFRs falls off exponentially with the Galactocentric distance (R) (Bovy & Rix 2013), and second, each source should be associated with a spiral arm (Reid et al. 2014). For the first constraint, the maser radial distribution follows Cheng et al. (2012)

$$n(R) \propto e^{-R/h_R}, \quad (3.1)$$

where $n(R)$ is the number of sources and h_R the exponential scale length, which has been estimated from the maser parallax data assuming a Persic Universal rotation curve formulation to be 2.44 kpc (Reid et al. 2014) which we assumed valid for massive young stars. The top right panel of Fig. 3.1 shows the radial distribution of the simulated masers.

For the second constraint, the spiral arm positions were set following an analytic approximation made by Wainscoat et al. (1992). Each spiral arm (four main arms and the local arm) can be located in the Galactic plane using a simple relation in polar coordinates. The left plot of Fig. 3.1 depicts the position of the spiral arms as seen from the north galactic pole (NGP). In order to populate the spiral arms with 6.7 GHz methanol masers, a rejection sampling Monte Carlo method was implemented. For this, the model takes a source from the radial distribution (Eq. 3.1) and then the distance is calculated between the source and the closest spiral arm. That distance d is evaluated in a probability density function of a Gaussian distribution

$$P(d) \propto \exp\left(\frac{-(d - \mu)^2}{2\sigma_d^2}\right), \quad (3.2)$$

where $\mu = 0$ kpc, yielding the same likelihood of the source to be behind or in front of the spiral arm. We took $\sigma_d = 0.35$ kpc, which corresponds to the maximum spiral width arm observed for HMSFRs (Reid et al. 2014). The model evaluates $P(d)$ for each source and compares it with a random value k ($0 < k < 1$). If $k > P(d)$, the source is rejected and the model takes another source from the radial distribution to calculate $P(d)$ again and compare it with a new k . However, if a source satisfies $k < P(d)$, then the source is taken as a part of the model. The acceptance process will continue until it reaches the total number of sources (N). One example of a resulting spatial distribution can be seen in Figs. 3.1 and 3.2.

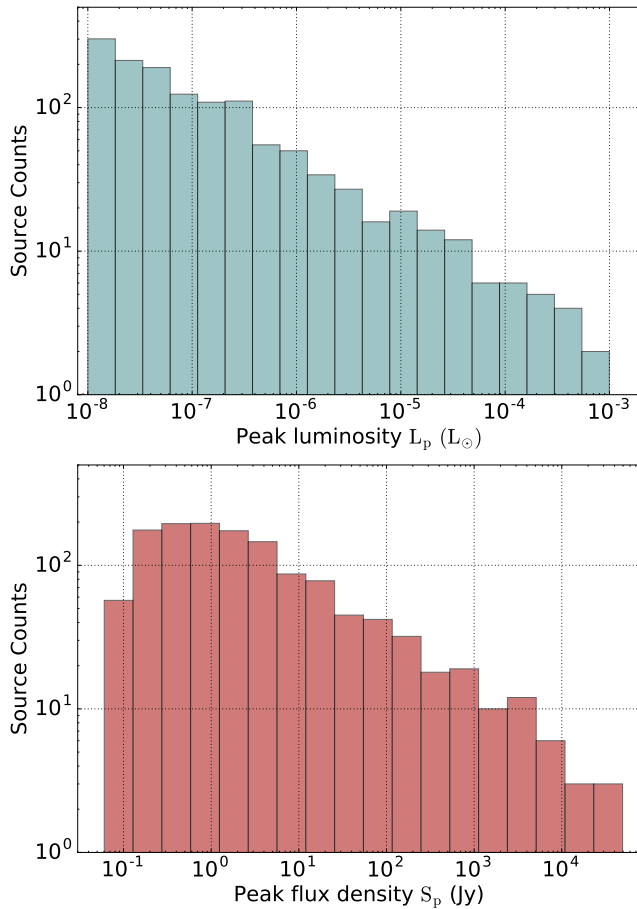


Figure 3.3: **Top:** Peak luminosity function adopted in the model using the fitted values for the total number of 6.7 GHz methanol masers ($N = 1300$) and the slope of the luminosity function ($\alpha = -1.43$), see Sect. 3.2.5 and 3.3.1. **Bottom:** Peak flux density function obtained without sensitivity limit.

3.2.3 Velocity distribution

For the velocity distribution, we used a cylindrical coordinate system (U, V, W) in a rotational frame with an angular velocity of $\Theta(R)$ in the direction of the Galaxy rotation, i.e., clockwise seen from the NGP. In this system, U is the radial component defined positive towards the center of the Galaxy, V is the tangential velocity component defined positive in the direction of the Galactic rotation and W is the vertical velocity component defined positive towards the NGP.

We drew Gaussian distributions for each velocity component independently using the values, distributions and dispersions related in Table 3.1. For the tangential velocity, we adopted a Gaussian distribution with a mean value given by $\Theta(R) = \Theta_0 + d\Theta/dR(R - R_0)$ and a dispersion of $\sigma_t = 9 \text{ km s}^{-1}$ (see Table 3.1). The values for Θ_0 , $d\Theta/dR$ and R_0 are provided in Table 3.2. The lower right panel of Fig. 3.1 and Fig. 3.2 show the distribution of the Galactic tangential velocities $\Theta(R)$ and the maser velocities with respect to LSR as a function of Galactocentric distance and Galactic longitude respectively, assuming the values listed in Table 3.2.

The adopted dispersions for radial and vertical velocity components ($\sigma_{r,v} = 5 \text{ km s}^{-1}$) are consistent with our estimates of virial motions of individual massive stars, based on BeSSeL data, whereas σ_t was set larger to allow for the possible effects of gravitational accelerations in the presence of material near spiral arms.

3.2.4 Methanol masers represented in the model

The BeSSeL survey determined proper motions and parallaxes of water masers (at 22 GHz) and methanol masers (at 6.7 and 12 GHz) and fit them to an axially symmetric Galactic model to estimate the Galactic parameters. Compared with the BeSSeL survey, we have made a simplification by assuming that all sources are selected from 6.7 GHz methanol masers surveys, but observed with VLBI at 12 GHz.

3.2.5 Luminosity distribution

Notably, for our model it is important to estimate astrometric observational errors based on maser detectability, which are directly related to the peak flux density (S_p) of each maser, i.e., the flux density emitted in a specific line integrated over a single channel width. The peak flux density function can be estimated if the peak luminosity function and the spatial distribution are known, assuming isotropic emission. Although the individual maser spots may not radiate isotropically, we assume that this holds over the sample of randomly oriented masers.

Pestalozzi et al. (2007) have suggested that the 6.7 GHz methanol maser luminosity distribution takes the form of a single power law with sharp cutoffs of $10^{-8} L_\odot$ and $10^{-3} L_\odot$ and a slope (α) between -1.5 and -2 . We assume the same dependence for the peak luminosity function (see Fig. 3.3), but we refine it by varying the parameters to match the results of the MMB survey. The results of this procedure are presented in Sect. 3.3.1.

3.2.6 Error allocation

In order to be able to use simulated data in tests to estimate the Galactic parameters, it is necessary to assign observational error distributions. For our model, the errors in the parallax and proper motions were estimated following a calculation for relative motions of maser spots and statistical parallaxes, i.e., $\sigma_\pi \propto \Theta_{res}/(S/N)$ and $\sigma_{\mu_{\alpha,\delta}} = \sigma_\pi/(1\text{yr})$, where Θ_{res} is the VLBA resolution for 12 GHz methanol masers. The signal-to-noise ratio (S/N) depends on the peak flux density value (S_p) and given that most of the current data of the BeSSeL survey are based on VLBA observations, we adopted a channel width of 50 kHz (1.24 km s^{-1}) at 12 GHz and an integration time of 2 hr. This was used to estimate the S/N and thus the errors in parallax and proper motions. Reid et al. (2014) estimated an additional error term for $\sigma_{V_{los}}$ (5 km s^{-1}), which is associated with the uncertainty on transferring the maser motions to the central star. This error dominates the BeSSeL observations of V_{los} , and this uncertainty is reflected in the value of $\sigma_{V_{los}}$.

Parallax estimates in Reid et al. (2014) are often dominated by residual, whereas troposphere-related errors dominate in the astrometry, and so we adopted a simple prescription for parallax uncertainty (as shown above), which does not directly include systematic effects. However, when a large number of simulated sources are used, many weak masers are included that would be S/N limited. Figure 3.4 shows a comparison between the two error distributions for observational and simulated parallax measurements in which our S/N error estimate yields a similar distribution to the uncertainties used in Reid et al. (2014).

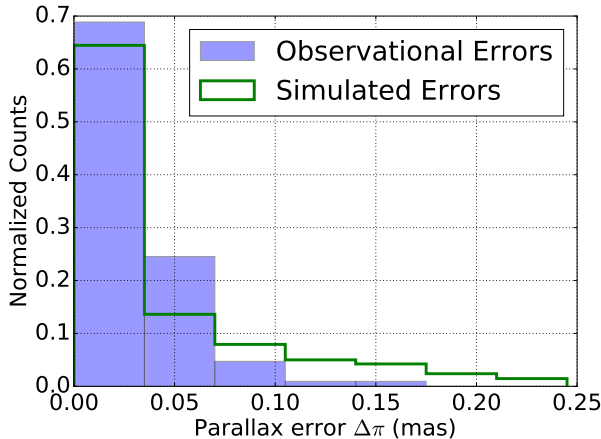


Figure 3.4: Comparison between the error distribution for observational and simulated parallax measurements. Observational errors are based on 103 astrometric sources published in Reid et al. (2014) as part of the BeSSeL survey.

	MMB		Arecibo	
	Observation	Simulation	Observation	Simulation
Sensitivity (3σ)	≤ 0.71 Jy		≤ 0.27 Jy	
Sky coverage	$-174^\circ \leq l \leq 60^\circ$		$35.2^\circ \leq l \leq 53.7^\circ$	
	$-2^\circ \leq b \leq 2^\circ$		$-0.4^\circ \leq b \leq 0.4^\circ$	
Sources	908	800 ± 20	76	95 ± 10
β	-0.60 ± 0.1	-0.44 ± 0.1	-0.36 ± 0.1	-0.38 ± 0.1

Table 3.3: Limits in sensitivity and source location, numbers of masers detected and the slope of the flux density functions (β) for the 6.7 GHz methanol masers surveys: MMB and Arecibo. Limits of both surveys, numbers of masers (N) and slope of the luminosity function (α) fitted in Sect. 3.3.1, were applied to our Galactic model; the results are displayed in the columns labeled "Simulation". The simulated errors correspond to the standard deviation after running 100 simulated galaxies.

The fitting procedure described by Reid et al. (2014) used to determine the Galactic parameters (combining BeSSeL and VERA data) requires high accuracy VLBI data as input. This data consists of a 3D position vector (α, δ, π), a 3D velocity vector ($\mu_\alpha, \mu_\delta, V_{los}$), and the errors $\sigma_\pi, \sigma_{\mu_\alpha}, \sigma_{\mu_\delta}$ and $\sigma_{V_{los}}$. Although the model gives exact values for position and velocities of each maser source seen from the Earth, we are interested in realistic values as input for the fitting procedure. Therefore, we add a noise component to each observable quantity ($\pi, \mu_\alpha, \mu_\delta, V_{los}$), using random values following Gaussian distributions with standard deviations equal to the estimated errors previously calculated. By changing the error distribution, we can control the quality of the data entered in the fitting procedure.

3.2.7 Fitting procedure

The fitting procedure used was adopted from the BeSSeL survey (see Reid et al. 2009a, 2014). The input data for the fitting procedure are 3D position and 3D velocity information of the masers, conservative priors for the solar motion, the average source peculiar motion, and the Galactic scale and rotation. Convergence on the best Galactic parameters to match the spatial-

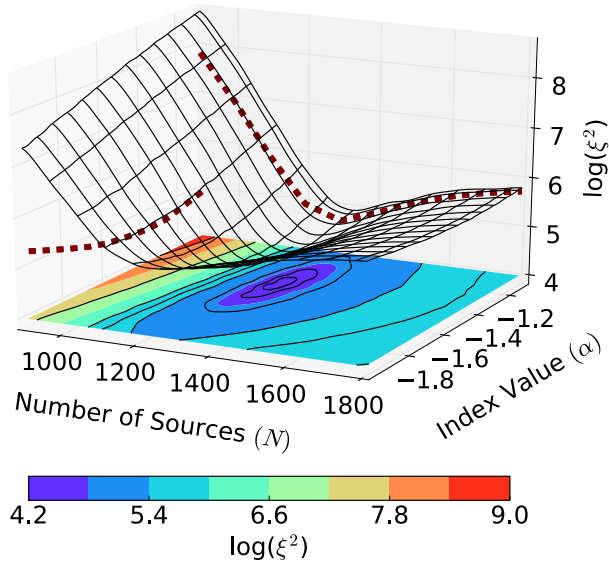


Figure 3.5: Grid of initial parameters displaying the ξ^2 calculation for each N , α pair. The dark blue region represents the best values of N and α that most closely match the MMB results. The projected gray dashed lines show the profiles of the surface close to the minimum values of ξ^2 .

kinematic model was made using a Bayesian fitting approach, where the velocities were used as known data to be fitted, and the sky positions and distances were used as coordinates. The posterior probability density function (PDF) of the Galactic parameters were estimated with Markov chain Monte Carlo (MCMC) trials that were accepted or rejected by a Metropolis-Hastings algorithm (see Reid et al. 2009a, 2014, for a detailed explanation). Finally, the procedure returns the best Galactic parameter values that match the simulated data to the spatial-kinematic model. The fitting procedure was improved compared to that used in Reid et al. (2009a, 2014): first, the fitting procedure now corrects for bias when inverting parallax to estimate distance, which becomes significant when fractional parallax uncertainties exceed $\approx 15\%$ (note this is not a trivial inference problem, see e.g. Bailer-Jones 2015); second, the fitting procedure was improved by adding a term to the motion uncertainties, which comes from parallax uncertainty. After these two modifications, the fitting procedure yielded unbiased Galactic parameter values, even when weak and/or very distant masers with large fractional parallax uncertainties were simulated.

3.3 Results

A comparison of the systematic 6.7 GHz methanol maser observational surveys and the simulated model peak flux density is shown in Sect. 3.3.1. In Sect. 3.3.2, different sample selections are used to compare the Galactic parameters obtained with respect to the initial values used (Table 3.2). Finally, in Sect. 3.3.3, the Pearson correlation coefficients are calculated to quantify correlations among the Galactic parameters.

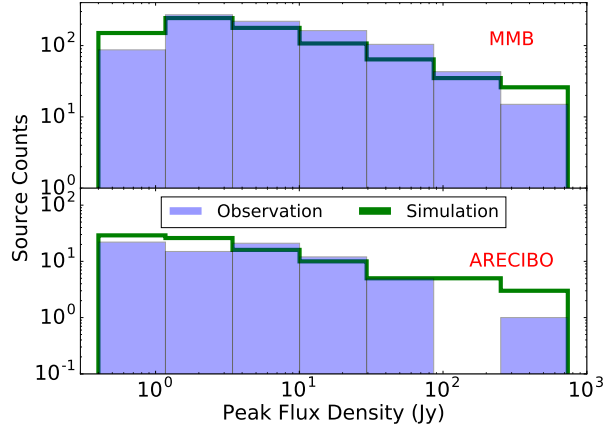


Figure 3.6: In blue: flux density function obtained for the MMB (top) and the Arecibo survey (bottom). In green: simulated flux density function obtained in the model (using $N = 1300$ and $\alpha = -1.43$) after the MMB and Arecibo limits were applied (Table 3.3).

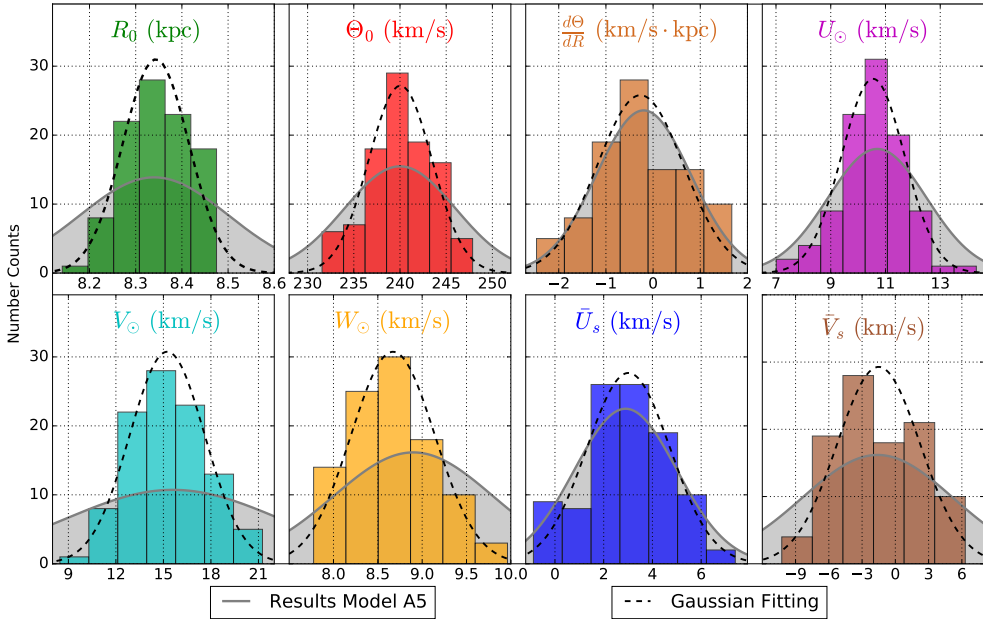


Figure 3.7: Galactic parameters distributions found for 100 simulated galaxies mimicking the BeSSeL data sample selection (Sect. 3.3.2). The values listed in Table 3.4 correspond to the fitting made to the histograms and shown as black dashed lines. Bayesian fitting results for the A5 model reported in Reid et al. (2014) are shown as gray regions.

3.3.1 Luminosity function for 6.7 GHz methanol masers

We compared the flux density distribution functions of the MMB survey and the Arecibo survey with the current model to fit two parameters: the total number of sources (N) and the slope of the peak luminosity function (α). The MMB survey is the most sensitive unbiased survey yet undertaken for 6.7 GHz methanol masers. The Parkes Observatory was upgraded

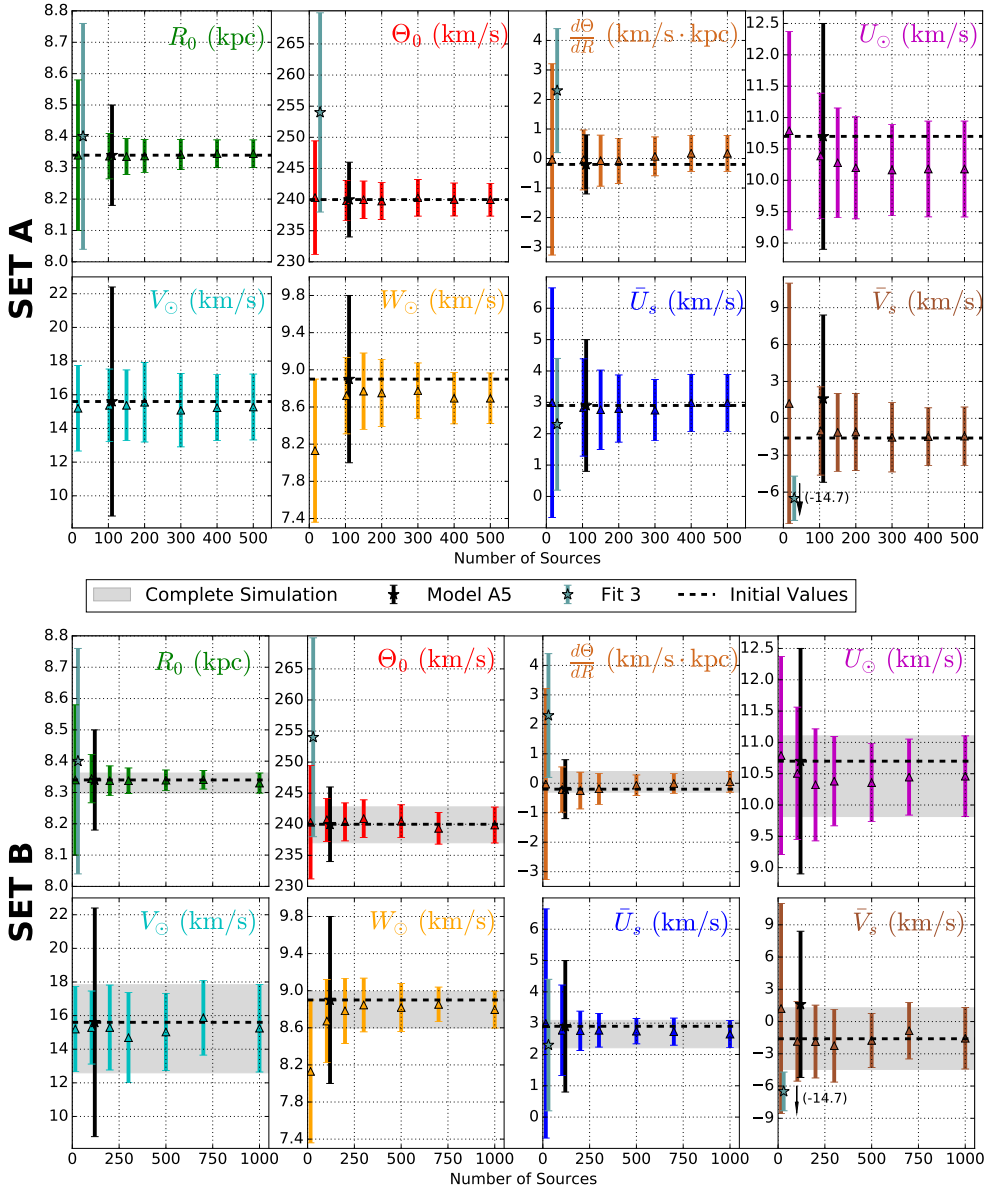


Figure 3.8: Galactic parameter values obtained for samples in sets A and B. In each sample, sources are added in the northern hemisphere simulating the future BeSSeL results (set A) and without location limit simulating samples when southern arrays can contribute with data (set B). First and current BeSSeL results published in Reid et al. (2009a, 2014), respectively labeled "Fit 3" and "Model A5", are shown as stars for comparison. The initial values adopted in the model are represented as dashed lines. Gray regions correspond to values and uncertainties obtained for the complete sample ($N = 1300$).

with a seven-beam receiver to carry out a full systematic survey of the Galactic Plane (Green et al. 2012, and the references within). The Arecibo Survey was a deep a 6.7 GHz methanol maser survey over a limited portion of the Galactic plane (Pandian et al. 2007).

Table 3.3 summarizes the survey limits in sensitivity and sky coverage for the MMB and Arecibo surveys. The last two rows list the number of sources detected and the slope of the flux density function (β) for each survey. By using these data, we were able to make a direct comparison between the simulated and observed flux density functions for each survey (green and blue histograms in Fig. 3.6). For our comparison, we excluded MMB sources that reside inside a Galactocentric radius of 3 kpc as this region is not part of the model.

In order to fit N and α to the results of the surveys, a grid of initial parameters (Fig. 3.5) was sampled using similar ranges to those proposed by Pestalozzi et al. (2007) for $N = [900, 1800]$ and van der Walt (2005) for $\alpha = [-1.1, 2.0]$. The grid was constructed such that each point represents a pair of initial parameters (N, α) and for each pair, a set of simulated galaxies was generated following the initial conditions described in Sect. 3.2. Next, the surveys limits (Table 3.3) were applied, and we compared the flux density function obtained for each N, α pair with the flux density function of the MMB survey (blue histogram in the top of Fig. 3.6). Through a minimization procedure, we found values of N and α that best match the MMB results. This procedure was implemented only for the MMB data since it represents a larger and more complete sample than the Arecibo survey. The minimization procedure compares the MMB observed (blue) and the simulated (green) flux density functions (see Fig. 3.6) and minimizes a quantity called ξ^2 , where

$$\xi^2 = \sum_{bins} \frac{(y - y_{obs})^2}{y_{obs}}, \quad (3.3)$$

and y represents the number of sources per luminosity bin. Given that our Galactic model generates galaxies based on a stochastic method, the position, velocity and luminosity values for each maser vary each time the model is executed (even using the same pair of N and α). By generating sets of ten independent galaxy simulations per N, α pair, we found that the fluctuations in the simulations were smaller than the uncertainties in the binned data, and hence this procedure was applied.

Figure 3.5 shows the values obtained for ξ^2 per N, α pair as a 3D surface. The dark blue region in the projected contour plot represents the best set of parameters that mimic the MMB survey results. We found that the surface near the minimum can be approximated by a Gaussian in two dimensions (see projections in Figure 3.5). Using the maximum likelihood estimation, which is well defined for multivariate Gaussian distributions, we estimated the mean and its respective uncertainty. The best parameters were found to be $N = 1300 \pm 60$ sources and $\alpha = -1.43 \pm 0.18$. Finally, Fig. 3.6 shows the flux density function for the MMB (top), and Arecibo survey (bottom) in blue, and their respective simulated flux density function are shown in green for the best parameters of N and α found. Additionally, the number of sources detected and the slope of the flux density function (β) for the simulated surveys are listed in Table 3.3.

3.3.2 Galactic parameters and selection of sample

The model can reproduce the methanol maser distribution for the entire Galaxy including observational errors. In order to evaluate the possible biases introduced by the observed BeSSeL sample (equivalent to the 103 brightest sources in the declination region, $-30^\circ \leq \delta \leq 70^\circ$, which is equivalent to $-2^\circ \leq l \leq 242^\circ$), 100 galaxies were simulated to mimic the BeSSeL

Galactic Parameter	Simulated BeSSeL Sample	A5 Model
R_0 (kpc)	8.34 ± 0.07	8.34 ± 0.16
Θ_0 (km s ⁻¹)	240.0 ± 3.4	240.0 ± 8.0
$d\Theta/dR$ (km s ⁻¹ kpc ⁻¹)	-0.3 ± 0.9	-0.2 ± 0.4
U_\odot (km s ⁻¹)	10.5 ± 1.2	10.7 ± 1.8
V_\odot (km s ⁻¹)	15.2 ± 2.4	15.6 ± 6.8
W_\odot (km s ⁻¹)	8.7 ± 0.5	8.9 ± 2.1
U_s (km s ⁻¹)	3.0 ± 1.7	2.9 ± 2.1
V_s (km s ⁻¹)	-1.5 ± 3.8	-1.5 ± 6.8

Table 3.4: Galactic parameter results for 100 simulated galaxies mimicking the BeSSeL data sample. Additionally, the Bayesian fitting results for the A5 model reported in Reid et al. (2014), which were also the initial values adopted in the model (Table 3.2), are shown for comparison.

sample. Then, they were fitted to test whether the adopted Galactic parameters were returned. Figure 3.7 shows the distribution obtained on each Galactic parameter for the simulated BeSSeL sample compared with the values reported in Reid et al. (2014). The histograms were fitted to Gaussian distributions, and the results are shown in Table 3.4. Clearly, in all cases the distributions of fitted values are centered on the adopted value, and in most cases the widths of the distributions are smaller than those reported in Reid et al. (2014).

In addition to the 100 simulated galaxies that mimic the BeSSeL sample, we also simulated the first BeSSeL data sample, where only 16 HMSFRs over the northern hemisphere were used to estimate the same Galactic parameters but not the solar motion (Reid et al. 2009a). Moreover, we also started adding sources to form two additional sets of simulated data. Set A was made to study the impact of future viable observations with the VLBA, EVN, and VERA to obtain up to 500 sources in the northern hemisphere. Again, we selected the brightest sources first to fall in the same declination range that BeSSeL is targeting for this. We generated samples from 16 up to 500 sources, which were drawn from the total number sources ($N = 1300$) that may lie in the declination range proposed. Set B represents the conditions for a more complete effort when VLBI arrays in the Southern hemisphere can contribute to the astrometric sample. As was done in set A, we selected the brightest sources but now without declination limitation, generating samples from 16 up to the complete sample ($N = 1300$). Each additional sample in both sets was simulated for 100 galaxies. We note that in all cases the errors continued to be based on the VLBA observations characteristics.

Figure 3.8 shows how the Galactic parameter values change as more sources are added to the sample selection for sets A and B. The dashed lines represent the initial values adopted in the model, and the error bars represent the standard deviation found for each parameter. The first and current BeSSeL results are also shown as stars and labeled following the same convention used in Reid et al. (2009a) and Reid et al. (2014), i.e., Fit 3 and Model A5 respectively.

Our objective was to investigate the accuracy with which the Galactic parameters can be recovered in the presence of measurement errors. It was therefore important that we verify the robustness of the fitting algorithm and its dependence on the choice of initial parameters. To make sure the fitting procedure recovers the Galactic parameters in an unbiased way over a large range, we ran the algorithm over a number of values in the multi-dimensional parameter space that defines our Galactic models. We varied the most relevant parameters over a broad range ($\pm\Delta$ and $\pm3\Delta$ for the obtained simulated BeSSeL values related in Table 3.4) and cal-

	R_0	Θ_0	$d\Theta/dR$	U_\odot	V_\odot	W_\odot	\bar{U}_s	\bar{V}_s
R_0	1.00 (1.00)							
Θ_0	0.48 (0.47)	1.00 (1.00)						
$d\Theta/dR$	0.27 (0.10)	0.21 (0.14)	1.00 (1.00)					
U_\odot	0.32 (0.45)	0.01 (0.24)	0.08 (-0.12)	1.00 (1.00)				
V_\odot	0.02 (0.02)	-0.73 (-0.80)	0.05 (-0.01)	0.05 (-0.01)	1.00 (1.00)			
W_\odot	-0.01 (0.00)	0.02 (-0.01)	-0.01 (0.03)	-0.06 (-0.02)	0.01 (0.01)	1.00 (1.00)		
\bar{U}_s	0.51 (0.52)	-0.09 (0.17)	0.01 (-0.09)	0.51 (0.84)	0.05 (-0.01)	-0.04 (0.00)	1.00 (1.00)	
\bar{V}_s	0.09 (0.00)	0.62 (0.81)	-0.47 (0.02)	-0.16 (-0.03)	-0.68 (-0.99)	0.01 (-0.01)	0.13 (0.03)	1.00 (1.00)

Table 3.5: Pearson product-moment correlation coefficients calculated for 100 galaxies simulated to mimic the BeSSeL data sample selection. The respective Pearson coefficient reported in Reid et al. (2014) for the observed sample are listed in parentheses.

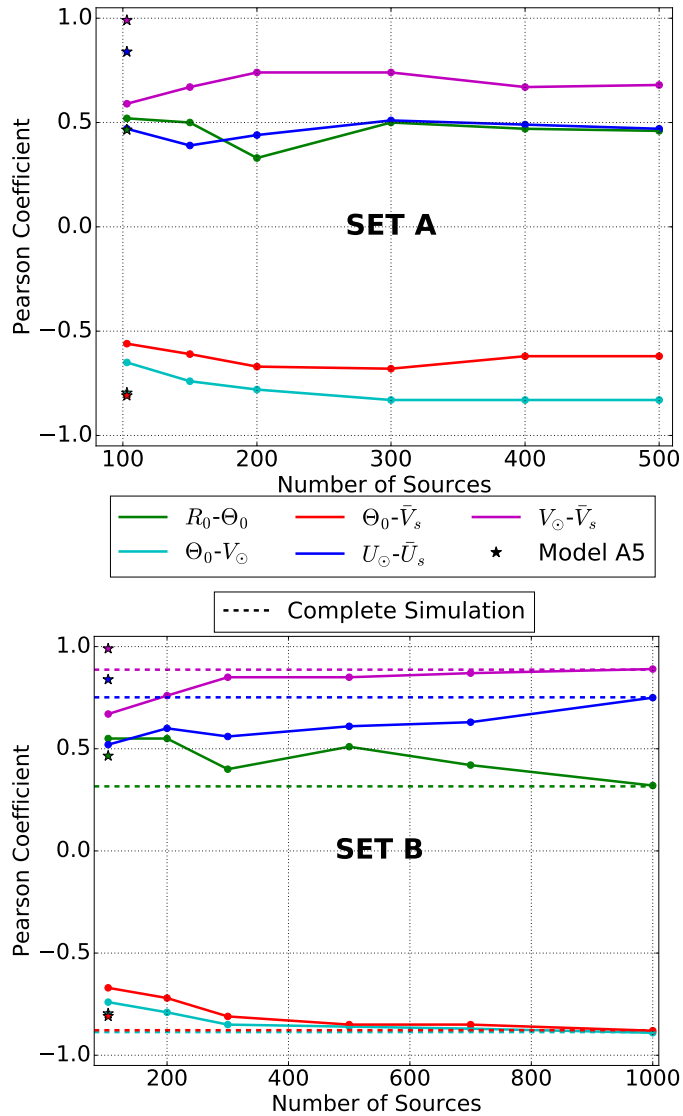


Figure 3.9: Pearson product-moment correlation coefficients calculated for initially highly correlated values (see Table 3.5), when more sources are added in sets A (top panel) and B (bottom panel). Pearson coefficients reported by Reid et al. (2014) are shown as stars and those for the complete sample ($N = 1300$) are represented by dashed lines.

culated a normalized difference between the input parameters and the returned fits. We found that indeed the fitting procedure can properly recover the starting values.

3.3.3 Parameter correlations

Using the Galactic parameter values obtained for 100 simulated galaxies mimicking the BeSSeL data sample selection, we calculated the Pearson product-moment correlation coefficients between all the parameters from the output distributions. The coefficients found are shown in

Table 3.5; for comparison, the Pearson coefficient estimates reported in Reid et al. (2014) from the fitting procedure are also listed. Pearson coefficients in Reid et al. (2014) were calculated by MCMC trials, but in our case we have a large number of samples, which provides an independent way to estimate the correlations. Our findings seems to be consistent with the coefficients published in Reid et al. (2014).

We also estimated the Pearson coefficients variation as more sources are added to the sample selection. In order to see whether the dependence between various parameters can be reduced, we focused on the more correlated parameters reported in Reid et al. (2014), i.e., $r_{(R_0, \Theta_0)}$, $r_{(\Theta_0, V_\odot)}$, $r_{(\Theta_0, \tilde{V}_s)}$, $r_{(U_\odot, \tilde{U}_s)}$ and $r_{(V_\odot, \tilde{V}_s)}$. Figure 3.9 shows the Pearson coefficient evolution among these parameters in sets A and B. Moreover, the Pearson coefficients calculated for the complete sample and those published by Reid et al. (2014) are shown for comparison.

3.4 Discussion

3.4.1 Luminosity function of 6.7 GHz methanol masers

We found that $N = 1300 \pm 60$ and $\alpha = -1.43 \pm 0.18$ are the initial parameters that best match the MMB results. Using these values, the number of sources detected and the slope of the flux density function (β) are slightly underestimated with respect to the observational survey results (see Table 3.3). This difference could be related to the contamination from inner Galaxy sources included in the MMB, which were not included in the simulation. This can account for approximately 100 sources in the N estimate, producing a value of $N = 1300_{-160}^{+60}$. This estimate seems to be consistent with the initial calculation made by Green & McClure-Griffiths (2011) of $N = 1250$ and also with the minimum value settled by Pandian (2007) of $N = 1125$. Moreover, Green & McClure-Griffiths (2011) reported $\alpha = -1.44 \pm 0.4$ using kinematic distance resolution data from the International Galactic Plane Survey, which is very close to our calculation and also gives support to our estimate of N since in our method the two quantities were fitted simultaneously.

There is no physical argument that predicts the luminosity function to be a single power law distribution. However, for the scope of this paper, we are only interested in deriving an empirical relation for the peak luminosity function for a population of 6.7 GHz methanol masers with the proper characteristics. Additionally, a single power law peak luminosity function appears to be consistent with the results obtained for different systematic surveys (including the Arecibo survey, see Figure 3.6) and, for bright sources, it has been previously suggested by several authors (e.g. Pandian et al. 2007; Green & McClure-Griffiths 2011).

3.4.2 Galactic parameters analysis

The different samples described in Sect. 3.3.2 were created to test how accurately the BeSSeL methodology can determine the Galactic parameters. When the sample testing was initially made using the same fitting procedure employed in Reid et al. (2009a, 2014), the resulting parameters start deviating from the initial parameters when more sources were added. When sources with large fractional errors in parallax are numerous, we found that this biases the determination towards larger distances, resulting in parameters that map to a bigger Galaxy. This observational effect (see e.g. Bailer-Jones 2015) was corrected by allowing the fitting procedure to de-bias distance estimations based on measured parallax. We note that the improvements to the fitting code do not alter the results in Reid et al. (2014), which was based

on the brighter sources.

Figures 3.7 and 3.8 summarize the Galactic parameters obtained compared with the initial values adopted (see Table 3.2), using the current and possible future samples. The results in Table 3.4 and Fig. 3.7 obtained for 100 simulated galaxies using the BeSSeL data sample selection show that the Galactic parameter values can be determined very robustly. Figure 3.8 shows that the Galactic parameter results for the simulated samples of 100 sources (current BeSSeL data) in sets A and B are already very close to the initial parameters, and as more sources are added the uncertainties become smaller.

Fundamental Galactic parameters: R_0 , Θ_0 , and $d\Theta/dR$

The differences in R_0 and Θ_0 found when using 100 simulated galaxies mimicking the BeSSeL sample selection (Table 3.4 and Fig. 3.7) are less than 0.2%, demonstrating that indeed we can recover these parameters from the adopted model, even with samples that only contain northern hemisphere sources. Furthermore, the errors reported by Reid et al. (2014) for these parameters (i.e. 0.16 kpc for R_0 and 8 km s^{-1} for Θ_0), which are represented in Fig. 3.7 as gray regions, are double compared to our findings. Consequently, we conclude that the errors assigned by Reid et al. (2014) to R_0 and Θ_0 are conservative, and there do not appear to be any bias, given the available maser samples so far.

For the rotation curve, the situation is somewhat different. Although the values found for $d\Theta/dR$ are very close to the initial values adopted, the statistical spread is larger than expected. Reid et al. (2014) reported an error of $0.4 \text{ km s}^{-1} \text{ kpc}^{-1}$ in the rotation curve which is optimistic compared with our findings. From our simulations, we would constrain the rotation curve value as $-0.3 \pm 0.9 \text{ km s}^{-1} \text{ kpc}^{-1}$ given the BeSSeL data sample selection. The larger error possibly indicates that our assumed velocity distributions are too wide.

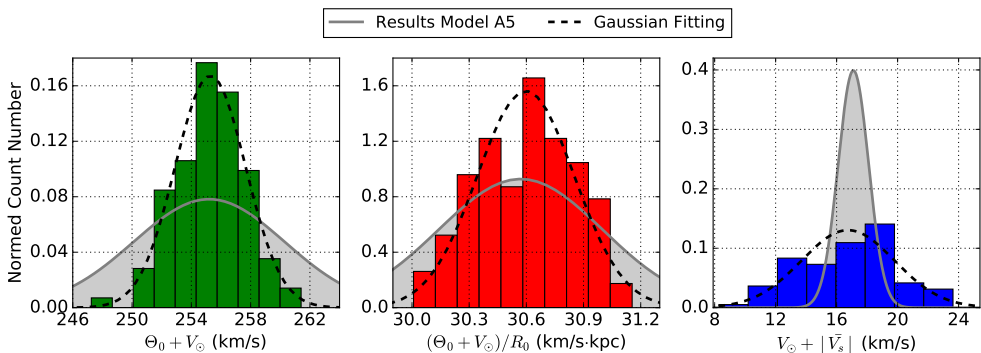


Figure 3.10: Marginalized posterior probability density distributions for correlated circular velocity parameters from 100 simulated galaxies mimicking the BeSSeL sample. Left panel: Circular orbital speed of the Sun. Middle panel: Orbital angular solar speed. Right panel: Difference between the circular solar motion and average source peculiar motions.

When more sources are added to the sample selection (sets A and B), Figure 3.8 shows an initial improvement in the accuracy of the fundamental Galactic parameters. For set A, the errors in R_0 , Θ_0 , and $d\Theta/dR$ can improve up to $\pm 0.04 \text{ kpc}$, $\pm 2.7 \text{ km s}^{-1}$, and $\pm 0.6 \text{ km s}^{-1} \text{ kpc}^{-1}$, respectively, when more northern hemisphere sources are added. In contrast when southern hemisphere sources are also added (set B), the errors can decrease to $\pm 0.03 \text{ kpc}$, $\pm 2.5 \text{ km s}^{-1}$, and $\pm 0.3 \text{ km s}^{-1} \text{ kpc}^{-1}$, respectively. Further improvements would require much better astrometry for weak sources, requiring for example much more sensitive observations.

Solar motion and average source peculiar motions

Figure 3.7 shows the distribution obtained for solar velocity components (U_{\odot} , V_{\odot} , and W_{\odot}). The uncertainties derived were around 2% for all solar velocity components with respect to the initial parameters. For U_{\odot} , the standard deviation found was 1.2 km s^{-1} , which compares well to the results published by Reid et al. (2014) (i.e., $U_{\odot} = \pm 1.8 \text{ km s}^{-1}$). In addition, the spread for V_{\odot} and W_{\odot} are narrower with values of 2.4 km s^{-1} and 0.5 km s^{-1} , respectively. Compared to the BeSSeL results (i.e., $V_{\odot} = \pm 6.8 \text{ km s}^{-1}$ and $W_{\odot} = \pm 2.1 \text{ km s}^{-1}$), we can affirm that the solar motion results published by Reid et al. (2014) have conservative estimates.

For the radial and tangential average peculiar motions (\bar{U}_s and \bar{V}_s), Table 3.4 shows that indeed these peculiar velocities can be fitted with high accuracy using the simulations; however, the relative spreads are high compared with other parameters (see Figure 3.7). Even so, compared to the BeSSeL results (i.e., $\bar{U}_s = \pm 2.1 \text{ km s}^{-1}$ and $\bar{V}_s = \pm 6.8 \text{ km s}^{-1}$), the errors in the simulated sample selection are still lower (i.e., $\bar{U}_s = \pm 1.7 \text{ km s}^{-1}$ and $\bar{V}_s = \pm 3.8 \text{ km s}^{-1}$).

The reason for higher dispersions for \bar{U}_s and \bar{V}_s could be related to the number of parameters that must fit independently. The parameters \bar{U}_s and U_{\odot} have largely the same effect on the observations for nearby sources and therefore are directly correlated (see Table 3.5). For \bar{V}_s , the correlation is high with two components (V_{\odot} , Θ_0), which affects the fitting and hence the estimated accuracy.

Parameter correlations

Pearson product-moment correlation coefficients are shown in Table 3.5. All the parameters are in agreement with those found by Reid et al. (2014), except for the Pearson coefficient between $d\Theta/dR$ and \bar{V}_s (labeled " $r_{d\Theta/dR, \bar{V}_s}$ ") where a low correlation was found in the observed sample instead of the moderate correlation found in the simulated sample. However, we focus the discussion on the parameters that were reported to have considerable correlation in Reid et al. (2014), as it is interesting to see how it is possible to disentangle these fundamental parameters.

For the first BeSSeL summary paper (Reid et al. 2009a), where only 16 HMSFRs were used, the estimated R_0 and Θ_0 were strongly correlated ($r_{R_0, \Theta_0} = 0.87$). Later on, in Reid et al. (2014), using a larger sample of 103 HMSFRs spanning a greater Galactic distribution, the correlation was significantly lower ($r_{R_0, \Theta_0} = 0.47$). We calculated the same coefficient by mimicking both samples using 100 simulated galaxies, finding similar results for each sample, i.e. $r_{R_0, \Theta_0} = 0.77$ and $r_{R_0, \Theta_0} = 0.48$. These results show that, indeed, our simulation produces similar correlation coefficients to those found in the observations, even when the method used to calculate the Pearson coefficients are completely different (see Sect. 3.3.3). When more sources are added to the sample selection, Figure 3.9 shows that the correlation between R_0 and Θ_0 is reduced. Furthermore, the Pearson coefficient will have a moderate value (0.3) when using the complete data sample, which demonstrates that the correlation between these parameters can be unraveled smoothly as more sources are added.

For the tangential velocity component, we have three different Galactic parameters giving similar effects: Θ_0 , V_{\odot} and \bar{V}_s . Figure 3.9 and Table 3.5 show that the Pearson coefficients among these parameters are always high, even when more sources are added. This implies that different types of data are needed in order to better disentangle these Galactic parameters. Finally, in the radial direction we have two Galactic parameters: U_{\odot} and \bar{U}_s . The correlation between these parameters is around 0.5 for a low number of sources, as it shown in Figure 3.9 and listed in Table 3.5. When more sources are added, the correlation parameter seems to maintain the same value or slightly increase in both sets of samples (see Figure 3.9). One could expect that the inclusion of southern hemisphere sources would help to disentangle

some of the dependences; however, comparing the top and bottom plots in Figure 3.9 we can see that using samples with a larger coverage of the Galaxy does not alter significantly the correlation values found for any of the Pearson coefficients discussed here.

As some of the parameter correlations persist, even when more sources are added to the sample selection, we estimated the marginalized PDFs for different combined parameters that were also reported in the latest BeSSeL survey paper. Figure 3.10 shows the PDFs for the circular orbital speed of the Sun, the orbital angular solar speed, and the difference between the circular solar and average source peculiar motions. Additionally, those PDFs reported by Reid et al. (2014) are shown as gray regions.

We found $255.3 \pm 2.4 \text{ km s}^{-1}$, $30.60 \pm 0.26 \text{ km s}^{-1} \text{ kpc}^{-1}$, and $16.7 \pm 3.1 \text{ km s}^{-1}$, respectively, for the correlated values of the parameters $\Theta_0 + V_\odot$, $(\Theta_0 + V_\odot)/R_0$ and $V_\odot + |\bar{V}_s|$. Reid et al. (2014) found more conservative values for $\Theta_0 + V_\odot = 255.2 \pm 5.1 \text{ km s}^{-1}$ and $(\Theta_0 + V_\odot)/R_0 = 30.57 \pm 0.43 \text{ km s}^{-1} \text{ kpc}^{-1}$ than we did. Although the mean value found for $V_\odot + |\bar{V}_s|$ is in agreement with the BeSSeL results (i.e., $17.1 \pm 1.0 \text{ km s}^{-1}$), we estimate a wider error of $\pm 3.1 \text{ km s}^{-1}$ based on our simulations.

3.5 Conclusions

We constructed simulations of 6.7 GHz methanol maser distributions to test whether the Galactic parameter results obtained by the BeSSeL survey (Reid et al. 2014) are biased in any way and investigated the interdependencies between some parameter estimates. We used our model to constrain the peak flux density function for the masers and obtained similar results to those of systematic unbiased surveys (MMB and Arecibo). This comparison allowed us to estimate the integral number of sources ($N = 1300_{-160}^{+60}$) and the slope of the luminosity function ($\alpha = -1.43 \pm 0.18$), which showed good agreement with Pandian (2007); Green & McClure-Griffiths (2011); Urquhart et al. (2013).

Assuming that the observations are predominantly of 12 GHz methanol masers found through 6.7 GHz surveys, we simulated the current database of the BeSSeL survey hundreds of times. We found that the fundamental Galactic parameters (R_0 , Θ_0 , $d\Theta/dR$), the solar velocity components ($U_\odot, V_\odot, W_\odot$) and the average peculiar motion (\bar{U}_s, \bar{V}_s) can be determined robustly. Furthermore, the results published by Reid et al. (2014) have a conservative error calculation given the current sample, except possibly for the rotation curve error estimate. Also, correlation coefficients for the various Galactic parameters in our simulations and those reported by Reid et al. (2014) are similar.

Additionally, the fitting procedures developed by Reid et al. (2009a, 2014) for use with the BeSSeL data and improved in this study estimate Galactic parameters correctly even when weak and/or distant sources with large fractional parallax uncertainties are included in the samples.

For future BeSSeL observations, the simulations demonstrate that the Galactic parameter estimates can be improved and the error bars reduced significantly. Moreover, using southern hemisphere data, the Galactic parameter estimates improve notably compared with samples limited to the northern sky.

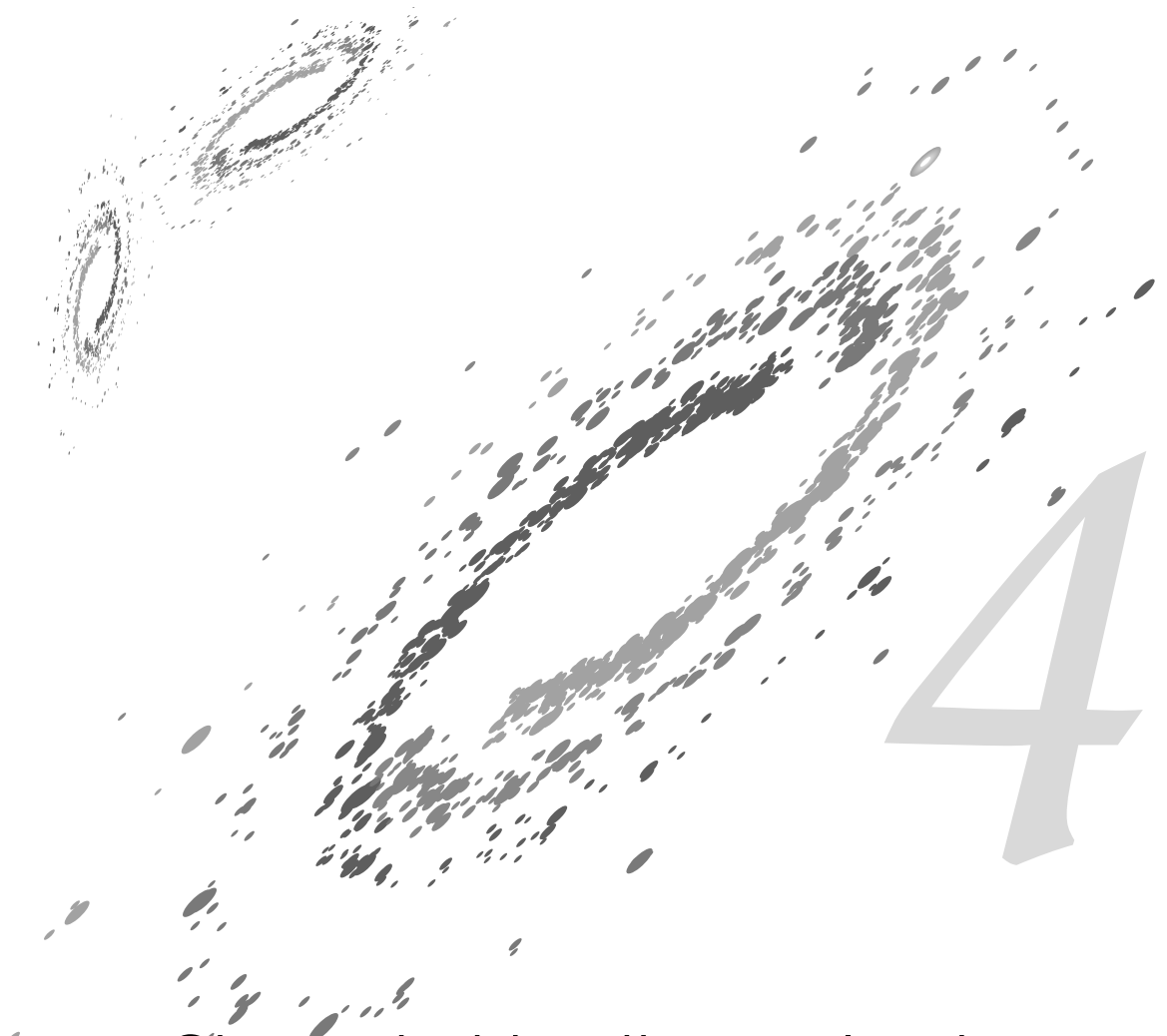
We find that the uncertainties in the values of certain combined velocity parameters that are highly correlated are similar to those published in Reid et al. (2014), except for the dispersion in $V_\odot + |\bar{V}_s|$. However, when more sources are added to the sample, the correlations among most Galactic parameters are smoothly reduced; for the highly velocity parameters the correlation coefficients do not decrease significantly.

The framework proposed to test the results of the BeSSeL survey is useful for defining re-

quirements for future astrometric campaigns that are similar or complementary to the BeSSeL data. Southern arrays – like the Australian Long Baseline Array (see e.g. Krishnan et al. 2015, 2017) and, in the future, the African VLBI Network and the Square Kilometre Array in Australia and South Africa – will supplement the lack of precise astrometric data in quadrants III and IV of the Milky Way plane, where only a few sources have been measured. Moreover, astrometric studies that include the inner Galactic region, such as the Bulge Asymmetries and Dynamic Evolution (BAaDE²) project, aim to resolve the dynamics of the bar by measuring proper motions and distances of SiO masers present in AGB stars (Sjouwerman et al. 2017). Out of the Galactic plane, Gaia will soon provide astrometric results for a large number of sources. All of these investigations will contribute to the determination of Galactic parameters with even better accuracy with new and improved astrometric data. Until then, Galactic simulations complement the current observations by demonstrating their robustness and potential.

Acknowledgements. We sincerely thank the anonymous referee for making valuable suggestions that have improved the paper. L.H.Q.-N. acknowledges the comments and suggestions regarding the model implementation made by S. Solorzano-Rocha at ETH Zürich.

²<http://www.phys.unm.edu/~baade/index.html>



Characterizing the evolved stellar population in the Galactic foreground

Quiroga-Núñez, L. H.; van Langevelde; Sjouwerman, L. O.; Pihlström, Y. M.; Brown, A. G. A.; Stroh, M.C.; H. J.; Rich, M. R. & Habing, H. J. *Characterizing the BAADE evolved stars in the Galactic foreground with Gaia* 2020, in preparation.

Abstract

Radio campaigns using maser stellar beacons have provided crucial information to characterize Galactic stellar populations. Currently, the Bulge Asymmetries and Dynamical Evolution (BAaDE) project is surveying infrared color-selected targets for SiO masers. This provides a sample of evolved stars that can be used to study the inner, optically obscured, Galaxy using line of sight velocities and possibly VLBI proper motions. In order to use the BAaDE sample for kinematic studies in the inner Galactic region, the stellar population should be characterized in terms of stellar evolutionary stage. In particular, it has been found before that BAaDE targets in the local disk and inner Galaxy originate from different stellar populations. The BAaDE targets, based on *MSX* colors, have been cross-matched with optical *Gaia*, infrared 2MASS, and preliminary radio (BAaDE, SiO maser) samples. By exploring the synergies of this cross-match together with *Gaia* parallaxes and extinction maps, the local ($d < 2$ kpc) BAaDE targets can be characterized. Additionally, the *Gaia* DR2 tables provide additional data on stellar classification and variability. We have defined a *BAaDe-Gaia* sample of 20,111 sources resulting from cross-matching BAaDE targets with IR and optical surveys. From this sample, a *local* sample of 2,060 stars with precise parallax measurements and within 2 kpc distance around the Sun was selected, for which absolute (bolometric) magnitudes are estimated. For 653 stars, *Gaia* also provides periods. These intrinsic properties are compared with samples of AGB stars from the literature finding that the original BAaDE color selection contains a contamination of low luminosity foreground objects. Objects with *Gaia* counterparts that are variable seem to be predominantly associated with AGB stars with moderate luminosity ($1,250 L_{\odot}$). The stars in the *local* sample for which there are SiO masers detected, are consistent with oxygen rich Mira stars with periods between 250 and 750 days.

4.1 Introduction

The characterization of Galactic stellar populations is a key ingredient to understand the structural (see e.g., Reid et al. 2019), chemical (see e.g., Ibata et al. 2017) and dynamical (see e.g., Martinez-Medina et al. 2017) evolution of the Milky Way, and indeed, its assembly through past merger events (e.g., Gómez et al. 2012). Typically, this is done by combining information on the spatial and kinematic distribution of a stellar population with an assessment of its age and origin (e.g., Mackereth et al. 2017). As the *Gaia* mission (Gaia-Collaboration et al. 2018; Lindegren et al. 2018) delivers more accurate, reliable data, it is revolutionizing our understanding of the assembly of the Galaxy. Many recent results demonstrate that mergers have been frequent over the history of the Milky Way and seem to occur also in the present era (Antoja et al. 2018; Helmi et al. 2018; Belokurov et al. 2019; Bland-Hawthorn et al. 2019).

Starting with the discovery of its HI spiral arms (Oort et al. 1958, and references therein), it has been clear that the Sun is a star in a spiral galaxy. In the inner region, the Milky Way seems to be dominated by a massive bar (e.g., Dwek et al. 1995) and an X-shaped structure (e.g., Wegg & Gerhard 2013), similar to what it is seen in extragalactic edge-on boxy bulges. As these are the most prominent dynamic features in the inner Galaxy, research of the kinematics and stellar populations that compromise the bar and the bulge is necessary to understand the morphology, structure and evolution of the Milky Way (Bland-Hawthorn & Gerhard 2016). Evolved stars, that are prominent in the mid-Infrared (IR), are possibly the best targets for such studies (Kunder et al. 2012). Indeed, the bar and bulge have been probed by counting IR stellar densities (Blitz & Spergel 1991; Babusiaux & Gilmore 2005), studying their metallicities and sometimes their variability, which for some stars can be used to obtain distance estimates.

Typically, these stars are too distant to measure proper motions or direct parallax distances from their stellar photosphere, as their Spectral Energy Distributions (SED) peak in IR, while their optical images are hidden behind circumstellar and interstellar dust. However, the most extreme of these evolved stars harbor circumstellar masers (Höfner & Olofsson 2018). Circumstellar masers are useful as they are bright beacons of a specific evolutionary stage in which evolved stars develop a thick circumstellar shell with specific molecular content and exceptional physical conditions. Moreover, the masers deliver accurate line of sight velocities through the Doppler effect. Finally, stellar maser emission reaches high brightness temperatures, allowing in principle Very Long Baseline Interferometry (VLBI) astrometry with micro-arcsecond accuracy (Reid & Honma 2014).

Previous surveys first focused on OH masers (Sevenster et al. 2001; Fish et al. 2006) and later targeted SiO masers with single dish telescopes (Messineo et al. 2018). When it was realized that the new capabilities at 7mm of the VLA and 3mm of ALMA offer efficient ways to study SiO masers, the Bulge Asymmetries and Dynamical Evolution project (BAaDE¹) was proposed. Using *MSX* infrared color selections, many thousands of SiO masers are found (Sjouwerman et al. 2017; Stroh et al. 2019). This sample may thus facilitate a detailed study the kinematics of the bulge, bar and inner Galaxy.

Since only very few SiO masers are known from young stars (Colom et al. 2015), those stars that show emission at 43 and/or 86 GHz are almost exclusively Asymptotic Giant Branch (AGB) stars. But stars of a very wide mass range are expected to spend time in this phase, as they become unstable towards the end of their lives. As a consequence, the ages of these star can vary considerably, ranging from 100 Myr to a fraction of the age of the universe (e.g. Salaris et al. 2014, and the references therein). Metallicity effects also affect the observables of the AGB population, as stars for which the envelope becomes low in oxygen may not easily produce sufficient SiO (e.g., Sande et al. 2018). Although the *Gaia* mission cannot

¹<http://www.phys.unm.edu/~baade/>

provide information on all of the BAaDE targets — and certainly not the majority of targets that sample the inner Galaxy — it can be used to characterize the stars in the BAaDE sample, particularly those in the local region ($d < 2$ kpc).

In this paper we cross-match the BAaDE sample with 2MASS and *Gaia* DR2. Because the BAaDE sample is based on *MSX*, it contains predominantly stars at low Galactic latitude. The cross section of the various surveys has infrared photometric information, as well as optical. Through the *Gaia* DR2, we can also evaluate other parameters as the parallax and proper motion, but also information derived from the survey such as variability and stellar classification. Finally, for a subsample there are already SiO detections. The objective of this work is to understand the nature of stars that enter the BAaDE survey. As we selected objects from their *IR* colors in *MSX* (with SiO maser emission detected for $\sim 70\%$, Trapp et al. 2018, Stroh et al. 2019 subm.), one can expect it to contain predominantly Long Period Variable (LPV) stars, likely Miras, with a modest circumstellar shell. But this sample can contain young stars, that are very luminous, or older, less massive stars that progress on the AGB track with lower luminosity. In order to address these issues, we present the cross-matches in Sect. 4.2, results for the various sub-samples are presented in Sect. 4.3. We discuss the characterization and distribution of the samples in Sect. 4.4, where we are in particular well positioned to comment on the nature of evolved stars in the foreground Galactic plane, for which we have *Gaia* counterparts with accurate distances.

Table 4.1: Number of sources obtained for different samples and cross-matches used in this research. See Sect. 4.2.1 and 4.2.2 for a detailed description of how the cross-matches were done and the filtering criteria.

			Sources / Cross-matches
BAaDE (MSX)			28,062
\cap	2MASS		25,809
	\cap	Gaia DR2	20,111
			SiO Observed
			4,154

Notes. The intersection symbol (\cap) indicates cross-match where the arrow indicates subsample. The “SiO Observed” refers to the subsample for which SiO maser flux densities and radial velocities from spectral lines are already available. Note that this observed SiO maser sample is still in preliminary stage.

4.2 Cross-match between radio, IR and optical observations

We have cross-matched the *MSX*-based BAaDE target sample with 2MASS and *Gaia* DR2 (see Table 4.1), using the *Gaia* data archive interface². This sample was defined as the *BAaDE-Gaia* sample (see Sect. 4.2.2) In the following subsections, we describe how this process was implemented, starting from the BAaDE target selection, followed by the cross-match criteria, the filters we applied to reduce false positives (including the extinction maps used), and finally arriving at the resulting sample of evolved stars in the foreground Galactic plane, which we define as the *local* sample (see Sect. 4.2.4 and Table 4.2).

²<http://gea.esac.esa.int/archive/>

Sample name	Description / Filters used	Sources/Cross-matches
<i>BAaDe-Gaia</i>	BAaDE (MSX) \cap 2MASS \cap Gaia DR2	20,111
	Variable \hookrightarrow	3,017
	SiO Observed \hookrightarrow	395
	$\sigma_\pi / \pi < 0.2$ \hookrightarrow	2,277
<i>Local</i>	< 2 kpc \hookrightarrow	2,061
	SiO Observed \hookrightarrow	147
<i>Variable</i>	Variable \hookrightarrow	908
<i>Periods</i>	Periods \hookrightarrow	653
<i>SiO maser</i>	SiO Observed \hookrightarrow	42

Table 4.2: Number of sources obtained for each subsample of the BAaDE-Gaia sample. Each row represents a filter used. See Sect. 4.2.3 and 4.2.4 for a detailed description of each filter. The definition of the BAaDE-Gaia and local samples is given in Sects. 4.2.2 and 4.2.4, respectively.

Notes. The arrow symbols indicate subsample. When two arrows are aligned in the same column, it means that the corresponding sample was split by two different criteria.

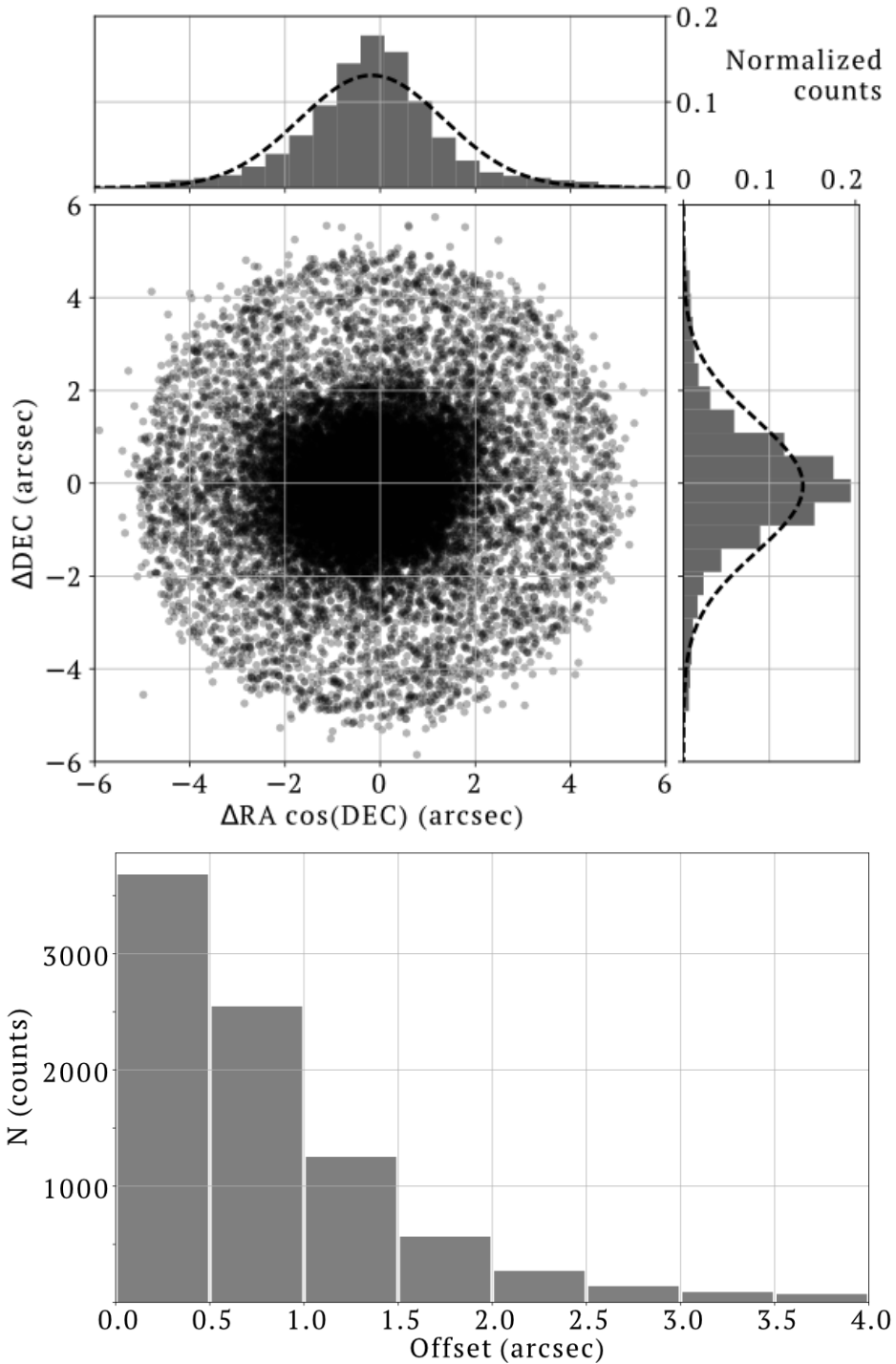


Figure 4.1: Upper panel: Distribution of the equatorial coordinate offsets between BAaDE targets and Gaia DR2 counterparts. Each offset component can be well-represented by a 1D Gaussian distribution. **Lower panel:** Histogram distribution of the total offset between BAaDE targets and Gaia DR2 counterparts. The histogram follows a Rayleigh distribution were sources with offsets of $>3''$ are likely false positives (see Sect. 4.2.2).

4.2.1 BAaDE target sample selection

The BAaDE target selection was based on IR photometry and designed to identify red giant stars with envelopes likely to harbor SiO maser emission. Starting from the IRAS color-color diagram (CCD), van der Veen & Habing (1998) studied dust and gas envelopes of AGB stars. They pointed out that circumstellar shell properties of AGB stars appear in a sequence in the IRAS CCD, suggesting an evolutionary track with increasing mass-loss rate. In the IRAS CCD, SiO maser stars are expected to be found in a specific color region, facilitating a selection based on the IRAS colors. However, the astrometric accuracy of IRAS is limited to one arc-minute for sources in the Galactic plane, prohibiting a large-scale survey. Later, Sjouwerman et al. (2009) were able to transform the IRAS CCD sequence to colors in the mid-IR, using *MSX* data. By doing this, the angular resolution was improved to $2''$ (Price 1995), and a new sample of AGB star candidates with mid-IR information was obtained. This way, 28,062 stellar targets were selected with the objective to sample the evolved stellar population in the Galactic plane, bar and bulge, mostly limited to $|b| < 5^\circ$. It is expected that one third of the BAaDE target sample lies in the Galactic bulge (Sjouwerman et al. 2017). These 28,062 targets are being followed up in order to detect SiO maser emission at 43.1 GHz ($J = 1 \rightarrow 0$ [$\nu = 1$]), 42.8 GHz ($J = 1 \rightarrow 0$ [$\nu = 2$]) with the VLA or 86 GHz ($J = 2 \rightarrow 1$ [$\nu = 1$]) with ALMA. So far, 20,600 candidates have been observed, of which 4,996 have already been analyzed (3,209 with the VLA and 1,787 with ALMA) and the scientific products are planned to be released publicly soon. The remaining sources are expected to be observed with ALMA in future cycles. Preliminary BAaDE results for 80 targets, comparing quasi-simultaneous observations at 43 and 86 GHz SiO maser lines have been already published by Stroh et al. (2018).

4.2.2 Cross-match description

In order to match the BAaDE targets with other surveys in position, we considered a conservative sky-projected circular area with $3''$ radius around the BAaDE targets. The motivation for a $3''$ maximum separation was based on the assumption that the distribution of deviations from the actual positions is dominated by the *MSX* data (as confirmed by Pihlström et al. 2018b) and has Gaussian distributions in both components ($\Delta\text{ff} \cos(\text{ffi})$, Δffi) with absolute mean values $< 0.2''$ and positional accuracy of $2''$ (see upper panel of Fig. 4.1). This 2D Gaussian distribution is represented as a the Rayleigh distribution. The lower panel of Fig. 4.1 shows the offset distribution, where sources at offsets above $\sim 3''$ are likely false positives. Note that the criterion we use here is more restrictive than the first cross-match done for a pilot of BAaDE sources and 2MASS (i.e., $5''$ in Trapp et al. 2018).

After defining a sky-projected circular area, we proceed with cross-matching the BAaDE target sample with 2MASS and *Gaia* DR2. Although the cross-match in principle can be done directly with *Gaia*, as it has typically lower positional offsets with respect to SiO masers positions (Pihlström et al. 2018b), we started instead by cross-matching BAaDE and 2MASS, motivated by two different arguments. First, BAaDE targets that display both mid-IR emission (*MSX*) and optical emission (*Gaia*) are not expected to be extinct at NIR (2MASS). Hence, by initially cross-matching with 2MASS, we are already avoiding some false positives (see Sect. 4.2.3). Second, the cross-match between 2MASS and *Gaia* was already established by Marrese et al. (2019), using a robust best neighbor algorithm, which found more than 90% overlap between both surveys.

By using the 2MASS survey, we have found 25,809 counterparts for the BAaDE target list. Next, after cross-matching with *Gaia* DR2, the sample was reduced to 20,111 cross-matches

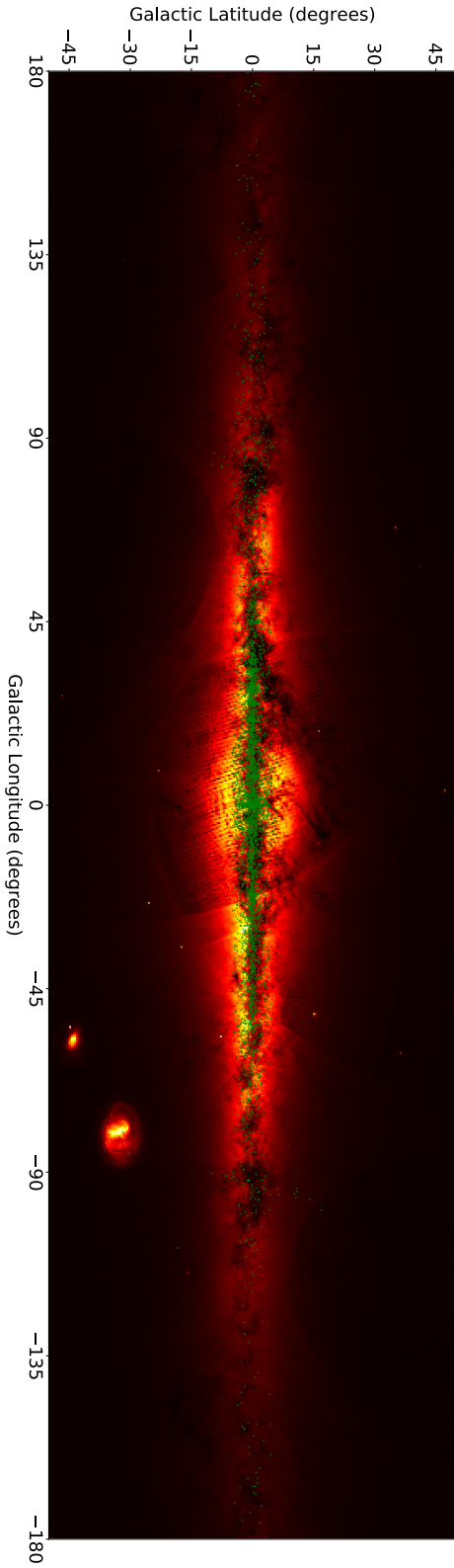


Figure 4.2: Galactic distribution of the BADE stellar targets without a Gaia counterpart (green points) overlaid on the first Gaia sky map. This sample accurately correlates with highly obscured regions in the optical regime. Credit: ESA/Gaia/DPAC.

(see Table 4.1), where all of them were found to be one-one correspondences. This last sample of 20,111 is called *BAaDE-Gaia* sample throughout the paper and thus includes 2MASS information. Notably, for 8,491 BAaDE targets, there were no *Gaia* counterparts, probably due to the fact that these targets lie behind considerable dust extinction at optical wavelengths. Figure 4.2 shows how the distribution of these “missing” sources indeed correlates with the dust obscured regions that *Gaia* could not penetrate.

Statistics of the cross-matches

Assuming a uniform distribution of sources in the bulge for the *Gaia* detections, as well as for BAaDE targets, one can calculate the number of sources that will give random matches at the given resolution of each survey. We estimated that the number of random matches should be less than 1,200; this is a small fraction of the 20,111 cross-matches that we have. Moreover, in this statistical estimate we have assumed that there is no optical extinction limiting the number of *Gaia* sources. Therefore, the actual number of chance matches will be much lower than 1,200 indicating that our sample has a modest contamination of sources with unrelated counterparts.

4.2.3 Refining the *BAaDE-Gaia* sample

As the objective is to characterize the BAaDE targets, we consider additional refinements of the cross-matches in order to identify contaminating sources. Several filters have been considered, which in turn have generated several subsamples from the *BAaDE-Gaia* sample of 20,111 sources. Below, we outline the criteria that have been applied. Table 4.2 summarizes the resulting subsamples, also indicating the number of sources that have already been observed by the BAaDE project with the *VLA* or *ALMA* and subsequently analyzed for SiO maser emission.

Parallax measurements

Obtaining distance estimates from noisy parallax measurements can be a complex issue (see e.g., Bailer-Jones 2015). Several tools are available to extract statistically robust distances from parallax measurements with limited accuracy — even from negative parallaxes — (see e.g. Bailer-Jones et al. 2018; Luri et al. 2018). However, such distance estimates strongly rely on robust expectations on the stellar properties for a target sample. In our case, the best approach would be to compute the parameters of a probability distribution specifically for AGB stars by maximizing a likelihood function, so that under an assumed statistical model the distance distribution for the observed evolved stellar data is the most probable. However, since (1) the aim of this research is to study foreground population of evolved stars and (2) precise extinction maps are limited to 2 kpc (see following subsection), we have found that 91% of the stars in the relevant sample have a $\sigma_\pi/\pi < 0.2$, which allows a direct and precise estimate of the distance without further considerations (Bailer-Jones 2015). Moreover, an analysis of the foreground sample can be considered an initial step for doing a full statistical analysis.

Extinction maps up to 2 kpc

Capitani et al. (2017) and Lallement et al. (2019) have produced local dust maps, based mainly on a regularized Bayesian inversion of individual color excess measurements using *Gaia* data. Additionally, the authors combined several tracers to confirm accurate extinction

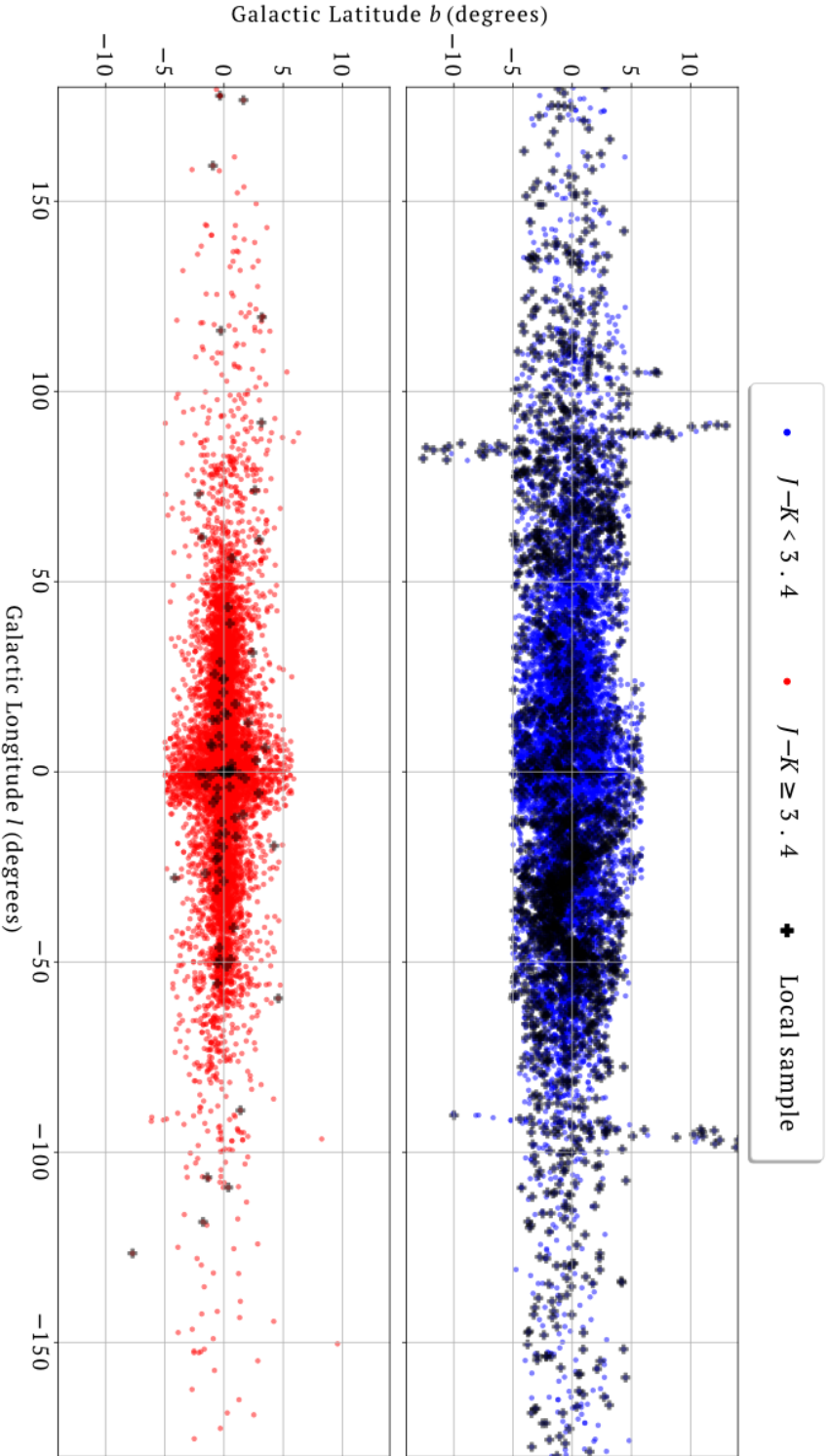


Figure 4.3: Galactic longitude-latitude diagram for the cross-matches obtained between BADE, 2MASS and Gaia defined as the BADE-Gaia sample. This sample was split in two populations (upper and lower panel) based on the mean 2MASS color ($J - K$) obtained, similar to what Trapp et al. (2018) have done to identify “cold” and “hot” kinematic populations within the BADE database. Black crosses represent the defined local sample, a subsample of the BADE-Gaia sample with precise parallax measurements at < 2 kpc distance (see Sect 4.2.4 for further details). The local sample is mainly made of foreground Galactic stars. The linear features observed at $l \sim 85^\circ$ and $l \sim -85^\circ$ for sources with $|b| > 8^\circ$ are part of MSX target list (and are also BADE targets) caused by the rotation of the spacecraft to map the entire Galactic plane (Price 1995).

maps and reddening estimates up to 2 kpc. This tool is extremely useful to estimate intrinsic luminosities for the stars in our sample, which is an important physical property that can be used to characterize the stellar population. Although for local AGB stars, which emit mostly in the (mid-) IR, the effects will be small, we do adopt these maps, and thus a distance limit of 2.0 kpc.

4.2.4 Resulting cross-match: *local* sample

Using the 20,111 cross-matched sources that we have found between BAaDE, 2MASS and Gaia DR2 (*BAaDE-Gaia* sample), we have applied the additional filters (previously described), leaving a sample of 2,061 stellar sources that we have defined as *local* sample. This sample contains BAaDE targets within 2 kpc distance around the Sun with precise distance estimates, IR and optical photometry and proper motions. From those, for 147 sources we have already obtained radio data, i.e., flux densities and radial velocities from SiO maser spectral lines at 43.1, 42.8, and/or 86 GHz. These samples uniquely enable us to study the late-type stars in the Galactic plane.

In addition, the *local* sample can be filtered by variability. For this, we have used the *Gaia* DR2 variability information contained in the *Gaia* table `vari_classifier_result`, and extract those objects that were flagged as variables of any kind, and named it as *variable* sample (908 sources). Next, we have refined the sample by extracting the sources with period estimates from the *Gaia* table `vari_long_period_variable`, and named it as *periods* sample (653 sources). Note that all the sources within the *local* sample contained in the table `vari_classifier_result` were classified by *Gaia* as Mira or semi-regular stars (`MIRA_SR`). Then, from the sources in the *periods* sample where we already have SiO maser emission confirmed, we defined the *SiO maser* sample (42 sources). All of the characteristics previously described helped us to generate subsamples of the *local* sample, as shown in Table 4.2. Finally, it should be noted that there are two effects that play a role when distances to individual AGB stars are estimated. First, the strong colour variations on the stellar photosphere (see e.g., Lindegren et al. 2018; van Langevelde et al. 2019), and second, the photocenter movements caused by large atmospheres with convective motions (Chiavassa et al. 2018). We have checked and added the *Gaia* `astrometric_excess_noise` uncertainty when discussing individual objects.

4.3 Results

In this section we present the main features of the different samples that resulted from the cross-matching. We start with the *BAaDE-Gaia* sample of 20,111 targets described in Sect. 4.3.1. Next, in Sect. 4.3.2, we characterise the *local* sample in terms of IR photometry, variability and Galactic distribution.

4.3.1 Features of the *BAaDE-Gaia* sample

Since the *BAaDE-Gaia* sample was obtained through 2MASS, the mean value of near-IR color ($J - K$) can be used to split the sample in two equal sized subsamples: i.e., $(J - K) < 3.4$ for the bluer stars and $(J - K) \geq 3.4$ for the redder stars. More extreme AGB stars (more luminous and with thicker shells) are to expected to have steeper slope in their SEDs at IR wavelengths, resulting in increasingly redder IR colors. Figure 4.3 shows the subsamples of red and blue stars in a Galactic latitude-longitude diagram. Red stars seem to better trace

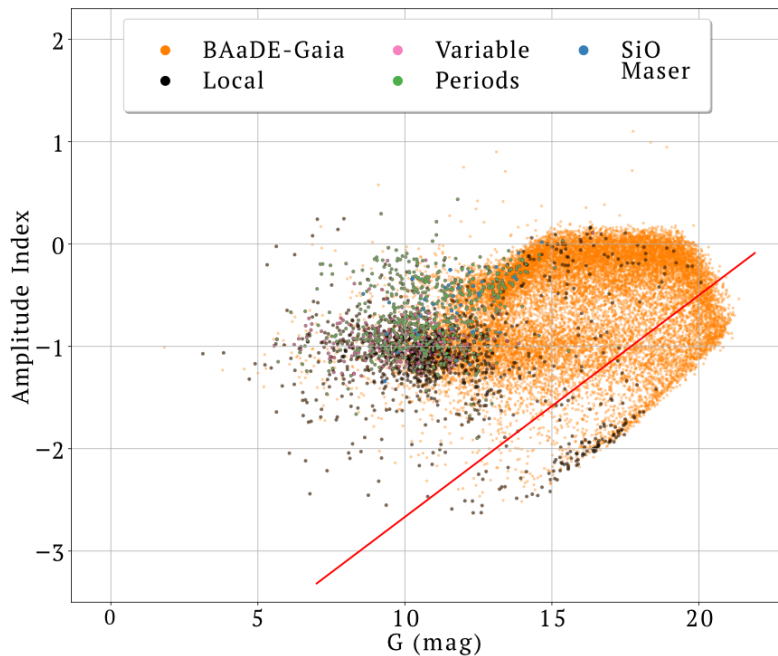


Figure 4.4: Amplitude-magnitude diagram suggested by Belokurov et al. (2017) to distinguish variable stars where larger amplitudes are likely associated with pulsating AGB stars. The green points represent the BAaDE-Gaia sample ($BAaDE \cap 2MASS \cap Gaia\ DR2$), whereas black sources represent the variable stars within the local sample (i.e., precise distance estimates at <2 kpc). The various subsamples were derived from the local sample following Table 4.2. The solid red line represents a threshold above which stars are considered variable Belokurov et al. (2017).

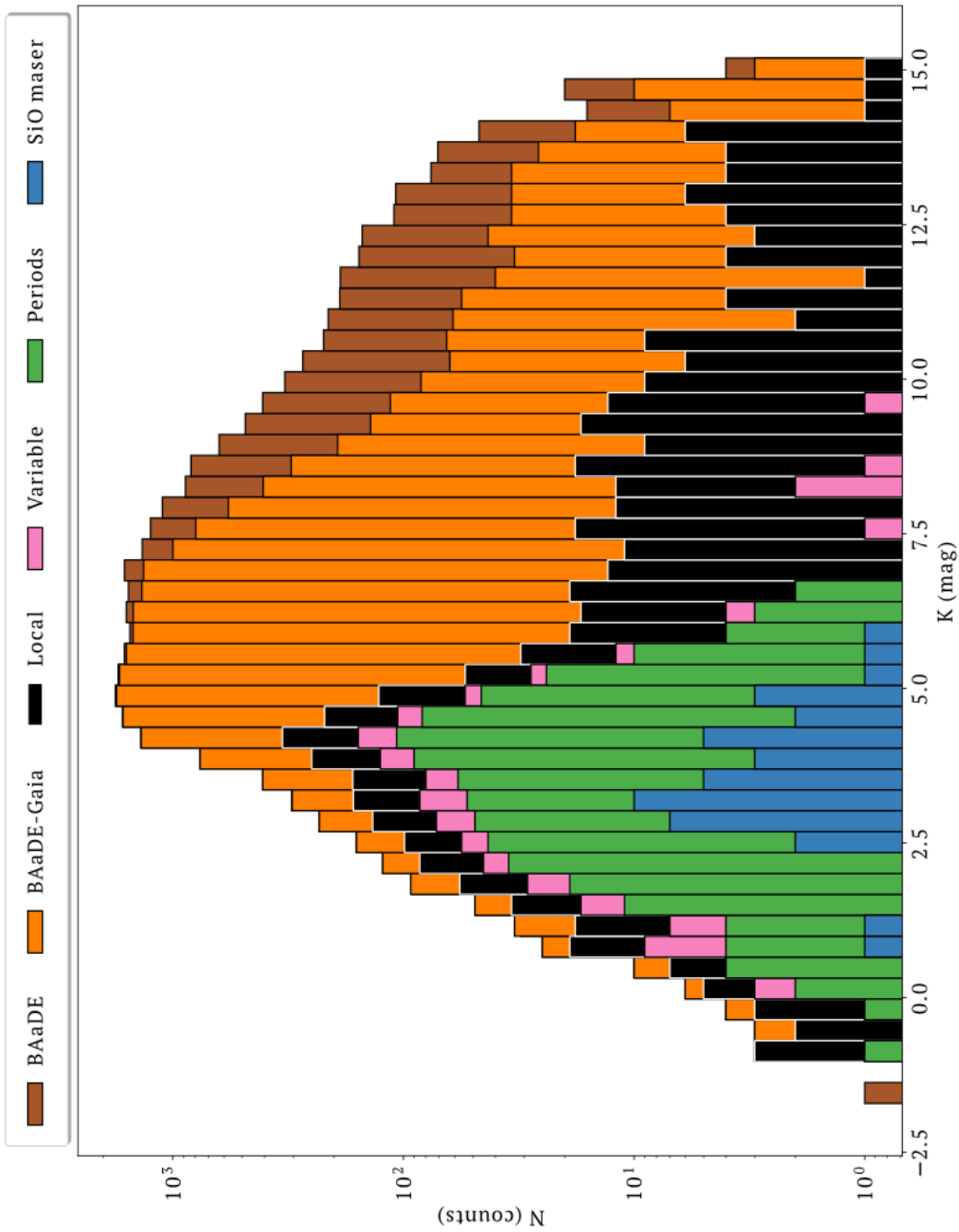


Figure 4.5: Cumulative histogram comparison for the distribution of K-magnitude observed by 2MASS for different samples. Each distribution results from a drawn bigger sample as shown in Tables 4.1 and 4.2. The figure shows that as more filters are applied, the apparent K-magnitude range is narrower.

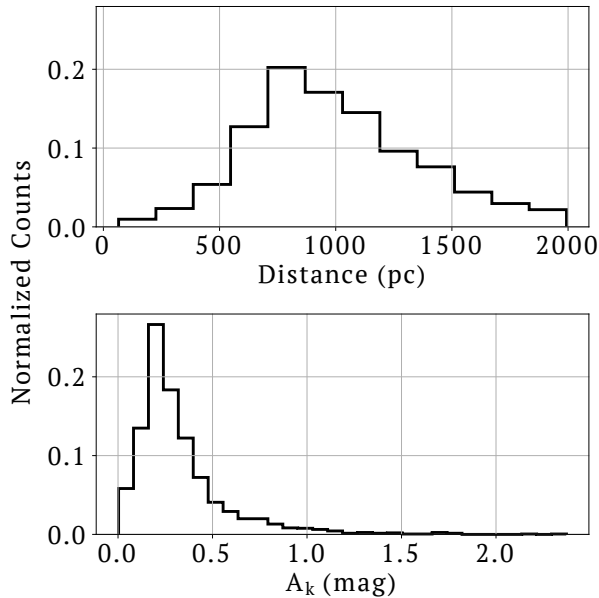


Figure 4.6: *Upper panel:* Distribution of distance to the Sun for the *local* sample. *Lower panel:* Extinction in the *K*-band obtained from the optical extinction maps developed by Capitanio et al. (2017) and Lallement et al. (2019), and converted to IR *K*-band following Messineo (2004).

the inner part of the Galaxy (Galactic bulge and plane) while bluer stars seem to dominate the foreground population. Indeed, the figure also shows that the sources of the *local* sample are mainly stars that are bluer (in the context of the BAaDE selection). We confirm that by splitting sample using IR photometry, two populations can be traced. This was also observed by Trapp et al. (2018), who made the split using *K* magnitudes, and labeled the two a kinematic populations “cold” (the bluer, less red, stars in the Galactic disk) and “hot” (the redder stars in the bulge/bar).

Another property that can be investigated for the *Gaia*-BAaDE sample is variability. Although the *Gaia* DR2 has variability information for a considerable number of stars (Mowlavi et al. 2018), Belokurov et al. (2017) has shown that —already in *Gaia* DR1— flux uncertainties quoted in the *Gaia* catalogue reflect the dispersion of the *G*-band flux measurements, which will thus lead to apparently larger uncertainties for variable stars. They have defined an amplitude variation over error, which we refer as amplitude index, using the flux in the optical *G*-band as $\log_{10}(\sqrt{N_{obs}} \frac{\alpha_g}{g})$, where N_{obs} is the number of observations. Using this quantity, Belokurov et al. (2017) calculated the amplitude for different stellar populations in the Large Magellanic Cloud (LMC) and Small Magellanic Cloud (SMC), finding that Mira variables are located in the upper region of Fig. 4.4, where the amplitude index is > -1.0 . Figure 4.4 shows an amplitude-magnitude plot for the *Gaia*-BAaDE sample, where stars with amplitudes larger than -1 in this diagram are likely pulsating stars. At the same time, we also have described in Sect. 4.2.4 that in *Gaia* DR2, sources were classified as “Variable”, following the criteria described in Mowlavi et al. (2018), and defined the *variable* sample. Figure 4.4 shows that these variable stars coincide with larger amplitude values as expected, confirming that indeed the IR classification made by the BAaDE project correlates with variable stars. However, this

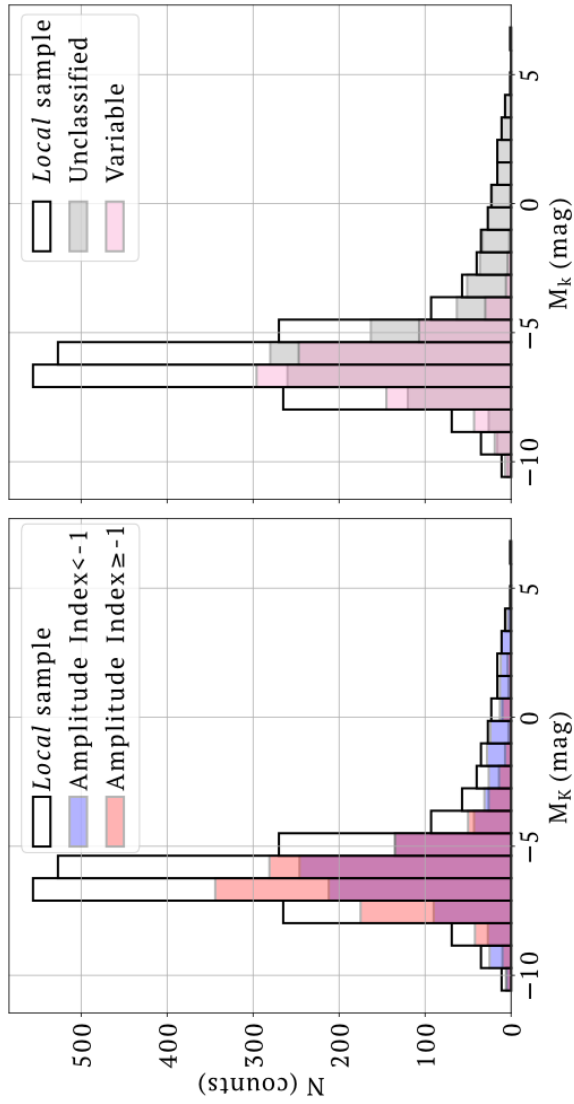


Figure 4.7: Absolute K -magnitude distribution for the local sample. In each panel, the distribution was split by variability criteria, i.e., using their Amplitude (Belokurov et al. 2017) and the *Gaia* variability classification, in left and right panel, respectively.

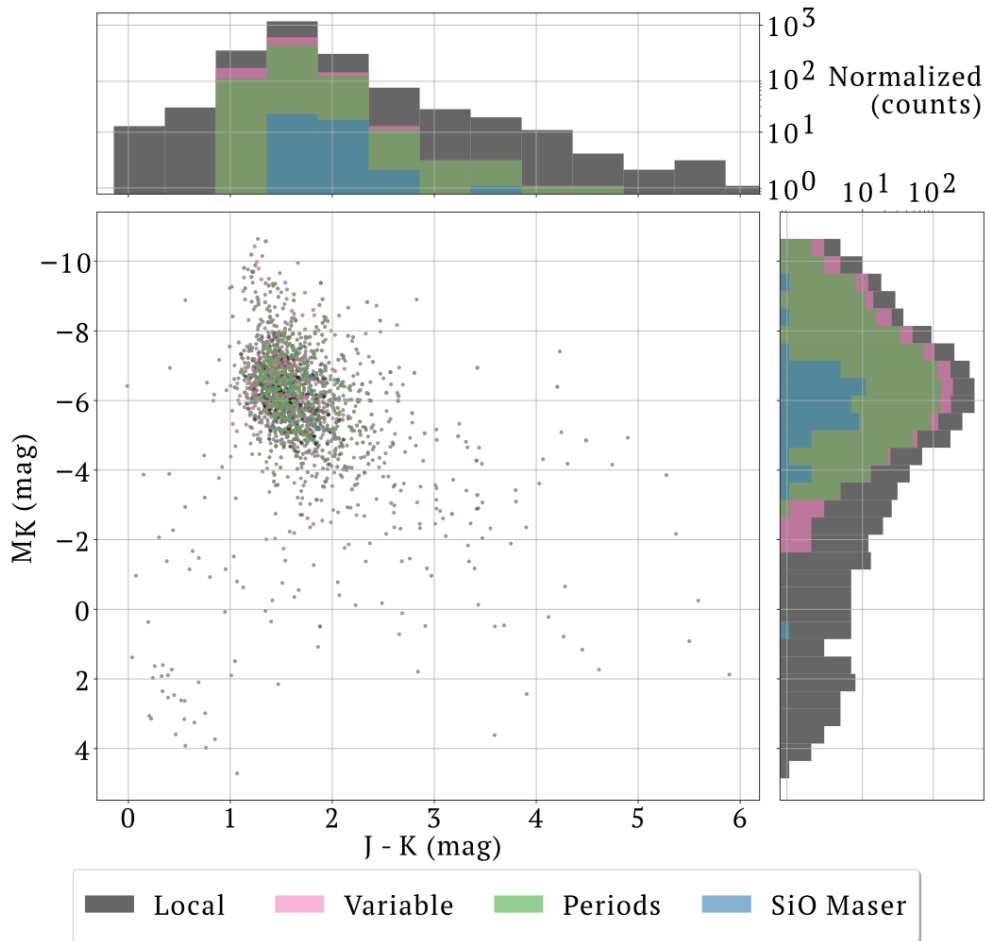


Figure 4.8: Magnitude (K -band) color diagram for the local sample (black) and the different subsamples obtained (Table 4.2). The distribution for each component is also shown.

qualification is restricted to stars that are bright in the G band.

4.3.2 The *local* sample

We study the Galactic foreground sample of BAaDE targets in terms of IR photometry, variability and Galactic distribution.

Infrared photometry

AGB stars can be identified by their IR colors, given that their SEDs peak at these wavelengths (see e.g., van der Veen & Habing 1998). In particular, after the 2MASS data release (Skrutskie et al. 2006), K measurements have been widely used to characterize these populations (Whitelock et al. 2008; Messineo et al. 2018). Figure 4.5 shows the distribution of the apparent K magnitude obtained from 2MASS for the entire cross-matched sample, with the different sub-samples related in Table 4.2. We note that by filtering the foreground sample with *Gaia* counterparts (the *local* sample), we are selecting brighter stars in the K -band.

Next, using the optical extinction maps described in Sect. 4.2.3, we can obtain the extinction and reddening estimates at K -band by assuming $A_V/A_K = (A_V/2.12\ \mu\text{m})^{-1.9}$ (Messineo 2004). As one could expect for the region around the Sun, the IR extinction estimates at the infrared K -band for the filtered sample are usually lower than 0.5 mag (see lower panel of Fig. 4.6). Finally, as we have precise distance estimates for the *local* sample (see upper panel of Fig. 4.6), we are able to estimate the absolute K magnitude distribution (M_K). Figure 4.7 shows this distribution where we have split the sample in terms of variability, as will be explained in the following subsection. Moreover, using the absolute K magnitudes together with *MSX* and 2MASS colors, we have constructed a Magnitude-color diagram (Fig. 4.8) for the *local* sample. This diagram confirms that the population of variable stars are restricted to well-defined ranges of mid-IR colors, as it was pointed out by van der Veen & Habing (1998); Sjouwerman et al. (2009); Lewis et al. (2018).

Variability

In Sect. 4.2.4, we have described the tables from *Gaia* DR2 that yield the variability classification that can be used for the *local* sample. And we noted that also the ratio between the flux error and mean in G magnitude can be used to identify pulsating stars when the amplitude index > -1 (Sect. 4.3.1). We have considered both methods, in particular in relation to the K -band apparent and absolute magnitude distributions. Figures 4.4 and 4.7 show these distributions split according to both variability criteria. Although both methods seem to produce similar results, the variability criterion from the *Gaia* DR2 tables, achieves narrower ranges of absolute magnitudes (particularly for less luminous objects). In other words, the amplitude estimator based on the G variance can presumably also pick up variability from objects that are not classified as variables in the *Gaia* DR2.

Galactic spatial distribution

Under the assumption that distances can be directly derived from *Gaia* parallax measurements (Sect. 4.2.3), the projected spatial distribution of the *local* sample can be generated (Fig. 4.9). The Galactic distribution of the *local* sample displays a number of distinct features:

1. The number of sources in the vicinity of the Sun (<0.5 kpc) is considerably lower than further out. This is to be expected as the BAaDE targets only sample latitudes of $|b| < 5^\circ$,

therefore the volume sampled increases with distance away from the Sun, until it covers the height of the galactic disk (scale height of ~ 300 pc, Jackson et al. 2002).

2. The inter-arm region between the Local arm and the Carina-Sagittarius arm seem to be the most populated region. The location of the main spiral arm is anti-correlated with the occurrence of stellar sources, which we speculate is related to regions with higher extinction.
3. At a Galactic longitude of $\sim 45^\circ$, there is a region depleted, which is possibly caused by the clouds of high optical depth that block this entire line of sight (Capitani et al. 2017).
4. The Outer Galactic region contains a lower number of sources from the BAaDE target selection. This is expected as the stellar density for AGB stars decreases as SiO maser detection.
5. In Fig. 4.9, there is no notable difference in the spatial distribution of variable stars compared to the unclassified (non-variable) sources according with *Gaia* DR2.

4.4 Discussion

4.4.1 Absolute magnitudes for the foreground Mira population

AGB stellar populations have been characterized by IR absolute magnitudes, because they radiate predominantly at these wavelengths (Vassiliadis & Wood 1993). Such IR observations allows one to study large populations, given the low extinction at these wavelengths, but unbiased distance estimates can be hard to obtain.

Several studies have been carried out to estimate IR absolute magnitudes of the AGB populations in the LMC and SMC, where the distance to the stellar system is known, and therefore, the distance modulus (and presumably also the IR extinction) can be assumed the same for each object. Figure 4.7 shows the distribution of absolute magnitude for the *local* sample with various indicators for variability. Although the magnitude values found correspond to those found at LMC and SMC, our distributions are much broader in terms of absolute magnitude range if we consider the entire *local* sample. This can be partly explained, as the current sample is mostly based on a single 2MASS observation and include the effects of large amplitude variability. However, when we filter the sample by a variability qualification (as shown in both panels of Fig. 4.7), the low luminosity tail (in M_K) is cut out. In this sense, the *Gaia* classification as Mira or Semi-Regular (SR) variable seems to narrow the distribution more, with a corresponding a peak at $M_K = -6.4 \pm 1.2$ mag. Preliminary results of the SiO masers detected by the BAaDE project also suggest that the variability classification (together with the IR color selection that generated the BAaDE target list) is selecting stellar objects in a specific M_K range between -7.2 and -3.6 with a peak at -6.5 . Following a similar discussion in Mowlavi et al. (2018), we argue that the low luminosity tail in Fig. 4.7 and also Fig. 4.5 is due to contamination with Young Stellar Objects (YSOs) that can also peak in the infrared, but do not show the same variability (Lewis, et al., in prep.).

4.4.2 Bolometric magnitudes for the foreground Mira population

The bolometric luminosity is a fundamental property useful for classifying stellar populations and evolutionary stages (Srinivasan et al. 2009), since they measure the intrinsic stellar power.

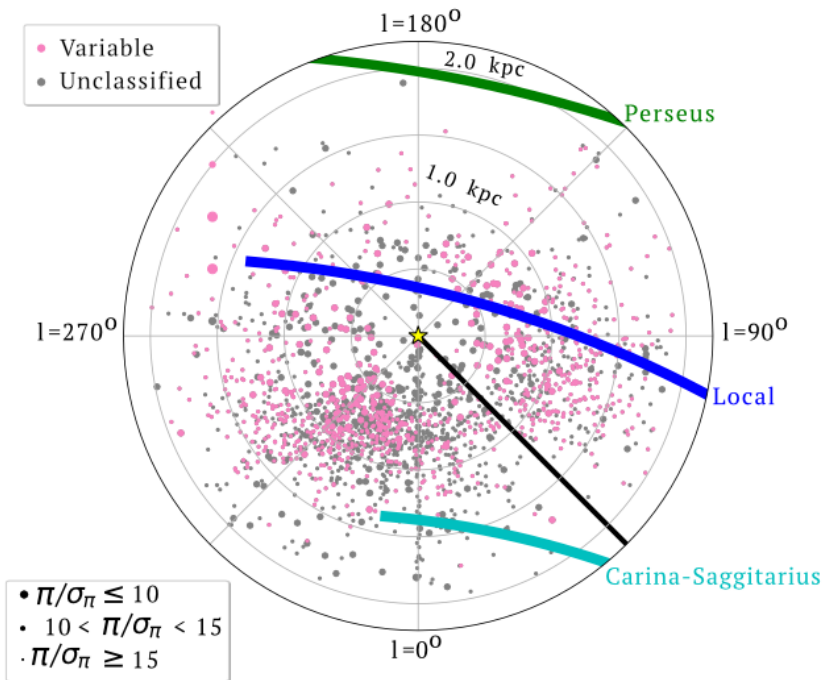


Figure 4.9: Foreground Galactic distribution of the local sample. The sample was split “Variable” and Unclassified according with *Gaia* DR2 (Mowlavi et al. 2018). The size of the marker is a measure of the relative parallax uncertainty, and therefore, distance uncertainty for each source. The spiral arms location and width (with of the lines) are based on Reid et al. (2014). The black line represent Galactic longitude of 45° , where a high extinction line of sight is expected (see 4.3.2).

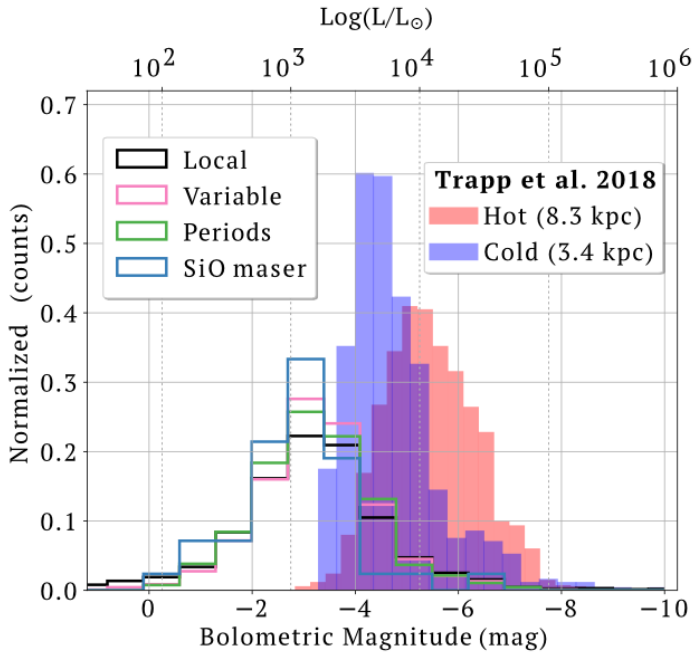


Figure 4.10: Luminosity and bolometric magnitude distributions for the *local* sample and the subsamples resulting from different filters (Table 4.2). These distributions were obtained by applying the BC proposed by Messineo et al. (2018) to the absolute magnitudes in the *K*-band. The absolute *K*-magnitudes were estimated from 2MASS *K*-band, Gaia parallaxes and extinction maps from Capitanio et al. (2017) and Lallement et al. (2019). The bolometric distribution estimated by Trapp et al. (2018) for the “hot” and “cold” kinematic populations are shown as filled histograms. Note that the kinematic cold population proposed by Trapp et al. (2018) is made up of stars in the disks and not in the bulge, therefore, similarities with respect to the *local* sample defined in this work are expected.

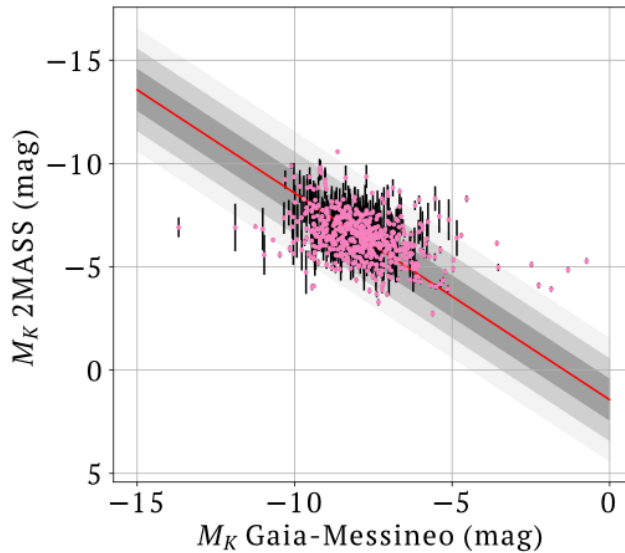


Figure 4.11: Comparison between the absolute K -magnitudes estimated from 2MASS data, *Gaia* parallaxes and extinction maps with respect to the absolute bolometric estimates reported for variable stars in *Gaia* DR2 that were transformed to absolute K -magnitude using the BC_K in Messineo et al. (2018). The red line describes the linear fitting that was forced to have slope of 1. The grey layers contains 1, 2, and 3 σ deviation from the linear fitting.

Although its definition is straightforward formulated as the total integrated power overall frequencies, in practice complete photometric measurements that allow a direct bolometric luminosity estimates are hardly ever available. Therefore, under various assumptions a limited set of photometric measurements, preferably near the peak of the SED, can be used to apply a bolometric correction (BC) in order to determine the integrated stellar luminosity. In particular, for AGB stars IR absolute magnitudes are converted to bolometric luminosities using a bolometric correction, which is usually parameterized using IR colors (see e.g., Messineo et al. 2018; Whitelock et al. 2008; Lebzelter et al. 2019).

Trapp et al. (2018) have estimated the bolometric magnitude for a sub-set of the BAaDE sample. They considered a kinematically “cold” population disk stars, which is similar to what is defined here as the foreground population or *local* sample. In their analysis, they have assumed a common distance of 3.8 kpc for this population and have applied a BC_K based on Messineo (2004). In order to compare the *local* sample with their kinematically “cold” population, we have applied the same BC_K , but not before confirming that other proposed BC_{K_s} for AGB samples produced similar results (Whitelock 2003; Srinivasan et al. 2009). Figure 4.10 shows these bolometric distributions. The offset between the two distributions is likely caused by the distance assumption made by Trapp et al. (2018), which is equivalent to ~ 3.5 mag when taking the average distance of the *local* sample (767 pc, upper panel of Fig. 4.6).

We did our bolometric magnitude estimates from M_K , using 2MASS IR photometry, *Gaia* parallaxes and extinction maps. The *Gaia* data also provide bolometric corrections based on G magnitudes, allowing us to derive estimates of the bolometric magnitudes in particular for the stars classified as variables. But, one would assume that the 2MASS bolometric corrections are more robust for the IR selected stars in our sample. To compare our results with the

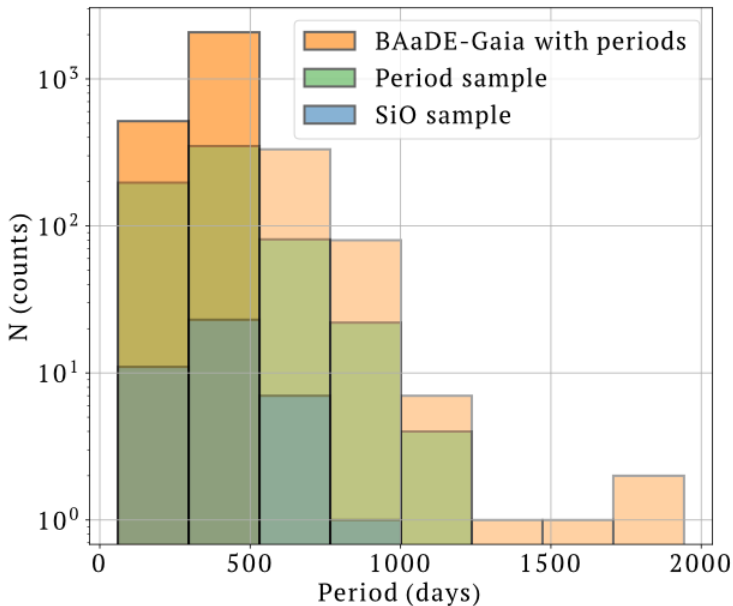


Figure 4.12: Histogram of periods obtained for variable stars in *Gaia* DR2 for the different samples used in this research (Table 4.2).

estimated that *Gaia* provides, we have compared the M_K that we have obtained in 4.3.2 with estimates of M_K obtained by working back from the *Gaia* bolometric magnitudes using the BC_K from Messineo (2004). The result in Fig. 4.11 shows a substantial difference of -1.6 mag, indicating that the bolometric corrections in the *Gaia* DR2 are overestimating the total luminosity estimated by *Gaia* DR2 (Andrae et al. 2018) of our very red objects. We continue to use only the M_K based using 2MASS IR photometry, *Gaia* parallaxes and extinction maps.

In Fig. 4.10, we also present the luminosity distribution for the *local* sample. It shows that our sample is made up of giant stars with a luminosity range that is consistent with AGB stars, mostly Mira variables (Srinivasan et al. 2009). In particular the sub-set of stars that have SiO masers has a similar luminosity distribution. Compared to previous studies of stars in the LMC, SMC or Galactic bulge (where fixed distances have been assumed), we have found less luminous objects. This is of course expected in our selection that was based on a combination of IR detections, optical *Gaia* counterparts, extinction maps and distance selection. The typical luminosity for the *local* sample was estimated in $1,250 L_{\odot}$.

4.4.3 Mira distribution around the Sun

The Galactic distribution of AGB stars has been studied extensively using IRAS, WISE, 2MASS and MSX data (Jackson et al. 2002; Habing 1996; Lian et al. 2014; Messineo et al. 2018; Sjouwerman et al. 2009). Generally, it has been found that AGB stars are tracing the relaxed stellar population of the Galactic (thick) disk and bulge. In particular, Jackson et al. (2002) found a density distribution based on revised IR photometric data from IRAS that they called universal, implying that there are no statistically significant differences in the spatial distribution of AGB stars based on IR colors. Adopting their radial scale length of 1.6 kpc (outside of $R > 5$ kpc) and scale height of 300 pc, we consider Fig. 4.9. We attribute the

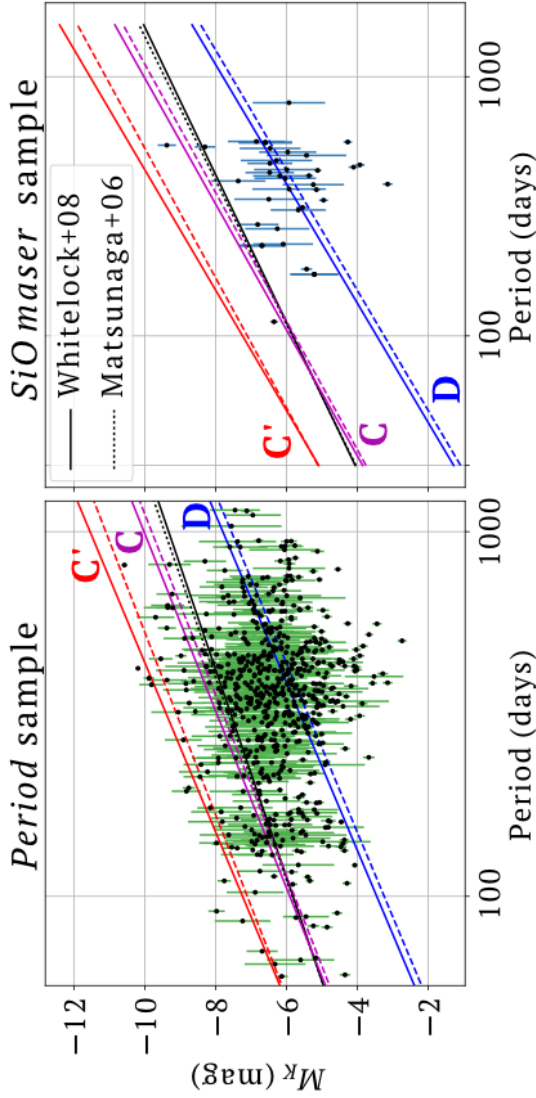


Figure 4.13: Period-Luminosity relations found for the variable stars with in the local sample (**left panel**) and those with SiO maser emission detected (**right panel**). The sequences marked as C, C' and D represent different known variability sequences, associated with distinct pulsation modes that have been derived for LMC based on Gaia data (Lebzelter et al. 2019). Note that the sequences were corrected for a distance modulus of 18.49 mag. Period-Luminosity relations reported for LMC using other surveys are also shown (Whitelock et al. 2008; Matsunaga & Team 2006).

depletion of targets < 500 pc around the Sun to the fact that the *MSX* catalogue, on which our sample is based, is mostly limited to $|b| < 5^\circ$. The corresponding scale height is estimated to be 100 pc, equally for all objects in the *local* sample, as well as for identified Mira variables. This seems to suggest that the scale height for our BAaDE targets is a bit lower than that estimated for previous AGB stars, but it requires detailed simulations to confirm that.

From Fig. 4.9, we note that contrary to a homogeneous distribution, there is an anti-correlation with the location of spiral arms as defined by Reid & Honma (2014). It appears that, the *local* sample is severely affected by interstellar extinction in the *Gaia* band. But, there is still a radial gradient detectable with more targets towards the center than observed in the anti-center direction. This can possibly arise, because the *MSX* criteria defined by Sjouwerman et al. (2009) were optimised for detecting SiO masers, O-rich AGB stars. It has been established that outside of the solar circle the AGB population contains a higher fraction of carbon rich stars (Lian et al. 2014; Groenewegen & Sloan 2018). This will become clearer when the SiO detections are discussed in Sect. 4.4.5.

Finally, we point out that in our sample there is one variable star standing out for its proximity. The source *IRAS* 17375-3434 is part of the *local* sample, it has been classified as a Mira by *Gaia* with a period of 373.5 ± 47.5 days and a distance of 65.5 ± 3.9 pc. Although we have confirmed SiO maser emission at 42 GHz coming from that region ($V_{\text{LSR}} = -15.5 \text{ km s}^{-1}$), its luminosity was estimated in $2.6 L_\odot$, which is unrealistically low for an evolved star. Based on DSS images of the region, we confirm that this star is located in a very crowded region in the Galactic plane, suggesting that it is likely a false positive.

4.4.4 Period-Luminosity relations

Figure 4.12 displays the distribution of periods available from *Gaia* for sources in the *BAaDE-Gaia* sample, the *local* sub-sample and for those stars bearing SiO masers (*SiO maser* sample). It can be noted that the whole sample contains LPV stars with a wide range of periods, but that SiO masers are mostly restricted to stars with periods of $\lesssim 750$ days, presumably Mira variables.

It has been established that Period-Luminosity (P-L) relations are a very powerful tool to distinguish AGB stars of different nature (Wood et al. 1999; Ita et al. 2004; Lebzelter et al. 2019). By recognising that Mira variables pulsate dominantly in the fundamental mode, they can be promising candidates for distance determinations of remote galaxies, using empirical relations based on the LMC and SMC (Whitelock et al. 2008). With 2MASS K -magnitudes, *Gaia* DR2 parallaxes, extinction maps and periods for a sub-sample of the *local* sample (*period* sample), we are able to make a comparison of the BAaDE targets with previously studied variable stars.

In Fig. 4.13, we present the P-L relation for those BAaDE stars in the *local* sample with measured *Gaia* periods (*period* sample), where there is a spread in the magnitude, resulting from uncertainties in apparent K magnitude, extinction and distance (indicated by the error bars) and infrared variability (not indicated). We present a separate panel for those stars that have confirmed SiO maser emission (*SiO maser* sample). A comparison is made of the P-L distribution with known variability sequences, associated with distinct pulsation modes, that have been derived from *Gaia* DR2 data for LMC (and SMC) populations as discussed by Lebzelter et al. (2019). These sequences have been transformed to M_K , using the LMC distance modulus in that work (18.49 mag). Moreover, the established P-L relations for Miras from Whitelock et al. (2008); Matsunaga & Team (2006) in the LMC and SMC are added.

In comparison with the analysis by Lebzelter et al. (2019), it is possible to interpret Fig. 4.13, where it should be noted that these results were obtained for the stellar popula-

tions in the Milky Way satellites, i.e. a different metallicity. At short periods one can identify stars associated with sequence *C*, while at the most extreme long periods most stars lie closer to sequence *D*. Supposedly both these sequences are being traced by low mass, oxygen rich Miras. At the intermediate periods, where there is the highest density of objects, there is no clear distinction between the two sequences. In Lebzelter et al. (2019), the corresponding objects are mostly (extreme) carbon rich Miras. It is quite remarkable that the stars that have confirmed SiO masers, have dominantly longer periods and lie on sequence *D*, as expected for oxygen-rich Miras. Typically, stars in that period range have a mass slightly over the solar mass and ages below 1 Gyr (Grady et al. 2019).

Finally, it is clear that most of the stars in the *local* sample are below the empirical P-L relation for the LMC (and SMC) Whitelock et al. (2008); Matsunaga & Team (2006). Possibly this is again related with the fact that we preferably select the closer, less luminous AGB stars, when we make our *BAaDE-Gaia* sample, while in the LMC (and SMC) the sample is biased towards the most luminous stars.

4.4.5 SiO maser emission from Mira variables

Although the subsample from the *local* sample for which SiO maser emission lines are detectable, is not complete and currently limited to 42 stars, preliminary statistics of this subsample can be presented briefly. Figure 4.14 shows the distribution of these stars and their motions from *Gaia* DR2 projected on the Galactic plane. Although this result is preliminary, it is clear that there is a preference to find SiO masers in the direction of the Galactic center. As discussed before, this can be due to an asymmetry between carbon rich stars and oxygen rich stars with respect to the solar circle. Otherwise, the stars appear to be found in the region between the high extinction regions associated with the local and Carina-Sagittarius arm. The apparently random motions with an rms of 30 km s^{-1} (mainly in the direction of the Galactic rotation component) are consistent with the expected kinematics for a relaxed, old stellar population (e.g., Schubert et al. 2010).

VLBI astrometry of selected bright BAaDE targets is currently being considered, in order to provide parallaxes and 3D orbits with a target accuracy of $\sim 50 \mu\text{as}$. This can provide orbits of stars beyond the *local* sample, allowing us to study the kinematics in the inner Galaxy. Astrometric VLBI would also provide a direct comparison of the parallax technique between optical (*Gaia* DR2) and radio, verifying alignment between the stellar photosphere and the origin of the circumstellar masers. Notably, synergies between VLBI and *Gaia* data are currently being used to refine astrometric measurements for *Gaia* objects (Lindgren 2019).

4.5 Conclusions

We have cross-matched the BAaDE target list, which consists of 28,062 IR sources preselected from the MSX colors at latitudes $|b| < 5^\circ$ to match evolved stars in the inner Galaxy (van der Veen & Habing 1998; Sjouwerman et al. 2009), with the *Gaia* DR2 catalogue (Gaia-Collaboration et al. 2018), finding 20,111 cross-matches. The cross-match was made using a conservative radius of $3''$ around the MSX position which has a positional accuracy of $2''$ (Price 1995). The 7,951 sources from the BAaDE target list that were not detected in *Gaia* DR2 correlate with lines of sight of high optical extinction in the Galactic plane. From the 20,111 cross-matched sources, stars with precise parallax estimates and within a 2 kpc radius around the Sun (where we can obtain accurate extinction maps) were selected. The remaining 2,060 stars constitute our *local* sample, representing a foreground population of evolved stars in the Galactic plane.

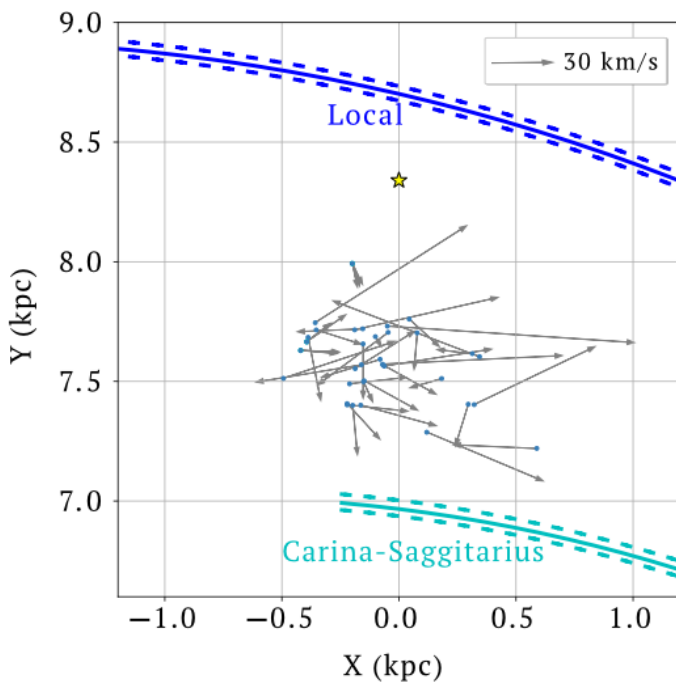


Figure 4.14: Galactic projection of the motion of BAADE targets within the local sample with confirmed SiO maser emission. In this view, the Sun is located at $[0, 8.34]$ kpc (Reid et al. 2014), and the Galactic center at $[0.0]$. The location of the spiral arms and their widths follow (Reid et al. 2014).

Among the *local* sample, the Gaia DR2 shows large amplitude variability for 908 stars that have been classified as Mira variables (Mowlavi et al. 2018), of which another 653 have period estimates. Moreover, the BAaDE survey has already observed 395 of those 653 sources with the VLA and ALMA detecting SiO maser emission lines at 42 and 86 GHz coming from 45 sources.

Using radio, infrared and optical data for this sample, we have characterized the evolved stellar population around the Sun in terms of spatial, variability, bolometric luminosity distribution. The population of evolved stars close to the Sun displays the following features:

1. The absolute magnitude distribution at K-band peaks at -6.4 ± 1.2 mag with a spread of approximately 4 mag around the peak for the stars classified by *Gaia* as variables. While the brightest sources are consistent with the expected luminosities for optically identified Mira variables, it is clear that our sample, at distances <2 kpc, is contaminated by red, low luminosity objects, most likely YSOs. By applying additional filters based on variability we can restrict the sample to LPV stars, which have a narrower K magnitude distribution.
2. Using extinction and bolometric corrections from the literature, we are able to estimate bolometric magnitudes for the *local* foreground Galactic sample. The distribution peaks at -3.0 with a width of 1.8 mag. This peak is at fainter magnitudes than that obtained for Miras in the LMC (Whitelock et al. 2008) and also at a lower value than inferred for BAaDE sources in the inner Galaxy (Trapp et al. 2018). Although variability and uncertainties in the extinction and bolometric corrections are important, we argue that the main reason is the selection of faint, but nearby, sources that can be identified in the optical regime.
3. For those BAaDE objects that have *Gaia* periods, we are able to associate these with fundamental mode and first overtone pulsation sequences. The BAaDE foreground population contains moderate mass Mira variables, which are the sources that have a high probability to show SiO masers. Among the targets in the sample, carbon rich LPV stars also seem to be abundant.
4. The SiO masers detected so far are associated with fundamental mode pulsators inside Solar circle. Moreover, the kinematic distribution is consistent with that expected for a relaxed, old stellar population.

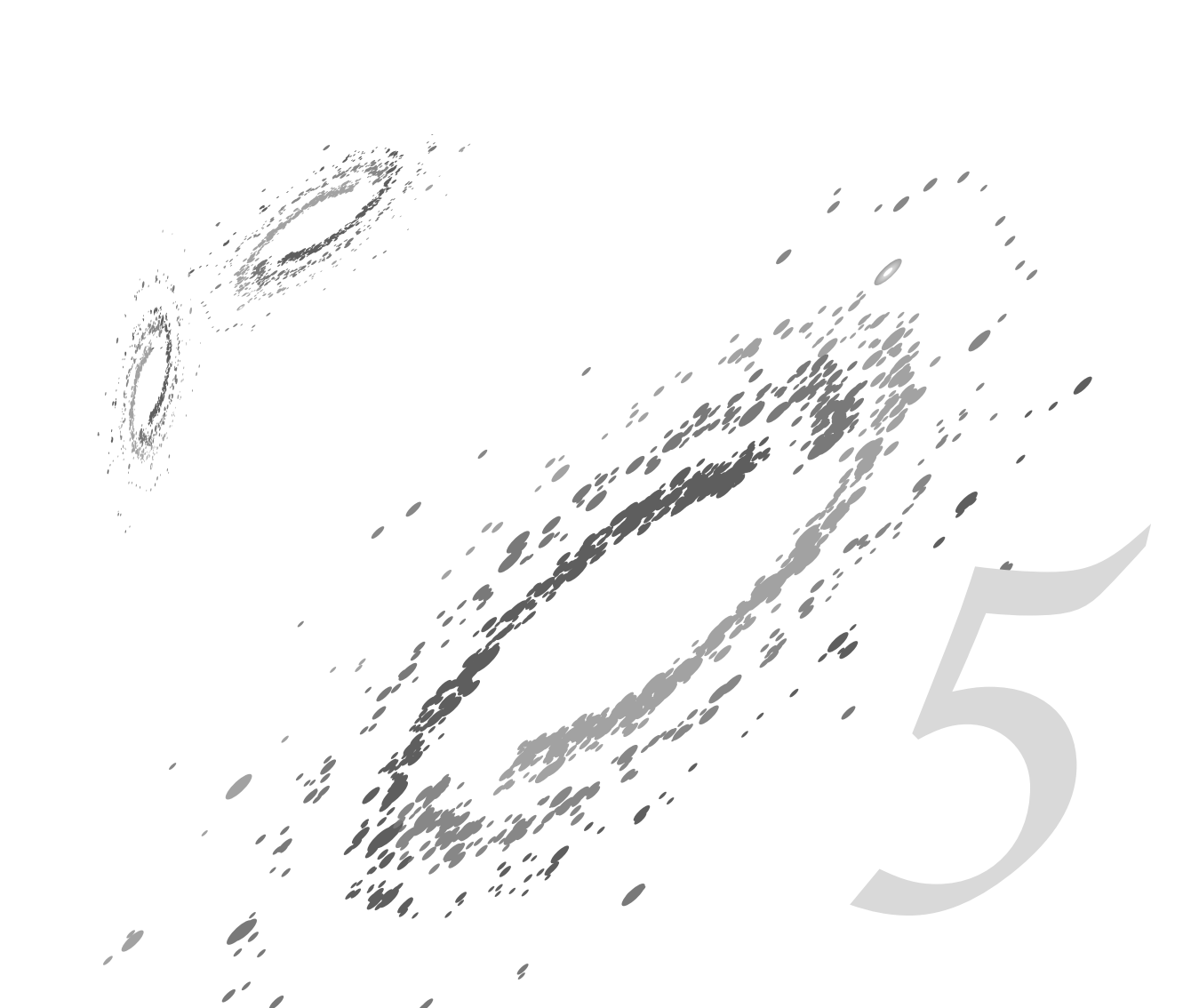
Overall we conclude that the BAaDE targets are predominantly made up of LPVs, optically detectable Miras and carbon stars. The infrared selection also picks up lower luminosity objects within 2 kpc from the sun. The sample of evolved stars at these distances is made up of AGB stars of moderate luminosity. To understand the nature of stars that make up the BAaDE sample in the inner Galaxy, advanced statistical methods that can use more uncertain *Gaia* data in a robust way will be required.

Acknowledgements. The BAaDE project is funded by National Science Foundation Grant 1517970/1518271. This paper uses data products obtained with instruments run by the National Radio Astronomy Observatory (NRAO): NSF's Karl G. Jansky Very Large Array (VLA; program ID: VLA/13A-331) and the Atacama Large Millimeter/submillimeter Array (ALMA). This paper makes use of the following ALMA data: ALMA/2013.1.01180.S. ALMA is a partnership of ESO (representing its member states), NSF (USA) and NINS (Japan), together with NRC (Canada), MOST and ASIAA (Taiwan), and KASI (Republic of Korea), in cooperation with the Republic of Chile. The Joint ALMA Observatory is operated

by ESO, AUI/NRAO and NAOJ. The National Radio Astronomy Observatory is a facility of the National Science Foundation operated under cooperative agreement by Associated Universities, Inc. This research made use of data products from the Midcourse Space Experiment. Processing of the data was funded by the Ballistic Missile Defense Organization with additional support from NASA Office of Space Science. This research has also made use of the NASA/IPAC Infrared Science Archive, which is operated by the Jet Propulsion Laboratory, California Institute of Technology, under contract with the National Aeronautics and Space Administration.

This publication makes use of data products from the Two Micron All Sky Survey, which is a joint project of the University of Massachusetts and the Infrared Processing and Analysis Center/California Institute of Technology, funded by the National Aeronautics and Space Administration and the National Science Foundation.

This work also has made use of data from the European Space Agency mission *Gaia*, processed by the *Gaia* Data Processing and Analysis Consortium (DPAC). Funding for the DPAC has been provided by national institutions, in particular the institutions participating in the *Gaia* Multilateral Agreement. This material is based upon work supported by the National Science Foundation under Grant Number 1517970.



Differences in radio emission from similar M dwarfs in the binary system Ross 867-8

Quiroga-Nuñez, L. H.; Intema, H. T.; Callingham, J. R.; Villadsen, J.; van Langevelde, H.J.; Jagannathan, P. & Shimwell, T.W. *Differences in radio emission from similar M dwarfs in the binary system Ross 867-8*. 2020, A&A, 633, A130.

Abstract

Serendipitously, we have rediscovered radio emission from the binary system Ross 867 (M4.5V) and Ross 868 (M3.5V) while inspecting archival Giant Metrewave Radio Telescope (GMRT) observations. The binary system consists of two M-dwarf stars that share common characteristics such as spectral type, astrometric parameters, age and emission at infrared, optical and X-rays frequencies. The GMRT data at 610 MHz taken on July 2011 shows that the radio emission from Ross 867 is polarized and highly variable on hour time scales with a peak flux of 10.4 ± 0.7 mJy/beam. Additionally, after reviewing archival data from several observatories (VLA, GMRT, JVLA and LOFAR), we confirm that although both stars are likely coeval, only Ross 867 has been detected, while Ross 868 remains undetected at radio wavelengths. As they have a large orbital separation, this binary stellar system provides a coeval laboratory to examine and constrain the stellar properties linked to radio activity in M dwarfs. We speculate that the observed difference in radio activity between the dwarfs could be due to vastly different magnetic field topologies or that Ross 867 has an intrinsically different dynamo.

5.1 Introduction

Given that M dwarfs are the most common stellar type (Henry et al. 2006), the understanding of eruptive events in these stars—e.g., stellar flares and stellar coronal mass ejections—is a fundamental astrophysical subject. Moreover, it could be important for assessing the habitability on orbiting exoplanets (Crosley & Osten 2018) around dwarfs, which have been already detected (Dressing & Charbonneau 2013). It is known that these stars show dynamic activity in their stellar atmosphere, especially for mid- to late-M dwarfs (e.g., West et al. 2008). This effect has usually been attributed to magnetic energy release in the outer atmosphere that accelerates particles and gives rise to chromospheric and coronal heating, producing photons at all wavelengths (Bochanski et al. 2007). Particularly, at radio wavelengths, the flux intensity changes are not well understood, and although the physical mechanisms that produce this radio variability have been studied in the Sun (e.g., Shibata & Magara 2011), recent studies show that radio flares coming from M dwarfs do not have a clear solar analog (see e.g. Villadsen & Hallinan 2019, and the references within). In order to establish the physical mechanisms occurring in M dwarfs that could lead to radio intensity changes, previous investigations have analyzed a wide range of stellar properties (White et al. 1989; Berger 2002; Wright et al. 2011; Houdebine & Mullan 2015; Houdebine et al. 2017; Newton et al. 2017; Yang et al. 2017). Factors such as the stellar spectral type, the Rossby number and ages of dwarf stars may be related to the magnetic activity and therefore dynamic radio activity (West et al. 2008; López-Santiago et al. 2010; McLean et al. 2012; West et al. 2015; Barnes et al. 2017; Ilin et al. 2019).

In this letter, we present a serendipitous flare detection of the variable radio source Ross 867 (a.k.a. V639 Her or Gliese 669B) based on archival observations from the Giant Metrewave Radio Telescope (GMRT; Swarup 1991) that targeted the galaxy cluster RXJ1720.1+2638 (Giacquintucci et al. 2014; Savini et al. 2019). Although Ross 867 was already marked as being radio loud by Jackson et al. (1987), there was no evidence of variability or circular polarized emission reported. Ross 867 is part of a binary system with Ross 868 (a.k.a. V647 Her, Gliese 669A or HIP 84794), which are separated by 179.3 ± 0.1 AU (or $16.854 \pm 0.001''$) in projection, and both stars have been classified as optical flaring stars (Samus et al. 2004; Nakajima et al. 2010). Using their stellar position together with recent parallax measurements in *Gaia* DR2 (Gaia-Collaboration et al. 2018), we confirm that both sources are close enough to be gravitationally bound, but separate enough to discard any stellar material transfer or significant tidal interaction. What is remarkable about this binary system is that although both stars are similar in terms of spectral type, age, high 3D motion, IR, optical (same thermal emission processes can be assumed) and X-ray emission (see Table 5.1), only Ross 867 seems to be radio loud. Hence, this binary stellar system provides a coeval laboratory to examine and constrain the stellar properties present in radio-loud flare stars, and hence, discuss the physical mechanisms behind the radio flare emission in M dwarfs. In order to study this binary system in more detail, we initiated a search for other historical radio data identifying several radio continuum observations in the archives of the GMRT, the Very Large Array (VLA; Thompson et al. 1980), and the Low Frequency Array (LOFAR; van Haarlem et al. 2013) observed at different epochs and different radio frequencies. In this paper, we present an analysis of this set of observations, confirming that Ross 867 is indeed a source of time-variable, bright radio emission, whereas Ross 868 remains undetected.

5.2 Observations

The GMRT observed the galaxy cluster RXJ1720.1+2638 four times at various frequencies, one of which is a dual-frequency observation (project codes 11MOA01 and 20_016; see Tables 5.2 and 5.4 for details). In three observations, the star Ross 867 was located within the field-of-view. GMRT observations amounted to integrations of four to six hours, consisting predominantly of blocks of ~ 30 minutes on RXJ1720.1+2638 interleaved with phase calibrator observations of several minutes (see details in Table 5.2). All but the dual-frequency observation recorded instrumental *RR* and *LL* visibilities, while the dual-frequency observations recorded *RR* visibilities only at 610 MHz, and *LL* visibilities only at 235 MHz. Full polarization calibration was not possible for any of these data sets. However, under the general assumptions that the circular feeds are mostly orthogonal with around $\lesssim 10\%$ leakage per antenna (Joshi & Chengalur 2010; Roy et al. 2010), and the sources are not linearly polarized at these low frequencies (Faraday rotation would wipe out the linearly polarised light given the density of the plasma, Dulk 1985; White & Franciosini 1995), *RR* and *LL* visibilities can be converted into Stokes *I* and *V* visibilities. For the dual-frequency observations, the individual *RR* and *LL* visibilities are approximately equal to Stokes *I* visibilities, assuming that (1) the radio sky emission is predominantly circularly unpolarized (which is generally the case except for gyro-synchrotron emitters such as planets, stars and the Galactic center), and (2) the instrumental polarization over the relevant part of the field-of-view is negligible (Wielebinski 2012; Farnes 2014).

We have used the SPAM pipeline (Intema et al. 2017) to process the archival GMRT observations — a concise description is provided in Appendix 5.6.1— and generated calibrated Stokes *I* visibilities and images for all observations. Additionally, to look for evidence of circular polarization in observations with both *RR* and *LL* present, we split off each polarization and processed these independently using the same pipeline. The resulting sensitivities and resolutions of the wide-field images generated by the pipeline are listed in Table 5.4.

The source extraction software PyBDSF (Mohan & Rafferty 2015) was used to measure the position and flux density of all detectable sources in the primary-beam-corrected images. The measured positions and flux densities of Ross 867 are reported in Table 5.2. The flux density calibration procedure for GMRT is typically accurate to about 10 percent (e.g., Chandra et al. 2004), so a systematic 10 percent error is added (in quadrature) to all the random flux uncertainties as reported by PyBDSF (and to all GMRT flux measurements in the remainder of the article). Table 5.2 also contains the flux densities of the bright neighboring extragalactic source NVSS J171949+263007 (0.8' west of Ross 867), which we use as a reference source. The reported 1.4 GHz flux densities of this source in the NVSS and FIRST surveys are 17.3 ± 0.6 and 17.9 ± 0.9 mJy, respectively (see Table 5.3 for details). Given the difference in resolution and observing epochs, this indicates that the reference source is compact and not variable on short time scales (months to years). The position of the reference source is measured to be $17^{\text{h}}19^{\text{m}}49.31^{\text{s}} +26^{\circ}30'07.7''$ in all GMRT images within $0.1''$ accuracy.

5.3 Results

By comparing two separate observations at 610 MHz from 2007 and 2011, we discover that one of the radio sources shifted its position and changed its flux density, between the epochs. After aligning the observations using the close-by quasar NVSS J171949+263007 (at 0.8') as astrometric reference source, we found that the variable radio emission unambiguously coincided with the sky position of Ross 867 in both observations. The radio properties obtained

Table 5.1: Astrophysical information of the binary system Ross 867-8.

	Ross 867	Ross 868
Spectral Type ⁽¹⁾	M4.5V	M3.5V
Mass ⁽²⁾ (M_{\odot})	0.311 ± 0.132	0.376 ± 0.040
Parallax ⁽³⁾ (mas)	92.967 ± 0.061	92.988 ± 0.050
Distance ^(3,14) (pc)	10.753 ± 0.007	10.751 ± 0.006
Radius (R_{\odot})	$[0.27-0.51]^{(9,7)}$	$[0.478-0.535]^{(6,4)}$
$V_{\text{LSR}}^{(1)}$ (km s^{-1})	-34.6 ± 0.2	-34.9 ± 0.1
$\mu_{\alpha}^{(3)}$ (mas yr^{-1})	-226.1 ± 0.1	-214.8 ± 0.1
$\mu_{\delta}^{(3)}$ (mas yr^{-1})	355.3 ± 0.1	351.0 ± 0.1
Age ⁽¹²⁾ (Myr)	[90-300]	[25-300]
T_{eff} (K)	$2667^{(2)}$	$3319 \pm 100^{(6)}$
$V \sin i$ (km s^{-1})	$[6.79-10]^{(5,8)}$	$[1.0-28.5]^{(4,6,7,10,11,12,13)}$
B ⁽¹⁾ (mag)	14.67	12.98
R ⁽¹⁾ (mag)	12.65 ± 0.06	11.34 ± 0.02
G ⁽¹⁾ (mag)	11.456 ± 0.001	10.137 ± 0.001
J ⁽¹⁾ (mag)	8.23 ± 0.02	7.27 ± 0.02
H ⁽¹⁾ (mag)	7.64 ± 0.03	6.71 ± 0.03
K ⁽¹⁾ (mag)	7.35 ± 0.03	6.42 ± 0.02
XMM ⁽¹³⁾ [0.2-12keV] ($10^{-12} \text{ erg s}^{-1} \text{ cm}^{-2}$)	3.4 ± 0.1	2.1 ± 0.1
Chandra ⁽¹³⁾ [0.3-11keV] ($10^{-12} \text{ erg s}^{-1} \text{ cm}^{-2}$)	1.26 ± 0.03	1.25 ± 0.02

Notes. When several measurements differ, a range in square brackets is given. **References.** (1) The SIMBAD astronomical database (Wenger et al. 2000). (2) Jenkins et al. (2009). (3) Gaia-Collaboration et al. (2018). (4) Houdebine (2012). (5) Jeffers et al. (2018). (6) Houdebine et al. (2016). (7) Caillault & Patterson (1990). (8) McLean et al. (2012). (9) White et al. (1989). (10) Moutou et al. (2017). (11) Reiners et al. (2012). (12) Shkolnik et al. (2012). (12) Kiraga & Stepień (2007). (13) This work. (14) Assuming geometrical distance calculation from parallax made by Bailer-Jones et al. (2018).

Table 5.2: Measured radio properties of Ross 867 using GMRT data.

Date (yyyy-mm-dd) and UTC range	Frequency (MHz)	Blocks \times time per block (min)	Observational time (min)	Correlation parameters	$\alpha \pm \Delta\alpha$ (arcsec)	$\delta \pm \Delta\delta$ (l) (arcsec)	S_ν (l) (mJy)	Ref S_ν (l) (mJy)
2007-03-08 23:28-06:11(+1)	325	7.5 \times 37	275	<i>I</i> <i>LL</i> <i>RR</i>	52.87 \pm 0.11 52.84 \pm 0.05 52.84 \pm 0.19	05.7 \pm 0.11 05.6 \pm 0.07 05.7 \pm 0.21	5.3 \pm 0.8 11.6 \pm 1.2 3.5 \pm 0.6	57.0 \pm 5.7 67.2 \pm 6.7 62.2 \pm 6.2
2007-03-10 23:17-06:09(+1)	610	12 \times 26	313	<i>I</i> <i>LL</i> <i>RR</i>	52.85 \pm 0.08 52.83 \pm 0.09 52.80 \pm 0.19	05.4 \pm 0.10 05.1 \pm 0.08 05.7 \pm 0.26	1.7 \pm 0.2 2.4 \pm 0.3 0.9 \pm 0.2	39.1 \pm 3.9 41.0 \pm 4.1 38.0 \pm 3.8
2011-07-24 13:30-21:25	235 610	11 \times 31	346	<i>LL</i> <i>RR</i>	52.78 \pm 0.23 52.76 \pm 0.01	06.6 \pm 0.21 06.9 \pm 0.01	6.8 \pm 0.6 7.8 \pm 0.8	96.2 \pm 9.7 39.6 \pm 4.0

Notes. (1) Source position and uncertainty of right ascension (α) and declination (δ) measured from 17^h19^m00^s and +26°30'00" in sexagesimal notation. (2) Source flux density and uncertainty. (3) Reference flux density and uncertainty of neighboring source NVSS J171949+263007.

for Ross 867 and NVSS J171949+263007 are described in Table 5.2, which reveals several important properties:

1. There is a noticeable shift in the position of Ross 867 between March 2007 and July 2011, which is much larger than the expected parallax shift expected ($0.1''$) for this stellar source. When using the 610 MHz positions (highest resolution) in the *LL* images (only polarization available at both epochs), the shift is $-0.6''$ in right ascension and $1.2''$ in declination over 4.37 yr, which translates in a proper motion of -137 ± 44 and 275 ± 60 mas yr⁻¹ for right ascension and declination, respectively. These values differs by nearly two sigma with respect to the recently estimated values by *Gaia* DR2 (Table 5.1). The discrepancy is likely due to the astrometric measurement uncertainties caused by limited resolution and signal-to-noise in GMRT.
2. There is a significant increase in the flux density of Ross 867 at 610 MHz between March 2007 and July 2011. The flux ratio lies in the range of 3–10 taking into account the flux uncertainties and the stokes measurement selected. Note that the change in flux density over time of the quasar reference source (NVSS J171949+263007) is negligible and lies within the uncertainties.
3. There is a significant difference in the flux density of Ross 867 between the correlation parameters *RR* and *LL* for the cases where both visibilities were recorded, namely at 325 and 610 MHz in March 2007. At both frequencies, the flux density in *LL* is 3 ± 1 times higher than in *RR* (see Table 5.2). Whereas for the quasar reference source (NVSS J171949+263007) the difference between the *RR* and *LL* is consistent with unpolarized emission. This observational evidence demonstrates unambiguously that time-variable, likely circularly-polarized radio emission is originating from Ross 867.

5.3.1 Radio Light Curves

Since the GMRT observations are integrations of several hours, consisting of blocks of 0.5 hours, this allowed us to look for radio variability of Ross 867 on minutes to hours time scales, by re-imaging time slices of the calibrated and flagged visibility data as generated by the pipeline. As we are only interested in Ross 867 and the reference source NVSS J171949+263007, we pre-subtracted all radio source flux outside a $2'$ radius circle centered on Ross 867 from the full visibility data set. When splitting an observation up into N time slices of equal duration, the theoretical sensitivity in a single time slice image is worse by a factor of \sqrt{N} as compared to the full time range. We used this scaling to determine the minimum size of each time slice and the depth to which we deconvolve (CLEAN) the time slice image.

After making a time series of images per data set, we measured the flux density of Ross 867 and NVSS J171949+263007 by integrating over tight apertures (2.5 times the theoretical beam size of each image) around measured peak position for each source. By measuring the flux density in each time slice, we attempted to construct radio light curves of Ross 867 for the available observations. This worked best for the GMRT observations at 610 MHz because of significant signal-to-noise limitations in the other observations. At 610 MHz, the flux measurements on the reference source NVSS J171949+263007 show a mild (<10 percent) variation over time, which can be attributed to (1) limited image quality per snapshot, and (2) higher-order primary-beam effects, as we explain as follows. First, our snapshots are very short observations yielding poor UV-coverage (due to earth rotation), which leads to less accurate flux density measurements. Second, instrumental amplitude variations of a few percent may be expected as the beam patterns of all antennas in the interferometer cannot be

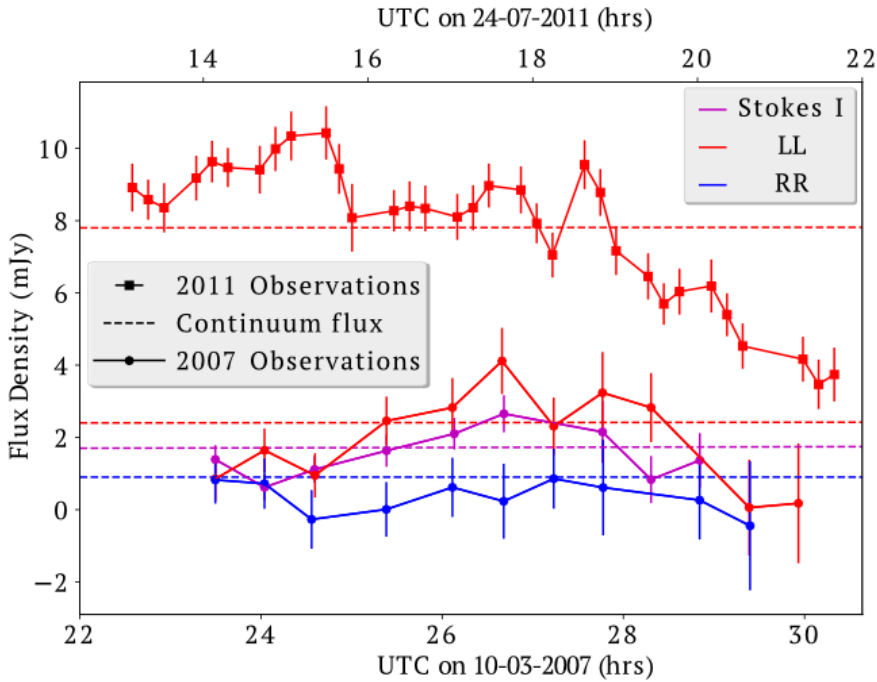


Figure 5.1: Comparison between radio light curves of Ross 867 as measured with the GMRT at 610 MHz during observations in 2007 (lower six curves and axis) and 2011 (upper two curves and axis). All neighboring points are connected with lines to help guide the eye. The vertical error bars represent the flux density measurement uncertainties. The time ranges of the snapshot image in which the flux measurement was made were ~ 0.40 and ~ 0.15 hours for the 2007 and 2011 observations respectively, and are shown as horizontal error bars in the legend. The dashed horizontal lines indicate the average continuum flux density of Ross 867 as measured in the image from the full time range.

assumed to be same, specially far from the the pointing center (RXJ1720.1+2638) where Ross 867 and the reference source are located.

We have corrected the snapshot flux density measurements of Ross 867 by multiplying them with the full/snapshot flux ratios of the reference source; for which we are making the assumption that its flux density does not change on a timescale of hours. Figure 5.1 shows the resulting light curves from the two available 610 MHz observations, with a peak flux of 10.4 ± 0.7 mJy/beam in 2011. The time resolution of the 2007 radio light curve is about three times worse than the 2011 radio light curve due to signal-to-noise limitations.

5.4 Discussion

5.4.1 Identical stellar origin

The recent *Gaia* DR2 measurements (Table 5.1) show that Ross 867 and Ross 868 have equal distance within the errors. Moreover, their relative velocity is 0.7 ± 0.3 km s⁻¹ and their separation is 179.3 ± 0.1 AU in projection. Their large separation allows us to argue that they are not magnetically interacting since the magnetosphere of such stars cannot extend further than approximately five stellar radii (Güdel 2002). Therefore, their flare emissions can arguably be studied as independent events from similar stellar sources. Furthermore, although the age estimates for Ross 867-8 have large margins (Table 5.1), their similar peculiar 3D motion, spectral type and orbital separation strongly suggest that both stars are coeval—likely related within the Hyades group, Nakajima et al. (2010); Shkolnik et al. (2012)—, which establishes another constraint for the flaring-age relation of dwarfs in open clusters (Ilin et al. 2019).

5.4.2 Nature of the flare emission

Since the GMRT observations obtained in 2011 were only recorded at *LL* polarization, we can not establish if the emission from Ross 867 was circularly polarized at that epoch. However, the observations made in 2007 at 325 and 610 MHz with the GMRT indicate that the emission is indeed polarized (see Fig. 5.1). While we lack the cross-polarization terms in our 610 MHz observation, we can argue that stellar emission is likely not linearly-polarized (e.g. Villadsen & Hallinan 2019). With this assumption, we infer that the 610 MHz emission from Ross 867 in 2011 is $\sim 40\%$ circularly polarized. We also estimate that the brightness temperature of the emission is $> 0.7 \times 10^{12}$ K—assuming that the emission site is the entire photosphere—meaning that it is unlikely to be gyrosynchrotron emission (Melrose & Dulk 1982; Dulk 1985). Therefore, the emission coming from Ross 867 is likely caused by a coherent process, either electron cyclotron maser instability or plasma emission. Furthermore, the emission detected in 2011 at 610 MHz shows that the flare emission lasted for at least seven hours, which is longer than usual for flares of this type (Lynch et al. 2017), but still consistent with timescales for coherent emission on M dwarfs (Slee et al. 2003; Villadsen & Hallinan 2019). It is possible that Ross 867 is already a fully convective star, explaining the polarized flare emission detected, whereas Ross 868 would still have a radiative core. However, note that non-fully convective stars (e.g. the Sun) can also produce strongly polarized emission from plasma emission (Bastian et al. 1998).

5.4.3 Historical radio observations

We have extensively reviewed archival data from several radio observatories for the field of view that contains Ross 867-8. Table 5.4 displays technical information for each data set

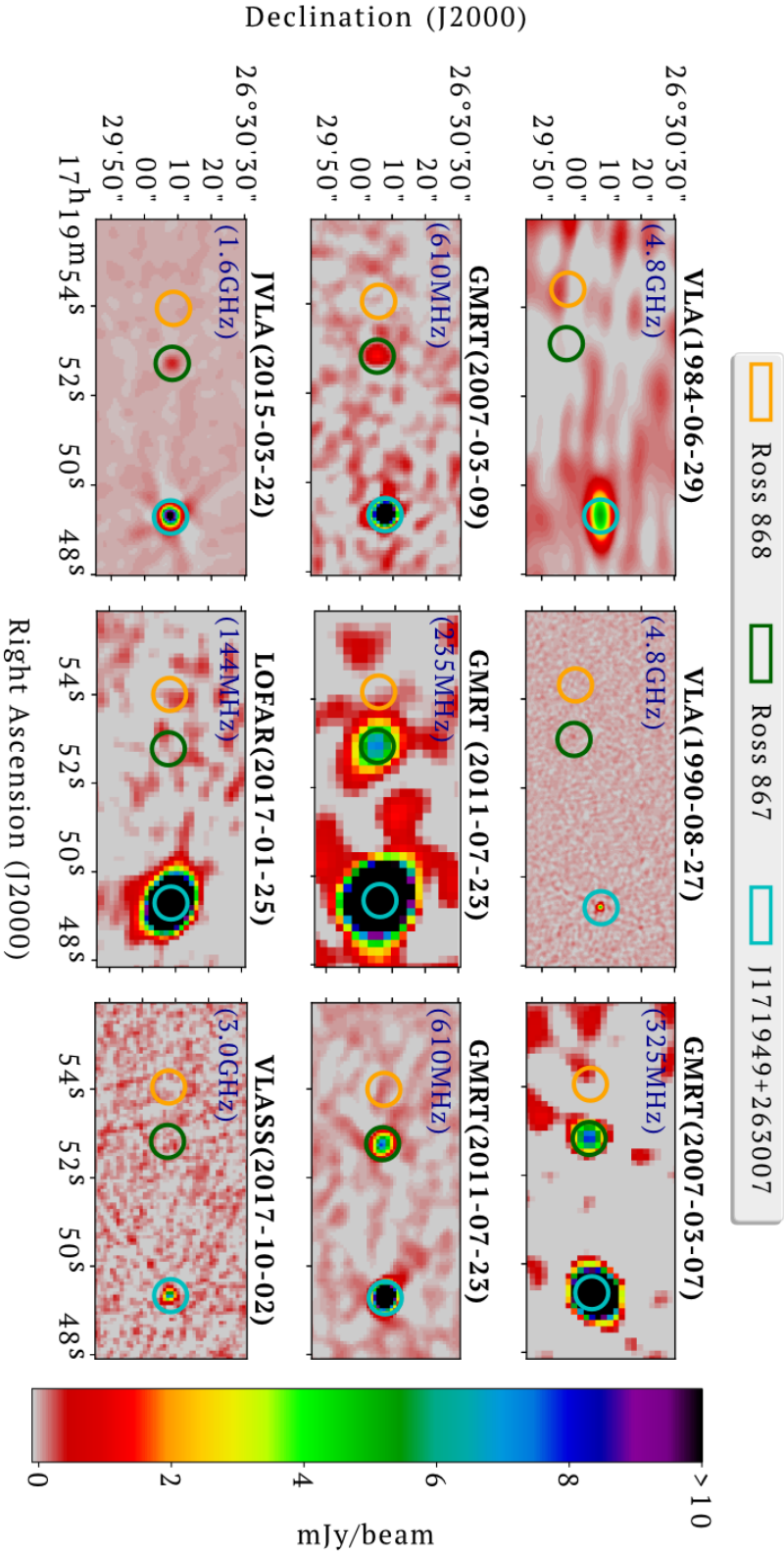


Figure 5.2: Multiple radio observations at different epochs and frequencies of the field of view that contains Ross 867, Ross 868 and NVSS J171949+263007 (orange, green and light blue apertures, respectively). Although Ross 867 shows stellar activity at different epochs and frequencies, its similar binary (Ross 868) remains undetectable at all epochs and radio frequencies. The apertures were estimated assuming the proper motions measured by *Gaia* for each observed date. Table 5.2 displays technical information for each data set inspected.

inspected, and Figure 5.2 shows the field of view from different radio observatories at several epochs and frequencies, where the expected positions at each observational time for Ross 867 and Ross 868 (assuming the proper motion measured by *Gaia* DR2) are highlighted. Since in all observations Ross 868 was undetected, we only relate below on Ross 867 detection.

A candidate radio detection of Ross 867 with Arecibo at 430 MHz ($\sim 10'$ resolution) was first reported by Spangler (1976), but given the high flux density reported (320 ± 90 mJy), and the vicinity of a bright extragalactic radio source (NVSS J171949+263007) at $0.8'$ distance from Ross 867 as seen in higher-resolution observations, this is likely an incorrect association. About a decade later, the same region was observed with the VLA four times in 1984 and 1986. Ross 867 was not detected in the observation made in 1984, likely related to dynamic range limitations. Then, for the observations made in February and July of 1986, White et al. (1989) reported that Ross 867 was marginally detected (0.69 and 0.71 mJy at C and L band, respectively) only in the first observation. For the observations made in August 1986, Jackson et al. (1987) established that Ross 867 is a radio-loud source at 1.4 and 4.8 GHz. They report stokes I flux densities of 0.69 ± 0.13 and 0.51 ± 0.13 mJy, respectively. In all observations made in 1986, no significant circularly polarized emission (stokes V) nor time-variability of the radio emission was detected. More recently, two observations using JVLA and LOFAR were made in 2015 and 2017 at 1.6 and 0.14 GHz, respectively. Although the JVLA observed a flux density emission of 0.38 ± 0.02 mJy from Ross 867, there was no significant detection of circularly polarized emission. Ross 867 was not detected in the LOFAR observation (part of the LOFAR Two-metre Sky Survey, LoTSS, Shimwell et al. 2017) at 144 MHz, which could be caused by local dynamic range limitations in the presence of the bright radio source (NVSS J171949+263007) that was used as the reference source in this study (Figure 5.2). Additional details of the LOFAR observation are presented in Appendix 5.6.2. Finally, preliminary results from the The Karl G. Jansky Very Large Array Sky Survey (VLASS¹, Lacy et al. 2019) show that there was no detection of either dwarfs in Ross 867-8 at S-band for the observations made in 2017, likely associated with low effective integration time (5 seconds).

5.4.4 Probability of observing during a non-flaring event

Given our time sampling, one could consider that by chance we only detected Ross 867 despite Ross 868 being radio active too. To assess the possibility that in eleven radio observations made at different times (Table 5.4) we have observed Ross 868 during non-flaring states, we assume that flare events follow a Poisson distribution (Gehrels 1986; Pettersen 1989) and Ross 868 has similar flaring properties (rates, flux density, etc.) to those of Ross 867. Under this assumption, we find that the probability of detecting Ross 868 at least once in those eleven observations should be $> 99\%$. Therefore, since we do not detect Ross 868, it is unlikely that Ross 868 is as radio active as Ross 867.

5.4.5 Comparison of stellar properties with respect to a similar binary system

UV Ceti is one of the most studied dwarf binary systems with flare emissions, where both stars are similar and one of the stars is radio loud while the companion remains radio undetectable for some observations. The physical processes behind the flare emission are found to be different for each star, as flares in UV Cet A seem to be radio-loud and highly circularly polarized, implying coherent emission mechanisms; whereas UV Cet B shows polarized gyrosyn-

¹<https://science.nrao.edu/science/surveys/vlass>

chrotron flares and periodic coherent bursts (Benz et al. 1998; Bingham et al. 2001; Villadsen & Hallinan 2019; Zic et al. 2019). However, if we compare UV Ceti with Ross 867-8, the latter presents several particular characteristics, which we highlight below.

1. The substantial X-ray emission difference between UV Ceti A and B has been taken as one of the factors that could be related to the different radio emission due to chromospheric activity (see e.g., Audard et al. 2003). Given this fact, we have recalculated the X-ray emission for Ross 867 and Ross 868 from XMM Newton and Chandra observations (see Table 5.1). It has been found that the dwarfs in Ross 867-8 are equally bright in X-rays, and therefore, it is unlikely that there is a one-to-one relation between X-ray and radio activity for both stellar components.
2. Since UV Ceti is closer to the Sun than Ross 867-8, it offers higher angular resolution observations. However, although UV Ceti's orbital separation of ~ 5 AU separation is too large for a shared magnetosphere, stellar wind interactions are possible, and hence, there has been a tentative claim of sympathetic flaring (Panagi & Andrews 1995). In contrast, since Ross 867-8 has 100 times greater separation than the UV Ceti binary system, any energy flux between the two stars due to stellar wind or other magnetic processes is reduced by a factor of 10^4 , making it highly unlikely that binary magnetic interaction causes detectable effects in the stellar activity.
3. Berger (2002) has studied the flaring radio activity in rotating M and L stars, concluding that the rotation is crucial in determining the physical process behind the flare emission. In this sense, Audard et al. (2003) first suggested that for UV Ceti the stellar rotation could play an important role, as UV Ceti A is a rapid rotator ($V \sin i = 58 \text{ km s}^{-1}$), while the companion lacked rotation measurements at that time. However, Barnes et al. (2017) have recently measured rotation periods for the UV Ceti system finding that both stars are rapid rotators with similar values (i.e, $V \sin i = 28.6 \pm 0.2$ and $32.2 \pm 0.2 \text{ km s}^{-1}$). For Ross 867-8, discrepancies in the rotation period measurements have also been reported. For Ross 868, Kiraga & Stepień (2007) reported a rotation period of 0.950 days ($V \sin i \sim 28.5 \text{ km s}^{-1}$) based on photometric observations, which was debated by Houdebine & Mullan (2015) who obtained 1.86 km s^{-1} using a cross-correlation technique for a selected narrow spectral range. This same technique was also used by López-Santiago et al. (2010) and Houdebine et al. (2017) obtaining 1.0 and 6.30 km s^{-1} , respectively. Moreover, using high-resolution spectra, Reiners et al. (2012) reported $< 4.0 \text{ km s}^{-1}$, which was later measured by Moutou et al. (2017) who reported 3.20 km s^{-1} .

For Ross 867, an upper limit of $\leq 10 \text{ km s}^{-1}$ was established by Jenkins et al. (2009), which was later refined by Jeffers et al. (2018) to 6.79 km s^{-1} . If we do not consider the rotation velocity measured by Kiraga & Stepień (2007), Ross 867 and Ross 868 can be both categorized as slow rotators (different to what has been found for UV Ceti A), however, we cannot confirm this similarity between the dwarfs given the different values reported, and the unknown inclination angles (i) that affect the rotation velocity estimates. Additional high-resolution spectra of Ross 867-8 are necessary to confirm this hypothesis.

4. Another speculation suggested for the changes observed in radio activity in M dwarf binary systems (as NLTT33370 and UV Ceti, Williams et al. 2015; Kochukhov & Lavail 2017, respectively) is related with the differences in magnetic morphology. For late

M dwarfs ($\geq M6$), there is evidence that they can have two different types of magnetic field morphology, i.e., a strong global dipole field or a weaker multipolar field (Morin et al. 2010; Gastine et al. 2013). The strong dipole field might play a role in generating radio emission (see e.g., for modeling and observations, Nichols et al. 2012; Hallinan et al. 2015; Kao et al. 2016; Leto et al. 2016; Kuzmychov et al. 2017; Turnpenney et al. 2017), but this dynamo bistability so far has only been observed for late M dwarfs. Given that the stars in Ross 867-8 are both mid-M dwarfs, they could provide a test of the theory that magnetic morphology indeed causes the differences in the radio emission observed. In this sense, the binary system Ross 867-8 is a potential target for spectropolarimetric observations (Zeeman Doppler Imaging) in order to enlighten the role of the magnetic morphology in the radio activity observed in the stellar atmosphere of mid-M dwarfs. Moreover, considering the differences in stellar mass between the dwarfs in Ross 867-8, it is possible that Ross 867 has a fully convective core, while Ross 868 has a part-radiative and part-convective core (see Section 5.4.2). Such situation will drive a different dynamo that could lead to different magnetic field topologies (Browning & K. 2007; Yadav et al. 2016), and therefore, different radio activity (McLean et al. 2012).

5.5 Summary and conclusions

The radio emission from Ross 867 was serendipitously rediscovered by us while inspecting GMRT data at $\sim 8'$ from the field center (galaxy cluster RXJ1720.1+2638, Giacintucci et al. 2014; Savini et al. 2019). Comparing two separate observations at 610 MHz from 2007 and 2011, we noticed that one of the radio sources shifted its position between the epochs by about $2''$, and changed a factor of ~ 4 in flux density. After ruling out any astrometric or flux density calibration errors, we found that the variable radio emission coincided with the sky position of Ross 867 at the times of observation.

We noted that Ross 867 forms part of a binary system with Ross 868. Both stars shared the same stellar origin and are identical in terms of spectral type, age, high 3D motion, infrared, optical and X-ray emission. However, after inspecting radio observations of this system, ranging from 1984 to 2017, Ross 868 remains undetected, which was confirmed to be improbable that Ross 868 was not flaring at any observation. In contrast, Ross 867 displays radio variability likely associated with a coherent process given the radio circular polarized emission detected, and the brightness temperature estimated ($> 0.7 \times 10^{12}$ K).

Dwarf binaries with similar companions showing radio flares (where one of the stars is radio loud while the companion remains radio undetectable) are limited to two known similar cases (as NLTT33370 and UV Ceti, Williams et al. 2015; Kochukhov & Lavail 2017, respectively). Nevertheless, the binary system Ross 867-8 presents a case with closer stellar features between the dwarfs when it is compared to UV Ceti and NLTT33370, where the most remarkable difference is their rotational component, which lacks convincing measurements. Moreover, given its large orbital separation (> 180 AU), we can discard any magnetic or tidal interaction that could contaminate the independent physical interpretation of the radio activity present in each dwarf. We conclude that there are two intriguing possibilities for such difference in radio activity, like observed in Ross 867-8, namely (1) a different magnetic field topology or (2) a vastly different dynamo. These are linked to the rotation component that is measured as $V \sin i$, so the Rossby number would be a more appropriate parameter given the lack of measurements for the inclination angle (i) (see e.g., McLean et al. 2012)—. Finally, by observing Ross 867-8, there is a unique opportunity to disentangle the stellar properties

that are linked to the flare emission at radio wavelengths. Further wide-band and higher angular resolution observations of the binary system Ross 867-8 are already scheduled, and their results are expected to be promising for the radio stellar field.

Acknowledgements. We sincerely thank the anonymous referee for making valuable suggestions that have improved the paper. In addition, we thank the staff of the GMRT that made these observations possible. GMRT is run by the National Centre for Radio Astrophysics of the Tata Institute of Fundamental Research. LOFAR is the Low Frequency Array designed and constructed by ASTRON. It has observing, data processing, and data storage facilities in several countries, which are owned by various parties (each with their own funding sources), and which are collectively operated by the ILT foundation under a joint scientific policy. The ILT resources have benefitted from the following recent major funding sources: CNRS-INSU, Observatoire de Paris and Universit   d'Orl  ans, France; BMBF, MIWF-NRW, MPG, Germany; Science Foundation Ireland (SFI), Department of Business, Enterprise and Innovation (DBEI), Ireland; NWO, The Netherlands; The Science and Technology Facilities Council, UK; Ministry of Science and Higher Education, Poland. This research made use of the Dutch national e-infrastructure with support of the SURF Cooperative (e-infra 180169) and the LOFAR e-infra group. The J  lich LOFAR Long Term Archive and the German LOFAR network are both coordinated and operated by the J  lich Supercomputing Centre (JSC), and computing resources on the Supercomputer JUWELS at JSC were provided by the Gauss Centre for Supercomputing e.V. (grant CHTB00) through the John von Neumann Institute for Computing (NIC). The University of Hertfordshire high-performance computing facility and the LOFAR-UK computing facility located at the University of Hertfordshire and supported by STFC [ST/P000096/1]. This work also has made use of data from the European Space Agency (ESA) mission *Gaia*², processed by the *Gaia* Data Processing and Analysis Consortium (DPAC³). Funding for the DPAC has been provided by national institutions, in particular the institutions participating in the *Gaia* Multilateral Agreement. This research has made use of the SIMBAD database, operated at CDS, Strasbourg, France. L.H.Q.-N. deeply thanks Dr. L.O. Sjouwerman at NRAO Socorro for the support reducing archival VLA observations.

5.6 Appendix

5.6.1 SPAM pipeline for GMRT data on Ross 867-868

The SPAM pipeline converts the observations into Stokes I visibilities in an early stage of the processing. This conversion is done on a best effort basis, meaning that if RR and LL are both available, Stokes I is formed through $I=(RR+LL)/2$, while if just one of RR or LL is available, $I=RR$ or $I=LL$, respectively. Using the pipeline, we generated calibrated Stokes I visibilities and images for all observations.

In addition, the SPAM pipeline derives flux density, bandpass, and instrumental phase calibrations from a primary calibrator (typically 3C 48 or 3C 147) and applies these to the target field data (in our case RXJ1720.1+2638). Then it self-calibrates and images the target field data several times, initially bootstrapping to an externally supplied radio sky model, and ultimately applies SPAM ionospheric calibration to correct for direction-dependent phase errors (for details, see Intema et al. 2009). For the initial (phase-only) self-calibration of the 235 MHz observations, we bootstrapped to a radio sky model derived from the GMRT 150 MHz all-sky survey (TGSS; Intema et al. 2017). For every higher frequency, we bootstrapped to an image model derived from the frequency just below it, e.g., a source model from the 235 MHz image was used for bootstrapping the 325 MHz observations, etc. This

²<https://www.cosmos.esa.int/gaia>

³<https://www.cosmos.esa.int/web/gaia/dpac/consortium>

has proven to work well because of the relatively small distance in frequency between adjacent bands and the simple nature of the majority of radio sources, generally providing a good match in terms of resolution, flux density and sensitivity. Also, the larger field-of-view at the lower frequency guarantees a model that fully encloses the higher frequency observation.

5.6.2 LOFAR observations

The LOFAR data was observed as part of the LOFAR Two-metre Sky survey (LoTSS; Shimwell et al. 2017, 2019), pointing P260+28 in project ID LC7_024. Initially the data were processed on LOFAR archive compute facilities (e.g., Mechev et al. 2017) using PreFactor which is the standard LOFAR direction independent calibration pipeline (see van Weeren et al. 2016; Williams et al. 2016) which corrects for direction independent effects such as the band-pass (e.g., De Gasperin et al. 2019). After this, direction dependent calibration was performed to remove the ionospheric errors that are severe at low radio frequencies and to correct for errors in the LOFAR beam model. The direction dependent calibration was performed using the LoTSS processing pipeline⁴ that makes use of kMS (Tasse 2014; Smirnov & Tasse 2015) and DDFacet (e.g., Tasse et al. 2018) for calibration and imaging whilst applying direction dependent solutions.

5.6.3 Radio observations for NVSS J171949+263007 and for Ross 867-8

⁴<https://github.com/mhardcastle/ddf-pipeline>

Table 5.3: Observation details for the source NVSS J171949+263007 (0.8' west of Ross 867) reported in the NVSS and FIRST surveys. The source NVSS J171949+263007 was used as a reference source.

Survey	$\alpha, \delta^{(3)}$ (J2000)	Flux density (mJy)	Major ⁽⁴⁾ (arcsec)	Minor ⁽⁴⁾ (arcsec)	PA ⁽⁴⁾ (degrees)	Mean Epoch ⁽⁵⁾ (year)
FIRST ⁽¹⁾	17 ^h 19 ^m 49.314 ^s +26°30'07.69''	17.9 ± 0.9	5.52	5.37	172.8	1995.874
NVSS ⁽²⁾	17 ^h 19 ^m 49.24 ^s +26°30'07.2''	17.3 ± 0.6	<19.0	<18.3	-	1995±2.0

Notes. (1) Faint Images of the Radio Sky at Twenty-Centimeters (FIRST) survey was made using the NRAO Very Large Array (VLA) producing images with 1.8'' pixels, a typical rms of 0.15 mJy, and a resolution of 5 arcseconds (White et al. 1997). (2) The NRAO VLA Sky Survey (NVSS) was made at 1.4 GHz with a resolution of 45 arcseconds and a limiting peak source brightness of about 2.5 mJy/beam (Condon et al. 1998). (3) Source position right ascension (α) and declination (δ) in sexagesimal notation. (4) Source major axis, minor axis and position angle measured directly from map before deconvolving synthesized beam. No PA reported for NVSS observation.

Table 5.4: Historical observation details for the field of view that contains Ross 867-8.

Date Observation (YYYY-MM-DD)	Telescope	Frequency (MHz)	Bandwidth (MHz)	Correlations parameters	Time (min)	Sensitivity ⁽¹⁾ (-Jy)	S ⁽²⁾ (mJy)	Resolution ⁽³⁾
1984-06-29	VLA	4,860	100	RR,LL,RL,LR	141	81	ND ⁽⁴⁾	11.7''×4.7'' (-89°)
1986-02-10	VLA	1,540	50	RR,LL,RL,LR	50	250	NA ⁽⁵⁾	NA ⁽⁵⁾
1986-07-10	VLA	1,465	50	RR,LL,RL,LR	27	NA ⁽⁵⁾	NA ⁽⁵⁾	NA ⁽⁵⁾
1986-08-06	VLA	1,464	50	RR,LL,RL,LR	24	NA ⁽⁵⁾	NA ⁽⁵⁾	NA ⁽⁵⁾
		4,760	50	RR,LL,RL,LR	15	NA ⁽⁵⁾	NA ⁽⁵⁾	NA ⁽⁵⁾
1990-08-27	VLA	1,565	100	RR,LL,RL,LR	67	320	ND ⁽⁴⁾	4.2''×4.0'' (-65°)
		4,785	100	RR,LL,RL,LR	64	38	0.20±0.04	1.32''×1.20'' (-45°)
		8,515	100	RR,LL,RL,LR	64	42	ND ⁽⁴⁾	0.69''×0.68'' (-27°)
2007-03-08	GMRT	325	32	RR,LL	280	356	5.3±0.8	9.7''×8.4'' (-53°)
				LL		224	11.6±1.2	10.3''×8.4'' (-36°)
				RR		248	3.5±0.6	8.9''×8.6'' (-23°)
2007-03-10	GMRT	610	32	RR,LL	310	52	1.7±0.2	4.5''×3.9'' (37°)
				LL		82	2.4±0.3	4.6''×4.0'' (41°)
				RR		94	0.9±0.2	4.5''×4.2'' (13°)
2011-07-24	GMRT	235	17	LL	346	350	6.8±0.6	12.4''×10.7'' (59°)
		610	33	RR		40	7.8±0.8	5.0''×4.1'' (77°)
2015-03-22	JVLA	1,519	64	RR,LL,RL,LR	40	15	0.38±0.02	1.32''×1.20'' (-42°)
2017-01-25	LOFAR	145	48	XX,YY,XY,YX	8	200	ND ⁽⁴⁾	8.78''×6.43'' (62°)
2017-10-02	JVLA	2,988	150	RR,LL,RL,LR	0.83	124	ND ⁽⁴⁾	2.56''×2.14'' (52°)

Notes. (1) Sensitivity at the image center. (2) Flux density detected for Ross 867. Where all correlation parameters were available, the value reported corresponds to Stokes I. (3) Restoring beam major × minor axis (position angle). (4) No detection. (5) Not available: Some observations made in 1986 with the VLA did not have a flux calibrator, and were not well-centered in the target. Hence, any flux measurement is hard to interpret. We relied on what Jackson et al. (1987) and White et al. (1989) reported for these observations (see Section 5.4.3).

Bibliography

- Amado, P. J., Suárez, J. C., Moya, A., et al. 2004, *A&A*, 414, 163
- Andrae, R., Fouesneau, M., Creevey, O., et al. 2018, *A&A*, 616, A8
- Antoja, T., Helmi, A., Romero-Gómez, M., et al. 2018, *Nature*, 561, 360
- Asaki, Y., Imai, H., Sobolev, A. M., & Yu Parfenov, S. 2014, *ApJ*, 787, 54
- Audard, M., Gudel, M., & Skinner, S. L. 2003, *ApJ*, 589, 983
- Baade, W. 1951, *Publ. Michigan Obs.*, 10, 7
- Babusiaux, C. & Gilmore, G. 2005, *MNRAS*, 358, 1309
- Bailer-Jones, C. A. L. 2015, *PASP*, 127, 994
- Bailer-Jones, C. A. L., Rybizki, J., Fouesneau, M., Mantelet, G., & Andrae, R. 2018, *AJ*, 156, 58
- Barnes, J. R., Jeffers, S. V., Haswell, C. A., et al. 2017, *MNRAS*, 471, 811
- Bastian, T. S., Benz, A. O., & Gary, D. E. 1998, *ARA&A*, 36, 131
- Battersby, C., Bally, J., & Svoboda, B. 2017, *ApJ*, 835, 263
- Becker, W. & Fenkart, R. 1970, in *IAU Symposium, Vol. 38, Proc. Int. Astron. Union*, ed. W. Becker & G. I. Kontopoulos, 205
- Belokurov, V., Erkal, D., Deason, A. J., et al. 2017, *MNRAS*, 466, 4711
- Belokurov, V., Sanders, J. L., Fattahi, A., et al. 2019, *ArXiv e-prints* 1909.04679, 1909.04679
- Benz, A. O., Conway, J., & Güdel, M. 1998, *A&A*, 331, 596
- Berger, E. 2002, *ApJ*, 572, 503
- Bingham, R., Cairns, R. A., & Kellett, B. J. 2001, *A&A*, 370, 1000
- Bland-Hawthorn, J. & Gerhard, O. 2016, *ARAA*, 54, 529
- Bland-Hawthorn, J., Sharma, S., Tepper-Garcia, T., et al. 2019, *MNRAS*, 486, 1167
- Blitz, L. & Spergel, D. N. 1991, *ApJ*, 379, 631
- Bobylev, V. V. & Bajkova, A. T. 2016, *Astronomy Letters*, 42, 182
- Bochanski, J. J., West, A. A., Hawley, S. L., & Covey, K. R. 2007, *AJ*, 133, 531
- Bonnarel, F., Fernique, P., Bienaymé, O., et al. 2000, *A&AS*, 143, 33
- Bovy, J. & Rix, H.-W. 2013, *ApJ*, 779, 115
- Breen, S. L., Ellingsen, S. P., Contreras, Y., et al. 2013, *MNRAS*, 435, 524

- Browning, M. & K., M. 2007, *ApJ*, 676, 1262
- Brunthaler, A., Reid, M., Menten, K., et al. 2011, *Astron. Nachrichten*, 332, 461
- Brunthaler, A., Reid, M. J., Falcke, H., Greenhill, L. J., & Henkel, C. 2005, *Science*, 307, 1440
- Burns, R. A., Handa, T., Imai, H., et al. 2017, *MNRAS*, 404, 1029
- Caillault, J.-P. & Patterson, J. 1990, *AJ*, 100, 825
- Capitanio, L., Lallement, R., Vergely, J. L., Elyajouri, M., & Monreal-Ibero, A. 2017, *A&A*, 606, A65
- Carpenter, J. M., Snell, R. L., & Schloerb, F. P. 1990, *ApJ*, 362, 147
- Caswell, J. L., Fuller, G. A., Green, J. A., et al. 2010, *MNRAS*, 404, 1029
- Caswell, J. L., Fuller, G. A., Green, J. A., et al. 2011, *MNRAS*, 417, 1964
- Chandra, P., Ray, A., & Bhatnagar, S. 2004, *ApJ*, 612, 974
- Cheng, J. Y., Rockosi, C. M., Morrison, H. L., et al. 2012, *ApJ*, 752, 51
- Chiavassa, A., Freytag, B., & Schultheis, M. 2018, *A&A*, 617, L1
- Churchwell, E., Babler, B., Meade, M., et al. 2009, *PASP*, 121, 213
- Clegg, A. W. 1993, in *Astrophysical Masers*, ed. A. W. Clegg & G. E. Nedoluha (Berlin, Heidelberg: Springer Berlin Heidelberg), 279–282
- Colom, P., Lekht, E. E., Pashchenko, M. I., & Rudnitskij, G. M. 2015, *A&A*, 575, A49
- Condon, J. J., Cotton, W. D., Greisen, E. W., et al. 1998, *AJ*, 115, 1693
- Crosley, M. K. & Osten, R. A. 2018, *ApJ*, 856, 39
- Dame, T. M., Hartmann, D., & Thaddeus, P. 2001, *ApJ*, 547, 792
- De Gasperin, F., Dijkema, T. J., Drabent, A., et al. 2019, *A&A*, 622, A5
- De Propriis, R., Rich, R. M., Kunder, A., et al. 2011, *ApJL*, 732, L36
- Dressing, C. D. & Charbonneau, D. 2013, *ApJ*, 767, 95
- Drimmel, R. 2000, *A&A*, 358, L13
- Dulk, G. 1985, *ARA&A*, 23, 169
- Dwek, E., Arendt, R. G., Hauser, M. G., et al. 1995, *ApJ*, 445, 716
- Efremov, Y. N. 2011, *Astronomy Reports*, 55, 108
- Eiroa, C., Casali, M., Miranda, L., & Ortiz, E. 1994, *A&A*, 290, 599
- Elitzur, M. 1992, *ARA&A*, 30, 75
- Farnes, J. S. 2014, *NCRA Tech. Rep.*, 2

- Fish, V. L., Briskeen, W. F., & Sjouwerman, L. O. 2006, *ApJ*, 647, 418
- Gaia-Collaboration, Brown, A. G. A., Vallenari, A., et al. 2018, *A&A*, 616, A1
- Gaia Collaboration, Brown, A. G. A., Vallenari, A., et al. 2016a, *A&A*, 595, A2
- Gaia Collaboration, Prusti, T., de Bruijne, J., et al. 2016b, *A&A*, 595, A1
- Gastine, T., Morin, J., Duarte, L., et al. 2013, *A&A*, 549, L5
- Gehrels, N. 1986, *ApJ*, 303, 336
- Georgelin, Y. M. & Georgelin, Y. P. 1976, *A&A*, 49, 57
- Ghez, A., Morris, M., Becklin, E., Tanner, A., & Kremenek, T. 2000, *Nature*, 407, 349
- Giacintucci, S., Markevitch, M., Brunetti, G., et al. 2014, *ApJ*, 795, 73
- Gilmore, G. & Reid, N. 1983, *MNRAS*, 202, 1025
- Godbout, S., Joncas, G., Durand, D., & Arsenault, R. 1997, *ApJ*, 478, 271
- Gómez, F. A., Minchev, I., O'Shea, B. W., et al. 2012, *MNRAS*, 423, 3727
- Goodman, A. A., Alves, J., Beaumont, C. N., et al. 2014, *ApJ*, 797, 53
- Grady, J., Belokurov, V., & Evans, N. W. 2019, *MNRAS*, 483, 3022
- Green, J. A., Caswell, J. L., Fuller, G. A., et al. 2009, *MNRAS*, 392, 783
- Green, J. A., Caswell, J. L., Fuller, G. A., et al. 2010, *MNRAS*, 409, 913
- Green, J. A., Caswell, J. L., Fuller, G. A., et al. 2012, *MNRAS*, 420, 3108
- Green, J. A., Caswell, J. L., McClure-Griffiths, N. M., et al. 2011, *ApJ*, 733, 27
- Green, J. A. & McClure-Griffiths, N. M. 2011, *MNRAS*, 417, 2500
- Groenewegen, M. A. & Sloan, G. C. 2018, *A&A*, 609
- Güdel, M. 2002, *ARA&A*, 40, 217
- Habing, H., Sevenster, M., Messineo, M., van de Ven, G., & Kuijken, K. 2006, *A&A*, 458, 151
- Habing, H. J. 1996, *A&A*, 7, 97
- Hachisuka, K., Brunthaler, A., Menten, K. M., et al. 2009, *ApJ*, 696, 1981
- Hachisuka, K., Choi, Y. K., Reid, M. J., et al. 2015, *ApJ*, 800, 2
- Hallinan, G., Littlefair, S. P., Cotter, G., et al. 2015, *Nature*, 523, 568
- Helmi, A., Babusiaux, C., Koppelman, H. H., et al. 2018, *Nature*, 563, 85
- Henry, T. J., Jao, W., Subasavage, J. P., et al. 2006, *AJ*, 132, 2360
- Herrnstein, J., Moran, J., Greenhill, L., et al. 1999, *Nature*, 400, 539

- Heydari-Malayeri, M., Testor, G., Baudry, A., Lafon, G., & de La Noe, J. 1982, *A&A*, 113, 118
- Heyer, M. & Dame, T. 2015, *ARA&A*, 53, 583
- Höfner, S. & Olofsson, H. 2018, *A&AR*, 26, 1
- Hollenbach, D., Elitzur, M., & McKee, C. F. 2013, *ApJ*, 773, 70
- Honig, Z. N. & Reid, M. J. 2015, *ApJ*, 800, 53
- Honma, M. 2013, *New Trends Radio Astron ALMA Era 30th Anniv Nobeyama Radio Obs Proc a Symp held Hakone*, 476, 81
- Honma, M., Bushimata, T., Choi, Y. K., et al. 2007, *PASJ*, 59, 889
- Honma, M., Hirota, T., Kan-Ya, Y., et al. 2011, *PASJ*, 63, 17
- Honma, M., Nagayama, T., Ando, K., et al. 2012, *PASJ*, 64, 136
- Honma, M., Nagayama, T., & Sakai, N. 2015, *PASJ*, 67, 70
- Houdebine, E. R. 2012, *MNRAS*, 421, 3180
- Houdebine, E. R. & Mullan, D. J. 2015, *ApJ*, 801
- Houdebine, E. R., Mullan, D. J., Bercu, B., Paletou, F., & Gebran, M. 2017, *ApJ*, 837, 96
- Houdebine, E. R., Mullan, D. J., Paletou, F., & Gebran, M. 2016, *ApJ*, 822, 97
- Howard, C. D., Rich, R. M., Reitzel, D. B., et al. 2008, *ApJ*, 688, 1060
- Hubble, E. P. 1926, *ApJ*, 64, 321
- Hubble, E. P. 1929, *ApJ*, 69, 103
- Humphreys, R. 1976, *PASP*, 88, 647
- Ibata, R. A., McConnachie, A., Cuillandre, J.-C., et al. 2017, *ApJ*, 848, 129
- Ilin, E., Schmidt, S. J., Davenport, J. R. A., & Strassmeier, K. G. 2019, *A&A*, 622, A133
- Intema, H. T., Jagannathan, P., Mooley, K. P., & Frail, D. A. 2017, *A&A*, 598, A78
- Intema, H. T., van der Tol, S., Cotton, W. D., et al. 2009, *A&A*, 501, 1185
- Ita, Y., Tanabé, T., Matsunaga, N., et al. 2004, *MNRAS*, 347, 720
- Jackson, P. D., Kundu, M. R., & White, S. M. 1987, in *Cool Stars. Stellar Syst. Sun* (Berlin, Heidelberg: Springer), 103–105
- Jackson, T., Ivezić, Ž., & Knapp, G. R. 2002, *MNRAS*, 337, 749
- Jacobson, H. R., Pilachowski, C. A., & Friel, E. D. 2011, *AJ*, 142, 59
- Jeffers, S. V., Schöfer, P., Lamert, A., et al. 2018, *A&A*, 614, A76
- Jenkins, J. S., Ramsey, L. W., Jones, H. R., et al. 2009, *ApJ*, 704, 975

- Jiang, Z., Yao, Y., & Yang, J. 2003, *ApJ*, 596, 1064
- Joshi, S. & Chengalur, J. 2010, in *Proc. Sci. ISKAF2010*, Vol. 112
- Kao, M. M., Hallinan, G., Pineda, J. S., et al. 2016, *ApJ*, 818, 24
- Katarzyński, K., Gawroński, M., & Goździewski, K. 2016, *MNRAS*, 461, 929
- Kent, S. M. 1986, *AJ*, 91, 1301
- Kettenis, M., van Langevelde, H. J., Reynolds, C., & Cotton, B. 2006, *Astron. Data Anal. Softw. Syst. XV ASP Conf. Ser.*, 351, 497
- Kiraga, M. & Stepień, K. 2007, *Acta Astron.*, 57, 149
- Kochukhov, O. & Lavail, A. 2017, *ApJ*, 835, L4
- Koo, B. C., Park, G., Kim, W. T., et al. 2017, *PASP*, 129, 094102
- Krishnan, V., Ellingsen, S. P., Reid, M. J., et al. 2017, *MNRAS*, 465, 1095
- Krishnan, V., Ellingsen, S. P., Reid, M. J., et al. 2015, *ApJ*, 805, 129
- Kunder, A., Koch, A., Michael Rich, R., et al. 2012, *AJ*, 143
- Kuzmychov, O., Berdyugina, S. V., & Harrington, D. M. 2017, *ApJ*, 847, 60
- Lacy, M., Baum, S. A., Chandler, C. J., et al. 2019, *ArXiv e-prints*, arXiv:1907.01981
- Lallement, R., Babusiaux, C., Vergely, J. L., et al. 2019, *A&A*, 625, A135
- Lasker, B. M. & McLean, B. J. 1994, *STSci Newsl.* 11, 2, 39
- Lebzelter, T., Trabucchi, M., Mowlavi, N., et al. 2019, *A&A*, 631, A24
- Lekht, E. E., Pashchenko, M. I., & Berulis, I. I. 2001a, *Astron. Reports Transl. from Astron. Zhurnal Orig. Russ. Text Copyr. c*, 45, 949
- Lekht, E. E., Silant'ev, N. A., Mendoza-Torres, J. E., Pashchenko, M. I., & Krasnov, V. V. 2001b, *A&A*, 377, 999
- Leto, P., Trigilio, C., Buemi, C. S., et al. 2016, *MNRAS*, 459, 1159
- Lewis, M., Pihlstrom, Y., Sjouwerman, L., Stroh, M., & Team, B. 2018, in *Proc. Annu. New Mex. Symp.*, Vol. 34, 2
- Lian, J., Zhu, Q., Kong, X., & He, J. 2014, *A&A*, 564, A84
- Liljeström, T. & Gwinn, C. R. 2000, *ApJ*, 10, 781
- Lindblad, B. 1927a, *MNRAS*, 87, 420
- Lindblad, B. 1927b, *MNRAS*, 87, 553
- Lindgren, L. 2019, *ArXiv e-prints* 1906.09827
- Lindgren, L., Hernández, J., Bombrun, A., et al. 2018, *A&A*, 616, A2
- Litvak, M. 1969, *Science*, 165, 855

- López-Santiago, J., Montes, D., Gálvez-Ortiz, M. C., et al. 2010, *A&A*, 514, A97
- Luri, X., Brown, A. G., Sarro, L. M., et al. 2018, *A&A*, 616, A9
- Lynch, C. R., Lenc, E., Kaplan, D. L., Murphy, T., & Anderson, G. E. 2017, *ApJL*, 836, L30
- Mackereth, J. T., Bovy, J., & Schiavon, R. P. 2017, *MNRAS*, 471, 3057
- Marrese, P. M., Marinoni, S., Fabrizio, M., & Altavilla, G. 2019, *A&A*, 621, 144
- Martinez-Medina, L. A., Pichardo, B., Peimbert, A., & Carigi, L. 2017, *MNRAS*, 468, 3615
- Matsunaga, N. & Team, t. I. 2006, in *ASP Conf. Ser.*, Vol. 378, 86
- McLean, M., Berger, E., & Reiners, A. 2012, *ApJ*, 746, 23
- McWilliam, A. & Rich, R. M. 1994, *ApJS*, 91, 749
- McWilliam, A. & Zoccali, M. 2010, *ApJ*, 724, 1491
- Mechev, A., Oonk, J. B. R., Danezi, A., et al. 2017, *Proc. Int. Symp. Grids Clouds 2017*, 2
- Melrose, D. B. & Dulk, G. A. 1982, *ApJ*, 259, 844
- Messineo, M. 2004, PhD thesis, Leiden University
- Messineo, M., Habing, H. J., Sjouwerman, L. O., Omont, A., & Menten, K. M. 2018, *A&A*, 619, 35
- Min, C., Matsumoto, N., Kim, M. K., et al. 2014, *PASJ*, 66, 38
- Minier, V., Booth, R. S., & Conway, J. E. 2002, *A&A*, 383, 614
- Miyoshi, M., Asaki, Y., Wada, K., & Imai, H. 2012, *New Astron.*, 17, 553
- Moffat, A. F. J., Fitzgerald, M. P., & Jackson, P. D. 1979, *A&AS*, 38, 197
- Mohan, N. & Rafferty, D. 2015, *PyBDSF: Python Blob Detection and Source Finder*
- Monet, D. G., Dahn, C. C., Vrba, F. J., et al. 1992, *AJ*, 103, 638
- Morgan, W., Whitford, A., & Code, A. 1953, *ApJ*, 118, 318
- Morin, J., Donati, J. F., Petit, P., et al. 2010, *MNRAS*, 407, 2269
- Moutou, C., Hébrard, E. M., Morin, J., et al. 2017, *MNRAS*, 472, 4563
- Mowlavi, N., Lecoœur-Taïbi, I., Lebzelter, T., et al. 2018, *A&A*, 618, A58
- Murray, N. 2011, *ApJ*, 729, 133
- Nakajima, T., Morino, J. I., & Fukagawa, M. 2010, *AJ*, 140, 713
- Ness, M., Freeman, K., Athanassoula, E., et al. 2012, *ApJ*, 756, 22
- Ness, M. & Lang, D. 2016, *AJ*, 152, 14
- Netopil, M., Paunzen, E., Heiter, U., & Soubiran, C. 2016, *A&A*, 585, A150
- Newton, E. R., Irwin, J., Charbonneau, D., et al. 2017, *ApJ*, 834, 85

- Nichols, J. D., Burleigh, M. R., Casewell, S. L., et al. 2012, *ApJ*, 760, 59
- Oort, J. 1927, *BAN*, 3, 275
- Oort, J. H., Kerr, F., & Westerhout, G. 1958, *MNRAS*, 118, 379
- Panagi, P. M. & Andrews, A. D. 1995, *MNRAS*, 277, 423
- Pandian, J. D. 2007, PhD thesis, Cornell University
- Pandian, J. D., Goldsmith, P. F., & Deshpande, A. A. 2007, *ApJ*, 656, 255
- Pasetto, S., Natale, G., Kawata, D., et al. 2016, *MNRAS*, 461, 2383
- Perryman, M., Lindegren, L., Kovalevsky, J., et al. 1995, *A&A*, 304, 69
- Perryman, M. A. C., de Boer, K. S., Gilmore, G., et al. 2001, *A&A*, 369, 339
- Perryman, M. A. C., Lindegren, L., Kovalevsky, J., et al. 1997, *A&A*, 323, L49
- Pestalozzi, M. R., Chrysostomou, A., Collett, J. L., et al. 2007, *A&A*, 463, 1009
- Petterson, B. R. 1989, *Sol. Phys.*, 121, 299
- Pihlström, Y. M., Sjouwerman, L. O., Claussen, M. J., et al. 2018a, *ApJ*, 868, 72
- Pihlström, Y. M., Sjouwerman, L. O., Claussen, M. J., et al. 2018b, *ApJ*, 868, 72
- Pirogov, L. 1999, *A&A*, 348, 600
- Price, S. D. 1995, *Space Sci. Rev.*, 74, 81
- Quiroga-Nuñez, L. H., Van Langevelde, H. J., Reid, M. J., & Green, J. A. 2017, *A&A*, 604, 72
- Reid, M. & Honma, M. 2014, *ARA&A*, 52, 339
- Reid, M., Menten, K., Brunthaler, A., et al. 2014, *ApJ*, 783, 130
- Reid, M., Menten, K., Zheng, X., et al. 2009a, *ApJ*, 700, 137
- Reid, M. J. & Honma, M. 2014, *ARA&A*, 52, 339
- Reid, M. J., Menten, K. M., Brunthaler, A., et al. 2019, *ApJ*, 885, 131
- Reid, M. J., Menten, K. M., Brunthaler, A., et al. 2009b, *ApJ*, 693, 397
- Reiners, A., Joshi, N., & Goldman, B. 2012, *AJ*, 143, 93
- Rich, R. M., Origlia, L., & Valenti, E. 2007, *ApJL*, 665, L119
- Rix, H.-W. & Bovy, J. 2013, *A&A Rev.*, 21, 61
- Roy, S., Hyman, S. D., Pal, S., et al. 2010, *ApJL*, 712, L5
- Sakai, N., Honma, M., Nakanishi, H., et al. 2012, *PASJ*, 64, 108
- Sakai, N., Nakanishi, H., Matsuo, M., et al. 2015, *PASJ*, 67, 69
- Salaris, M., Weiss, A., Cassarà, L. P., Piovan, L., & Chiosi, C. 2014, *A&A*, 565, 9

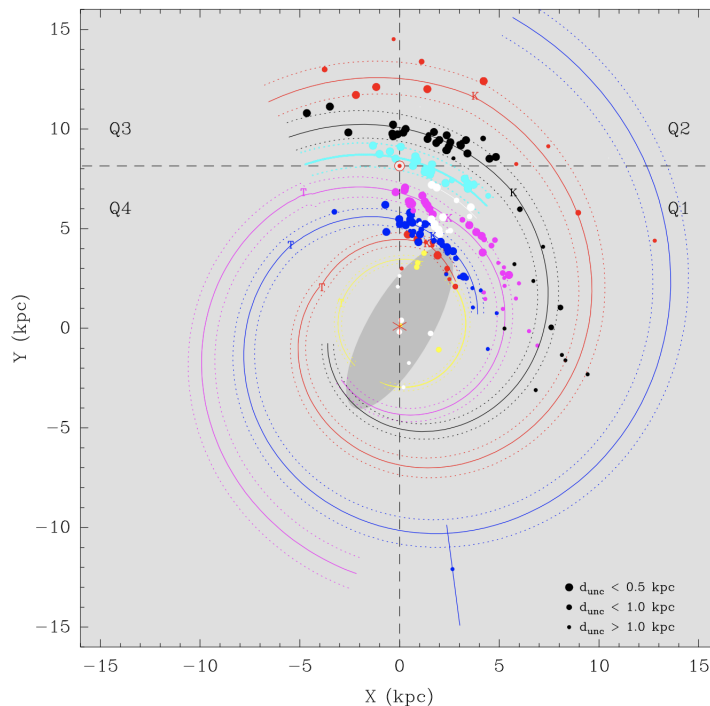
- Samus, N., Durlevich, O., & al., E. 2004, *VizieR Online Data Cat.*, II/250
- Sande, M. V. D., Decin, L., Lombaert, R., et al. 2018, *A&A*, 609, 63
- Sanna, A., Reid, M. J., Dame, T. M., Menten, K. M., & Brunthaler, A. 2017, *Sci*, 358, 227
- Sanna, A., Reid, M. J., Dame, T. M., et al. 2012, *ApJ*, 745, 82
- Sanna, A., Reid, M. J., Menten, K. M., et al. 2014, *ApJ*, 781, 108
- Savchenko, S. S. & Reshetnikov, V. P. 2013, *MNRAS*, 436, 1074
- Savini, F., Bonafede, A., Brueggen, M., et al. 2019, *A&A*, 622, A24
- Sawada-Satoh, S., Fujisawa, K., Sugiyama, K., Wajima, K., & Honma, M. 2013, *PASJ*, 65, 79
- Schödel, R., Ott, T., Genzel, R., et al. 2003, *ApJ*, 596, 1015
- Schuberth, Y., Richtler, T., Hilker, M., et al. 2010, *A&A*, 513
- Sevenster, M. N., Van Langevelde, H. J., Moody, R. A., et al. 2001, *A&A*, 366, 481
- Sharpless, S. 1959, *ApJS*, 4, 257
- Shibata, K. & Magara, T. 2011, *Living Rev. Sol. Phys.*, 8, 6
- Shimwell, T. W., Röttgering, H. J., Best, P. N., et al. 2017, *A&A*, 598, A104
- Shimwell, T. W., Tasse, C., Hardcastle, M. J., et al. 2019, *The LOFAR Two-metre Sky Survey: II. First data release*
- Shkolnik, E. L., Anglada-Escudé, G., Liu, M. C., et al. 2012, *ApJ*, 758, 56
- Sjouwerman, L. O., Capen, S. M., & Claussen, M. J. 2009, *ApJ*, 705, 1554
- Sjouwerman, L. O., Pihlström, Y. M., Claussen, M. J., & Collaboration, B. 2015, *Why Galaxies Care about AGB Stars III A Closer Look Sp. Time*, 497, 499
- Sjouwerman, L. O., Pihlström, Y. M., Rich, R. M., Claussen, M. J., & Morris, M. R. 2017, in *Proc. Int. Astron. Union*, Vol. 336, 180–183
- Sjouwerman, L. O., Pihlström, Y. M., Rich, R. M., Morris, M. R., & Claussen, M. J. 2017, in *IAU Symposium*, Vol. 322, *The Multi-Messenger Astrophysics of the Galactic Centre*, ed. R. M. Crocker, S. N. Longmore, & G. V. Bicknell, 103–106
- Skrutskie, M. F., Cutri, R. M., Stiening, R., et al. 2006, *ApJ*, 131, 1163
- Slee, O. B., Willes, A. J., & Robinson, R. D. 2003, *Publ. Astron. Soc. Aust.*, 20, 257
- Smirnov, O. M. & Tasse, C. 2015, *MNRAS*, 449, 2668
- Sofue, Y. 2017, *PASJ*, 69, 1
- Spangler, S. R. 1976, *PASP*, 88, 187
- Sparks, W. B., Bond, H. E., Cracraft, M., et al. 2008, *AJ*, 135, 605
- Srinivasan, S., Meixner, M., Leitherer, C., et al. 2009, *ApJ*, 137, 4810

- Stroh, M. C., Pihlström, Y. M., Sjouwerman, L. O., et al. 2018, *ApJ*, 862, 153
- Stroh, M. C., Pihlström, Y. M., Sjouwerman, L. O., et al. 2019, *ApJS*, 244, 25
- Surcis, G., Vlemmings, W., Torres, R., van Langevelde, H., & Hutawarakorn Kramer, B. 2011, *A&A*, 533, A47
- Surcis, G., Vlemmings, W. H. T., van Langevelde, H. J., Hutawarakorn Kramer, B., & Quiroga-Nuñez, L. H. 2013, *A&A*, 556, A73
- Swarup, G. 1991, *Proc. Int. Astron. Union*, 131, 376
- Tan, J. C., Beltran, M. T., Caselli, P., et al. 2014, *Protostars Planets VI*, 149
- Tarter, J. C. & Welch, W. J. 1986, *ApJ*, 305, 467
- Tasse, C. 2014, *ArXiv e-prints* 1410.8706
- Tasse, C., Hugo, B., Mirmont, M., et al. 2018, *A&A*, 611, A87
- Thompson, A. R., Clark, B. G., Wade, C. M., & Napier, P. J. 1980, *ApJS*, 44, 151
- Trapp, A. C., Rich, R. M., Morris, M. R., et al. 2018, *ApJ*, 861, 75
- Trumpler, R. 1930, *Lick Obs. Bull.*, 420, 154
- Turnpenney, S., Nichols, J. D., Wynn, G. A., & Casewell, S. L. 2017, *MNRAS*, 470, 4274
- Ungren, A. 1978, *AJ*, 83, 626
- Urquhart, J. S., Moore, T. J. T., Schuller, F., et al. 2013, *MNRAS*, 431, 1752
- Van De Hulst, H. 1949, *Physica*, 15, 740
- van der Veen, W. & Habing, H. 1998, *A&A*, 194, 125
- van der Walt, J. 2005, *MNRAS*, 360, 153
- van Haarlem, M. P., Wise, M. W., Gunst, A. W., et al. 2013, *A&A*, 556, A2
- van Langevelde, H., Quiroga-Nuñez, L. H., Vlemmings, W., et al. 2019, in *Proc. Sci. EVN2018*, 43
- van Weeren, R. J., Brunetti, G., Brüggén, M., et al. 2016, *MNRAS*, 818, 204
- Vásquez, S., Zoccali, M., Hill, V., et al. 2013, *A&A*, 555, A91
- Vassiliadis, E. & Wood, P. R. 1993, *ApL*, 413, 641
- Villadsen, J. & Hallinan, G. 2019, *ApJ*, 871, 214
- Wainscoat, R. J., Cohen, M., Volk, K., Walker, H. J., & Schwartz, D. E. 1992, *ApJS*, 83, 111
- Wegg, C. & Gerhard, O. 2013, *MNRAS*, 435, 1874
- Wenger, M., Ochsenbein, F., Egret, D., et al. 2000, *A&AS*, 143, 9
- West, A. A., Hawley, S. L., Bochanski, J. J., et al. 2008, *AJ*, 135, 785

- West, A. A., Weisenburger, K. L., Irwin, J., et al. 2015, *ApJ*, 812
- White, R. L., Becker, R. H., Helfand, D. J., & Gregg, M. D. 1997, *ApJ*, 475, 479
- White, S. M. & Franciosini, E. 1995, *ApJ*, 444, 342
- White, S. M., Jackson, P. D., & Kundu, M. R. 1989, *ApJS*, 71, 895
- Whitelock, P. 2003, *Astrophys. Sp. Sci. Libr.*, 283, 19
- Whitelock, P. A., Feast, M. W., & Van Leeuwen, F. 2008, *MNRAS*, 386, 313
- Wielebinski, R. 2012, *J. Astron. Hist. Herit.*, 15, 76
- Williams, P. K., Berger, E., Irwin, J., Berta-Thompson, Z. K., & Charbonneau, D. 2015, *ApJ*, 799, 192
- Williams, W. L., Van Weeren, R. J., Röttgering, H. J., et al. 2016, *MNRAS*, 460, 2385
- Wood, P. R., Alcock, C., Allsman, R. A., et al. 1999, in *Proc. Int. Astron. Union*, Vol. 191, 632
- Wouterloot, J. & Brand, J. 1989, *A&AS*, 80, 149
- Wright, N. J., Drake, J. J., Mamajek, E. E., & Henry, G. W. 2011, *ApJ*, 743, 48
- Xu, Y., Hou, L.-G., & Wu, Y.-W. 2018, *RAA*, 18, 146
- Xu, Y., Reid, M., Dame, T., et al. 2016, *Sci. Adv.*, 2, e1600878
- Xu, Y., Voronkov, M. A., Pandian, J. D., et al. 2009, *A&A*, 507, 1117
- Yadav, R. K., Christensen, U. R., Wolk, S. J., & Poppenhaeger, K. 2016, *ApJ*, 833, L28
- Yang, H., Liu, J., Gao, Q., et al. 2017, *ApJ*, 849, 36
- Yusof, N., Hirschi, R., Meynet, G., et al. 2013, *MNRAS*, 433, 1114
- Zic, A., Stewart, A., Lenc, E., et al. 2019, *MNRAS*, 488, 559

Nederlandse Samenvatting

Honderd jaar geleden was de kennis van ons sterrenstelsel, de Melkweg, nog zeer basaal. Het was onduidelijk of de sterren aan de hemel deel uitmaakten van één van vele groepen in het universum, of dat de sterren alom verspreid waren. Hierover vond destijds een debat plaats tussen twee gerenommeerde Amerikaanse astronomen die op basis van de beschikbare waarnemingen verschillende hypothesen voorstelden. Enerzijds stelde Harlow Shapley voor dat we in een eiland-universum leven en dat andere eiland-universums niet konden worden ontdekt omdat ze zo ver weg waren. Aan de andere kant verdedigde Heber Curtis dat we in een klein sterrenstelsel leven en dat andere sterrenstelsels niet konden worden waargenomen door de verduistering in het galactische vlak. Als men hierop terugkijkt, vindt men dat aan de basis van deze tweedracht een gebrek ligt aan nauwkeurige metingen van de afstand tot andere sterren. Omdat een betrouwbare verdeling van de sterren rond de zon niet beschikbaar was, was het onmogelijk om te bepalen welke objecten aan de hemel op veel grotere afstand staan dan de omringende objecten.



Figuur A1: *Overzicht van de Melkweg met de posities van gebieden waar massieve sterren vormen zoals gemeten in het kader van het BeSSeL project, waarbij de afstandonzekerheid wordt gegeven door de symboolgrootte. En daarbij weergegeven de afgeleide posities van de spiraalarmen (Reid et al. 2019). In deze voorstelling staat de zon op positie (0,8.15) kpc van het melkwegcentrum en roteert de melkweg met de klok mee.*

In de loop van de tijd kwamen er steeds nieuwe technologieën die ons in staat stelden om meer nauwkeurige schattingen van afstanden en eigenbewegingen te maken en te ontdekken dat de eiland-universums, of sterrenstelsels, extragalactische objecten zijn die ten opzichte van ons bewegen. Bovendien bleek dat ons sterrenstelsel een specifieke vorm heeft waarbij de sterren zich bevinden in een draaiende schijf met een specifieke morfologie, met prominente spiraalarmen en een centrale galactische balk (Fig. A1 and A2).

Tijdens de totstandkoming van dit proefschrift leverde de *Gaia*-ruimtemissie nauwkeurige astrometrische metingen aan voor meer dan een miljard sterren in de Melkweg. Maar de grote hoeveelheid stof die het visuele licht absorbeert en verstrooit, met name in het galactische vlak, is een beperking voor de door *Gaia* aangeleverde gegevens. Radio straling, daarentegen, wordt niet gehinderd door stof en kan dus gemakkelijk het galactische vlak doordringen en zo gebruikt worden voor aanvullende metingen (Fig. A3). Recente campagnes in het radio regime (bijvoorbeeld BeSSeL ⁵ en BAaDE ⁶) hebben posities en bewegingen van heldere stellaire bronnen (bekend als masers ⁷) gemeten in het galactisch vlak, door gebruik te maken van een techniek die Very Long Baseline Interferometry (VLBI) genoemd wordt. Met deze techniek wordt een stellaire bron waargenomen met verschillende radio antennes die ver uit elkaar staan, zelfs op verschillende continenten. De gemeten signalen worden gecombineerd tot een zeer gedetailleerde kaart van de radio bron. Door het bestuderen van de posities en snelheden van de sterren in het galactische vlak met VLBI is de structuur van de Melkweg in kaart gebracht (Fig. A1 en A2).

Dit proefschrift toont aan hoe robuuste, astrometrische metingen op de radio golflengten zijn te verwezenlijken voor jonge massieve sterren in de Melkweg. De resultaten worden vergeleken met simulaties voor stukken van de Melkweg die nog niet zijn waargenomen, met als doel de toepasbaarheid van deze techniek te testen. Bovendien worden optisch en radio gegevens gecombineerd voor geëvolueerde sterren in de buurt van de zon, hetgeen gebruikt wordt om deze specifieke sterren te karakteriseren met behulp van aanvullende informatie uit het infrarood. Ten slotte werd er een studie gedaan aan een speciale dubbelster, waarbij werd aangetoond dat nieuwe astrofysische informatie kan worden verkregen door nauwkeurige astrometrische metingen op verschillende momenten en verschillende frequenties te vergelijken.

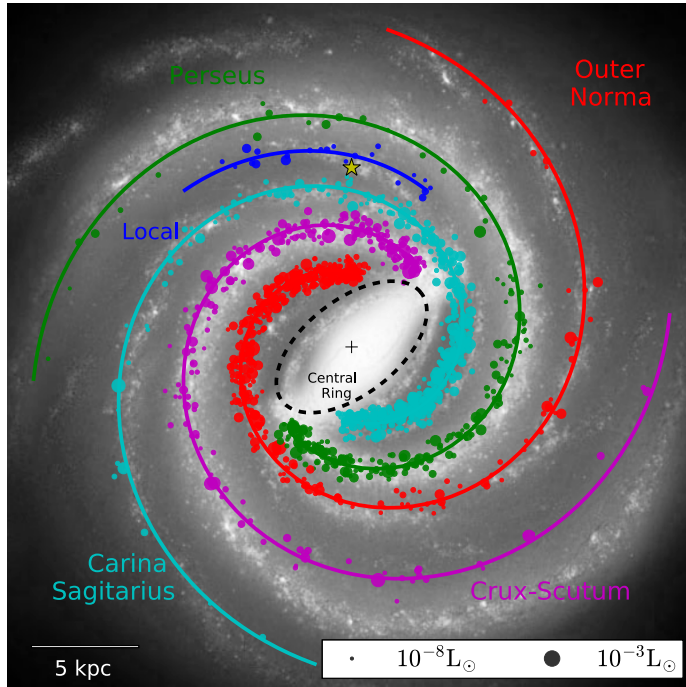
Het doel van dit proefschrift is om aan te tonen hoe de precieze astrometrische metingen van stellaire radiobakens kunnen worden gebruikt om cruciale informatie te verkrijgen over de eigenschappen van verschillende stellaire systemen. Ook kunnen belangrijke galactische structuren en parameters bepaald worden. Hierbij is gebruik gemaakt van astrometrische en fotometrische waarnemingen op verschillende golflengtes, geavanceerde Monte Carlo-simulaties en theoretische modellen. Dit proefschrift probeert de volgende vier vragen te beantwoorden:

- **Hoofdstuk 2:** Hoe kunnen VLBI-astrometrische metingen van de gebieden waar massieve sterren vormen worden gebruikt om de structuur van spiraalarmen te traceren?
- **Hoofdstuk 3:** Hoe nauwkeurig kunnen we de fundamentele galactische parameters schatten als onze waarnemingen beperkt zijn wat betreft de gevoeligheid en de locaties van de telescopen?
- **Hoofdstuk 4:** Hoe kunnen verschillende astrometrische datasets op verschillende golflengten gebruikt worden om oude stellaire populaties in de buurt van de zon te bestuderen?

⁵<http://bessel.vlbi-astrometry.org/>

⁶<http://www.phys.unm.edu/baade/>

⁷Straling doe van nature kan voorkomen in de ruimte rond speciale sterren en die volgens hetzelfde principe werkt als een lasers, maar dan op radio golflengtes.



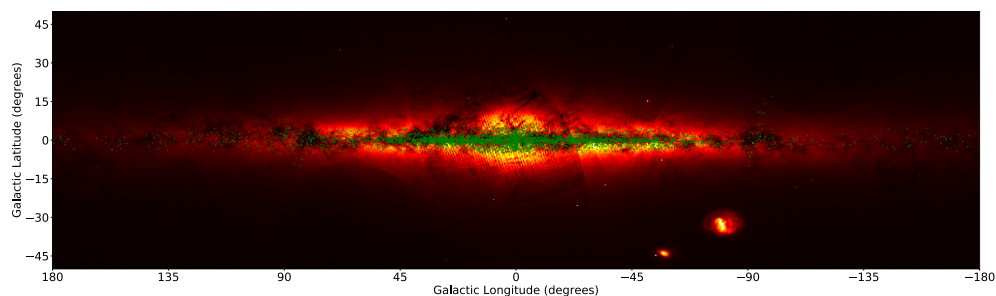
Figuur A2: *Galactisch vlak: een gesimuleerde distributie van de locaties van massieve sterren, geprojecteerd op een grafiek van de Melkweg (R. Hurt: NASA/JPLCaltech/SSC). De grootte van de symbolen geeft de helderheid van elke bron weer.*

- **Hoofdstuk 5:** Hoe kunnen astrometrische metingen gebruikt worden om de variabele radio-emissie van een dubbelster te ontdekken en te bestuderen?

In de volgende paragrafen beschrijf ik de inhoud van elk wetenschappelijk hoofdstuk van dit proefschrift door te laten zien hoe de hierboven gestelde vragen worden beantwoord.

In hoofdstuk 2 wordt onderzoek gepresenteerd aan een gebied met massieve stervorming in de buitenste spiraalarm van de Melkweg: Sharpless 269 (S269). Met behulp van 16 waarnemingen met de Very Large Baseline Array (VLBA) in de Verenigde Staten, werd een nauwkeurige metingen gedaan van de afstand en eigenbewegingen van de water masers in S269. De verkregen astrometrische resultaten bevestigen dat de rotatiecurve op grote afstand van het centrum van de Melkweg vlak is. Gebruikmakend van de verkregen afstand, in combinatie met een galactische simulatie en waarnemingen van andere jonge massieve sterren in het buitengebied, was het mogelijk om het bestaan van een knik in de buitenste arm te aan te tonen. Bovendien werden drie sterren gevonden in de *Gaia* catalogus die waarschijnlijk lid zijn van dezelfde sterrengroep, gezien hun eigenbeweging, parallax en leeftijd (het zijn namelijk massieve, jonge sterren).

In hoofdstuk 3 wordt onderzoek gepresenteerd aan de populatie van jonge massieve sterren in de Melkweg, waarbij heel veel datasets worden gesimuleerd en vervolgens vergeleken met de waargenomen dataset van het BeSSeL-onderzoek. Hierbij kan geverifieerd worden dat de diverse structuur parameters van de Melkweg, die verkregen werden uit de BeSSeL waarnemingen, niet beïnvloed zijn door de gebruikte selectie van maser bronnen. Het blijkt zelfs dat de gepubliceerde foutschattingen van de meeste parameters aan de conservatieve



Figuur A3: De galactische verdeling van de radio sterren die worden gebruikt in het BAaDE-project, maar waarvoor geen *Gaia* tegenhanger bekend is (groene punten), geplote over de eerste hemelkaart van *Gaia*. Deze selectie correleert sterk met de gezichtslijnen waar in het optische regime veel stof het zicht belemmert. Credit: ESA / *Gaia* / DPAC.

kant zijn. We laten zien dat toekomstige waarnemingen met behulp van masers aan de het zuidelijke hemel de schattingen van deze parameters van de Melkweg zullen verbeteren.

In hoofdstuk 4 zijn de objecten van het BAaDE-project bestudeerd met gegevens uit catalogi waargenomen in verschillende golflengtegebieden, zoals het optisch, infrarood en radio. Door deze verzamelingen met elkaar te vergelijken kunnen we de BAaDE-bronnen selecteren rond de zon (2.060 sterren), waarbij voornamelijk geëvolueerde sterren werden gevonden. De absolute (bolometrische) magnitudes werden vergeleken met verzamelingen van geëvolueerde sterren uit de literatuur, waarbij een vervuiling werd aangetoond met lichtzwakke objecten, waarschijnlijk jonge sterren. Niettemin hebben we aangetoond dat de eigenschappen van sterren waarvoor SiO-masers worden gedetecteerd consistent zijn met wat we verwachten voor zuurstofrijke Mira-sterren met perioden tussen de 250 en 750 dagen.

In hoofdstuk 5 hebben we bij toeval de radio-emissie van de dubbelster Ross 867-8 herontdekt, toen we de astrometrie van archiefgegevens van de Giant Metrewave Radio Telescope in India inspecteerden. In dit dubbelster systeem hebben beide dwergsterren vergelijkbare kenmerken zoals het spectrale type, astrometrische parameters, leeftijd en emissie in het infrarood, optisch en röntgen gebied. Nadat we de archieven van verschillende radiotelescopen hebben bestudeerd, konden we bevestigen dat alleen Ross 867 erg helder is op radiogolflengten, terwijl Ross 868 onopgemerkt blijft, hoewel beide sterren waarschijnlijk even oud zijn. Omdat ze in een wijde omloopbaan om elkaar draaien, is dit dubbelstersysteem een laboratorium om de eigenschappen gerelateerd aan de activiteit in het radio van zulke dwergsterren te onderzoeken. Ten slotte wordt gespeculeerd dat het waargenomen verschil in activiteit in radiostraling tussen de twee sterren te wijten zou kunnen zijn aan verschillen in magnetische veldtopologieën of dat Ross 867 een intrinsiek andere dynamo heeft.

English Summary

One hundred years ago, we still had a very basic knowledge of our Galaxy, the Milky Way. It was unclear whether the stars in the sky were part of a group, and therefore there could be other groups of stars in the universe, or the stars were widely spread in the universe. That is why a debate was organized between two renowned American astronomers at the time who proposed different hypotheses based on the available observations. On the one hand, Harlow Shapley proposed that we live in an island universe and that other island universes have not been detected because they were so far away. On the other hand, Heber Curtis proposed that we live in a small galaxy, and that other galaxies cannot be observed because of the dust present in our Galaxy that absorbs the light coming from other galaxies. By looking back, one finds that the basis of this discord was the lack of accurate measurement of the distances to other stars. By not having a reliable distribution of the stars around the Sun, it was impossible to determine which objects in the sky are part of our Galaxy or those that seem well beyond.

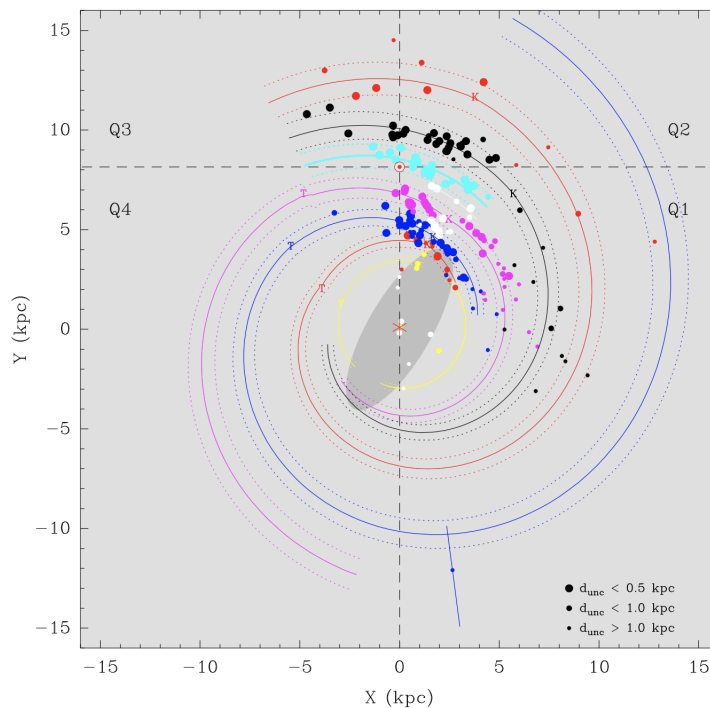


Figure B1: Plane view of the Milky Way showing the positions of the high-mass star-forming regions measured by the BeSSeL survey and the inferred positions of the spiral arms (Reid et al. 2019), where the distance uncertainty is expressed as the marker size. In this view, the Sun is located at (0,8.15) kpc from the center and the Galaxy rotates in the clockwise direction.

Over time, new technologies came into use, that allowed astronomers to establish more accurate distances and stellar motions finding that the island universes, or galaxies, are extra-

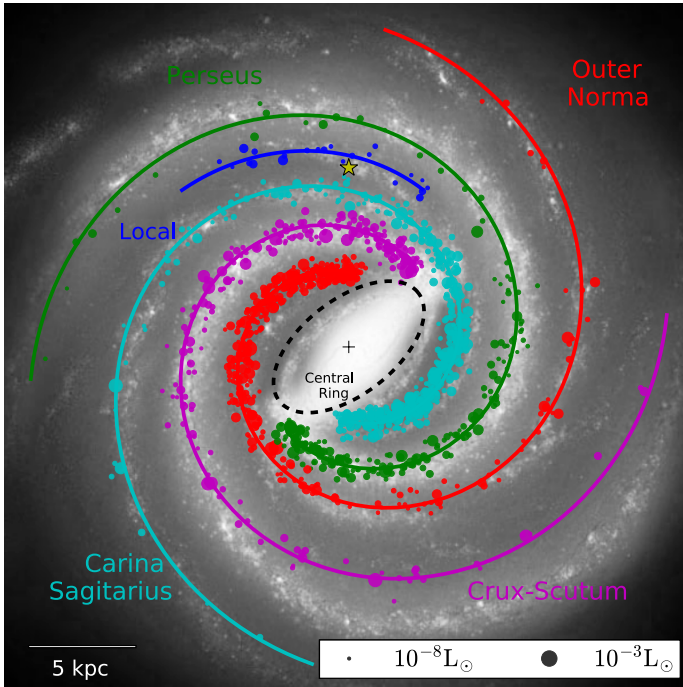


Figure B2: Simulated distribution of High Mass Star-Forming regions overlaid on an artist impression of the Milky Way (R. Hurt: NASA/JPL/Caltech/SSC). The size of the points represents the luminosity for each source.

galactic objects that are moving with respect to us. In addition, it was found that our Galaxy has a specific shape where the stars are found in a rotating disk that exhibits several morphological peculiarities such as prominent spiral arms and a central bar (Fig. B1 and B2).

During the time of this thesis, the *Gaia* space mission provided accurate position and velocity measurements for more than a billion stars in the Milky Way. However, the data provided by *Gaia* is limited by the large amount of dust that absorbs and scatter the light at optical wavelengths, particularly forward the Galactic plane. In contrast, radio waves are not affected by the dust and therefore, can easily penetrate the Galactic plane providing complementary data (Fig. B3). Recent campaigns in the radio wavelength regime (see for example BeSSeL⁸ and BAaDE⁹) have measured accurate positions and motions of bright stellar sources (known as masers¹⁰) in the Galactic plane using a technique called Very Long Baseline Interferometry (VLBI). In this technique, a stellar object is detected by several radio antennas spread at long distances, even at different continents. The signals detected are combined generating a detailed image of the object. By studying the positions and velocity of the stars in the Galactic plane using VLBI, large Galactic structures have been detected (Fig. B1 and B2).

This thesis demonstrates how robust astrometric measurements can be done in the radio regime for young massive stars throughout the Galaxy. Such results are compared with simulations for Galactic areas which have not been observed to determine the limits of this

⁸<http://bessel.vlbi-astrometry.org/>

⁹<http://www.phys.unm.edu/baade/>

¹⁰Which are naturally generated in different stellar environments and follows the same physical principle as lasers but in the radio regime.

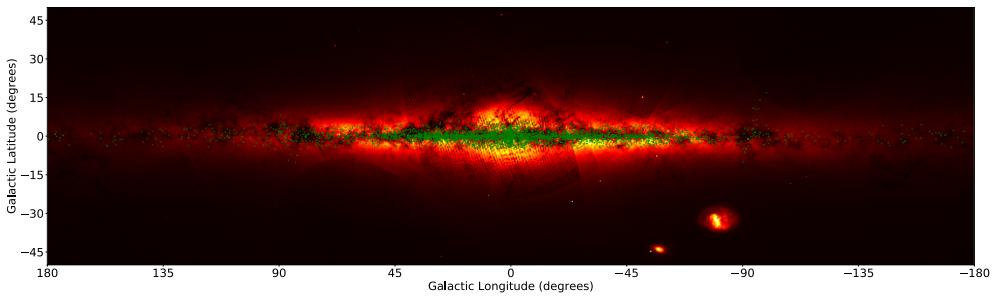


Figure B3: The Galactic distribution of the radio stellar targets used in the BAaDE project without a *Gaia* counterpart (green points) overplotted on the first sky map projection produced by *Gaia*. This sample accurately correlates with highly obscured regions in the optical regime. Credit: ESA/*Gaia*/DPAC.

technique. In addition, the matching between the optical and the radio data are established for evolved stars around the Sun, which are used to characterize the stellar population in the Galactic plane using additional information at infrared wavelengths. Finally, a study of a particular binary system was carried out that demonstrates how much stellar information can be obtained by having accurate astrometric measurements from different epochs and at different frequencies.

The goal of this thesis is to demonstrate how accurate astrometric measurements of radio stellar beacons can be used to obtain crucial information of particular stellar properties of different stellar systems, as well as to deduce major Galactic structures and parameters. To do that, we made use of astrometric and photometric observations at different wavelengths, advanced Monte Carlo simulations, and theoretical modeling. This thesis aims at answering these four questions:

- **Chapter 2:** How can VLBI astrometric measurements of High Mass Star-Forming Regions be used to trace spiral arm structures?
- **Chapter 3:** How accurate can we estimate the structural parameters of the Milky Way if we have observations with limited sensitivity and a fixed location of the telescopes?
- **Chapter 4:** How can cross-matches of astrometric data at different wavelengths be used to study old stellar populations in the Solar neighborhood?
- **Chapter 5:** How can astrometric measurements be used to discover and study variable stellar radio emission from a binary stellar system?

In the following paragraphs, I describe the content of each scientific chapter of this thesis by illustrating how they answer the questions related above.

In Chapter 2, an investigation is presented on one High Star-Forming Region located in the Outer spiral arm of the Milky Way: Sharpless 269 (S 269). Using 16 observations with the Very Large Baseline Array (VLBA) in the United States, accurate measurements of the distance and proper motions of the water masers in S269 were made. The astrometric results obtained confirm a flat Galactic rotation curve at large distances from the center of the Milky Way. Using the obtained distance together with a Galactic simulation and observations of other young massive stars in the Outer region, it was possible to prove the existence of a kink in the Outer arm. In addition, three sources were found in the *Gaia* catalog that are likely

members of the same stellar association given their proper motion, parallax and evolutionary stage (very massive young stars).

In Chapter 3, the population of young massive stars in the Milky Way has been simulated, generating many samples, and comparing them with observed samples from the BeSSeL survey. It was verified that the structural parameters of the Milky Way obtained by BeSSeL are not biased by the sample selection used. In fact, the published error estimates appear to be conservative for most parameters. We show that future BeSSeL data and future observations using masers from the southern region of Milky Way will improve the estimates of the structural parameters of the Milky Way and reduce their mutual correlation.

In Chapter 4, the targets of the BAaDE project have been studied with data from several surveys optical, infrared and radio. By cross-matching these surveys, we have characterized the BAaDE target sample around the Sun (2,060 stars), which mainly consists of evolved stars. The absolute bolometric magnitudes (stellar emission in the spectrum) were compared to samples of evolved stars from the literature finding that our selection is contaminated with low luminous objects, likely Young Stellar Objects. Nevertheless, we found that the properties of stars, for which there are SiO masers detected, are consistent with oxygen-rich Mira stars with periods between 250 and 750 days.

In Chapter 5, we have serendipitously rediscovered the radio emission of the binary system Ross 867-8 when we were inspecting the astrometry of archival data of the Giant Metrewave Radio Telescope in India. In this binary system, both dwarf stars share similar characteristics such as spectral type, astrometric parameters, age and emission in infrared, optical and X-rays. In addition, after reviewing the archival data of several radio observatories, we confirm that although both stars were likely coeval, only Ross 867 is very bright at radio wavelengths, while Ross 868 remains undetected. As they have a large orbital separation, this binary star system provides a laboratory to examine and restrict the stellar properties linked to radio activity in dwarf stars. Finally, it was speculated that the difference observed in radio activity between the stars could be due to differences in magnetic field topologies or that Ross 867 has an intrinsically different dynamo.

Resumen en Español

Hace cien años, todavía teníamos un conocimiento muy básico de nuestra galaxia: la Vía Láctea. No estaba claro si las estrellas en el cielo eran parte de un grupo, y por lo tanto, podría haber otros grupos de estrellas en el universo, o en cambio, sí las estrellas estaban ampliamente difundidas en el universo. Es por eso que se organizó un debate entre dos astrónomos estadounidenses que propusieron diferentes hipótesis basadas en observaciones. Por un lado, Harlow Shapley propuso que vivimos en un universo isla y que no se han detectado otros universos isla porque estaban muy lejos. Por otro lado, Heber Curtis propuso que vivimos en una pequeña galaxia y que no podíamos observar otras galaxias debido a que su luz era absorbida por el polvo presente en nuestra galaxia. Al mirar hacia atrás, uno encuentra que la base de esta discordia era la falta de mediciones precisas de las distancias a otras estrellas. Al no tener una distribución fiable de las estrellas alrededor del Sol, era imposible determinar qué objetos en el cielo son parte de nuestra galaxia o aquellos que parecen estar más allá.

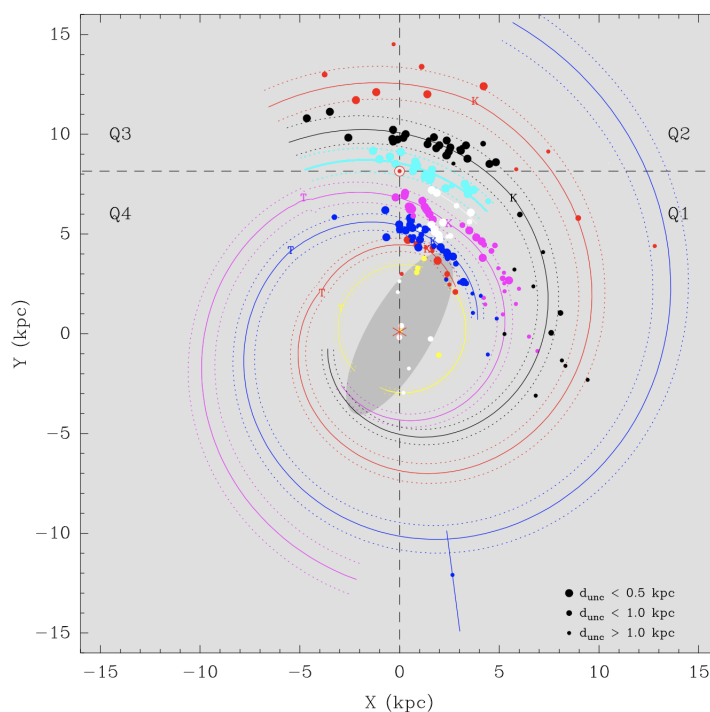


Figura C1: Vista de la Vía Láctea desde el polo norte galáctico que muestra las posiciones de las regiones de formación de estrellas masivas usadas en el proyecto BeSSeL y las posiciones inferidas de los brazos espirales (Reid et al. 2019), donde la incertidumbre de la distancia se relaciona con el tamaño de los puntos. En esta vista, el Sol se encuentra a (0,8.15) kpc y la Galaxia gira en el sentido de las agujas del reloj.

Con el tiempo, se usaron nuevas tecnologías que permitieron a los astrónomos estable-

cer distancias y movimientos de las estrellas más precisos, para encontrar que los universos isla o galaxias son de hecho objetos extragalácticos que se mueven con respecto a nosotros. Además, se descubrió que nuestra galaxia tiene una forma específica donde las estrellas se encuentran en un disco giratorio que exhibe varias particularidades morfológicas, tales como brazos espirales prominentes y una barra central (Fig. C1 y C2).

Durante el tiempo de esta tesis, la misión espacial *Gaia* proporcionó mediciones precisas de posición y velocidad para más de mil millones de estrellas en la Vía Láctea. Sin embargo, los datos proporcionados por *Gaia* están limitados por la gran cantidad de polvo que absorbe y dispersa la luz en longitudes de onda en el óptico, particularmente en el plano galáctico. En contraste, las ondas de radio no se ven afectadas por el polvo y, por lo tanto, pueden penetrar fácilmente en el plano galáctico proporcionando datos complementarios (Fig. C3). Campañas recientes en el radio (vease por ejemplo BeSSeL ¹¹ y BAaDE ¹²) han medido posiciones y movimientos precisos de fuentes estelares brillantes (conocidas como máseres ¹³) en el plano galáctico usando un técnica llamada interferometría de muy larga base (VLBI, por sus siglas en inglés). En esta técnica, un objeto estelar es detectado por varias antenas de radio distribuidas a largas distancias, incluso en diferentes continentes. Las señales detectadas se combinan generando una imagen detallada del objeto. Al estudiar las posiciones y la velocidad de las estrellas en el plano galáctico usando VLBI, se han detectado varias estructuras galácticas (Fig. C1 y C2).

Esta tesis demuestra cómo se pueden realizar mediciones astrométricas robustas en el régimen de radio para estrellas masivas jóvenes en toda la galaxia. Dichos resultados son comparados con simulaciones de áreas en la galaxia que no se han observado para determinar los límites de esta técnica. Además, se estableció la correspondencia entre los datos ópticos y de radio para las estrellas evolucionadas alrededor del Sol, utilizando información adicional en las longitudes de onda infrarrojas. Finalmente, se realizó un estudio de un sistema binario en particular que demuestra cuánta información estelar se puede obtener al tener mediciones astrométricas precisas de diferentes épocas y en diferentes frecuencias.

El objetivo de esta tesis es demostrar cómo se pueden utilizar mediciones astrométricas precisas de emisores estelares de radio para obtener información crucial de propiedades particulares de diferentes sistemas estelares, así como determinar las principales estructuras y parámetros de nuestra Vía Láctea. Para hacer eso, hicimos uso de observaciones astrométricas y fotométricas a diferentes longitudes de onda, simulaciones avanzadas de Monte Carlo y modelos teóricos. Esta tesis tiene como objetivo responder estas cuatro preguntas:

- **Capítulo 2:** ¿Cómo se pueden usar las mediciones astrométricas de VLBI en regiones de formación de estrellas masivas para trazar las estructuras de brazos espirales?
- **Capítulo 3:** ¿Qué tan precisos se pueden estimar los parámetros estructurales de la Vía Láctea si tenemos observaciones con sensibilidad limitada y una ubicación fija de los telescopios?
- **Capítulo 4:** ¿Cómo se pueden usar los datos astrométricos a diferentes longitudes de onda para estudiar las poblaciones estelares antiguas en el vecindario solar?
- **Capítulo 5:** ¿Cómo se pueden usar las mediciones astrométricas para descubrir y estudiar la emisión de estelar de radio que es variable de un sistema estelar binario?

¹¹<http://bessel.vlbi-astrometry.org/>

¹²<http://www.phys.unm.edu/baade/>

¹³Los cuales se producen naturalmente en diferentes ambientes estelares y siguen el mismo principio físico que los láseres pero en el régimen del radio.

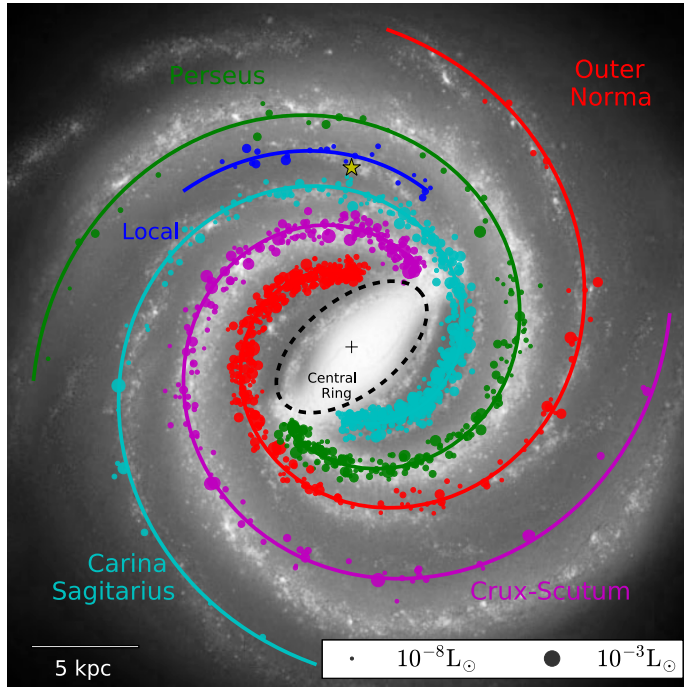


Figura C2: Simulación de la distribución de regiones de formación de estrellas masivas superpuesta en una impresión artística de la Vía Láctea (R. Hurt: NASA / JPLCaltech / SSC). La gráfica también incluye la luminosidad para cada fuente representada en el tamaño de los puntos.

En los siguientes párrafos, se describe el contenido de cada capítulo científico de esta tesis ilustrando cómo responden las preguntas relacionadas anteriormente.

En el Capítulo 2, se presenta una investigación sobre una región de formación de estrellas masivas ubicada en el brazo espiral exterior de la Vía Láctea: Sharpless 269 (S 269). Utilizando 16 observaciones con el Very Large Baseline Array (VLBA) en los Estados Unidos, se realizaron mediciones precisas de la distancia y los movimientos de los máseres de agua en S269. Los resultados astrométricos obtenidos confirman una curva de rotación galáctica plana a grandes distancias desde el centro de la Vía Láctea. Utilizando la distancia obtenida junto con una simulación galáctica y observaciones de otras estrellas masivas jóvenes en la región exterior, fue posible demostrar la existencia de un pliegue en el brazo exterior. Además, se encontraron tres fuentes en el catálogo de *Gaia* que probablemente sean miembros de la misma asociación estelar dado su movimiento, paralaje y etapa evolutiva (estrellas jóvenes muy masivas).

En el Capítulo 3, se simuló la población de estrellas masivas jóvenes en la Vía Láctea, generando muchas muestras y comparándolas con las muestras observadas del proyecto BeSSeL. Se verificó que los parámetros estructurales de la Vía Láctea obtenidos por BeSSeL no están sesgados por la selección de la muestra utilizada. De hecho, las estimaciones de error publicadas parecen ser conservadoras para la mayoría de los parámetros. Mostramos que los datos futuros de BeSSeL y las observaciones futuras utilizando máseres de la región sur de la Vía Láctea mejorarán las estimaciones de los parámetros estructurales de la Vía Láctea y reducirán

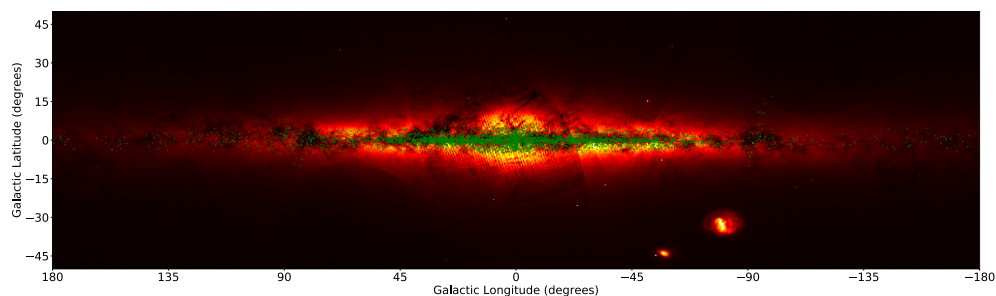


Figura C3: *Distribución galáctica de los objetivos estelares propuestos por el proyecto BAADE que no poseen contrapartes en Gaia (puntos verdes) superpuestos en el primer mapa del cielo que it Gaia obtuvo. Esta muestra se correlaciona con precisión con regiones muy oscuras en el régimen óptico. Crédito: ESA / Gaia / DPAC.*

su correlación mutua.

En el Capítulo 4, los objetivos del proyecto BAADE se han estudiado con datos de varias misiones en el óptico, infrarrojo y radio. Al comparar estas observaciones, se ha caracterizado la muestra del proyecto BAADE alrededor del Sol (2,060 estrellas), que consiste principalmente en estrellas evolucionadas. Las magnitudes bolométricas absolutas (emisión estelar en todo el espectro) se compararon con muestras de estrellas evolucionadas de la literatura encontrando que nuestra selección está contaminada con objetos de baja luminosidad, probablemente objetos estelares jóvenes. Sin embargo, descubrimos que las propiedades de las estrellas, para las cuales se detectan máseres de SiO, son consistentes con estrellas tipo Mira ricas en oxígeno con períodos entre 250 y 750 días.

En el Capítulo 5, hemos redescubierto por casualidad la emisión de radio del sistema binario Ross 867-8 cuando estábamos inspeccionando la astrometría de los datos de archivo del Radiotelescopio Gigante de Ondas Metricas en India. En este sistema binario, ambas estrellas enanas comparten características similares, como el tipo espectral, los parámetros astrométricos, la edad y la emisión en infrarrojo, óptico y rayos X. Además, después de revisar los datos de archivo de varios observatorios de radio, confirmamos que aunque ambas estrellas nacieron juntas, solo Ross 867 es brillante en las longitudes de onda de radio, mientras que Ross 868 permanece sin ser detectada. Como tienen una gran separación orbital, este sistema estelar binario proporciona un laboratorio para examinar y restringir las propiedades estelares vinculadas a la actividad de radio en las estrellas enanas. Finalmente, se especuló que la diferencia observada en la actividad de radio entre las estrellas podría deberse a diferencias en las topologías de campo magnético o que Ross 867 tiene una dinamo intrínsecamente diferente.

List of Publications

Refereed Publications

- **Quiroga-Nuñez L. H.**, van Langevelde H., Sjouwerman L., Pihlström Y., Brown A., Stroh M., Rich M. & Habing H., 2020, *Characterizing the BAaDE evolved stars in the Galactic foreground with Gaia*, in preparation
- **Quiroga-Nuñez L.H.**, Intema H., Callingham J., Villadsen J., et al., 2020, *Differences on radio emission from similar M dwarfs in the binary system Ross 867-8*, A&A 633, A130
- Immer K., Li J., **Quiroga-Nuñez L.H.**, Reid M., Wu Y. & Moscadelli L., 2019, *Trigonometric parallaxes in the far part of the Scutum arm*, A&A, 632, A123
- Reid M., Menten K., Brunthaler A., Zheng X., Dame T., Xu J., Li L., et al. (including **Quiroga-Nuñez L.H.**), 2019, *Trigonometric parallaxes of high-mass star forming regions: our view of the Milky Way*, ApJ, 885, 131
- **Quiroga-Nuñez L.H.**, Immer K., van Langevelde H., Reid M. & Burns, R., 2019, *Resolving the Distance Controversy for Sharpless 269*, A&A, 625, A70
- Pihlström Y., Sjouwerman L., Claussen M., Morris M., Rich M., van Langevelde H. & **Quiroga-Nuñez, L.H.**, 2018, *Positional Offsets Between SiO Masers in Evolved Stars and their cross-matched Infrared Counterparts*, ApJ, 868, 72
- **Quiroga-Nuñez L.H.**, van Langevelde H., Reid M. & Green J., 2017, *Galactic methanol maser distribution to constrain Milky Way parameters*, A&A, 604, A72
- Pinilla P., **Quiroga-Nuñez L.H.**, Benisty M., Natta A., Ricci L., Henning T., van der Plas G., et al., 2017, *Millimeter spectral indices and dust trapping by planets in brown dwarf disks*, ApJ, 846, 70
- Pinilla P., Benisty M., Birnstiel T., Ricci L., Isella A., Natta A., Dullemond C.P., **Quiroga-Nuñez L.H.**, et al., 2014, *Millimetre spectral indices of transition disks and their relation with the cavity radius*, A&A, 564, A51
- Surcis G., Vlemmings W., van Langevelde H., Hutawarakorn Kramer B. & **Quiroga-Nuñez L.H.**, 2013, *EVN observations of 6.7 GHz methanol maser polarization in massive star-forming regions II*, A&A 556, A73

Conference Proceedings

- van Langevelde H., **Quiroga-Nuñez L.H.**, Vlemmings W., Loinard L., Honma M., et al., 2019, *The Synergy between VLBI and Gaia astrometry*, PoS, EVN2018, V344, 43
- Immer K., Li J., **Quiroga-Nuñez L.H.**, Reid M., Zhang B. & Moscadelli L., 2019, *Where are you, Scutum? Tracking down a spiral arm with maser astrometry*, PoS, EVN2018, V344, 55
- Sjouwerman L., Pihlström Y., Trapp A., Stroh M., **Quiroga-Nuñez L.H.**, Lewis, M., et al., 2018, *A Masing BAaDE's Window*, IAU Proceedings 14 (S343), 334
- Forbrich, J., Williams, P.K.G., Drabek-Maunder, E., Howard, W., et al. (including **Quiroga-Nuñez L.H.**), 2018, *Meter- to Millimeter Emission from Cool Stellar Systems*, Proceedings 20th Workshop on Cool Stars, Stellar Systems, and the Sun.
- Monnier J., Ireland M., Krauss S., et al., 2018, (including **Quiroga-Nuñez L.H.**) *Planet Formation Imager: Project Update* Proceedings SPIE 10701,1070118 (2018)
- **Quiroga-Nuñez L.H.**, van Langevelde H., Sjouwerman L., Pihlström Y., Reid, M., et al., 2018, *Maser, infrared and optical emission for late-type stars in the Galactic plane*, IAU Proceedings 13 (S336), 184
- **Quiroga-Nuñez L.H.**, van Langevelde H., Reid M., Sjouwerman L., Pihlström Y., et al., 2018, *Astrometric Galactic maser measurements cross-matched with Gaia*, IAU Proceedings 13 (S334), 351
- **Quiroga-Nuñez L.H.**, van Langevelde H., Pihlström Y., Sjouwerman L. & Brown, A., 2018, *Finding evolved stars in the inner Galactic disk with Gaia*, IAU Proceedings 12 (S330), 245
- Kraus S., Monnier J., Ireland M. J., et al. (including **Quiroga-Nuñez L.H.**), 2016, *Planet Formation Imager: science vision and key requirements*, SPIE Proceedings, 99071K
- Mosquera H., Sanchez L., Pardo D., Caproni A., Abraham Z. & **Quiroga-Nuñez, L.H.**, 2011, *GWs from Ejection of Superluminal Components and Precession of Disks Driven by Bardeen-Petterson Effect*, IJMPCS 3, 482

Curriculum Vitae

I was born on September 15th, 1989 in Bogotá, Colombia. My parents Hector Enrique Quiroga Cubillos and Flor Nancy Nuñez Torres, come from a small town called Paime (Cundinamarca). Both came to the capital city Bogotá, where later they became lawyers. I spent my childhood between Bogotá and La Vega, a town 80 km away from Bogotá where my grandmother was working as a high school teacher. I remember my grandmother as my first math mentor since we spent the two hours car journey from Bogotá to La Vega solving math riddles that she created to enhance my memory and math skills.

During my high school years, I joined the Colegio Mayor de Nuestra Señora del Rosario. A private catholic school founded by the King of Spain in 1653 with a long tradition and recognition, mainly for being considered as the “cradle of the Colombian Republic”, since several Colombian presidents, writers, scientists and artists attended this school. During this time, the school awarded me with the Jose Celestino Mutis prize, the highest honor that a student can receive. This award allowed me to waive all tuition fees at the school, but also gave me direct and waived access to the private university associated to the school, The University of Rosary. Unfortunately, this university was at that time mainly focused on health and political studies, while I prefer to find my scientific path in other university. At this time, my objective was already set to Astronomy.

In 2007, I enrolled in the Physics undergraduate program at the National University of Colombia, the biggest public university of the country, always keeping the hope to one day become an astronomer. During my bachelor, I have acquired the needed skills to develop scientific research at the highest standards. I do remember spending long and stressful nights with my classmates (who are also my best friends) studying for different exams in Electrodynamics, Quantum Mechanics and Experimental Physics. Moreover, I also had the opportunity to take several graduate courses in Astronomy and Education. In fact, I was sent by the University to the San Andres Island in the Caribbean to train math teachers in public high schools in how to engage young people to science.

During the last years of the undergraduate program, I had the opportunity to attend several national and international scientific events that allowed me to learn about astrophysics, build a scientific network and meet other cultures. In particular, I recognize two that became really important for my future prospectives. The first Colombia Congress of Astronomy and Astrophysics (COCOA) in 2012 held in Medellin, where I met several Colombian astronomers that later became my guide. And the European Research Interferometry School held in Rimini (Italy) in 2011, organized by RadioNet. This school was my first contact with radio astronomy.

After defending my bachelor thesis in gravitational waves, I did internships at two different astronomy related institutions. One at the ASTRON/JIVE summer program in 2012. This first was the time I visit the place that has become my second home in The Netherlands: Dwingeloo. In this internship, I started working with “masers”, and therefore, it set the basis for my long term career. My second intern position was held at the Space Telescope Science Institute at Johns Hopkins University in Baltimore (USA). This last position has been one of the most rewarding experiences as a young scientist that I have ever had by being the only Latinamerican in the Summer Astronomy Space Program 2013. In the time between these intern positions, I was contracted by the local government in the city of Bogotá to develop public policies in Astronomy for the Planetarium of Bogotá. These three labor experiences

have forged the basis of my career that was just starting. For fall 2013, I was planning to start a master program at McGill University with a scholarship from this Canadian university. However, Leiden University has made an offer that I hardly could not reject: The Oort Scholarship. This scholarship was given to the best non-Dutch student planning to follow a scientific career in astronomy. Coming back to my loved Holland made me really happy, and also because I brought with me my half soul, my best friend, my unconditional support: my wife. At the same time in Colombia, the Mazda foundation awarded me as one of the best prospective young physicists of the country for which I am deeply honored.

My time as a master student at Leiden was very challenging: living a married life, learning about a new culture, taking astronomy lessons in English for the first time, while I was meeting new people. I did the two research projects that each Leiden master student must develop in order to graduate. In my case, they were Galactic masers simulations, and work on pipelines to improve HST images of debris disks. These projects were hardly enough to set my expectations of how would be the life as a professional astronomer, for which I was determined to continue as a PhD researcher.

During 2015, at the same time that I was ending my master studies, I was searching for a PhD position. Although very good offers came from MPA, MPIfR, Manchester and Lund, two PhD offers were especially attractive: Leiden/JIVE and Cambridge. However, when I was deciding where to go, my wife got an art scholarship at Erasmus University in Rotterdam at around 40 km in the south of Leiden. By taking the joint position between Leiden and JIVE, I was not only very glad to stay in the Netherlands, but also we (together with my wife) found a temporary solution for our 2-body problem, where we both could do what we love (Science & Art).

For the whole PhD period (from Fall 2015 until now), I can only describe it as the most dynamic 4 years of my life. Living in Rotterdam, and commuting daily to Leiden and weekly to Dwingeloo to do research in Astronomy was my daily basis. However, I also learned other skills by becoming a Volleyball trainer for expats and the sacristan of the Catholic Church at Rotterdam. Important events also came such as the birth of my lovely daughter, the loss of my younger brother, a change of nationality, a meeting with Pope Francis and visiting more than 20 countries between business and holiday trips. Now by looking backward, I must say THANK YOU, particularly to God, my family and all the people that contributed with this crazy astronomical dream. Now, my next step continues in the United States of America, as a Jansky Fellow at National Radio Astronomy Observatory (Socorro) and the University of New Mexico (Albuquerque), where I am expecting to actively continue enjoying this life.

Acknowledgments

I want here to thank all the people that have contributed with my career... (in no particular order)

... to my school friends that have shown that no matter the time, they are always happy for my achievements: Felipe, Sebastian, Raulo, Manolo, Mauricio, Efrain, Juan, Juan Manuel, Marco and Pato.

... to my classmates in Physics who are still helping me to solve my academic and life problems: Checho, S. Solorzano, Dany, Ligia, Laura, Jota, Paisa (pillo!), Monica, Nicolas, Juan David, and Nataly.

... to my first astronomy mentors who, since when I was in Colombia, have shown interest in my career: Cesar Ocampo, Herman Mosquera and Luis Felipe Rodriguez.

... to my supervisors in each internship and astronomy project that I have been involved in Colombia, Netherlands and the USA for giving me these fantastic opportunities to learn: Natalia Rippe, Gabrielle Surcis, Mathew Kenworthy and John Debes.

... to my fellow Astro-citizens, who has always supported me with advices and open arms when I am presenting my science worldwide: David Ardila, Rafael Martinez, Julian Alvarado, Gustavo Cruz and Paola Pinilla.

... to all the people at JIVE that have been so patient with my slow radio learning: Paco, Bob, Zsolt, Yvonne, Giuseppe, Paul, Aard, Leonard, Ilse, Waleed, Katharina, Benito, Olga, Dhanya, Jay, Minnie, Tatiana and Ross.

... to three radio astronomy mentors: Michael Garret, Michael Wise and Mark Reid for showing me this wonderful branch of astronomy.

... to my scientific collaborators worldwide to keep interested in the science that I work on: Huib Intema, Joe Callingham, Andreas Brunthaler, Harm Habing, Jackie Villadsen, Michael Stroh and Jimmi Green.

... to my Ph.D. mentors: Huib van Lagevelde and Anthony Brown for being much more than supervisors by regularly being concern about my academic and personal performance.

... to my fellows at Leiden Observatory for supporting me when I need it: Santiago, Liz, Pablo, Francisca, Nienke, Josh, Martijn, Auckland, Raymond, Andres and Ciriaco.

... to all the supportive people at Leiden Observatory who, despite the inconveniences, were always there to help: Evelijn Gerstel, Huub Rottgering and Xander Tielens.

... to my young astro colleagues that I met during different astronomy events for showing me that we can keep collaborating and laughing after a long time: Saavi, Janez, Natasha, Mia, Nimisha, Gerardo, Andres, Pavol, Agustin, Anny, Harold, Sabine, Marta and Rupert.

... to my Dutch teachers for all the patience with my terrible accent and who has profoundly affected (positively) my inburgering exams: Mandy, Cees and Mona.

... to the Vatican Observatory in head of Br. Guy Consolmagno, who has given me one of the most rewarding experience in my life, but particularly for my daughter's life.

... to my future mentors in New Mexico for supporting me during my PhD to achieve the position that I was dreaming of: Lorant Sjouwerman and Ylva Pihlström.

... to the church La Sagrada Familia in Rotterdam in the head of P. Theo Hansen and its community as they have brought to my life the spiritual calm in moments that I thought I would not make it.

... to all my Volley friends at Rosario, SKC, Libanon, and Expats clubs for allowing me to share with you delightful moments.

... Finally and most importantly, to my family in Colombia (Maria Leonor Torres Cardenas, Flor Nancy Nuñez Torres, Hector Miguel Quiroga Nuñez and Nancy Beatriz Quiroga Nuñez) and in The Netherlands (Katherin Daza Cañón, Chiara Quiroga Daza and Pipo): you have been my motivation and strength! All that I have made (and also will make) is not only dedicated to you, but are also your achievements given all the trust that you had set up on me.

... Lastly, to you dear reader for keep reading until here. Since there are always too many people to thank, I apologize if I forget to mention you.

